UNIVERSITÉ DE RENNES 1

THÈSE DE DOCTORAT DE

L'UNIVERSITÉ DE RENNES 1

ÉCOLE DOCTORALE N° 601
Mathématiques et Sciences et Technologies de l'Information et de la Communication
Spécialité : Mathématique et leurs intéractions

Par
Mohamed Yacine BEN ALI

Investigating Data-Model coupling using adjoint techniques for wind engineering

Thèse présentée et soutenue à Rennes, le 24 mars 2021
Unité de recherche : Fluminance (IRMAR/INRIA-INRAE), Université de Rennes 1

Rapporteurs avant soutenance :

Rémi Manceau	Directeur de recherche, LMAP
Denis Sipp	Directeur de recherche, ONERA (Meudon)

Composition du Jury :

Président :	Roger Lewandowski	Professeur, Université de Rennes 1
Examinateurs :	Rémi Manceau	Directeur de recherche, LMAP
	Denis Sipp	Directeur de recherche, ONERA (Meudon)
	Jocelyne Erhel	Directrice de recherche, INRIA (Rennes)
	Marcello Meldi	Maitre de conférence, ENSMA/PPRIME
	Vincent Mons	Chercheur, ONERA (Meudon)
Dir. de thèse :	Etienne Mèmin	Directeur de recherche, INRIA (Rennes)
Co-Dir. de thèse :	Dominique Heitz	Chercheur, INRAE (OPAALE)

Invité(s) :

Sylvain Aguinaga	Ingénieur, CSTB (Nantes)
Gilles Tissot	Chercheur, INRIA (Rennes)

To my parents and sisters

Acknowledgement

Foremost, I would like to express my sincere appreciation to all my supervisors; Dr. Etienne Mémin, Dr. Dominique Heitz, Dr. Gilles Tissot and Dr. Sylvain Aguinaga for the continuous support of my Ph.D study and research, for their patience, motivation and immense support.Their guidance helped me in all the time of research and writing of this thesis.

Besides my advisors, I want to thank Dr. Denis Sipp and Dr. Rémi Manceau for their careful reading of my manuscript, their insightful comments and hard questions. I would like also to thank the rest of my thesis committee: Prof. Roger Lewandowski, Dr. Jocelyne Erhel, Dr. Marcello Meldi and Dr. Vincent Mons, for agreeing to be part of the jury.

The physical and technical contribution of Both INRIA-INRAE and CSTB Nantes is truly appreciated. Without their support and funding, this project could not have reached its goal.

I thank my fellow labmates, from team Scirocco: Anthoine Salomon, Sylvain Prigent, Emmanuel Moebel for the multiples breaks. A special thanks to Etienne Meunier for the stimulating discussions and encouragement and for all the sports session (with Thibault) we have had in the last year, to Anaîs Badoual for her kindness and the multiple breaks. From my team Fluminance, i would like to say thanks to my friends and colleagues Pranav Chandramouli and Long Li, for all the discussions, dinners, the trips and all the fun we have had during the hole journey. I also want to thanks Evgueni Denvay for the cycle trips we have had during the last couple of months.

Last but not the least, I am extremely grateful to my parents, Jalila and Fakhreddine for their love, caring and sacrifices for educating and preparing me for my future. Also I express my thanks to my sisters Sabrine and Hajer and brother in laws Amir for their support and valuable encouragement.

Table of Contents

List of Figures

List of Tables

Résumé en français

Contribution de la thèse

Dans cette thèse, nous étudions l'un des modèles de fermeture de turbulence les plus courants pour la modélisation RANS dans un cadre d'assimilation de données variationnelle. Contrairement à la majeure partie des études menées dans la littérature où des mesures de vitesse sont considérées sur des parties significatives du domaine (pour un écoulement 2D avec une direction homogène), nous considérons dans cette étude un écoulement tridimensionnel réaliste et complexes avec à notre disposition uniquement des mesures expérimentales pariétales. Cette différence est loin d'être cosmétique puisqu'elle est ici construite pour traiter un cadre expérimental pratique utilisé en particulier dans l'industrie de la construction. Une dérivation analytique du modèle adjoint qui permet l'estimation de la direction de descente de la fonction de coût associée à un probleme d'assimilation de donnée est effectuée puis discrétisée à l'aide d'un schéma de volumes finis. La bibliothèque open source multi-physique OpenFOAM (Jasak, 1996) a servi à l'implémentation des itérations internes, c'est-à-dire le solveur direct et adjoint RANS, et les itérations externes pour la procédure d'AD. La méthodologie adjointe est utilisée dans cette thèse pour répondre à deux objectifs particuliers, détaillés ci-après.

D'une part, nous étudions certains cadres méthodologiques permettant un diagnostic approfondi de la fermeture de turbulence. Comme point de départ, nous utilisons d'abord cette méthodologie pour étudier les champs de sensibilité des coefficients de fermeture globale du modèle réalisable $k - \epsilon$ (Shih et al., 1995). Leur interprétation physique nous permettra de mettre en évidence les limites de l'applicabilité de tels modèles de fermeture à des fins de couplage modèle–données, en particulier pour les champs de vent autour d'un immeuble de grande hauteur (étude de cas choisie pour la thèse). Ce cadre discutera des limites et des améliorations dans l'estimation des charges de vent et des vitesses moyennes autour du bâtiment.

D'autre part, visant un couplage efficace entre le modèle et les données, nous considérons la méthode comme un outil de reconstruction de l'écoulement. Dans cette optique, une limitation est posée par la rigidité du modèle, c'est-à-dire que l'ensemble des solutions admissibles par le modèle n'inclus pas de région de l'espace d'état correspondant à une estimation pertinente. Afin de s'affranchir de cette difficulté nous avons considéré une assimilation dite sous *contrainte faible*. Dans ce cadre, nous avons en premier lieu les régions spatiales se prétant au mieux à l'intégration de nouveaux termes permettant de corriger les erreurs de modélisation. Dans une première classe de stratégies, en définissant un terme de forçage additif comme paramètre de contrôle, nous permettons à la solution de s'écarter des contraintes du modèle par défaut, pour corriger directement la diffusion de quantité de mouvement résultant du modèle de viscosité turbulente. Dans une seconde

classe, on considère plutôt l'adjonction d'un paramètre distribué qui permet d'identifier un terme manquant dans l'équation où la fermeture du modéle de turbulence est effectuée. Au-delà du fait qu'il offre une meilleure structure physique à la reconstruction grâce aux informations préalables apportées par le modèle RANS et qu'il évite le surajustement des données, le paramètre de contrôle optimal nous permet d'identifier des caractéristiques manquente dans les hypothèses de fermeture RANS initiales. En raison des observations clairsemées, le champ de sensibilité est généralement peu régulier pour les paramètres distribués, une recherche de paramètre dans l'espace de Sobolev (H^1) est également proposée pour renforcer l'efficacité de la méthode, c'est-à-dire en fournissant une direction de descente robuste pour l'algorithme de minimisation par descente de gradient.

La thèse est divisée en sept chapitres dont cinq décrivent les principales contributions de l'étude. L'état de l'art est présenté dans le chapitre 1. Dans le chapitre 2, un focus est mis sur la modélisation des écoulements turbulents atmosphériques à l'échelle du milieu urbain. Le chapitre 3, est dédié au développement de l'approche variationnelle de la procédure d'assimilation de données. La technique variationnelle est ensuite appliquée pour une analyse plus approfondie de la fermeture du modèle de turbulence dans le chapitre 4. Dans le chapitre 5, nous présentons l'ensemble d'équations RANS modifié avec le terme de forçage additif comme paramètre de contrôle. Dans le chapitre 6, la reconstruction de l'écoulement est opérée sous une paramétrisation qui satisfait les contraintes physiques données par le modèle de turbulence. Le chapitre 7 conclut la thèse par un résumé des réalisations des travaux et quelques suggestions pour la poursuite des travaux. Les listes de références accompagnées des annexes suivent le dernier chapitre.

Résumé du Chapitre 1: L'état de l'art

D'abord, une brève revue historique des études menées sur le problème de l'ingénierie structurelle de vent est donnée. Ensuite, les techniques d'AD existantes sont énumérées. Un aperçu des travaux antérieurs appliquant ces techniques pour le couplage de modèle-données dans les études générales de dynamique des fluides computationnelle (CFD) est donné après. Le chapitre finis par un aperçu des travaux utilisant ces techniques associés à la modélisation numérique RANS.

Résumé du Chapitre 2: modélisation de la turbulence et configuration numérique

Le but de ce chapitre est d'identifier les paramètres de modélisation qui forment la socle des études de procédure d'AD dans la suite du manuscrit. Le modèle mathématique décrivant les équations de Navier-Stokes moyennées dans le temps, sa fermeture associée de la turbulence, le profil atmosphérique d'entrée du domaine et le traitement près de la paroi sont introduits. Parallèlement à cela, une brève description est faite du montage expérimental, mené précédemment par (Sheng et al., 2018). En rassemblant les

recommandations de la littérature qui garantissent une analyse numérique rigoureuse, une configuration de calcul a été construite pour l'étude d'un bâtiment parallépipédique.

La cohérence entre le profil du vent, de la couche limite atmosphérique (ABL) modélisé, et le traitement des parois du sol a été vérifiée dans un domaine vide. La vérification de cette cohérence requière que l'homogénéité (en amont) des profils de vent se voit persiste en aval en l'absence du bâtiment. Le chapitre se poursuit par une étude de validation pour évaluer les erreurs liées à la discrétisation (avant l'assimilation). Cela concerne la convergence de la grille et la vérification du schéma numérique. Dans le premier cas, la solution donnée (la pression à la paroi et la vitesse moyenne dans l'axe du sillage) par la grille choisie tombe dans la limite asymptotique. Dans le dernier cas, la capacité de différents schémas avec limiteurs de flux à savoir, Gamma, superBee, linéaire au vent sont testés en évaluant la pression pariétale et la vitesse moyenne dans le sens du courant. Ces résultats simulés sont comparés aux expériences en soufflerie. Les résultats ont montré que Gamma et Linear-Upwind ont conduis à des résultats identiques, alors que les résultats pour le limiteur de superBee ont légèrement dévié des données, notament pour la pression d'arrachement près des bords d'attaque et la longueur de recirculation . Sur les trois schémas, le limiteur de flux linéaire au vent semble prometteur pour le développement de la procédure d'assimilation, car il assure une meilleur convergence itérative du solveur RANS par rapport au schéma Gamma.

Résumé du Chapitre 3: Développement de méthodes pour la procédure d'AD variationnelle

Ce chapitre est dédié à la construction d'une méthodologie d'assimilation de donnée pouvant être appliquée à toute fermeture de turbulence arbitrairement complexe. Sur la base de la théorie du contrôle optimal, une différenciation, cohérente avec les équations de transport réalisables $k-\epsilon$ (Shih et al., 1995) et de la loi proche paroi de l'écoulement moyen a été effectuée. On note que la construction des équations de flux adjoint éclaire le rôle des conditions aux limites adjoints. Cela a abouti à la définition d'un modèle adjoint continu, avec ses conditions aux limites cohérentes, de l'opérateur tangent linéaire du modèle RANS. Les conditions aux limites adjointes induites par la loi de fermeture à la paroi ont été dérivées. De plus, quelques traitements spécifiques liés à la discrétisation des volumes finis ont été donnés.

Les équations différentielles adjointes (formelles) sont introduites et les détails de leur dérivation sont donnés dans l'annexe 7.2.

Résumé du Chapitre 4: L'assimilation des données comme outil de diagnostic pour la structure de fermeture de turbulence

Compte tenu de la double description de la dynamique composée du modèle direct RANS et de l'adjoint de son modéle tangent linéaire, nous avons exploré un dispositif méthodologique qui permet une analyse de sensibilité efficace et un diagnostic approfondi de la fermeture du modéle de turbulence.

Dans un premier temps, nous avons inspecté les variables d'état adjointes en relation avec leur signification physique. Les cartes de sensibilité des coefficients globaux du *realizable* $k-\epsilon$ avaient révélé un grand intérêt pour leur optimisation principalement au niveau des couches de cisaillement résultant de la séparation de l'écoulement sur les bords latéraux avant et au sommet du bâtiment. Cependant, une faible sensibilité dans la majeure partie de la région de recirculation du sillage a été observée. Malgré la variabilité spatiale des champs de sensibilité, il a été montré que la condition d'optimalité réduit considérablement la dimension de la dépendance du modèle à chaque coefficient.

Par ailleurs une étude de calibration a été conduite afin d'étudier les conditions de validité du modèle de turbulence, à travers des scénarios de maintien/relâchement de certaines hypothèses utilisées dans la définition des coefficients du modèles. Cette étude a été menée dans le but de fournir une meilleure compréhension de la variabilité des solutions du modèle en fonction de ses constantes globaux. En ce qui concerne les hypothèses de modèle, un meilleur couplage avec les données est obtenu en imposant une contrainte qui équilibre la redistribution de l'énergie cinétique avec celle de la quantité de mouvement, bien que la sensibilité initiale au préfacteur du term de redistribution suggère une tendence à réduire, en préconisant globalement une couche de mélange turbulente plus mince. Cela suggère que c'est une hypothèse physiquement valide qui structure le modèle et contribue ensuite à la convergence. A l'inverse, en relâchant cette contrainte et en établissant une relation qui dicte une borne forte limitant la production du taux de dissipation d'énergie à sa redistribution (supposée valable dans la couche inertielle près du mur), conduit à un accord plus faible avec les données expérimentales. Dans la mesure où ces deux hypothèses constituent une pratique courante pour la définition de modéle de fermeture de viscosité turbulente, on s'attend à ce que ces résultats s'étendent à d'autres modèles de formes similaires. Les performances limitées de la procédure d'assimilation, obtenues lorsque on contrôle les paramètres globaux, sont une indication de la rigidité du modèle de turbulence considéré.

Résumé du Chapitre 5: Assimilation de données pour des corrections spatiallement distribuées de déformations

La méthode d'assimilation de données dans ce chapitre vise à reconstruire l'écoulement de vents moyen. Pour cela, un forçage spatialement distribué est ajouté à l'équation de la quantité de mouvement afin de déduire la correction de la force induite par le tenseur de Reynolds. Sans connaissance a priori sur sa forme analytique, un terme de forçage brut a été intialement considéré. Une analyse des champs de sensibilité, révèle un intérêt élevé pour l'optimisation de ce terme dans les régions englobant plusieurs régions clefs de l'écoulement. Cela concerne l'impact de l'écoulement amont (y compris la séparation amont et la formation du vortex en fer à cheval), les couches de cisaillement latérales et supérieures, et le sillage.

Pour réduire les risques de solutions non physiques associées à des minima locaux, et compte tenu des observations fortement partielles dont nous disposons et de la présence de paramètres de contrôle spatialement distribués, nous avons proposé d'explorer deux approches de régularisation différentes. D'une part, nous avons envisagé d'augmenter la fonction de coût par une pénalité sur les gradients spatiaux du paramètre de contrôle. En d'autre part, par la définition d'un produit interne H^1, nous avons considéré la recherche du paramètre de contrôle dans l'espace de Sobolev correspondant (Protas et al., 2004). Une comparaison numérique des résultats obtenu avec l'approche de pénalisation a montré que la recherche de paramètre sur H^1 conduisait à une convergence beaucoup plus rapide et des états optimaux d'énergie plus faibles. En ce qui concerne la capacité d'interpolations des mesures, par rapport à la calibration des coefficients, le modèle correctif de déformation conduit à un excellent accord entre les résultats numériques et les données de pression pariétale sur la pluspart des facades du bâtiment. En ce qui concerne la capacité de reconstruction de la méthode d'assimilation, les résultats du modele montrent une réduction considérable de l'extension de la zone de récirculation; cette réduction n'est cependant pas totalement satisfaisante. Celle-ci est accompagnée par une mauvaise qualité de reconstruction du champs de vent assoié à des caractéristiques non physiques. Il semble que la réduction de pression sur la façade arrière soit effectuée en approchant le point focal très près du mur dans le but de réduire la région de recirculation globale. Un manque de structuration du forçage semble être la cause principale de ce défaut.

Afin de remédier à cette situation, nous avons tenté d'affiner la forme du paramètre de contrôle dans le but d'assurer une certaine cohérence entre la correction de déformation prescrite par cette force et une force induite par des contraintes de Reynolds. L'anisotropie étant assez mal représentée par les modèles de viscosité turbulente (et la fermeture $k-\epsilon$), nous proposons ici de ne traiter que les corrections relatives à l'inhomogénéité de l'écoulement, i.e. les régions à fort gradient d'énergie turbulente. En effet, une analyse de sensibilité concentre de façon drastique des sources potentielles d'inadéquation des contraintes de Reynolds modélisées à une mince région à l'intérieur des couches de ci-

saillement, correspondant à l'extension du cisaillement latéral produit par la séparation de l'écoulement séparé sur les bords d'attaque. En contrepartie, une sensibilité plus faible en aval dans le sillage a été notée. En termes d'objectifs, les écarts avec les données de pression de paroies ont globalement diminué considérablement pour atteindre des niveaux plus proches de celle associée au terme de forcage brut avec une vitesse de convergence plus rapide. Du point de vue de la reconstruction, les résultats avec une force structurée préservent mieux les caractéristiques du sillage attendu, meme si le terme de forçage brut produit globalement une bulle de recirculation plus petite. Néanmoins, il est à noter que l'emploi d'une telle structuration accélère l'optimisation avec des performances comparables. Cela semble suggèrer que ces régions locale ont un poids important dans l'échec du modéle RANS.

Résumé du Chapitre 6: Assimilation de données pour des corrections structurées grâce à la modélisation de la turbulence

Dans ce chapitre, nous avons effectué une étude plus approfondie de l'approche variationnelle pour la reconstruction de l'écoulement moyen autour du bâtiment considéré. Après avoir abordé les sources potentielles d'erreurs de modélisation, relatives aux hypothèses utilisées pour construire le modèle de fermeture, nous avons vu que l'inférence d'un paramètre de contrôle intégré terme à terme, donne des matrices mal conditionnées du modèle adjoint et conduit à des instabilités numériques. Pour s'affranchir de ces problèmes, nous avons considéré l'adjonction de paramètres distribués permettant de reconsidérer la fermeture à un niveau structurel. Pour le modèle de turbulence considéré, nous avons introduit deux stratégies correctives pour sa fermeture; la prémiére repose sur l'équation de transport pour l'énergie k, et la seconde sur son taux de dissipation ϵ. Concernant la régularité du champs de sensibilité, L'utilisation du gradient de Sobolev a été proposée à la fois pour définir une direction de descente pour l'algorithme de minimisation et dans un but de régularisation. Notons qu'avec le gradient de Sobolev, la robustesse de la procédure d'assimilation a été assurée par l'utilisation de schémas numérique d'ordre un pour résoudre le RANS et son modéle dual.

Les deux champs de sensibilité des paramètres ont mis en évidence des régions où les constantes globales ne sont pas trop sensibles (c'est-à-dire le sillage). Leurs plans ont en fait révélé des tendances binaires, séparant les régions de cisaillement latéral et supérieur et l'écoulement de sillage. Concernant la qualité de reconstruction, comparés à une calibration directe des coefficients, les modèles de fermeture modifiés ont donné de bien meilleurs résultats dans la plupart des régions proche paroies du bâtiment en termes de profils de charge de vent. Un excellent accord avec des expériences PIV indépendantes a été obtenu en terme d'extension transversale de sillage. Ce bon accord avec des mesures de nature différente et qui n'ont pas été utilisées dans l'assimilation a montré que nous ne sommes pas confronté à une sur-représentation des données de pression. Cependant,

comme l'ajustement du débit ne provient que des effets diffusifs (hypothèse de Boussinesq), les résultats suggèrent quelques restrictions persistentes car les profils reconstruits tendent vers le modèle d'origine dans certaines régions dans la mesure ou certains mécanismes d'échanges d'énergie ne sont pas représentés.

Pour proposer une solution alternative , tout en maintenant l'hypothèse de Boussinesq, nous avons proposé d'étudier le couplage d'une correction directe de déformation et l'ajustement de l'équation de fermeture du modèle de turbulence. La forme du paramètre de contrôle joue ici un rôle important afin de permettre une hybridation efficace. La force structurée a été choisie plutôt qu'un terme de forçage brut en raison de sa consistance et pour sa relation étroite (dans son effet) avec la partie isotrope du tenseur de Reynolds. Les observations qualitatives des caractéristiques principale de l'écoulement et les métriques mur/écoulement proposées montrent que la combinaison d'un forçage direct avec une forme de structuration simple et un ajustement de la fermeture locale est une stratégie assez prometteuse car elle garantit globalement une bonne qualité de reconstruction. De plus, la conjonction de la pénalisation du gradient H^1 / L^2 peut aider à affiner la qualité de reconstruction; cependant, un couple adéquat de mise à l'échelle est encore nécessaire pour fournir un compromis satisfaisant entre l'interpolation de la pression pariétale et des modèles d'écoulement réalistes.

INTRODUCTION

Thesis context

Because of their potential long-time exposure to strong atmospheric winds, high-rise buildings and big structures undergo extremely strong lateral aerodynamic forces. Yet, by having a prior understanding of the airflow surrounding these big structures, wind loads can be predicted and such issues avoided. To understand how theses turbulent flows affect the structures, experiments in wind tunnels along with numerical simulations are usually deployed.

On the one hand, for more than a century, experiments with scaled models of buildings have been carried out in wind tunnels (Cermak and Koloseus, 1954; Jensen, 1958). After years of advancement on measurement techniques together with an increased knowledge on wind dynamics, tunnel experiments have proven their reliability for loads prediction issues (Surry, 1999; Cochran and Derickson, 2011). High-Frequency Force Balance method (HFFB) (Tschanz and Davenport, 1983) and High-Frequency Pressure Integration (HFPI) (Irwin and Kochanski, 1995) are two examples of techniques employed for such effort measurements. Despite many improvements brought to deal with turbulent flows, such techniques provide only partial information of the complex wind-structure interactions involved. For instance, when the structure has a complex geometrical shape, the very sparse nature of the cladding pressure measurements brought by HFPI techniques may lead to a misrepresentation of the local pressure field. Moreover, although techniques such as Particle Image Velocimetry (PIV) (Adrian, 1991) in principle allow planar or even full 3D data (Elsinga et al., 2006) to be obtained in wind-tunnel tests, but the cost is considerably higher and application for complex geometries can be hampered by laser-light shielding caused by the model, e.g. in case of an urban model consisting of many buildings.

On the other hand, more recently, thanks to the significant progress of computational capabilities, computational fluid dynamics (CFD) techniques have proved their value to give a complete representation of these flows, enabling a better understanding of the relation between the flow structures and the wind loads. However, since an accurate description of such turbulent flows requires a fine enough resolution, this technique may rapidly become impractical due to the large computational resources required. To go beyond this computational limitation, turbulence model closures associated with the Reynolds averaged Navier-Stokes (RANS) simulation were widely adopted to give an insight into the time-averaged flow profile. Over the years, motivated by the available computational wind engineering guidelines (Tominaga et al., 2008; EN, 2005), several established turbulence models have been deeply investigated (Cochran and Derickson, 2011; Meroney and Derickson, 2014). While RANS simulations offer good qualitative results that are physically

relevant, due to their inherent assumptions built from accumulated knowledge on real turbulent flows, close inspection on wind loads reveals typical failures in their prediction (Tominaga and Stathopoulos, 2010, 2017; Yoshie et al., 2007).
This accuracy issue may strongly hinder the model predictive skill when compared to real-world measurements. One way to correct this deficiency consists in devising methods allowing to couple turbulence modelling with measurements.

During the last decades, a wide variety of coupling techniques has been increasingly considered in fluid mechanics applications. Such techniques, commonly termed as data assimilation (DA), have been employed to estimate an optimal flow state provided by a given dynamical model such that it remains close enough to observations. So far, two different classes of DA techniques have been applied to that end. On the one hand, Bayesian techniques, often referred to as sequential DA techniques, have been used to estimate optimal flow parameters from data affected by a high uncertainty level (Meldi and Poux, 2017; Mons et al., 2016). On the other hand, optimal control techniques, like variational DA or ensemble-variational DA, have been proposed for direct and large eddy numerical description models (Mons et al., 2016; Gronskis et al., 2013; Yang et al., 2015; Mons et al., 2017; Li et al., 2020; Chandramouli et al., 2020). In this latter kind of approaches, DA is formulated as a constrained optimisation problem (Bryson, 1975). A cost functional, reflecting the discrepancies between some (incomplete) measurements of the flow variables and a numerical representation of the flow dynamics, is minimised using a gradient-based descent method. In such an optimisation problem, the functional gradient's evaluation is efficiently carried out through the dynamical model's adjoint instead of a costly finite difference approach (Errico, 1997; Plessix, 2006). At this point, these DA methods were often used to reconstruct initial conditions and/or boundary conditions for nonstationary flow simulation issues (such as large eddy simulations).

In the last few years, mean flow reconstruction problems have also been considered with data assimilation techniques. In some studies (Foures et al., 2014; Symon et al., 2017), built from variational DA techniques, the authors considered laminar steady Navier-Stokes equations corrected by an unknown volume-force to directly model the turbulence effects. These studies showed that, in laminar or transitional flows, such models perform well to assimilate synthetic particle image velocimetry (PIV) data. Other DA studies at high Reynolds number were performed with RANS turbulence models (Li et al., 2017; Singh and Duraisamy, 2016; Franceschini and Sipp, 2020). In these works, mean flow DA approaches exploited the turbulence models' structure, which results from a trade-off between asymptotic theories on turbulence mixing and empirical tuning to fit experimental data. This was expressed through a calibration process of the closure constants or of a corrective source term added to the turbulence model. Experimental knowledge plays here a crucial role. Such studies dealt mainly with fundamental and industrial oriented flow configurations in which turbulence is often generated at a unique integral scale. However, to the authors' knowledge, for flow configurations involving complex flow interactions as in the case of an atmospheric boundary layer around a bluff-body, turbulence closure structure analysis using DA techniques are still largely unexplored. Nevertheless, it is

noteworthy that formal uncertainty quantification (UQ) techniques have been employed to interpret these closure models in probabilistic terms (Etling et al., 1985; Duynkerke, 1988; Tavoularis and Karnik, 1989; Edeling et al., 2014; Margheri et al., 2014). For example, in a recent work by Shirzadi et al. (2017), global coefficients of the standard $k-\epsilon$ model were adapted for unstable atmospheric boundary layer (ABL) flow around high-rise buildings using a Monte Carlo simulations based technique.

Present contribution

In this thesis, we investigate RANS modelling in conjunction with one of the most common turbulence models in the framework of variational data assimilation prediction of wind flows around big structures. Contrary to previous studies in which velocity measurements were considered on significant parts of the flow domain (for 2D flow with one homogeneous direction), we consider here the coupling of a RANS model with only parietal experimental measurements for a real world complex three-dimensional flows. This difference is far from being cosmetic as it is built here to deal with practical experimental settings, used classically in the industry of construction. An analytic derivation of the adjoint model enabling the estimation of the descent direction to the cost minimization algorithm has been performed and then discretized using a finite volume scheme. The library which served for the implementation of the inner iterations, i.e. RANS and its adjoint solvers, and the outer iterations for the DA procedure relies on the open source multi-physics library OpenFOAM (Jasak, 1996).

Given the dual description of the dynamics composed of a RANS direct model and the adjoint of its tangent linear representation, we explore the adjoint methodology as two distinct tool.

In the one hand, we investigate some methodological settings that enable an in-depth diagnosis of the turbulence closure. As a starting point, this methodology is used to investigate the sensitivity fields of the global closure coefficients of the high Reynolds realizable revision of the $k-\epsilon$ model (Shih et al., 1995). Their physical interpretations enable us then to point out the limits on the closure models' applicability for data-model coupling purposes, particularly for wind flows around a high-rise building (the chosen case study for the thesis). This study discusses the limitations and improvements in estimating wind loads and mean velocities surrounding the building.

In the other hand, aiming for an efficient data-model coupling, we consider the method as a flow reconstruction tool. A first strategy based on the the control of the turbulence model parameters shown a too strong rigidity of the model in the sense that it constrain too much the solution space to allow the estimation of very accurate estimations. The solutions of the numerical model calibrated on real pressure data are improved but only marginally.

Thus, we went one step further and considered a *weak constraint* data assimilation as it is called in the data assimilation community, which includes additional forcing error terms. Several strategies have been explored in this spirit. In the first strategy, by defining

an additive forcing term as control parameter, we allow the solution to deviate from the default model constraints, to directly correct the momentum diffusion associated to the eddy viscosity model. In the second strategy, we considered instead the adjunction of a distributed parameter enabling to correct the turbulence closure in some regions of the flow. Beyond the fact that it provides a better physical structure to the reconstruction thanks to the prior information brought by the RANS model and avoids overfitting to the data , the optimal control parameter enables us to identify features that are missing in the initial RANS closure hypotheses. As with sparse observations, the sensitivity field is generally not very regular for distributed parameters, searching for the control parameter in Sobolev's space (H^1) is also proposed to strengthen the efficiency of the method., i.e by providing a robust descent direction for the gradient minimization algorithm.

Contents of thesis

The thesis is divided into seven chapters of which five chapters describe the main contributions of the study. The state of the art is laid in chapter 1. Existing DA techniques are enumerated. A survey of previous works using DA for data-model coupling in general CFD studies is also given.

In chapter 2, a focus is made on the modelling of turbulent flows in urban flows. The aim of this chapter is to identify the modeling settings which forms the basis for the DA studies described in the subsequent chapters. The mathematical model outlining the time-averaged Navier-stokes equations; its associated closure for turbulence, its consistent wind inlet profile and the near-wall treatment are introduced. Along with this, a brief description is made of the experimental apparatus, conducted previously by (Sheng et al., 2018). By gathering literature recommendations that insure a rigorous numerical flow analysis, a computational setup was built for the building case study. This chapter continue with a solution validation study to asses discretization-related errors. The conditions for which the predictions become independent of the grid are first established. Then comparisons are made between the predicted distributions of wall-pressure and available data.

Chapter 3, is dedicated to the development of the variational data-assimilation procedure. The (formal) adjoint differential equations are given and their obtention is further detailed in appendix 7.2. A particular attention is addressed on the boundary treatment, and led us to define a consistent enforcement, especially at the wall.

The variational technique is then applied for a detailed analysis of the turbulence model in chapter 4. Local sensitivity to the models global turbulence coefficients are discussed and a calibration process was conducted in order to investigate models output limitations, through hold/relax closure hypothesis scenarios, toward data-fitting.

In the next chapter (5), we present the modified set of RANS equations with the additive forcing term used as a control parameter in the assimilation. To suppress non-physical oscillations of the sensitivity to the parameter during the reconstruction, we proposed the examination of two regularization approaches. In the first one, we augment the objective by a regularizing term. Whereas for the second one, the distributed parameter is sought in

a regular space, i.e. Sobolev space. After an initial sensitivity analysis, we discuss results by comparing reconstructed flows obtained with both regularization techniques. Since, forcing here is not affixed with the specified turbulence model, we hence investigates the effects of assumption of constant eddy viscosity (CEV), which enables major simplification to the adjoint model and its boundary conditions. In a following section, we considered a simple structuration of the forcing so as to enforce some physical constraints to the reconstructed flow features.

In chapter 6 , the flow reconstruction is operated under a parametrization that satisfies physical constraints given by the turbulence model. Discrepancy-corrective parameters are embedded into the turbulence model equations rather than at the level of the momentum equations and their effects on the mean flow are constrained by the specified stress-strain relationship. The chapter starts by addressing possible model structure errors resulting from the choice of the eddy-viscosity and the chosen type of turbulence model, i.e. realizable $k - \epsilon$. Comments are given on the possible corrections at each closure assumption layer, vis-a-vis the robustness of the DA procedure. Then, we introduce corrective models with new spatially distributed forms of closure. In a final section, after an initial sensitivity analysis, data-assimilation results are presented by comparing reconstructed flows obtained with the proposed corrective models.

Chapter 7 concludes the thesis with a summary of the achievements of the work and some suggestions for further work are given.

Lists of references together with the appendices follow the final chapter.

Chapter 1

A STATE OF THE ART

1.1 A structural wind engineering problem: a brief historical review

During there lifetime, buildings are continuously exposed to wind coming from all directions. Particularly, due to their extended exposed surface, high-rise buildings and big structures undergo extremely strong lateral aerodynamic forces. As a consequence, large lateral deflections or, even more, some problematic tearing affecting security may be observed (Murakami et al., 1992; Irwin, 2008; Cochran and Derickson, 2011). To understand how wind flow affect these structures, physical models and numerical simulations have been used for a long time.

Experiments with scaled models of buildings have been carried out in wind tunnels. Initially studies were performed in a uniform flow that produced spurious results (Bailey, 1933; Jensen, 1958). In the 1950s, atmospheric studies of Earth turbulent boundary layer have led to a greater understanding of its structure and complexity, and ultimately to a better modeling(Cermak, 1956). Cermak and Albertson (1958) demonstrated the criteria for Reynolds number independence for the modeling at reduced scale of atmospheric boundary layers. Other studies on phenomenological and metrological aspects of turbulence have been carried out from the early works of (Schubauer and Dryden, 1935; Davenport, 1965). Knowledge of the turbulent spectrum of the natural wind and incorporation of its scaled representation in wind tunnels led to the evolution from static to dynamical response investigations of structures. The description of the energy content of the wind via the turbulence spectrum by Davenport (1965) was a fundamental concept that pushed wind engineering to follow this evolution. Note that during the 1940s and 1950s dynamic wind-tunnel studies were generally limited to flexible, long-span bridge structures, after the collapse of the Tacoma Narrows Bridge, and the transition from studies of bridge dynamics to building dynamics was motivated by the twin towers of the World Trade Center in New York. Studies of buildings were performed frequently in the 1960s and rationalization of such works was given (Cermak and Peterka, 1966). In brief, it has been observed that the drag dependence for bluff bodies with sharp edges, as well as the boundary layer, too the Reynolds number were small when performed above a critical Reynolds number. Thus, a major similarity requirement was waived. In general, a similarity study can be performed if all similarity parameters such as the Mach, Rossby, Richardson, Prandtl and Eckert numbers are the same between model and prototype. In wind-engineering applications, at scales where atmospheric boundary layers and urban

buildings interact, it is reasonable to neglect compressible, thermal ans Coriolis effects, making the Reynolds number the principal similarity parameter.

Indeed, construction designs of challenging heights and shapes have seen a rapid growth of wind-tunnel simulations for the dynamic aspects of high-rise buildings. In the period up to 1975, some centres have initiated measurements on the CAARC Standard Tall Building Model (Holmes, 1975; Walshe and J., 1974) , i.e. a rectangular prismatic shape with full-scale dimensions ($30.48 \times 45.72 \times 183.88$ m). An initial comparison of their results by Melbourne (1980) have pushed to define a benchmark configuration: an isolated tall rectangular building geometry, so that other workers could "calibrate" individual techniques against a common set of data.

Meanwhile, during that time, much has been learned about the characteristics of flow surrounding buildings and the structure of the wake; and knowledge of building wake characteristics become considered in a variety of applications, e.g. pollutants dispersion in conventional or nuclear power plants, pedestrian wind comfort and wind loads on structures. To understand the wind flow behaviour around buildings, some investigations (Peterka and Cermak, 1977; Baker, 1980; Peterka et al., 1985) have pointed out the fundamental differences between three-dimensional and two-dimensional separated flows in wind engineering. After years of advancement on measurement techniques together with an increased knowledge on wind dynamics, wind-tunnel experiments have proven their reliability for loads prediction issues. A more detailed survey can be found in (Surry, 1999; Cochran and Derickson, 2011). High-Frequency Force Balance method (HFFB) (Tschanz and Davenport, 1983) and High-Frequency Pressure Integration (HFPI) (Irwin and Kochanski, 1995) are two examples of techniques employed for wind loads and wind-structure interaction studies.

Meanwhile, in early attempts, some analytical methods (Hunt and Smith, 1969; Hunt, 1971) which were developed to predicts the mean velocity defect (i.e. difference between upstream and downstream mean velocities) in the wake of a three dimensional bluff-body immersed within a turbulent boundary-layer flow have been acquired and compared to the available measurements on mean velocity defect, turbulence intensity, mean temperature and mean concentration of pollutants in the wake region downstream of buildings (Peterka et al., 1985). Relying on the assumptions that only small perturbations to the turbulent boundary layer are caused by the bluff-body and that the ratio of the model height to the boundary-layer thickness is very small, this theory is invalid in the separated region behind the building where flow structure cannot be considered to be a small perturbation of the approaching flow. In the same period, numerical simulations of turbulent flows over three-dimensional bluff bodies have been carried out (Hirt and Cook, 1972) and applied to wind flows over buildings (Yamada and Meroney, 1971; Summers et al., 1986; Paterson and Apelt, 1989; Murakami and Mochida, 1989). These studies corresponds to the first use of the Reynolds averaged equations in wind engineering, using mainly the standard $k - \epsilon$ model. By comparison with the earlier analytical methods, the numerical results obtained, when compared with full scale and wind tunnel measurements, were considered to be in a relatively good agreement for configurations such as cubic models

and rectangular surface-mounted building shapes. For practical situations and complex geometries, questions on the applicability for such numerical methods have been raised (Murakami and Mochida, 1989).

Motivated by further developments in turbulence modelling, giving rise to unsteady numerical methods with spatial filtering (i.e. Large eddy simulation (LES) (Smagorinsky, 1963)) and various improvement of the steady mean state models (*e.g.*, RNG by Yakhot et al. (1992), realizable by Shih et al. (1995), MMK by Tsuchiya et al. (1997)), several studies were conducted to compare their relative performances and asses their applicability on the prediction of flow around buildings, mostly on low-rise structures (Murakami et al., 1987; Murakami, 1990; Murakami et al., 1992; Murakami, 1993; Rodi, 1997; Thomas and Williams, 1999; Nozawa and Tamura, 2002). Together with later studies, they laid the foundations for the current best practice guidelines (Franke et al., 2004; Tominaga et al., 2008), by focusing on the importance of grid resolution, the influence of the boundary conditions on the numerical results and by comparing the performances of various types of turbulence models in steady RANS simulations, and comparisons of steady RANS versus LES.

In most of these studies, flow-field around cubic-bluff body were analysed and deficiencies of the eddy viscosity modelling in the $k-\epsilon$ model (Launder and Sharma, 1974) were addressed (e.g. by Murakami et al. (1992)). These include the stagnation point anomaly (Issa, 1995; Franke et al., 2004) with overestimation of turbulent kinetic energy near the frontal corner and the resulting underestimation of the size of separation and recirculation regions on the roof and the side faces, together with the underestimation of turbulent kinetic energy in the wake resulting in an overestimation of the size of the cavity zone and wake. Various revised linear and non-linear $k-\epsilon$ models and also second-moment closure models (e.g. algebraic stress model (Launder et al., 1975)) were also tested, and showed improved performances for several parts of the flow-field. Yet, recent studies have shown that such models still fail to reproduce an accurate recirculation region behind the building (Tominaga and Stathopoulos, 2010, 2017; Yoshie et al., 2007), thus, scrutinizing the main limitations of steady RANS modelling: its incapability to model the inherently transient features of the flow field such as separation and recirculation downstream of windward edges and vortex shedding in the wake. This accuracy issue may strongly hinder the model predictive skill to reproduce real-world measurements. Let us note that authors reported that the flow structure around a bluff body can be predicted by RANS models with a given accuracy; however, for accurate wall-pressure and turbulence kinetic energy, algebraic models and even more LES are seen as a more effective analysis tools. Although, LES leads to intrinsically superior performance of (Rodi, 1997; Thomas and Williams, 1999; Sohankar et al., 2000), they have specific disadvantages that are not easy to overcome. This includes in particular a huge computational burden and the difficulty to specify appropriate time-dependent inlet and wall boundary conditions (Gatski et al., 1996; Gosman, 1999; Dagnew and Bitsuamlak, 2010; Tabor and Baba-Ahmadi, 2010; Thordal et al., 2019). Let us note that hybrid approaches combining steady (RANS) and unsteady (LES) modeling (Fadai-Ghotbi et al., 2010) can be a solution to investigate in

alleviating these limitations .

1.2 A brief state of the art on data-model coupling

The concept of data-model coupling or more commonly refered to as data-assimilation (DA) comes from estimation theory, and was first been applied to the numerical weather prediction (Bergthörsson and Döös, 1955). The goal is to combine observations of the system state (for instance from weather stations and satellites in weather forecast) with a given dynamical model. Indeed, at an arbitrary time, data assimilation usually takes a forecast and applies a correction to it based on a set of collected data while estimating errors underlying both the measurements and the forecast itself. A weighting is applied to the data-model forecast discrepancy (i.e. the difference between the data and the model output forecast) to determine how much of a correction should be made to the forecast, yielding to a best estimate of the state. This correction is often termed as the analysis step.

1.2.1 Data-model coupling techniques

To define the mathematical context common to the data assimilation techniques, let us note the common goal which is to provide an optimal estimate X_a (where a stands for analysis) of a true initial state $X(t_0)$ and model parameters $\alpha(x,t)$ that are in practice unknown or known with a low confidence compared to its sensitivity. This requires first, a dynamic model $\mathbf{M}$ (generally non-linear) describing the evolution of the system from an a priori initial (or background) state X_{b_0}. Then, giving a set of measurements Y of the system, the data assimilation problem is formulated by the following system of equations,

$$\begin{aligned} \frac{\partial X(x,t)}{\partial t} + \mathbf{M}(X(x,t), \alpha(x,t)) &= \xi(x,t) \\ X(t_0,x) &= X_{b_0}(x) + \theta(x) \\ Y(x,t) &= \mathbf{H}(X(x,t)) + \varepsilon(x,t), \end{aligned}$$

where $\xi(x,t)$, $\varepsilon(x,t)$ and $\theta(x)$ would take into account, respectively, any potential model errors, measurement errors, and an *a priori* background error of the initial condition to which we associate the covariance matrix,

$$B = \mathbb{E}(\theta\theta^T) = \mathbb{E}(||X_{b_0} - X||^2),$$

and $\mathbf{H}()$ is an observation operator which maps any possible model state X to the observation space. This operator ensures consistency between model and measurements. In the first section, we address what we may consider as a basis for the development of a DA procedure. Thus, dynamics are omitted and we consider simple ideas from estimation theory. To take $\mathbf{M}$ into account, two main approaches are briefly introduced in further

subsections.

Linear estimation theory as a basis for data-assimilation

Under the linear estimation theory, the noise ε around measurements is assumed to be a zero mean Gaussian random field associated to the observation covariance tensor R. For sake of simplicity, we also consider $\mathbf{H}$ to be a linear observation operator. As such, the data-model discrepancy reads as

$$\mathbf{R} = \mathbb{E}((Y - \mathbf{H}X)(Y - \mathbf{H}X)^T) = \mathbb{E}(\varepsilon\varepsilon^T). \tag{1.1}$$

Thus, an estimation problem would aim at determining an estimator $\hat{X}$ of the true state that optimally reduces this discrepancy, based on the knowledge of Y, of X_b and the covariances matrices.

Least square fitting A classical approach to express the estimation problem consist in interpreting it as a least squares problem. In this approach, we seek the optimal estimator $\hat{X}$ that minimizes the cost function

$$\mathcal{J}(x) = \frac{1}{2}(Y - \mathbf{H}X)^T R^{-1}(Y - \mathbf{H}X). \tag{1.2}$$

By cancelling its gradient one can obtain an optimal state (assuming $\mathbf{H}^T R^{-1}\mathbf{H}$ is invertible):

$$\hat{X} = (\mathbf{H}^T R^{-1}\mathbf{H})^{-1}\mathbf{H}^T R^{-1} Y.$$

We note that in this naive approach, no information is given about the fact that X is solution of the model $\mathbf{M}$, about the background solution and about relative confidence between observations and model. This approach is doomed to fail in case of sparse and/or noisy measurements.

Basic Bayesian inference As we consider both the state vector X and data Y as random variables, in this approach, one may seek an estimation of the true state X^t associated with the conditional probability $P(X|Y)$ which verifies the Bayes rule (1.3),

$$P(X|Y) = \frac{P(Y|X)P(X)}{P(Y)} \tag{1.3}$$

where $P(X|Y)$ is the *a posteriori* probability distribution of the forecast X being accounted for by the available data Y, $P(x)$ is an *a priori* probability of the forecast X while $P(Y)$ an *a priori* distribution. Given this, a Bayesian estimator $\hat{X}$ can be built by minimizing a Bayesian risk $\mathbb{E}(Br(\hat{X}, X))$. For instance, the minimum variance estimator considers the mean square error, $Br(\hat{X}, X) = ||\hat{X} - X||_2$, Then by expressing the cost

function as the expectation of Br knowing Y:

$$\mathcal{J} = \mathbb{E}(||\hat{X} - X||^2|Y),$$

the optimal estimator can be obtained by cancellation of its gradient with respect to $\hat{X}$ giving

$$X^a = \mathbb{E}(X|Y). \tag{1.4}$$

We recall that so far we still did not take into account the dynamics. To take M into account, two main family of approaches have emerged for data assimilation issues.

Sequential approaches

The sequential approach can be seen as an extension of the Bayesian minimum variance estimation as the background state is evolving in time through a dynamical model. The goal of sequential data assimilation is then to correct the background state each time a new observation is available.

Kalman filter The Kalman filter introduced by (Kalman, 1960) can be seen as the direct extension of the best linear unbiased estimator (BLUE) for dynamical models. In this approach, say at discrete time t_{k+1}, one seek for the analysis state X^a_{k+1} that corrects the background state X^f_{k+1}, given the observation Y_{k+1}, which reads as

$$X^a = \mathbf{L}X^b + KY.$$

In fact, as we consider both background an data errors to be unbiased, this analysis is reduced to the following expression

$$X^a = X^b + K(Y - \mathbf{H}X^b) \tag{1.5}$$

where K is refered to as a Kalman gain that has to be defined. Moreover, as we assume the dynamical model to be linear with a model error q_k (associated to the covariance Q_k), we define the system,

$$\begin{aligned} X^f_{k+1} &= \mathbf{M}_k X^f_k, \\ Y_{k+1} &= \mathbf{H}_k X^t_{k+1} + \varepsilon_k, \\ X^t_{k+1} &= \mathbb{M}_k X^t_k + q_k. \end{aligned}$$

By choosing the cost function to be $\mathbb{E}(||X^a_k - X^t_k||^2)$, it can be shown (Robinson, 2015) that the gain K_k which cancels its gradient reads as follow

$$K_k = (\mathbf{H}_k P^f_k)^T (\mathbf{H}_k (\mathbf{H}_k P^f_k)^T + R_k)^{-1} \tag{1.6}$$

and that the analysis step reads as

$$
\begin{aligned}
P_k^f &= \mathbb{E}(||X^f - X^t||^2) = \mathbf{M}_{k-1} P_{k-1}^a \mathbf{M}_{k-1}^T + Q_{k-1} \\
X_k^a &= X_k^f + K_k(Y - \mathbf{H}_k X_k^f) \\
P_k^a &= (\mathbf{I} - K_k \mathbf{H}_k) P_k^f
\end{aligned}
$$

followed by a forecast step:

$$
\begin{aligned}
X_{k+1}^f &= \mathbf{M}_k X_k^a, \\
P_{k+1}^f &= \mathbf{M}_k P_k^a \mathbf{M}_k^T + Q_k.
\end{aligned}
$$

Let us note that the Kalman filter can be extended to non-linear dynamics and observation operators through linearisation. This extension is called the Extended Kalman Filter (EKF). Both the standard method and its extended versionhave the drawback to rely on the computation of the Kalman gain K and the error covariance matrices P^a and P^f. As a matter of fact, the covariance matrices require a significant computation and storage resources as the system dimensions become high, despite strategies based on the Cholesky decomposition of low-rank covariance matrices. Therefore, these techniques are only usable for systems of moderate size.

Ensemble Kalman filter The ensemble Kalman Filter (EnKF), first introduced by (Evensen, 2003), may be presented as an efficient alternative to the EKF using a Monte-Carlo approach. In this context, one consider an ensemble $\mathcal{N}$ of state sampled according to a given probability distribution, each referred to as a member, noted $(X_k^{f,1}, \ldots, X_k^{f,\mathcal{N}})$. This ensemble is generated from the randomization of the non linear dynamical model given the result X_k^a of a previous analysis step. Instead of directly computing and storing the error covariance matrices, the EnKF uses an empirical expression of the ensemble mean and covariance matrix to deduce a low-rank approximation of the gain matrix and the covariance matrices P^f and P^a. Let us recall that the more ensemble members are employed, the more accurate the approximations to the distributions are, and the bigger computational resources are involved. For further computational details regarding the forecast and analysis steps, reader is referred to the works of (Yang, 2014; Robinson, 2015).

Variational approaches

Based on control theory, an alternative approach for data assimilation is to define a minimisation problem, whose associated cost function embeds the data-forecast discrepancy. These are called variational methods, such as 3DVar (at a single time) and 4DVar (integrated over a time window). These approaches involve the use of iterative minimization algorithms.

With the variational approach (Le Dimet and Talagrand, 1986; Courtier and Talagrand, 1987) the assimilation is no more performed instantly (at each time an observation is available) but along an assimilation window in which we have the background trajectory generated by the model dynamics starting from an initial state X_{b_0}, and a set of successive observations Y. Thus, the goal of this approach consists in finding the initial state X_{b_0} which performs an adjustment to the integrated trajectory to make it as close as possible to the observations. This is done by solving an optimal control problem as described by Lions (1971). In practice, the assimilation is translated into the minimization of an objective functional which measures the mismatch between the model predictions and the data, under the constraint that the optimal state obeys to the model dynamics. The data assimilation problem, over an assimilation window $[t_0; t_f\ ]$, can be formulated as

$$\mathcal{J}(X_0) = \frac{1}{2}(X_0 - X_{b_0})^T B^{-1}(X_0 - X_{b_0}) + \frac{1}{2}\int_{t_0}^{t_f} (\mathbb{H}(X_t) - Y(t))^T R^{-1}(\mathbb{H}(X_t) - Y(t))\,\mathrm{d}t, \quad (1.7)$$

in which B and R are, respectively, the background and the observation covariance matrices. The minimization is performed by a gradient-based algorithm which requires the evaluation of the cost function gradient w.r.t the initial state x_0. There are basically two approaches to obtain numerically the gradient. The finite difference, or direct approach, that consists in approximating the gradient through infinitesimal variations of each variables of the cost function. For instance, a first order finite difference around x_0 in the direction $h\delta X_0$ is given by

$$\mathcal{J}(X_0) \simeq \frac{\mathcal{J}(X_0 + h\delta X_0) - \mathcal{J}(X_0)}{h}.$$

In order to meet the accuracy requirements, we need to fix a sufficiently small differentiation step h. For the whole gradient, if we consider N as the number of design variables, we have to solve N sensitivity equations. Thus as N increases, this approach become rapidly very expensive. Instead, the adjoint formulation is an elegant alternative based on the work of (Lions, 1971; Le Dimet and Talagrand, 1986). In the adjoint-based approach, we only require to solve the adjoint equation once. We note that if the nonlinear dynamics equation is time dependent, then the adjoint equation is time dependent and is solved backwards in time. Indeed, the standard 4DVar (and its incremental version (Courtier et al., 1994)) technique(s) is used to determine the initial optimal state x_{t_0} which is of the size of a given state (Gronskis et al., 2013). In general, as iterative gradient-descent algorithms are sensitive to numerical errors, the most accurate numerical adjoint associated to a given problem is required.

Hybrid approaches

More recently, there is a trend in the development of hybrid data assimilation techniques which combine the advantages of ensemble methods and variational assimilation approaches (Yang et al., 2015; Yang and Mémin, 2019). From a variational perspective,

hybrid methods would take advantage of the formalism of an iterative gradient descent procedure and one would incorporate an ensemble-based background covariance operator B, thus providing an exact descent procedure (Hamill and Snyder, 2000; Lorenc, 2003), without being constrained by the derivation of the adjoint equations and by the strong sequentiality of the 4D-Var algorithm. Compared to the ensemble Kalman filter formalism, when facing high dimension problems, the explicit analysis or update step are replaced in the hybrid approach by a computationally tractable iterative gradient descent procedure of a cost function. Reader is referred to the work by (Yang, 2014) for a further details about this kind of hybridization as well to works by (Beyou et al., 2013; Papadakis et al., 2010)for methods mitigating ensemble Kalman filtering for nonlinear filtering.

1.2.2 Data-model coupling in computational fluid dynamics

During the last decades, a wide variety of data assimilation coupling techniques have been increasingly considered in fluid mechanics applications. Such techniques, have been employed to estimate an optimal flow state provided by a given dynamical model such that it remains close enough to observations. So far, the two classes of DA techniques and their hybrid versions have been applied to that end. On the one hand, under the Bayesian inference, the sequential DA techniques have been used to estimate optimal flow parameters from data affected by a high uncertainty level (Colburn et al., 2011; Mons et al., 2016; Meldi and Poux, 2017). In the work by Colburn et al. (2011), DA study was conducted using the ensemble Kalman Filter (EnKF) technique (Evensen, 2003) for the estimation of near wall region of a turbulent channel flow, considered as the first step toward a flow control problem, based on wall measurements. Note that Meldi and Poux (2017) employed a reduced Kalman filter proposed by (Suzuki, 2012) in order to deal with the high costs associated with the manipulation of the covariance matrices in three-dimensional flows. In this work, the Kalman gain was embedded within the prediction-correction algorithms commonly involved in segregated solver for incompressible flow.

Within the iterative gradient descent formalisms, variational DA and hybrid ensemble-variational DA have been used for direct and large eddy numerical description models (Gronskis et al., 2013; Yang et al., 2015; Mons et al., 2014, 2016, 2017; Li et al., 2020; Chandramouli et al., 2020). A cost functional, reflecting the relative discrepancies between incomplete measurements of the flow variables and a numerical representation of the flow dynamics, is minimised. In the case of the purely variational approaches, the functional gradient's evaluation is efficiently carried out through the adjoint dynamical model instead of a costly finite difference approach (Errico, 1997; Plessix, 2006). As for the hybrid ensemble-variational approach, as performed by Mons et al. (2016), authors have used a Monte Carlo sampling technique to generate an ensemble which enables evaluation of prior statistics, thus, avoiding the adjoint formalism for the gradient estimation. At this point, these DA methods were often used to reconstruct initial conditions and/or boundary conditions for nonstationary flow simulation issues, such as large eddy simulations. Nonetheless in (Meldi and Poux, 2017), authors also have extrapolated the reduced-order

Kalman filter to steady state or mean flow reconstruction by assimilating the numerical marching iterations to time evolutions.

In fact, in the last few years, mean flow reconstruction problems are increasingly considered with data assimilation techniques. In such configuration, as the system of interest is governed only by boundary conditions, the model $\mathbf{M}$ can non-longer be seen as an evolution (or dynamic) model, i.e. where its solution is determined by its initial condition. In fact, the initial condition is now seen as only a guess from which the solution iterates until it reaches the stationary solution which approaches $\mathbf{M}(X(x)) = 0$. In such problem, one of the possible way to conduct DA is by adjusting model underlying parameters which act either in the flow bulk or at the boundary to constrain the mean state behaviour. Indeed, in some studies (Foures et al., 2014; Symon et al., 2017, 2020), built from variational DA techniques, the authors considered steady Navier-Stokes equations corrected by an unknown volume-force to directly model the fluctuating part around the mean state. These studies showed that, in laminar or transitional two-dimensional flows, such models perform well to assimilate synthetic particle image velocimetry (PIV) data.

As people starts to consider situations with high Reynolds number, DA techniques were performed with RANS turbulence models (Singh and Duraisamy, 2016; Parish and Duraisamy, 2016; Li et al., 2017; Franceschini and Sipp, 2020). In these works, mean flow DA approaches exploited the turbulence models' structure, which results from a trade-off between asymptotic theories on turbulence mixing and empirical tuning to fit experimental data. This was expressed through a calibration process of the closure constants or of a corrective source term added to the turbulence model.

In parallel to the above data assimilation issues or, in a broader sense, state estimation studies, researchers from the control community,have incorporated reduced order modelling and hydrodynamic stability analysis techniques, such as resolvent analysis [1] to perform efficient flow reconstruction (Beneddine et al., 2015, 2016, 2017; Franceschini, 2019; Symon et al., 2020). In fact, authors have aimed at the reconstruction of unsteady flow from mean flow (which can be obtained through mean DA procedure) and very sparse informations such as point sensor, that can be experimentally collected by hot wire anemometry for instance. In such approach, by interpreting the non-linear term arising from the time-dependent fluctuations around mean state in the Navier–Stokes equations (or in ensemble-averaged equations in URANS modelling in (Franceschini, 2019)) as a harmonic forcing (McKeon and Sharma, 2010), the fluctuation is reconstructed as a response to this forcing. By reduction of the resolvent operator, this response is then found as a weighted sum of resolvent modes in which the weighting is determined through data. Given this response, one can then account for its contribution through the Reynolds stresses to the time-averaged flow state. These results are very encouraging, and appear with great value for mean-flow reconstruction when data is very sparse. Caveats regarding the com-

1. The resolvent of a linear operator governs how harmonic forcing inputs are amplified by the linearised dynamics and mapped onto harmonic response outputs. Resolvent analysis refers to the inspection of this operator to find the most responsive inputs, their gains, and the most receptive outputs. The resulting low-rank approximation of the forcing-response dynamics of the full system is of a great value for modeling, controlling, and understanding the physics of fluid flows.

putational complexity and memory requirements, essential to consider three-dimensional cases, have been addressed by using techniques ranging from iterative approach (Bagheri et al., 2009; Loiseau et al., 2018) to randomized numerical linear algebra techniques (Moarref et al., 2013). Moreover, we believe in promising perspectives of these techniques by considering high-fidelity Reynolds-averaged models, e.g. RSM turbulence models that account better for the anisotropic behaviour of turbulence (Hanjalić and Launder, 1972; Manceau and Hanjalić, 2002).

1.2.3 Data-model coupling: specification to RANS turbulence modelling

State of the art Accurate simulations of turbulent flows is of great importance to many applications, ranging from fundamental to environmental and industrial configurations, as in the study considered in this thesis of wind engineering flows. Despite the enormous growth in computational resources, RANS modeling and simulation of many realistic turbulent flows has remained challenging, and in some cases even inaccessible. Most common closure to RANS models are strong simplifications of the complex dynamics of turbulent flows. Closure equations usually introduce a rough modelling of the exact transport terms with adjustable constants. These constants are mainly calibrated by a small number of simple, yet canonical flow configurations, such as homogeneous turbulence and thin-shear flows. This has the consequence to break the consistency, when the closure model is applied to practical problems which generally deviate from (or sometimes combine) the canonical calibrated configurations. It is the case for flows involving adverse pressure gradients, inhomogeneous flow directions and flow separations. In an attempt to increase this accuracy, some work have explored enrichments of turbulence models to better account for non-homogeneity produced by the presence of the wall (Durbin, 1993; Manceau et al., 2001).

As an alternative solution, the data-driven strategy, which constitutes the core of the present work, aims at moving beyond these limitations and provide an effective solution to address turbulence modelling errors at reasonable costs and through data obtained from experimentally realistic procedures. In this line of thought, formal uncertainty quantification (UQ) techniques have been employed to addresses the modelling errors underlying the closure constants of RANS system in probabilistic terms (Etling et al., 1985; Duynkerke, 1988; Tavoularis and Karnik, 1989; Kato and Obayashi, 2014; Edeling et al., 2014; Margheri et al., 2014). In a recent work by Shirzadi et al. (2017), global coefficients of the standard $k-\epsilon$ model were adapted for unstable atmospheric boundary layer (ABL) flow around high-rise buildings using optimisation techniques (*e.g.* by Monte Carlo simulations). Other studies have attempted to characterize errors that result from the eddy viscosity relationship, which links the Reynolds stress to the mean strain rate (Dow and Wang, 2011; Cheung et al., 2011; Emory et al., 2013; Ling and Templeton, 2015). For instance, using forward uncertainty quantification approaches, closure errors were addressed either into the relationship, by inferring it in the scaling coefficient, assuming it to be nor-

mally distributed (Dow and Wang, 2011), or by a perturbation of the predicted Reynolds stresses (Emory et al., 2013). More recently, Franceschini and Sipp (2020) has partly addressed structural model's errors to the transport equation of the eddy-viscosity in the Spalart-Allmaras model (Spalart and Allmaras, 1992). For its relevance with separated flows encountered in aeronautical applications, authors operated DA on 2D turbulent backward-facing step flow under the framework of an adjoint optimization approach. In other works (Duraisamy et al., 2015; Parish and Duraisamy, 2016; Singh and Duraisamy, 2016), data (either synthetic or experimental) were assimilated and turbulence model errors were addressed in the turbulent energy production as it constitutes one common issue for the prediction of a variety of flow configurations. In the work of Singh and Duraisamy (2016), a particular attention has been given on two model structures: Spalart-Allmaras and Wilcox $k-\omega$ (Wilcox, 1993) models. In their study, reconstruction of a number of benchmark flow configurations, ranging from a one-dimensional channel flows to 2D airfoil flows, were performed under the framework of both ensemble Kalman (Iglesias et al., 2013) and variational (*i.e.* adjoint, or inversion as they refer to) approaches. Let us note that in the spirit of the work in (Parish and Duraisamy, 2016), a possible goal is to extract modeling informations from data that can be used as a guidance (or training information) for deriving new closure terms. Machine learning techniques can be employed for that purpose (Zhang et al., 2015). Interested reader can be referred to the following list of paper reviews on this subject (Ferrero et al., 2019; Duraisamy et al., 2019; Bocquet et al., 2019; Brunton et al., 2020).

Present work Despite the increasing interest to couple stationary RANS modeling with data for flow analysis, let us note that all the above mentioned studies dealt mainly with fundamental and industrial oriented 2D flows in which turbulence is often generated at a unique integral scale. However, to the authors' knowledge, for flow configurations involving complex flow interactions as in the case of an atmospheric boundary layer around a bluff-body, turbulence closure structure analysis using DA techniques are still largely unexplored. The present work is thus a first attempt to investigate data-driven strategies for the analysis of 3D complex flow configurations using only wall-pressure as data input. Furthermore, beyond providing an efficient data-driven reconstruction technique, the proposed adjoint methodology is investigated here as an in-depth analysis tool of the turbulence closure.

Chapter 2

Flow configuration: Turbulence modelling and numerical setup

2.1 Introduction

In wind engineering, as any industrial context, the choice of a turbulence model comes from several years of expertise, obtained from a large number of tests and validations and from a deep experience in mesh generation. Moreover, it is easy to produce non-physical results, even with the best turbulence model. Hasty conclusions on the turbulence model can be made, while the problem could actually comes from an inadequate mesh, such as too coarse near the wall, or even from a specific way to initialise the computation. Without entering into details, $k-\epsilon$ models are a class of turbulence models. The equation on the turbulent kinetic energy k, trace of the Reynolds stress tensor, can be directly obtained from the transport equations on the Reynolds stress tensor components, while the equation on the dissipation rate ϵ is generally issued from modelling and requires a closure. As a consequence, there exists plently of models based on these two quantities. Among the several versions of $k-\epsilon$ and $k-\omega$ turbulence models which were tested in wind engineering related subjects, it seems that the preferred turbulence models were the *realizable* $k-\epsilon$, RNG $k-\epsilon$ and sometimes $k-\omega$ SST turbulence models (Menter, 1994). In particular, in studies on both low-rise buildings (Ozmen et al., 2016) or inquiring wind pressure coefficients prediction on tall buildings (e.g. CAARC (Meng et al., 2018)), it was suggested that the realizable $k-\epsilon$ turbulence model is sensitive to strong strain (high streamline curvature), flow separation; also lower discrepancy to data were achieved in the distribution of wind pressure coefficients, as compared to RNG and the standard $k-\epsilon$ model. Besides, this choice joins the fact that the realizable $k-\epsilon$ closure possesses stronger foundations since it is based on the transport equation of vorticity, on which additional closure assumptions are performed.

As the realizable $k-\epsilon$ model relies on the assumption of high Reynolds regimes, it requires a proper wall treatment since we have to enforce a no-slip condition.

In this chapter, both the experimental and physical models of the high-rise building that we have considered in the thesis are introduced. In section 2.2, the experimental set up is presented. In section 2.3, the governing equations used in the CFD are given. In section 2.4, the numerical details of the direct RANS simulation are presented, in accordance with the general recommendations of (Ferziger, 1990, 1993). Implementation details can be found in section 2.5. Finally, in section 2.6, validation by grid refinement

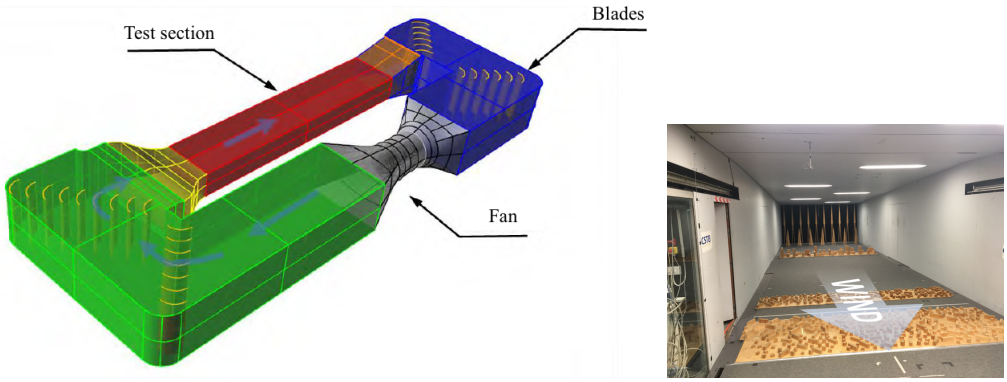

(a) (b)

Figure 2.1 – CSTB's NSA wind tunnel facility; (a), 3D set up of the wind tunnel facility at CSTB Nantes, (b), roughness elements disposal upstream the building model inside the test section

and comparison with experiments are conducted.

2.2 Description of the wind tunnel experiment

Experiments were held in CSTB (Nantes, France) as a part of the thesis of Sheng et al. (Sheng et al., 2018). Measurements were performed in a recirculating atmospheric wind tunnel called NSA [1] with a test section of 20 m long, 4 m wide and 2 m high. A 3D view is shown in figure 2.1a.

2.2.1 Generation of ABL profiles

The particularity of such wind tunnel facility lies in its fairly long test section. This great length allows the arrangement of roughness elements of different sizes upstream of the building model (see figure 2.1b). Indeed, these elements enables to reproduce the various turbulence scales of the natural wind. The larger elements are placed on the far upstream. They generates large coherent flow structures that maintain themselves far downstream. Conversely, small elements, which are arranged closer to the building model, create small eddies with a smaller spatial coherence. The goal is then to place all these roughness elements over the entire length of the test section so as to generate a relevant upstream turbulent flow representative of a realistic atmospheric boundary layer. Thus, before proceeding to wind-load and PIV measurements, it is necessary to carry out a characterisation without the model of the average velocity and turbulent intensity gradient, in order to ensure that the desired wind profile [2] is established when the wind

1. The abbreviation comes from the french designation "Nouvelle Souffle Atmosphérique"
2. Experimental profiles have to comply with national and/or international standards, such as, in this experiment, the ones provided in the Eurocode (EN, 2005).

reaches the building model. By adapting both the size and position of the roughness elements, this characterisation is carried out iteratively, using a so-called "fast" Pitot tube, which allows a high acquisition frequency (owing a short pneumatic connection between the pitot and pressure transducer) of the average velocity and of some information on the turbulence. Note that profile measurements are taken at the center of the test section, where the model will be positioned.

2.2.2 Metrology

The building case was modeled at scale 1/300th with a wall-mounted prism of square cross-section with the dimensions: 10 cm × 10 cm × 49 cm which corresponds to a tower of 147 m high at full scale. To perform measurements, two tower models were built: one for wind loads measurements and the other for PIV measurements.

Wind-load measurements

The objective here is to be able to accurately measure the fluctuations of pressure exerted by the wind on the tower facades.

Pressure taps The first model is equipped with 265 pressure taps. Their locations are illustrated in figure 2.2a. Note that a common practice is to place the pressure taps according to the areas of interest of the project in question and to the pressure field analysis which was obtained by prior numerical simulations or empirical knowledge.

Pressure sensors All the pressure taps are then connected by vinyl tubes to synchronous multi-channel pressure sensors. The length of these tubes (about 1m) is calibrated in order to maintain good dynamics of the pressure signal up to the sensor. The pressure sensors are 32-channel piezoresistive differential pressure sensors. In this experiments, 9 sensors were used.

Note that in addition to these local wind-load measurements, a global measurement of the aerodynamic forces is conducted simultaneously using a high sensitivity force transducer (shown in figure 2.2a). Besides providing a global structural dynamic response, it allows to check that the pressure taps distribution all over the building is sufficient by ensuring that the pressure integration is consistent with the wind loads measured by the force transducer.

PIV measurements

In order to understand the evolution of aerodynamic forces undergone by the building, the topology of the flow is studied using Particle Image Velocimetry (PIV). The second model was made of Plexiglas which allows for optical access and, thus, to use PIV. Seeded particles, here olive oil micro-droplets, are then illuminated by a high power pulsed laser

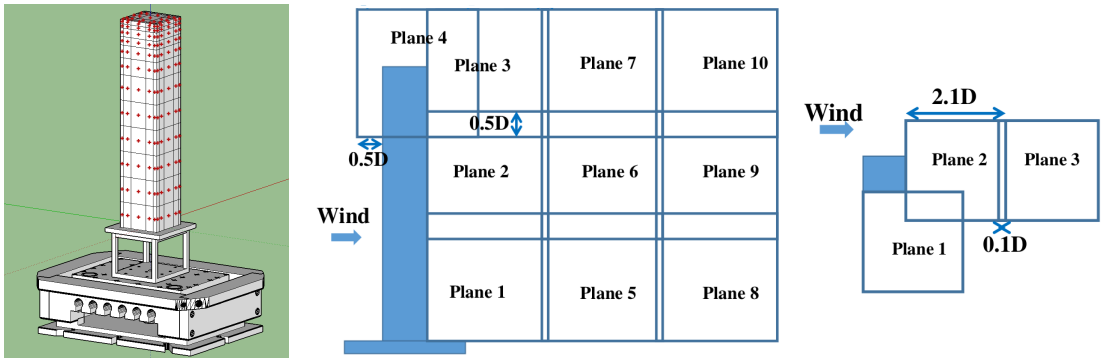

(a) (b) (c)

Figure 2.2 – Measurement configuration: (a), Pressure traps configuration; (b), Vertical PIV planes; (c), Horizontal PIV planes at normalized 4 heights; $z/H_{\text{ref}} = 1\,(z/D = 3.33)$, $z/H_{\text{ref}} = 0.75\,(z/D = 2.5)$, $z/H_{\text{ref}} = 0.38\,(z/D = 1.26)$, $z/H_{\text{ref}} = 0.19\,(z/D = 0.63)$.

sheet. The images are acquired using a special camera. Its optical sensor is square and highly resolved with a gray depth coded on 16 bits. Thus, being able to distinguish up to 65,000 shades of gray, this allows to have a very strong contrast in the images. Besides, the camera also consists of a special CCD sensor that can capture quickly a pair of successive images. The camera is finally mounted on a two-axis robot arm with 1m of travel on each axis. This makes it possible to "scan" the building by making several images to cover the whole flow. In his experiment, 9 vertical plans, of size 25cm × 25cm each, and 3 × 4 horizontal plans, 21cm × 21cm each, were combined (shown in figure 2.2, b and c). These plans once combined allow to cover the near wake flow at the symmetry plan, and 4 horizontal transverse plans.

2.2.3 Measurement extrapolation to full scale

It is reminded that wind tunnel measurements are carried out on a scaled model for a wind velocity lower than the full scale targeted speed requided by Eurocode regulations. In order to extrapolate the measurements to the full scale, and for a wind time scale of fifty years, it is necessary to define a geometric scale,

$$H^\star = \frac{H_{fs}}{H_{wt}},$$

and a velocity scale, computed at the reference height (generally 2/3 of the building's height and here $H_{ref} = 100\text{m}$), is defined as

$$U^\star = \frac{U_{fs}}{U_{wt}},$$

where subscripts $()_{fs}$ and $()_{wt}$ refers, respectively, to the full scale and wind tunnel scale. Given these two scales, it is then possible to define a time scale such that

$$t^\star = \frac{H^\star}{U^\star}.$$

While the two formers are strongly constrained by the wind-tunnel geometry and fan performances, the similarity argument leads to an acquisition time which ensures convergence and then fixes an acquisition frequency that captures well the full scale dynamics. To that end, it is generally recommended to reproduce a storm lasting more than 2 hours to ensure the statistical convergence of the peak pressure measured on the facades.

In these experiments, the size of the model is chosen as a compromise, such that it is large enough to allow access for pressure taps implantation, and small enough to reduce blockage effects, constrained by $H^\star = 300$. Regarding the velocity, at reference height, the full scale velocity is chosen [3] as $U_{fs} = 24\,\mathrm{m/s}$. Thus, considering a wind velocity in the wind tunnel of $U_{wt} = 10\,\mathrm{m/s}$, the dimensionless velocity is $U^\star = 2.4$, and thus the time scale is given as $t^\star = 125$. Therefore, with regard to pressure measurements, a common acquisition time of 2 min allows to achieve the equivalent of 4 hours at full scale, thus ensuring statistical convergence. In addition, it can be seen that, with an acquisition frequency of 512 Hz, an equivalent full scale frequency of 4.0 Hz is reached, which makes it possible to clearly capture events of 3 s bursts at full scale. For a given direction, a pressure tap (say is located in a zone of strong tearing) provides a temporal signal usually with very high pressure fluctuations with tearing peaks greater than three times the mean value. In order to have a representative value of these peaks, the signal is split into blocks of 10 minutes (at full scale), i.e. a period generally used in climatology to establish an average wind speed. The maximum and minimum values of the pressure are then recorded in each block. The peak value retained for the acquisition is then taken equal to the average of the peaks recorded in each block of 10 min.

Moreover, regarding the PIV, a lower acquisition frequency of $\simeq 7$ Hz was fixed by the camera acquisition rate. Therefore, for each PIV plan, 2500 pairs of images were acquired during an acquisition time of 6 min As the acquisition frequency is very low compared to the flow dynamics (at the scaled model), this enables an assumption of a statistically un-correlated pair of measured fields. With this assumption, the average field and its standard deviations provide the information on both the average speed and on the turbulent intensity of the flow.

3. This corresponds to a wind speed of $16m/s$ measured at a height of $10m$ which is in the range of reference speeds for most areas in France in the EN (2005)

2.3 Definition of the physical model

2.3.1 A RANS model

The incompressible airflow surrounding the building can be fully described by its velocity $\mathbf{u}$ and pressure p . This unsteady state, solution of the Navier-Stokes equations, can be further decomposed in terms of its mean $(\mathbf{U}, P)$, that will be resolved and a modeled fluctuation $(\mathbf{u}', p')$. By applying time averaging to the Navier-Stokes equations, one can obtain the partial differential equations (PDEs), called Reynolds averaged Navier-Stokes (RANS), written here in conservative form, whose solution provides the mean wind flow :

$$\frac{\partial(\rho U_j U_i)}{\partial x_j} = -\frac{\partial P}{\partial x_i} + \mu \frac{\partial}{\partial x_j}\left[\frac{\partial U_i}{\partial x_j}\right] - \frac{\partial}{\partial x_j}\left(\rho \overline{u_i' u_j'}\right), \tag{2.1}$$

$$\frac{\partial U_j}{\partial x_j} = 0.$$

Due to the non-linear term, the averaging procedure leads to a second-order moment $\overline{u_i' u_j'}$, called the Reynolds stress. Since all the unsteadiness and turbulence effects of the wind flow are contained in this term, without *a priori* specification of this term, the above system is not closed and cannot be solved. The immediate solution for the closure is to include additional transport equations to predict the turbulence second-order statistics. Relying on the Boussinesq analogy between turbulent fluctuations and thermal motion, Reynolds stresses are commonly modeled using a turbulent diffusion-like term, so-called eddy viscosity model. Several models have been proposed to relate quantities describing turbulent fluctuations.

A common practice associates the turbulent kinetic energy k, representing the isotropic part of the exact Reynolds stress, with the turbulence length scale l. Due to their simple structures, these models often require empirical closure functions or constants which are established and determined from experimental knowledge, trying to ensure their widest possible applications. For instance, the steady realizable k $-$ ϵ turbulence model (Shih et al., 1995), in which

$$\epsilon \sim \frac{k3/2}{l}$$

models the turbulence dissipation rate at the viscous scale, is often adopted for the expertise of wind flows around real-world buildings. In this model, the Reynolds stress is linearly linked to the mean shear stress by an eddy viscosity as follows:

$$-\rho\overline{u_i u_j} = \mu_t \left(\frac{\partial U_i}{\partial x_j} + \frac{\partial U_j}{\partial x_i}\right) - \frac{2}{3}\delta_{ij}\rho k, \tag{2.2}$$

where μ_t stands for the isotropic eddy viscosity coefficient, *i.e.* assuming that length and time scales of turbulence are smaller than those of the mean flow with no preferential

direction. Its value is calculated using the relation

$$\mu_t = C_\mu \rho \frac{k^2}{\epsilon}.$$

The coefficient C_μ, following the work of Shih et al. (1995), is a non uniform coefficient that depends on the mean strain-rate and ensures the realizability conditions, i.e. Schwartz inequality and the non-negativity of the diagonal Reynolds stress. It is defined by

$$C_\mu = \frac{1}{A_0 + A_s U_s \frac{k}{\epsilon}}, \tag{2.3}$$

with

$$\begin{aligned} U_s &= \sqrt{S_{ij}S_{ij} + \Omega_{ij}\Omega_{ij}} \\ S_{ij} &= \frac{1}{2}\left(\frac{\partial U_i}{\partial x_j} + \frac{\partial U_j}{\partial x_i}\right) \\ \Omega_{ij} &= \frac{1}{2}\left(\frac{\partial U_i}{\partial x_j} - \frac{\partial U_j}{\partial x_i}\right) \end{aligned}$$

and

$$\begin{aligned} A_s &= \sqrt{6}\cos(\phi), \quad \phi = \frac{1}{3}\arccos(\sqrt{6}W) \\ W &= \frac{S_{ij}S_{jk}S_{ki}}{S}, \quad S = \sqrt{2S_{ij}S_{ij}}, \end{aligned}$$

where S_{ij} and Ω_{ij} are, respectively, the mean strain (with its magnitude S) and rotation rates. The parameter A_0 is a closure tuning coefficient.

Substituting the Reynolds stress model (2.2) in the mean momentum equation (2.1) yields to

$$\frac{\partial(\rho U_j U_i)}{\partial x_j} = -\frac{\partial}{\partial x_i}\left(P + \frac{2}{3}\rho k\right) + \frac{\partial}{\partial x_j}\left[\mu_{eff}\left(\frac{\partial U_i}{\partial x_j} + \frac{\partial U_j}{\partial x_i}\right)\right], \tag{2.4}$$

where $\mu_{eff} = (\mu_t + \mu)$ stands for an effective viscosity. It can be noted that the isotropic component $\frac{2}{3}\rho k$ of the Reynold stress is absorbed in a modified mean pressure and only the anisotropic part plays an effective role in diffusing the momentum. It is worth noting that anisotropy here arises only from the mean flow strain and does not depend on the turbulent fluctuations. Moreover, in the computation of the pressure coefficient, required for the observation error in the data assimilation (in chapter 3).

With regards to the turbulence closure model, the transport of mean turbulent kinetic energy, k, is described by

$$\frac{\partial \rho U_j k}{\partial x_j} = \frac{\partial}{\partial x_j}\left[\left(\mu + \frac{\mu_t}{\sigma_k}\right)\frac{\partial k}{\partial x_i}\right] + \mu_t\left(\frac{\partial U_i}{\partial x_j} + \frac{\partial U_j}{\partial x_i}\right)\frac{\partial U_i}{\partial x_j} - \rho\epsilon, \tag{2.5}$$

where σ_k is a closure constant that enables the scalar mixing of k to be affected by other mechanisms than eddy viscosity. The hypothesis, associated to the value $\sigma_k = 1$, in which the eddy diffusion affects in the same way the momentum and the turbulent kinetic energy k, is analysed in section 4.4.2.

The turbulent dissipation rate transport is described by the model proposed by Shih et al. (1995)

$$\frac{\partial \rho U_j \epsilon}{\partial x_j} = \frac{\partial}{\partial x_j}\left[\left(\mu + \frac{\mu_t}{\sigma_\epsilon}\right)\frac{\partial \epsilon}{\partial x_i}\right] + C_1(S,k,\epsilon)S\epsilon - C_2\frac{\epsilon^2}{k+\sqrt{\mu\epsilon}}, \tag{2.6}$$

where

$$C_1 = \max\left(0.43, \eta/(5+\eta)\right)$$

and

$$\eta = Sk/\epsilon$$

is the normalised strain rate. The constants σ_ϵ and C_2 are closure coefficients that need to be calibrated. Assuming, that everywhere in the domain, the generation of ϵ is linked to its inter-scale redistribution, as it is established in an inertial sublayer, leads to a relationship between these coefficients (details in section 4.4.2). This closure hypothesis is analysed as well in section 4.4.2. To properly close this set of equations, an asymptotic behaviour has to be imposed near the wall, since the model can only be valid for high Reynolds regimes, broken hypothesis in the viscous layer.

2.3.2 The wall law

On the wall boundaries of the computational domain, no-slip condition must be verified, i.e., the velocity vector must be equal to zero. The region where the velocity evolves from zero to the free stream velocity, called boundary layer, is in practice extremely thin, leading to strong shear. This is even more pronounced when the object scales are very large compared to the eddy diffusive scale. To take into account the viscous shear near the wall when simulating a turbulent flow, it is necessary to construct sufficiently fine grids, which leads to substantial increase in the total number of nodes of the computational domain. In turbulent flows, and especially in wind engineering, such a direct full resolution is most of the times out of reach of actual computational resources. Instead, the semi-empirical method of wall functions enables the consideration of effects near the wall on coarse grids, which relaxes the requirements in computing resources. The principle of wall functions is to replace numerical schemes by new relations, coming from a physical knowledge, linking variables and their derivatives in order to compute surface integrals, i.e. the diffusive fluxes. This class of model is built in two parts. First for the mean flow, wall laws link conservative quantities to wall gradients through the shear stress. In the second part based on the knowledge of boundary layer flows, a simple boundary condition is introduced on the turbulence variables (Kalitzin et al., 2005; Mohammadi and Puigt, 2006). In our case, an simple homogeneous Neumann condition is given on k and

a Dirichlet condition is enforced on ϵ.

Historically, wall functions were first defined for smooth walls. Then roughness were token into account as it introduces significant changes in energy and momentum transfers between the wall and the flow compared with smooth walls For incompressible flows, usually, to take rough elements into account, a new coefficient, that vanishes on smooth boundaries is added, in order to modify the evaluation of the friction velocity involved in the boundary integral. As an example, one can consider the sand grain theory by Schlichting (1968), but such an approach issued from experiments cannot be extended easily to any roughness element shapes since there is no perfect law to find the equivalent sand-grain parameters in agreement with a general rough element shape. This is especially true for ABL wind inflows where rough element are mainly a consequence of far enough big objects, such as trees or small houses.

For large scale configurations (*i.e.*, ABL, high-rise buildings), the first grid centre closest to the wall usually falls at the high end of the logarithmic layer. The domain Ω_c, covered by the first grid cell closest to the wall centered on $|_c$ and with a boundary face centered on $|_f$ (see figure 2.3), the following relations hold

$$U^+|_c = \frac{1}{\kappa} f(y^+|_c), \tag{2.7}$$

$$\frac{\partial k}{\partial x_j} n_j|_f = \frac{\partial \epsilon}{\partial x_j} n_j|_f = 0, \tag{2.8}$$

$$P_k|_c = \epsilon|_c = \frac{u_\tau^3|_c}{\kappa y|_c} \tag{2.9}$$

$$y^+|_c = \frac{\rho u_\tau|_c y|_c}{\mu}, \tag{2.10}$$

$$\tau_{wall}|_c = \rho u_\tau^2|_c = \mu_{eff} \frac{U_i t_i|_c}{y|_c}, \tag{2.11}$$

$$U^+|_c = \frac{U_i t_i|_c}{u_\tau|_c}, \tag{2.12}$$

where U^+, y^+ are the dimensionless wall unit tangential velocity component and distance from wall, respectively, n_i and $t_i = 1 - n_i$ are the normal and tangential projections of the unit vectors onto the boundary face in the orthonormal frame (x, y, z). The log function f is an empirical function parametrised by constants which depends on the wall type (such as smooth or rough) and made consistent with the inlet wind profile; and $\kappa = 0.41$ is the von Kármán constant. As viscous effects are neglected at the center of the first cell where $y^+ \gg \mathcal{O}(1)$, the friction velocity u_τ is scaled by the square root of the fluctuations, following the empirical expression

$$u_\tau = C_\mu^{1/4} k^{1/2}$$

with $C_\mu = 0.09$. Let us note that (2.11) extends the constant shear stress to the wall as

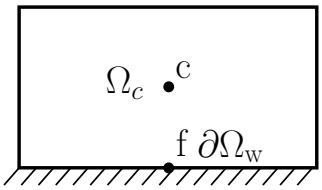

Figure 2.3 – First grid cell close to the wall.

we assume a linear behaviour inside the cell Ω_c in the second order finite volume scheme adopted in this work. In practice, this extension is of great importance as it enables the enforcement of the logarithmic law with a good numerical stability.

2.3.3 A neutral atmospheric boundary model (ABL)

In early experiments by (Jensen, 1958), it was reported that in wind-tunnel testings it is just as important to correctly model the wind as to correctly model the building. Thus, setting down the basic conditions for simulating the atmospheric boundary layer is of a great importance. In a later time, Richards and Hoxey (1993) recommended to model the atmospheric surface layer as a horizontally-homogeneous turbulent boundary layer (HHTBL), which consists in considering constant properties in the streamwise and spanwise directions. Thus, only variations along the vertical axis are considered. For computational studies, HHTBL velocity and turbulence statistics profiles were proposed, and adapted to the standard $k-\epsilon$ turbulence model (Yang et al., 2009; Richards and Norris, 2011). Therefore, in steady incompressible two-dimensional atmospheric boundary layer with the $k-\epsilon$ turbulence model, the existence of homogeneous flow has the following implications:

— The vertical velocity is zero.
— The pressure is constant in the streamwise direction.
— The shear stress is constant across the flow (in the vertical direction).
— The turbulent kinetic energy and its dissipation rate satisfy an energy equilibrium.

To enforce the inlet wind flow, profiles for U, k and ϵ are defined as

$$U_{in} = \frac{u_\tau^{ABL}\ln(z+z_0)}{\kappa z_0}, \qquad k_{in} = \frac{(u_\tau^{ABL})^2}{\sqrt{C_\mu}} \qquad \text{and} \qquad \epsilon_{in} = \frac{(u_\tau^{ABL})^3}{\kappa(z+z_0)}, \tag{2.13}$$

where $C_\mu = 0.09$ is chosen as for a standard $k-\epsilon$ model and u_τ^{ABL} is the friction velocity associated with the constant shear stress along the ABL width

$$u_\tau^{ABL} = \frac{\kappa U_{ref}}{\ln(\frac{H_{ref}+z_0}{z_0})}$$

in which U_{ref} and $H_{ref} = \frac{2}{3}H$ are, respectively, reference velocity and height chosen to

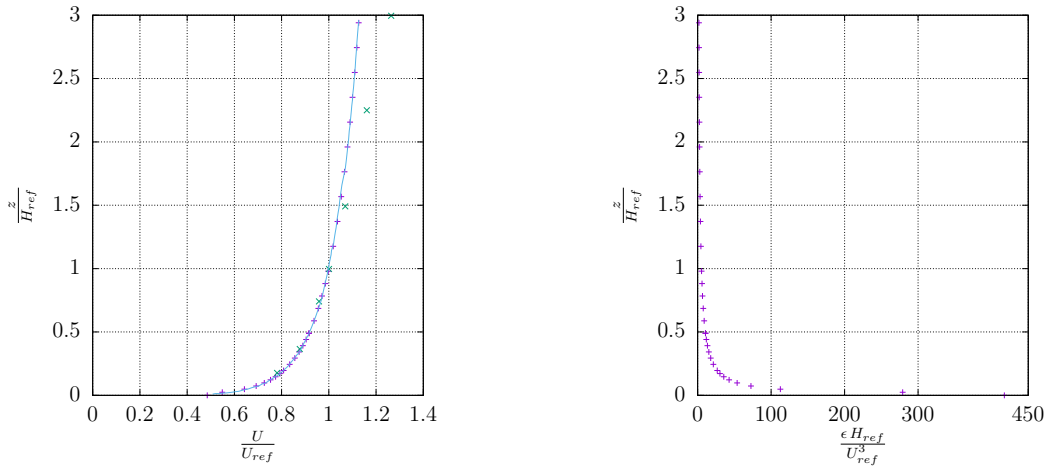

(a) (b)

Figure 2.4 – Profile of the neutral atmospheric boundary layer: (a), mean wind velocity; (b), turbulent dissipation rate ϵ.

match with the experimental profiles, and thus the eurocode (EN, 2005) (see figure 2.4). Let us note that these profiles are consistent with the wall treatment as we prescribe eddy viscosity ground-value by (3.28), such that $u_\tau = u_\tau^{ABL}$. As for roughness height z_0, it was set to 0.02, which was chosen as an intermediate between class I and class II roughness (EN, 2005).

2.4 Definition of the computational model

In this section, we present recommendations for a proper numerical setting for the simulation of wind flow around buildings, in particularly isolated cases. Comprehensive literature reviews on the use of CFD for these applications have been published. To list some: (Franke et al., 2004; Blocken et al., 2007; Tominaga et al., 2008; Tamura et al., 2008). Although full-scale building model can be realized in numerical simulation, it is still essential to reduce workload via the reduction of grid number and the dimension of the computational domains.

Domain size

To avoid the influence of the domain boundaries on the flow near the building and the wall-pressure, a sufficiently large domain is required. In order to choose the size of the entire computational domain, upon previously collected studies, the guidelines given by (Franke et al., 2004; Meng et al., 2018) suggest the following:

— The inlet and the lateral sides should be around $5H$ away from the building, where H is the building height,

— To prevent an artificial acceleration of the flow over the building, the top of the computational domain should be also at least $5H$ away from this building.
— For the blockage ratio $\delta_b = \frac{A_b}{A}$, where A_b is the projected building's area perpendicular to the wind direction and A is the area of the computational domain perpendicular to the wind direction, the limit of 3% is recommended,
— The outflow boundary should be positioned at least $10H$ behind the building to allow for inflow re-establishment downstream.

In this work, the dimension of computational domain is fixed as $18H \times 12H \times 6H$ (length $\times$ width $\times$ height). Meanwhile, the upstream and downstream distances were set as $\sim 6H$ and $\sim 12H$, respectively, providing wind with sufficient space to fully develop. The blockage ratio is 0.28 % less than the threshold of 3%.

Computational grid

When computing flows in wind engineering studies, it is often difficult to generate a "good one". In fact, the task of grid generation is also the most time-consuming task compared with the computation (in the case of steady-flow computation). If not designed correctly, the computational results may depend on the grid that is used to discretise the domain. Therefore, the grid has to be designed in such a manner that it does not introduce errors that are too large. This means that the resolution should be fine enough to capture the important flow local features, e.g. shear layers due to separation and recirculation, and the quality should be high.

The recommendations presented here are mainly based on up to date published results. Grid stretching/compression should be small in regions of high gradients (to keep the truncation error small), also expansion ratio (between two consecutive cells) should be below 1.3 in these regions. Besides, as we are adopting the Finite Volume methods, another criterion for grid quality is the angle between the normal vector of a cell face and the line connecting the centroids of neighbouring cells. Ideally they should be parallel. With regard to the shape of the computational cells, hexahedra are to be preferred over tetrahedra, as the former are known to introduce smaller truncation errors and display better iterative convergence (Hirsch et al., 2002; Franke et al., 2004). On walls, the grid lines should be perpendicular to the wall. Yet, for the necessary resolution it is impossible to make recommendations in advance as this is generally problem dependent. Since we employ the logarithmic law of the wall, the position of the first computational node should be of course placed in the logarithmic region, corresponding to a non-dimensional wall distance of at least $y^+ = 30$.

In this study, hexagonal structured grid was adopted to generate the background empty fetch, after which local mesh refinement approach was employed to densify the gird around the building model, as shown in figure 2.5. The minimum distance of grid centroid to the ground was set to $0.006 \times H$, approximate to one meter, while it reaches down to $0.0008H$ for the centroid of the cell adjacent to the building walls. Grid number reached approximately 3.5 millions cells in the computational domain. This grid is referred to by case mesh in the figures legends for this chapter. As for the section 2.6.3 in which we

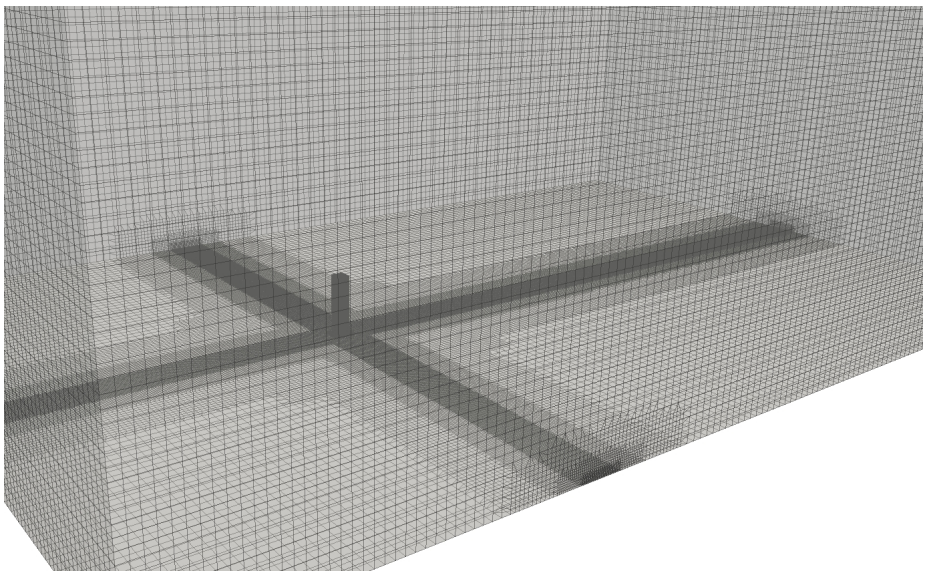

Figure 2.5 – Generated grid

check the grid convergence, both grid number and grid size were adjusted for comparison.

2.5 Definition of the numerical methods

The open source library OpenFOAM (Jasak, 1996) was used to implement the CFD and adjoint governing equations derived in the next chapter. The library utilizes a second order finite volume discretization approach (Patankar, 1980; Versteeg and Malalasekera, 2007; Moukalled et al., 2016) and a fully implicit first order method for time integration. The variables are usually defined at the centers of each control volume (CV). Moreover, the grid faces and there consecutive edges defining the CV's are assumed to be straight. A prediction-correction procedure is used for the pressure-velocity coupling using the SIMPLE-type methods. As non-staggered grids are used, the "checkerboard effect" [4] present in the pressure is efficiently eliminated using the Rhie–Chow interpolation (Rhie and Chow, 1983).

With regard to the discretization schemes, first, let us recall that in order to obtain maximum accuracy of convective fluxes (when using linear interpolation), the line connecting two neighbour CV centers should pass through the center of the common face. When the grid generator uses some kind of block-wise generation, such as the OpenFOAM built-in utility used to generate the mesh in this study, such situations is not achievable.

With regards to the diffusive fluxes, the maximum accuracy is achieved when the line

4. The "checkerboard effect" is a numerical artefact where two subsets of values are alternatively present in the adjacent cells distributed as in a checkerboard, leading to a very irregular solution even if each of the subsets are smooth.

connecting the neighbour CV centers is orthogonal to the cell face and passes through the cell-face center. This property constitutes a measure of the grid quality with the latter is often referred to as skewness while the former as mesh non-orthogonality, whose angle is expressed in degree.

The former measure is reduced by refining the grid as indicated in previous section, which reduces the distance between the cells sharing the same face-center and the location at which the straight line connecting the cells centroids. As for mesh non-orthogonality, iterative correction was applied for the Poisson solver. Thus, for this study, we have privileged mesh quality over computational cost, as to avoid additional sources of parametric errors and, also, to ensure computational stability. In fact, although OpenFOAM can be a reliable solver; yet, it is quite sensitive to grid quality, especially with the discretized RANS adjoint model.

Further, since wind around buildings are convection-dominated flows, the numerical approximation of the advective terms is very important. With regards to recommendations performed in the literature, Franke et al. (2004) denotes that the use of first order methods like the upwind scheme is highly discouraged, as it suffers from excessive numerical diffusion. Let us note that under the framework of data-model coupling in this thesis, it is shown that relaxing this requirement helps to provide a robust descent direction for the optimisation process. However for a first validation and in chapters 4 and 5, a second order scheme will be used and whenever numerical stability becomes an issue, we indicate it and shift to the upwind scheme. Indeed, the use of a first order scheme can be here justified, as it will be seen in chapter 6 that the results of the optimisation will be generally closer to the data than using the second order scheme.

Yet, the choice for an adequate second order scheme is much of a trial and check, as it is case dependent, and far from being straightforward. While traditional central differencing schemes does improve the accuracy, they generally generate non-physical oscillations, and more so unboundness, when the solution contains steep gradients (e.g, high strain rates at flow impingement) of the transported variable (Godunov, 1954; Tamamidis and Assanis, 1993; Zhang et al., 2015). As a remedial, a scheme with the boundedness property (although only guaranteed for one-dimensional cases) will be used herein. Basically, a flux-limiter will be used which combines a high-order scheme (e.g. the second order central difference) that acts in the smooth flow regions, with a low-order scheme near the sharp gradients. Choosing the suitable flux limiting scheme gives the appropriate interpolation between cell-centred value and it's face-centred value. It is performed through an efficient use of local informations on the gradients in order to limit the total variation of the variable. This ensures the physical boundedness and monotonicity.

In the purpose of validation, some of the well-known total variation diminishing (abbreviated usually as TVD (Sweby, 1984)) and normalized variation diminishing (NVD)(Leonard, 1988; Jasak et al., 1999) flux-limiters have been used in the current chapter:

— the superBee flux-limiter (Roe, 1986)
— the Gamma flux-limiter (Grinstein and Fureby, 2005)
— the second order upwind (or linear-upwind) scheme (Warming and Beam, 1976)

Let us note a "V" type of schemes for vector fields where the limiter is applied in the direction of greatest change. It is used for the advection of the mean flow. It should be noted that we are advocate of the latter scheme (i.e. linear-upwind) as it is shown to be one of the most efficient and accurate scheme for Reynolds Averaged Navier Stokes (RANS) simulations on bluff body flows (Robertson et al., 2015).

2.6 Validations

In order to ensure an accurate wind flow prediction, a validation of the CFD has to be conducted. Recommendation on the practice for CFD uncertainty analysis can be found in (Ferziger, 1993; Roache, 1997; Steffen et al., 1995; Peric, 1997; Ferziger et al., 2020). In the data-assimilation framework, this step ensures that the numerical errors of the initial solution are negligible, due to an adequate choice of grid refinement and convection scheme. In other words, as any numerical solution contains errors, the aim here is to quantify them, and thus to give some confidence that any remaining discrepancy are conceptual, i.e. arising from turbulence modelling. Some acquirements for a first solution verification can be summarized as follow,

- Verify the assumption of an established boundary layer corresponding to the HHTBL hypothesis, by performing a simulation in an empty domain with the same grid and boundary conditions.
- Judge iterative convergence of the solution by monitoring relevant values for the considered problem (e.g. wall-pressure here) in addition to the residuals, which can be done within a single calculation.
- Use local grid refinement in the regions of interest, such as shear layers, to check for grid dependence of the results. This requires a minimum of two calculations on different grids.

Let us note that discretization errors, also called order check, should be analyzed by comparing solutions on a sequence of systematically refined grids (through the latter acquirement). Systematic refinement is easy for uniformly sized grids and relatively small domains. As we simulate with a relatively large domain and, at the same time we have to fulfil the requirement for fine enough grid close to the wall (although the ideal range $30 < y^+ < 100$ is very hard to achieve), where non-uniform and variably refined grids (i.e. up to 6 levels of refinement in the chosen case) are used, this task is not straightforward. Instead, this check will be here performed through a two step process. At first, we run the simulation on three different meshes, where a local refinement is performed in a region of interest (i.e. near shear layers and wake), instead of an expensive uniform refinement. Doing so, we both verify the truncation order and we verify that the solution reaches an asymptotic range (Roache, 1994), i.e. the solution reaches a plateau as the mesh is refined. Then, if the asymptotic range is reached, we proceed for point-wise and profile-distributed comparisons.

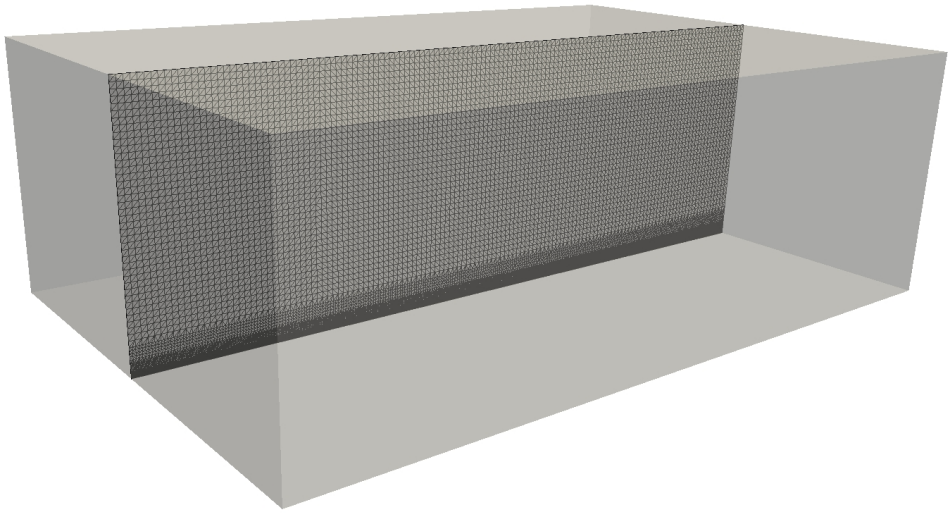

Figure 2.6 – A schematic of the empty domain.

2.6.1 ABL profile verification

Before performing the computation of the flow around the building, the conjunction of the boundary conditions and the turbulence model (i.e. realizable $k-\epsilon$) should be capable of producing a homogeneous boundary layer flow (HHTBL) in the absence of the object. As reported by (Hargreaves and Wright, 2007; Parente et al., 2011), this is an issue in itself. These problems have been highlighted in (Walshe, 2003) in which decay of the velocity profile with distance along the domain was identified. The authors postulate that the errors were due to an observed peak in the turbulent kinetic energy close to the ground. In this section, an empty domain is used to demonstrate that wind inlet boundary conditions, provided in section 2.3.3, are maintained until the building position. This check allows us to discard the hypothesis of unbalanced inflow conditions for explaining discrepancies between CFD and experimental measurements. Let us note that in order to ensure this sustainability, a proper modification to the wall boundary condition, as introduced in section 2.3.2, is already implemented in the OpenFOAM library.

The domain used in the investigation is shown in figure 2.6, its size is identical to the one including the building. Simulations were run until an acceptable level of convergence has been achieved ($\sim 10^{-8}$).

Figure 2.7 is a typical plot produced by computational wind engineers, when showing that their simulation of the ABL is satisfactory. It shows profiles of streamwise wind velocity, turbulent kinetic energy and the dissipation rate. Here it is also shown the eddy viscosity profiles function of the previously mentioned variables. The profiles along the symmetry plan $y = 0$ are up to a height $\sim 2H$ ($H = 1.47H_{ref}$) and at the streamwise positions $x = -6\,H$ (inlet) and $x = x_b$, where $x_b = -0.5\,D$ position where the building will

be placed. Theses profiles are used to demonstrate any variation caused by the boundary layer development. In the figure, a plot of the eddy viscosity replaces the commonly used $\frac{\partial U}{\partial z}$. This is to show that the turbulent viscosity is well represented.

At first sight, the profiles of the mean velocity are encouraging, with the profile being greatly maintained. The turbulent dissipation rate and the eddy viscosity are also seen to maintain themselves along the domain. However, when looking into the near-wall region of the boundary layer, the initially constant value of turbulent kinetic energy does barely maintain itself. The peak in kinetic energy is again clear, yet with a relative excess of less than 8%. Although, the peak in turbulent kinetic energy near the ground may give cause for concern, but it should be noted that it is present to some degree in reality (Hargreaves and Wright, 2007). Moreover, as found by Walshe (2003); Hargreaves and Wright (2007) this spike occurs in the second cell above the ground, this seems to be an intrinsic feature of the $k-\epsilon$ model and in this regard the model deviates due to an overproduction of k. Note that for the upper boundary of the domain (not shown here), some deviation on the eddy viscosity were observed, yet, still far up from the building such that it does not affect the results.

As an aside, the values of y^+ of the size of the first cell are in slight excess ($y^+ \sim 1500$), outside the range of 30 to 300 necessary for the consistent and accurate application of the logarithmic law of the wall. Let us recall that this is computed with the well documented sand-grain roughness effects (say K_s) and does not apply with the modeled wind profiles since the roughness height $z_0 >> K_s$ would shift the layer further from the wall. It is suggested that there may be a need for an alternative definition of y^+ in the modelling of the Boundary layer when rough walls are used for the ground, e.g. investigating a relationship that relates z_0 with K_s .

Nevertheless,in our case, when the building is added and more refinement were applied, the y^+ has dropped to ~ 600, which can be considered acceptable here.

2.6.2 Iterative convergence

Because the RANS equations are non-linear and the dimensions are quite large, an iterative marching method is used. The algorithm is composed by two iteration loops: the inner iterations involve solving the tangent-linear system, with a SIMPLE algorithm to determine the pressure, and the outer iterations for updating the non-linear term and the model coefficients function of the flow state (such as μ_t). Requiring that the norm of the residual (from solving the linear algebraic system at each inner iteration) falls three to four orders of magnitude is usually a safe criterion. In this study a residual error under 10^{-5} was reached by all the variables and this is verified also for all the grids considered for the validation. For conciseness, only the computed residual for the mesh case is shown in figures 2.8.

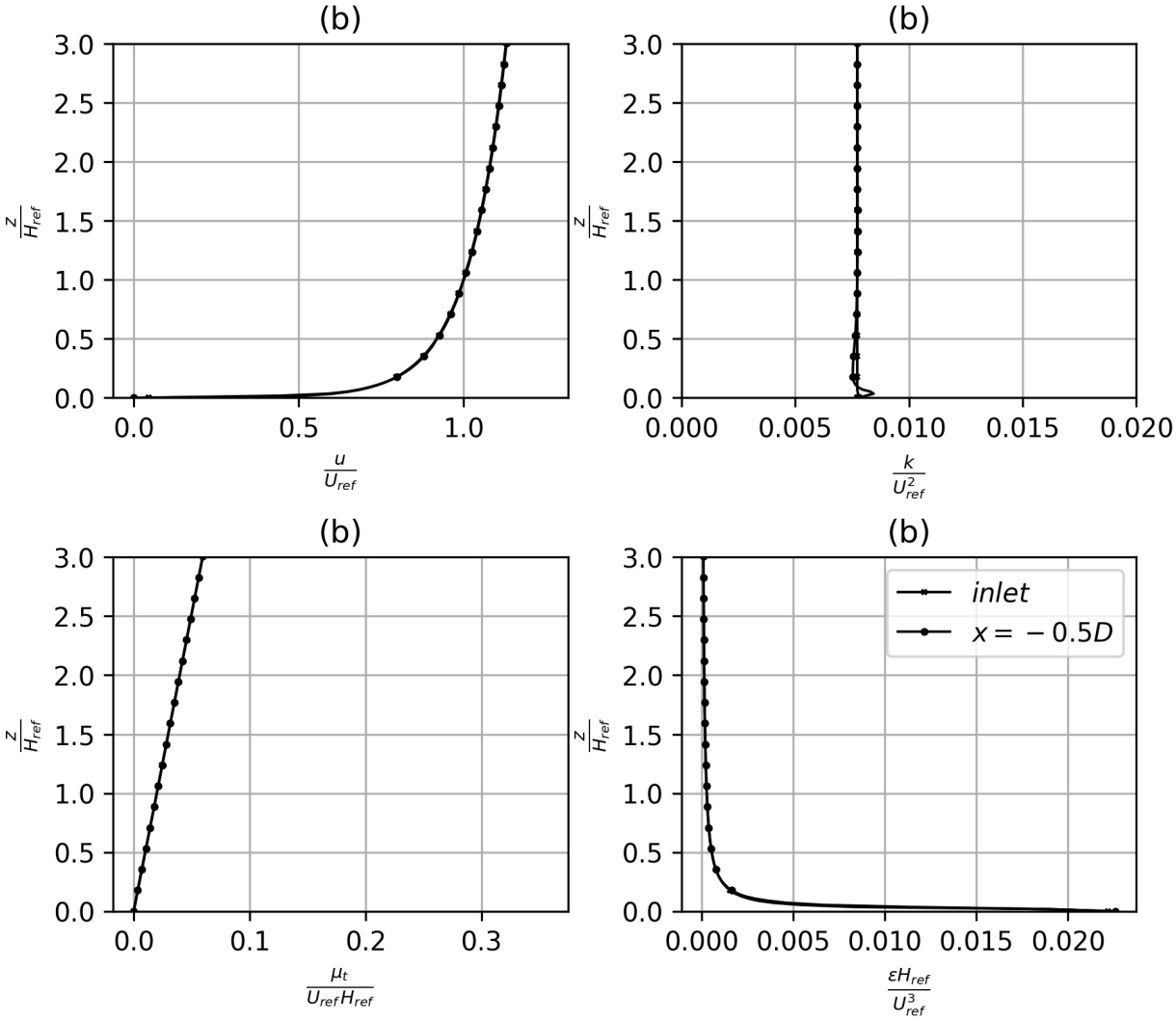

Figure 2.7 – Plots of the streamwise velocity, turbulent kinetic energy, dissipation rate and the eddy viscosity for the wind profile by (Richards and Hoxey, 1993), up to a non-dimensionalised height of $3H_{ref}$ and at distances of $x = -6\,H$ (inlet) and $x = x_b$ ($x_b = -0.5D$).

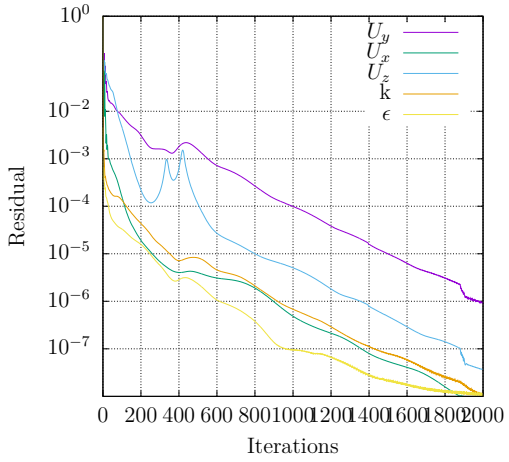

Figure 2.8 – Residual monitoring for the mesh case.

2.6.3 Grid convergence

In the complex case that we are considering, i.e. turbulence modeling and schemes in which flux limiters are used, it is difficult to predict a priori the order of accuracy of the discretized system. Roache (1997). Without an exact solution for the actual problem, it is necessary to posses at least three grid solutions to extract the discretization order, denoted $\mathcal{O}_{obs}$. If the grid refinement is performed with a constant ratio r (say $r = 2$ for doubling the coarse mesh), then a direct order evaluation can be obtained from the three grid solutions,

$$\mathcal{O}_{obs} = \frac{\log\left(\frac{f_3 - f_2}{f_2 - f_1}\right)}{\log(r)}$$

with subscripts 1, 2 and 3 denotes, respectively, the finest, the medium and the coarsest grid. Further, assessing the accuracy of the computation requires that the grid is sufficiently refined such that the solution is in the asymptotic range of convergence.

The methodology we are adopting here follows the work by (Roache, 1994) on uniform grid refinement studies, where the basic idea, as quoted from his work is to "approximately relate the results from any grid refinement test to the expected results from a grid doubling using a second-order method. The GCI (grid dependency index) is based upon a grid refinement error estimator derived from the theory of generalized Richardson Extrapolation". Roache (1994) suggests a grid convergence index GCI which enables reporting the results of grid convergence studies and provides an interval of the order of the estimated error. In this work, the GCI will be computed using the three levels of grid in order to check that the solution is within the asymptotic range of convergence. Provided the observed order of the method, i.e. $\mathcal{O}_{obs}$, if an exact solution is known to a model problem, we can estimate the error as $E \sim Ch^{\mathcal{O}_{obs}}$ with h is the grid size and ε is the relative error between the estimated solution and the exact one (as $h \sim 0$). Then the approximate constancy of E, i.e. $C = \frac{E}{h^{\mathcal{O}_{obs}}}$, is a faithful verification of the order $\mathcal{O}_{obs}$ and an indication

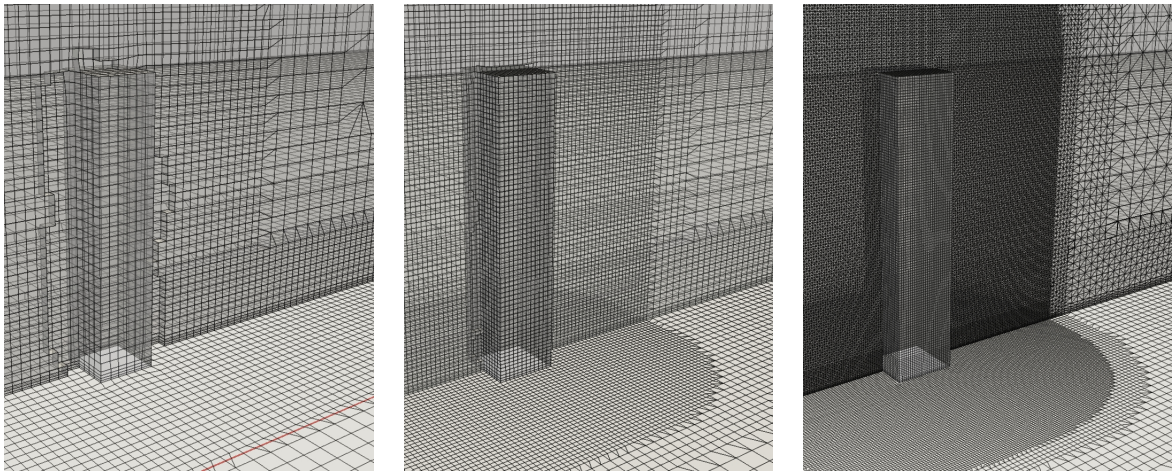

(a) (b) (c)

Figure 2.9 – Three mesh configurations for grid convergence; (a), mesh-1, (b), mesh-2, (c), mesh-3.

that the asymptotic range is achieved.

In the practical case where the exact solution is not known, we calculate as an alternative, two GCI, from fine grid to intermediate grid $GCI_{12} = \frac{\varepsilon_{12}}{r^{\mathcal{O}_{obs}}-1}$ and from intermediate grid to coarse grid $GCI_{23} = \frac{\varepsilon_{23}}{r^{\mathcal{O}_{obs}}-1}$. Then the estimate constancy, defined as $E \simeq \frac{GCI}{3h^{\mathcal{O}_{obs}}}$, leads to the verification that $GCI_{23} \simeq r^{\mathcal{O}_{obs}} GCI_{13}$, thus assessing that the asymptotic range is achieved.

The grid cell sizes in the region of interest (e.g. $-3\,H < x < 3\,H$) is halved in each direction. Three cases with different degrees of grid resolution, as mesh-1, mesh-2 and mesh-3, were generated. Their number of grid points were 0.98, 1.39 and 4.54 millions, respectively, for which refinement is illustrated in figure 2.9.

Note that we were not been able to afford another refinement level, as this halving leads to a 2^3 increase in the number of cells, with a grid number above 20 millions. Yet, note that the two finest grids are both fine enough so that monotone convergence is obtained and thus we are in the conditions of the extrapolation theory of Richardson. Therefore the grid convergence index (GCI) is valid to estimate when the grid-independent solution is reached (Roache, 1994; Peric, 1997; Ferziger et al., 2020).

Mean pressure coefficients on several points on the surface of the modelled building and in the bulk of the wake have been considered for order convergence verification and to verify that the solution reached a grid-independence (or asymptomatic) range, as presented in table 2.1.

Although the slightly variability from one point to another, the observed order of convergence $\mathcal{O}_{obs}$ is very close to the theoretical order $\mathcal{O}(2)$.

Based on theses observed orders, it is shown that grid uncertainty are overall gradually decreased $< 6\%$ by halving the cells size (as $GCI_{12} < GCI_{23}$) giving a mostly monotonic

Point	Pt. location (x,y,z)	$GCI_{12}(\%)$	$GCI_{23}(\%)$	$GCI_{23} \simeq r^{\mathcal{O}_{obs}} GCI_{12}$	ordre $\mathcal{O}_{obs}$
1	(0 50 124)	1.43	7.50	1.02	2.35
2	(0 50 100)	1.91	8.14	1.02	2.05
3	(0 50 19)	1.15	4.77	1.012	2.03
4	(15 50 100)	3.38	10.50	1.02	1.60
5	(15 50 19)	0.54	3.67	1.01	2.73
6	(0 -15 124)	0.99	3.96	1.009	1.97
7	(0 15 124)	5.79	15.96	1.03	1.41
8	(0 15 100)	1.12	4.84	1.01	2.087
9	(0 15 19)	-	-	-	-
10	(0 -15 100)	1.30	4.46	1.01	1.75
11	(0 -15 19)		-	-	-

Table 2.1 – Observed order of convergence, grid convergence indices and the asymptomatic range of convergence for the three mesh cases. This quantities accounted for at the wall-pressure at different points.

convergence as $GCI_{23} \simeq r^{\mathcal{O}_{obs}} GCI_{12} \sim 1$ (at most 2% error) for all points. A further qualitative illustration of the grid convergence (by the three grids), in figure 2.10, shows that the solution of the proposed mesh case lies appropriately within the asymptotic range estimated by the three grid cases. Thus, the current 3.5 million point grids are clearly sufficient to achieve monotonic convergence at least for the variable of interest C_p.

To further verify grid independence, wall-pressure profiles are compared to wind tunnel data as illustrated in figure 2.11. Let us note a forth grid case was generated for the data comparison which is based on the proposed mesh case with more refinement at the vicinity of the building (it is referred to in the figures by "fine mesh" plotted with dotted line). Globally, predicted wall-pressure coefficients of all cases have the same pattern as those of the wind tunnel data. When grids tend to be sparse, the accuracy of numerical results depends on the variable displayed on the building surfaces. Grid resolution implies minor impacts on positive pressure coefficients (i.e. at the frontal façade), while negative wind pressure coefficients witness significant variability (see the numerical results of the coarsest mesh-1 case). However, as the grid number increases, influences of grid resolution on the numerical wall-pressure decreases and all cases seems to collapse, as it is shown in figure 2.11.

2.6.4 Scheme convergence

This section presents several advection test cases to evaluate the relative performance of the proposed flux limiter schemes from section 2.5, that is superBee (TVD), Gamma (TVD) and linear-upwind (NVD). In these tests, the accuracy is qualitatively illustrated by the wall-pressure profiles (see figure 2.12) around the building façades and the mean

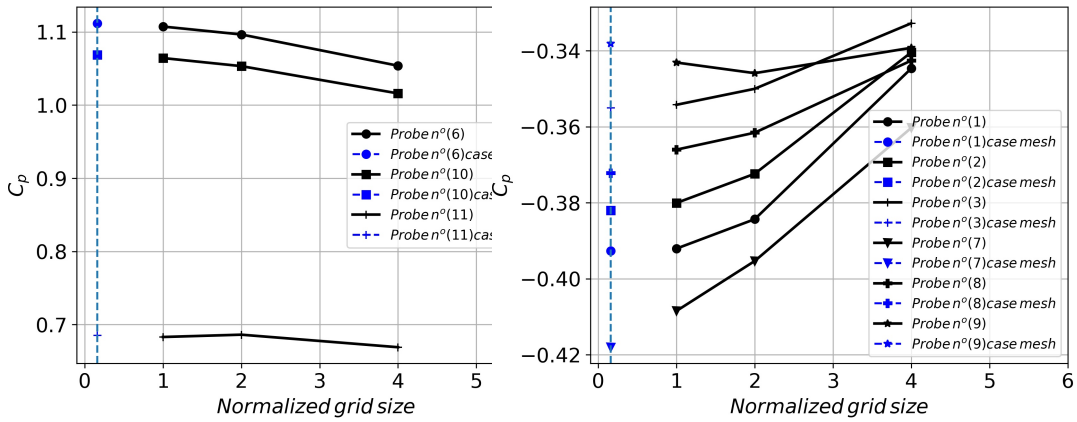

(a) (b)

Figure 2.10 – Richardson extrapolation of the mean pressure coefficients at different points, their locations are listed in table 2.1

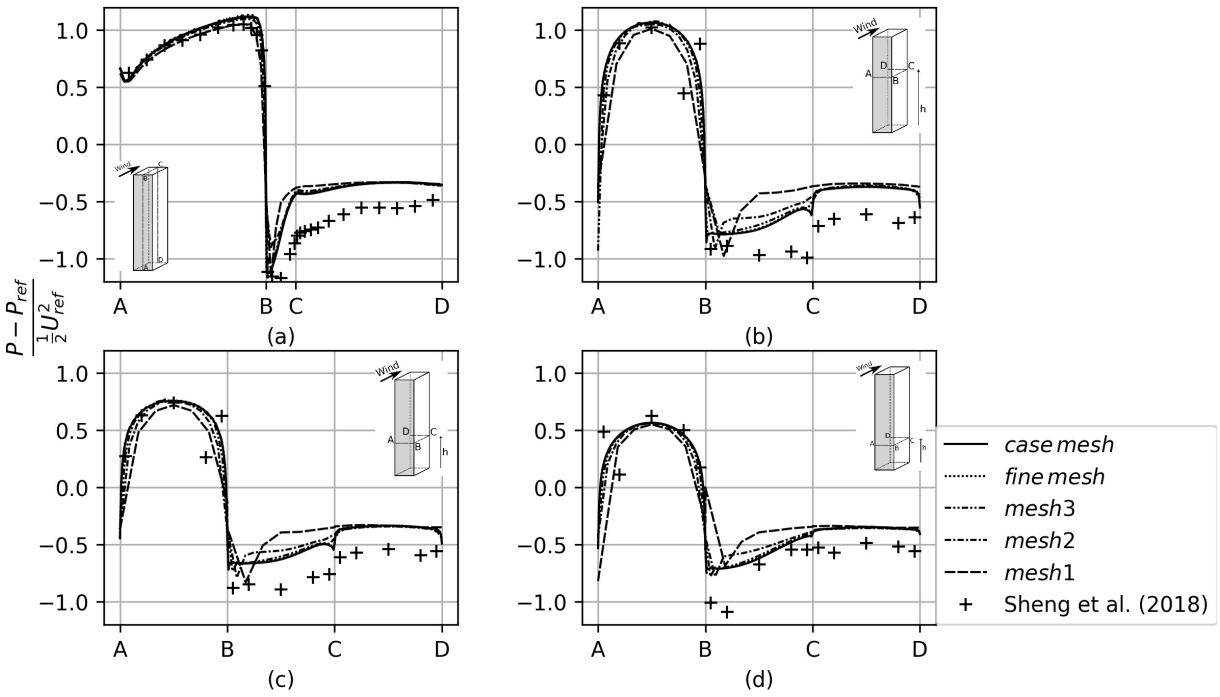

Figure 2.11 – Effects of near-structure mesh refinement on the mean pressure coefficients along the building facades.

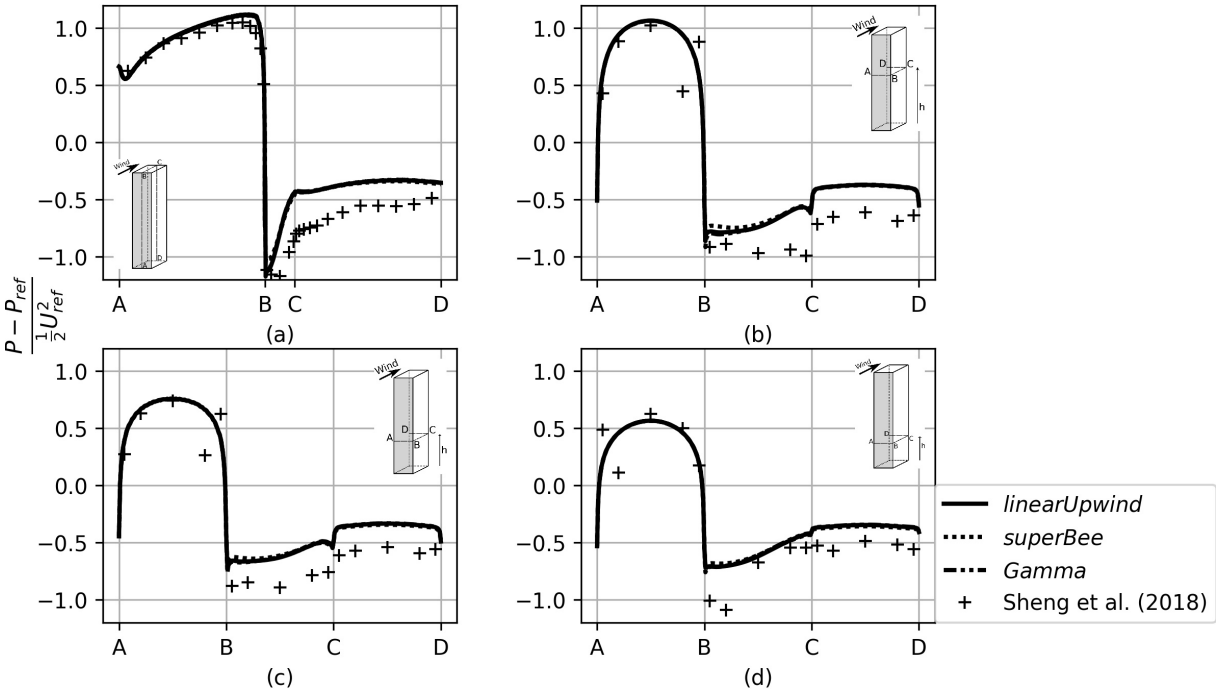

Figure 2.12 – Effects of convection scheme on the mean pressure coefficients along the building facades.

streamwise velocity at two heights $z/H_{ref} = 0.19$ and $z/H_{ref} = 1$ along the downstream flow at the symmetry plan (see figure 2.13). The results show that both Gamma and linear-Upwind provide almost identical results. While with superBee limiter, results have deviated slightly for the tearing wall-pressure near the leading edges and for predicting the recirculation length. Although, these deviations can be judged significant between the schemes, yet, it should be noted that the linear-upwind scheme has allowed reaching the lowest iterative convergence and a robust descent.

2.7 Conclusion

The principle of RANS modelling was introduced in this chapter. By gathering a set of recommendation from literature CFD studies, has allowed the definition of a proper computational set-up; e.g avoiding blockage effects, boundary effects, which enables non-biased comparison with the experimental data. The consistency between the wind profile, of the modelled ABL, and the wall treatment for the ground was verified in an empty domain. This consistency was verified as the (downstream) homogeneity of the wind profiles are seen persistent downstream with the absence of the disturbances, i.e. results from the presence of the building. Moreover, a first solution verification (before the assimilation) is conducted, that is grid convergence and the numerical scheme check. In the former, the solution given by the chosen grid does fall in the asymptomatic range, by judging

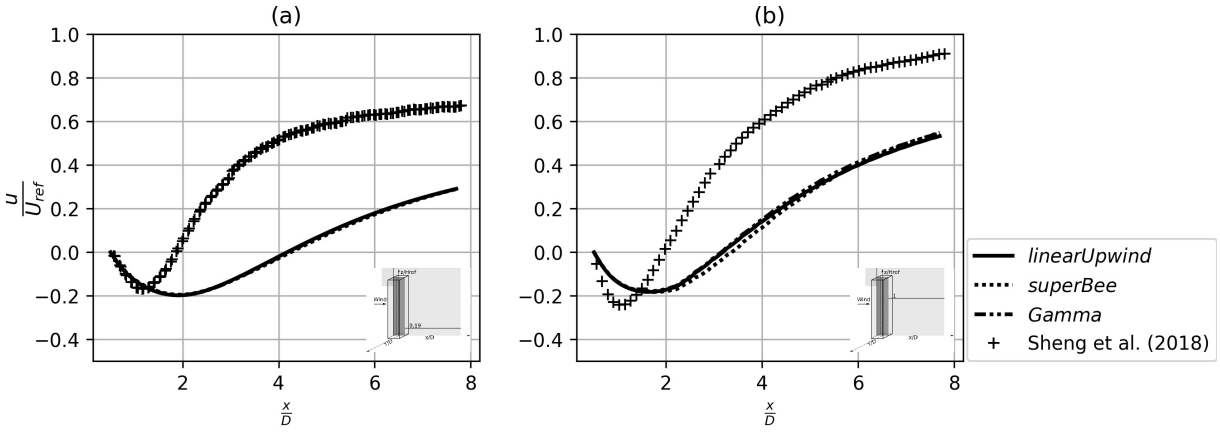

Figure 2.13 – Effects of convection scheme on the mean streamwise velocity along the wake centreline; comparison with experimental data at all horizontal plans levels.

the wall-pressure to be the first variable of interest. Nevertheless, in comparison with the data, the mean velocity at the wake centreline reaches also a grid convergent state. In the latter, the ability of different flux limiter schemes namely, Gamma, superBee, linear-upwind are assessed by evaluating the wall-pressure and the mean streamwise velocity. The simulated results are compared with the wind tunnel experiments. The results have shown that Gamma and linear-Upwind have lead to identical results, while superBee limiter results has deviated slightly, e.g. for the tearing wall-pressure near the leading edges and recirculation length. Over the three schemes, linear-upwind flux limiter is looking promising for the development of the assimilation procedure, as it enables lower iterative convergence of the RANS solver as compared to Gamma scheme. Therefore, this scheme will be chosen for the next chapters, unless numerical stability is of an issue as will be seen in chaptre 6.

Chapter 3

Method development: a variational data-assimilation procedure

3.1 Introduction

In this chapter, we present the variational data-model coupling framework. In variational data assimilation, the estimation problem is written as a constrained optimisation, and its resolution is based on optimal control techniques. A particular attention is given to the analytical derivation of the adjoint model of one of the most common turbulence models, the realizable revision of $k-\epsilon$, coupled with near wall closure.

3.2 Variational approach

A generic variational data-coupling problem can be formally described by the following optimisation problem :

$$\begin{aligned} \min_{\alpha} \quad & \mathcal{J}(\alpha, \mathbf{X}(\alpha), \mathbf{Y}_{\text{obs}}) \\ \text{subject to} \quad & M_i(\alpha, \mathbf{X}(\alpha)) = 0 \qquad i = 1, \ldots, N \end{aligned} \tag{3.1}$$

where $\mathcal{J}()$ is the cost function that quantifies the misfit between observations and the model, *i.e.* here measurements and CFD solution respectively, penalised by an *a priori* statistical knowledge of these discrepancies in the form of a covariance matrix. Here we refer to the flow measurements $\mathbf{Y}_{\text{obs}}$, and the predicted flow $\mathbf{X}$. N stands for the number of independent variables necessary for a full description of the flow. The minimisation of this function is constrained by the set of flow governing equations M_i. Such problem may be solved using a gradient-based algorithm. It consists in iteratively evaluating the cost functional and its sensitivity derivatives in order to find the minimum by successive updates of the control variables α. The sketch of the procedure is given in algorithm 1.

In order to properly define the cost function, one may proceed as follows. The only available experimental inputs are wall-pressure measurements. Ideally, the discrepancy between the experimental pressure measure and the model wall-pressure can be expressed as $\Delta P^w = P^w_{\text{obs}} - \mathcal{H}(P^w)$ where $\mathcal{H}(.)$ restricts the pressure at the measurement positions (the subscript w stands for wall). However, due to measurement errors, this difference must be weighted by their associated uncertainties. Having no access to the real pres-

Algorithm 1 $\min_{\alpha} \mathcal{J}(\alpha, \mathbf{X}(\alpha), \mathbf{Y}_{\text{obs}})$

Initialisation: $\alpha^m = \alpha_{\text{b}}$ and m=0
repeat
  Solve $\mathbf{M}(\mathbf{X}^m, \alpha^m) = 0$
  Compute sensitivity $\frac{\mathrm{D}\mathcal{J}}{\mathrm{D}\alpha}(\mathbf{X}^m, \alpha^m)$
  update $\alpha \rightarrow \alpha^{m+1}$; $m = m + 1$
until $\|\mathcal{J}^m - \mathcal{J}^{m-1}\| < \varepsilon$

sure values, these uncertainties have to be estimated. By assuming a normal distribution around the measured value, this can be introduced by means of an empirical covariance matrix. Concerning the projector $\mathcal{H}(.)$, in this work, we have considered interpolation by a Gaussian kernel of half size D, i.e. the building diameter, from the computational grid to the position of the measurements to ensure consistency between estimated observation and pressure measurements. So far, it should be pointed out that under the assumption of incompressible flow, the pressure solved numerically is only defined up to a constant. Thus, the experimental and numerical pressures can best be collated by comparing their respective pressure coefficient. Not that we have to subtract the isotropic part to obtain the pressure coefficient for the CFD with $C_p^w = \frac{P - P_\infty - \frac{2}{3}\rho k}{1/2 \rho U_{\text{ref}}^2}$ with P_∞ denoting the reference static pressure.

To ensure that the set of parameters α remains in a realistic set of values, we define a physically likely range for each component α_i. This can be formalised by a penalisation term on the cost functional, leading to

$$\mathcal{J}(P, \alpha) = ||\frac{1}{2}\rho U_{\text{ref}}^2 \Delta C_p^w||_{R^{-1}}^2 + ||\alpha - \alpha_b||_{B^{-1}}^2, \tag{3.2}$$

where R is the covariance matrix defined from measurement's uncertainties, B denotes the covariance matrix associated to the parameter validity range, and U_{ref} stands for the reference velocity of the simulation, i.e U_{inflow} at H_{ref}. Without loss of generality, a diagonal measurement covariance with a constant standard deviation $\sqrt{R_{ii}} = 1$ is used. This uniformity represents an equal degree of confidence for each measurement, and the diagonal structure ensues from an assumption of spatially uncorrelated errors, which can be assumed for sufficiently distant measurements. Matrix B corresponds to *a prior* knowledge on the range of values of the parameters. In practice, it is worth noting that the role of B matrix is twofold. In the one hand, it imposes a realistic interval in which the parameters can be optimised; while, on the other hand, it ensures a consistent scaling between inhomogeneous terms.

3.3 An adjoint RANS model

3.3.1 Differential equations: formal adjoint model

The optimisation problem (3.1) can be solved by augmenting the cost function with the constraint, *i.e.* the RANS model. This is done through Lagrange multipliers also called adjoint variables. The resulting unconstrained optimisation problem can be written in a compact form as

$$\mathcal{L}(\mathbf{X}, \mathbf{X}^*, \alpha) = \mathcal{J}(P, \alpha) + \langle \mathbf{X}^*, \mathbf{M}(\mathbf{X}, \alpha) \rangle_\Omega, \tag{3.3}$$

where $\langle ., . \rangle_\Omega$ stands for the spatial L^2 inner-product in the flow domain Ω. The mean flow state $\mathbf{X}$ is defined by the set $(\mathbf{U}, P, k, \epsilon, \mu_t)$. As for the adjoint state $\mathbf{X}^*$, we define it as $(\mathbf{U}^*, P^*, k^*, \epsilon^*, \mu_t^*)$. The term $\mathbf{U}^*$ stands for the adjoint velocity, P^* is the adjoint pressure field, k^* is the adjoint turbulent kinetic energy, ϵ^* the adjoint kinetic dissipation rate and μ_t^* the adjoint eddy-viscosity.

Solving the optimisation problem implies to find the set of parameters, the state vector and the adjoint state such that the derivatives of $\mathcal{L}$ with respect to all variables vanish. To this end, based on the application of the Green-Gauss theorem and the use of integrations by parts – see the Appendix7.2– the adjoint system reads as follows:

$$-\rho\frac{\partial U_j U_i^*}{\partial x_j} - \rho U_j \frac{\partial U_j^*}{\partial x_i} - \frac{\partial}{\partial x_j}\left[\mu_{eff}\left(\frac{\partial U_i^*}{\partial x_j} + \frac{\partial U_j^*}{\partial x_i}\right)\right] + \frac{\partial P^*}{\partial x_i} = D_{U^*,i} \tag{3.4}$$

$$\frac{\partial U_j^*}{\partial x_j} = 0 \tag{3.5}$$

$$-\frac{\partial \rho U_j k^*}{\partial x_j} - \frac{\partial}{\partial x_i}\left[\left(\mu + \frac{\mu_t}{\sigma_k}\right)\frac{\partial k^*}{\partial x_j}\right] - \rho\frac{2}{3}\frac{\partial U_i}{\partial x_i}k^* = D_{k^*} \tag{3.6}$$

$$-\frac{\partial \rho U_j \epsilon^*}{\partial x_j} - \frac{\partial}{\partial x_i}\left[\left(\mu + \frac{\mu_t}{\sigma_\epsilon}\right)\frac{\partial \epsilon^*}{\partial x_j}\right] - \rho\frac{\partial P_\epsilon}{\partial \epsilon}\epsilon^* + \rho\frac{\partial s_\epsilon}{\partial \epsilon}\epsilon^* = D_{\epsilon^*} \tag{3.7}$$

$$\frac{\partial P_k}{\partial \mu_t}k^* - \left(\frac{\partial U_i}{\partial x_j} + \frac{\partial U_j}{\partial x_i} -\right)\frac{\partial U_j^*}{\partial x_i} - \frac{1}{\sigma_k}\frac{\partial k}{\partial x_i}\frac{\partial k^*}{\partial x_i} - \frac{1}{\sigma_\epsilon}\frac{\partial \epsilon}{\partial x_i}\frac{\partial \epsilon^*}{\partial x_i} = \mu_t^*. \tag{3.8}$$

The right-hand sides are expressed as

$$\begin{aligned}
D_{U^*,i} &= k\frac{\partial k^*}{\partial x_i} + \epsilon\frac{\partial \epsilon^*}{\partial x_i} + \frac{2}{3}\frac{\partial k k^*}{\partial x_i} - \frac{\partial P_\epsilon}{\partial U_i}\epsilon^* - \frac{\partial P_k}{\partial U_i}k^* - \frac{\partial}{\partial x_i}\left(\frac{\partial \mu_t}{\partial U_i}\mu_t^*\right) \\
D_{k^*} &= \rho\frac{\partial P_\epsilon}{\partial k}\epsilon^* - \rho\frac{\partial s_\epsilon}{\partial k}\epsilon^* - \frac{\partial \mu_t}{\partial k}\mu_t^* \\
D_{\epsilon^*} &= -\frac{\partial \mu_t}{\partial \epsilon}\mu_t^*,
\end{aligned}$$

where P_k and P_ϵ stand for the production terms of turbulent energy (second term in the RHS of (2.5)) and for the turbulence dissipation rate (second term in the RHS of (2.6)), respectively. As for s_ϵ, it denotes the modeled sink of turbulence dissipation rate (third

term in the RHS of (2.6)). To solve this adjoint system, adjoint boundary conditions have to be derived consistently with the boundary conditions of the direct problem. The next section is dedicated to this crucial point.

3.3.2 Adjoint boundary conditions

The treatment of the adjoint boundary conditions is a central piece in adjoint methods in order to obtain consistency in the gradient computation. In our case with the transport equations of turbulent quantities, some treatments are not standard, particularly at the adjoint wall law. Moreover, some specific treatments are performed at the discrete level of the finite volume formulation. In this section, we propose to recall the general procedure to obtain adjoint boundary conditions, and then to detail the conditions to enforce at each boundary. Boundary conditions for the flow and adjoint fields are summarised in figure 3.1. Let us note that the wall boundary condition on the pressure $\nabla_n P = 0$ is an approximation that is commonly made in CFD by projecting the momentum equation on the boundary and by neglecting the viscous terms. Thus, we propose to develop the adjoint in a consistent way to this approximate model.

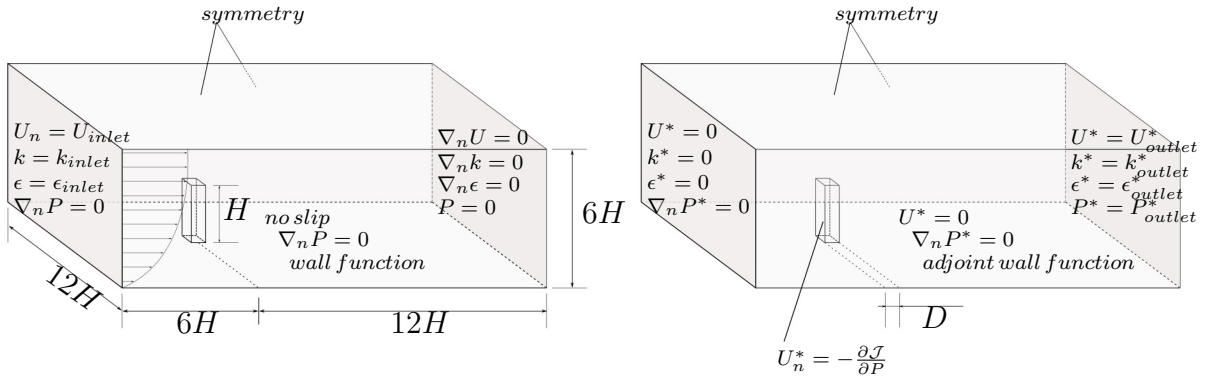

Figure 3.1 – Settings and boundary conditions of flow solution (a) and adjoint solution (b).A revoir les polices qui se chevauchent.

Derivation of (3.3) leads, in addition to system (3.4)-(3.7), to a system of boundary terms. Directional derivative with respect to P, leads to

$$[U_i^* n_i \delta P]_{\delta\Omega} = -\frac{\partial J}{\partial P}\delta P, \tag{3.9}$$

where the boundary integral is defined as $[\cdot]_{\partial\Omega} = \int_{\partial\Omega}(\cdot)\,\mathrm{d}\partial\Omega$. By deriving with respect to

U_i, we obtain

$$\begin{aligned}
&[P^*\delta U_i n_i]_{\delta\Omega} - \left[\rho\left((U_i^* n_i)(U_i n_i) + U_j U_j^* n_i\right)\delta U_i n_i\right]_{\delta\Omega} - \left[\mu_{eff}(U_i^* n_i + U_j^* n_j)\frac{\partial \delta U_i}{\partial x_j}\right]_{\delta\Omega} \\
&- \left[\delta U_i \mu_{eff}\left(\frac{\partial U_i^* n_i}{\partial x_j} n_i + \frac{\partial U_j^* n_j}{\partial x_i} n_i\right)\right]_{\delta\Omega} \\
&- \left[\delta U_i\left(\frac{5}{3}\rho k k^* n_i + \left(\frac{\partial P_k}{\partial U_j} n_i\right)k^* + \rho\epsilon\epsilon^* n_i + \left(\frac{\partial P_\epsilon}{\partial U_j} n_i\right)\epsilon^* + \left(\frac{\partial \mu_t}{\partial U_j} n_i\right)\mu_t^*\right)\right]_{\delta\Omega}.
\end{aligned} \tag{3.10}$$

Derivative with respect to k, leads to

$$\left[-\frac{2}{3}\rho U_i^* n_i \delta k\right]_{\delta\Omega} + [\rho U_i n_i k^* \delta k]_{\delta\Omega} - \left[\left(\mu + \frac{\mu_t}{\sigma_k}\right)k^*\frac{\partial \delta k}{\partial x_j} n_j\right]_{\delta\Omega} + \left[\frac{\partial\left(\mu + \frac{\mu_t}{\sigma_k}\right)k^*}{\partial x_j} n_j \delta k\right]_{\delta\Omega}, \tag{3.11}$$

and with respect to ϵ to

$$[\rho U_i n_i \epsilon^* \delta\epsilon]_{\delta\Omega} - \left[\left(\mu + \frac{\mu_t}{\sigma_k}\right)\epsilon^*\frac{\partial \delta\epsilon}{\partial x_j} n_j\right]_{\delta\Omega} + \left[\frac{\partial\left(\mu + \frac{\mu_t}{\sigma_k}\right)\epsilon^*}{\partial x_j} n_j \delta\epsilon\right]_{\delta\Omega}. \tag{3.12}$$

Finally by deriving with respect to μ_t, we obtain

$$\left[\delta\mu_t\left(\mu_t^* - \left(\frac{\partial U_j}{\partial x_i} n_j + \frac{\partial U_i}{\partial x_j} n_j\right)U_i^* - \frac{\rho}{\sigma_k} k^* \frac{\partial k}{\partial x_j} n_j - \frac{\rho}{\sigma_\epsilon}\epsilon^*\frac{\partial \epsilon}{\partial x_j} n_j\right)\right]_{\delta\Omega}. \tag{3.13}$$

Then at each boarder, variations of the direct boundary conditions are injected in the system (3.9)–(3.13), to obtain the corresponding adjoint boundary conditions.

Inlet: At the inlet, the direct boundary conditions lead to

$$\delta U_i t_i = 0 \quad ; \quad \delta U_i n_i = 0 \quad ; \quad \delta k = 0 \quad ; \quad \delta\epsilon = 0. \tag{3.14}$$

Substituting this in (3.9)–(3.12), the system reduces to

$$U_i^* t_i = 0 \quad ; \quad U_i^* n_i = 0 \quad ; \quad k^* = 0 \quad ; \quad \epsilon^* = 0. \tag{3.15}$$

This quite standard result at the continuous level is not straightforward to implement in the finite volume formulation. No condition is imposed on P^* and the inlet boundary condition for the adjoint pressure is left arbitrary. But, in accordance with (Zymaris et al., 2010; Othmer, 2008) and identically as the numerical treatment of the direct inlet pressure P, zero Neumann condition on P^* is imposed to ensure numerical stability. To obtain the other boundary conditions, the same approach is employed.

Outlet: At the outlet, the pressure value is prescribed while the other flow variables have their normal gradient imposed, leading to

$$P^* n_i = (U_i^* n_i)(U_i n_i) + (U_j^* U_j) n_i + \mu_{eff} \frac{\partial (U_j^* n_j)}{\partial x_i} n_i + \frac{5}{3} \rho k k^* n_i + \rho \epsilon \epsilon^* n_i + \left(\frac{\partial \mu_t}{\partial U_j} n_j \right) n_i \mu_t^*. \tag{3.16}$$

This provides a constraint on the boundary condition to determine the adjoint pressure at the outlet. In equation (3.16), the adjoint pressure at the next iteration is determined explicitly by evaluating U^* at the previous iteration. Projecting then the fluxes on the outlet tangent plane, we obtain:

$$\mu_{eff} \frac{\partial (U_j^* t_j)}{\partial x_i} n_i + (U_i^* t_i)(U_i n_i) = - \left(\frac{\partial \mu_t}{\partial U_i} n_i \right) t_i \mu_t^* - \left(\frac{\partial P_k}{\partial U_j} n_j \right) t_i k^* - \left(\frac{\partial P_\epsilon}{\partial U_j} n_j \right) t_i \epsilon^*. \tag{3.17}$$

This equation provides a boundary condition for the tangential component of the adjoint velocity.

It is worth noting that, instead, an alternative choice could be made by imposing $P^* = 0$ and determining the adjoint velocity by solving equations (3.16) and (3.17). Previous works, for a different turbulence model (Zymaris et al., 2010) or for frozen turbulence assumption (Othmer, 2008), showed that both implementations yields to identical sensitivities.

Derivation w.r.t. k, ϵ and μ_t leads, respectively, to

$$\rho k^* U_i n_i + \rho D_k \frac{\partial k^*}{\partial x_i} n_i = \frac{\partial \mu_t}{\partial k} \mu_t^*, \tag{3.18}$$

$$\rho \epsilon^* U_i n_i + \rho D_\epsilon \frac{\partial \epsilon^*}{\partial x_i} n_i = \frac{\partial \mu_t}{\partial \epsilon} \mu_t^*, \tag{3.19}$$

$$\left(\frac{\partial U_j}{\partial x_i} n_j + \frac{\partial U_i}{\partial x_j} n_j \right) U_i^* = \mu_t^*. \tag{3.20}$$

Therefore, for known outlet direct and adjoint velocities, the adjoint eddy viscosity is updated through equation (3.20). Then, conditions (3.18) and (3.19) can be imposed to solve k^* and ϵ^* respectively.

Side and top: As for the side and top, free-stream boundaries under symmetry condition are applied. We assume a zero flux of all flow variables,

$$\frac{\partial P}{\partial x_i} n_i = \frac{\partial (U_j t_j)}{\partial x_i} n_i = \frac{\partial k}{\partial x_i} n_i = \frac{\partial \epsilon}{\partial x_i} n_i = 0, \tag{3.21}$$

and zero normal velocity,

$$U_i n_i = 0. \tag{3.22}$$

We thus obtain the following boundary conditions for the adjoint variables:

$$U_i^* n_i = 0, \quad \frac{\partial (U_i^* t_i)}{\partial x_j} n_j = 0, \quad \frac{\partial k^*}{\partial x_i} n_i = 0, \quad \frac{\partial \epsilon^*}{\partial x_i} n_i = 0, \quad \mu_t^* = 0. \tag{3.23}$$

This shows that symmetric boundary conditions are conserved with the adjoint model.

Walls: The wall boundaries are split into two parts, namely $\partial\Omega_{\text{tower}}$ for the part where data are provided, *i.e.* the tower, and $\partial\Omega_{\text{gr}}$ for the walls at the ground modelling the surrounding environment, for which there is no data but roughness. Based on equation (3.9) we have

$$U_i^* n_i = \frac{\partial \mathcal{J}}{\partial P} \qquad \text{at} \qquad \partial\Omega_{\text{tower}}, \tag{3.24}$$

$$U_i^* n_i = 0 \qquad \text{at} \qquad \partial\Omega_{\text{gr}}, \tag{3.25}$$

$$U_i^* t_i = 0 \qquad \text{at} \qquad \partial\Omega_{\text{tower}} \cup \partial\Omega_{\text{gr}}. \tag{3.26}$$

Therefore exactly in the same way as for the inlet, the no-slip condition on the velocity, associated with a zero Neumann condition on the mean pressure, implies a homogeneous Dirichlet boundary condition for the adjoint velocity and a zero Neumann condition for the adjoint pressure at the ground walls $\partial\Omega_{\text{gr}}$. Let us note that due to the wall-pressure measurements, the Dirichlet condition on the adjoint variable U^* is inhomogeneous on the normal component along $\partial\Omega_{\text{tower}}$ at the sensor positions.

Considering the adjoint turbulence variables (k^*, ϵ^*, μ_t^*), it is important to consider the expression of the wall-law in order to derive their boundary conditions. From the equality (2.11), the log law is imposed by re-evaluating the wall viscous fluxes through a prescribed value of the eddy-viscosity. From the relations

$$U^+ = \frac{1}{\kappa} \ln(E y^+) \qquad \text{at} \qquad \partial\Omega_{\text{tower}},$$

and

$$U^+ = \frac{1}{\kappa} \ln(\frac{y + z_0}{z_0}) \qquad \text{at} \qquad \partial\Omega_{\text{gr}},$$

the eddy viscosity is then defined such that

$$\mu_t = \mu \left(\frac{y^+ \kappa}{\ln(E y^+)} - 1 \right) \qquad \text{at} \qquad \partial\Omega_{\text{tower}}, \tag{3.27}$$

$$\mu_t = \mu \left(\frac{y^+ \kappa}{\ln(\frac{y+z_0}{z_0})} - 1 \right) \qquad \text{at} \qquad \partial\Omega_{\text{gr}}, \tag{3.28}$$

where $E = 9.8$ is the roughness parameter for smooth walls (Versteeg and Malalasekera, 2007) and $z_0 = 0.02\,\text{m}$ is the roughness length which is relevant for an ABL flow scale. Recalling from figure 2.3 that $|_c$ and $|_f$ denote respectively the first cell centre and the

boundary face values, on both walls $\mu_t|_f$ is seen to be dependent on $k|_c$ solely. Furthermore, by imposing the inertial balance (2.9) we observe that $\epsilon|_c$ is an explicit function of $k|_c$. As a consequence, we conclude that the logarithmic wall-closure can actually be defined uniquely through the knowledge of the turbulent kinetic energy value at the first cell-center only. We propose thus to reconsider the derivation of these terms inside the domain included in the cells adjacent to the wall. Replacing $\epsilon|_c$ by its function of $k|_c$ (equation (2.9)), we are led to consider a zero Neumann boundary condition, which is fully consistent with the homogeneity assumption near the wall. This yields to the following modification to the source terms at the wall adjacent cell

$$D_{k^*} = \rho\frac{\partial P_\epsilon}{\partial k}\epsilon^* - \rho\frac{\partial s_\epsilon}{\partial k}\epsilon^* + \rho\left(\frac{\partial P_k}{\partial k}|_c - \frac{\partial \epsilon}{\partial k}|_c\right)k^*|_c \qquad \text{and} \qquad D_{\epsilon^*} = 0 \qquad \text{in} \qquad \Omega_c, \tag{3.29}$$

with P_ϵ and s_ϵ, the dissipation production and sink terms, being modified accordingly. At the continuous level, the third term in the RHS vanishes assuming turbulence homogeneity. However, at the discrete level, as discussed in section 2.3.1, it is kept for numerical consistency.

Furthermore, as we impose a homogeneous Neumann boundary condition for k in equation (2.8), it can be observed that this leads to the same set of conditions as in the outlet (equations (3.18), (3.19) and (3.20)). Moreover, with the no slip condition and the set of conditions for the adjoint velocity ((3.24), (3.25), (3.26)), the wall boundary conditions for the adjoint dissipation rate and eddy viscosity reads as

$$\frac{\partial \epsilon^*}{\partial x_i}n_i = 0 \qquad \text{at} \qquad \partial\Omega_{\text{tower}} \cup \partial\Omega_{\text{gr}}, \tag{3.30}$$

$$\mu_t^* = \left(\frac{\partial (U_i n_i)}{\partial x_j}n_j + \frac{\partial (U_j n_j)}{\partial x_i}n_i\right)U_i^* n_i \qquad \text{at} \qquad \partial\Omega_{\text{tower}}, \tag{3.31}$$

$$\mu_t^* = 0 \qquad \text{at} \qquad \partial\Omega_{\text{gr}}. \tag{3.32}$$

Concerning the boundary condition on k^*, we propose to consider (3.18) at $|_c$ while we impose zero Neumann condition at $|_f$. This leads to the following boundary condition for k^*:

$$\frac{\partial k^*}{\partial x_j}n_j|_f = 0 \qquad \text{at} \qquad \partial\Omega_w \tag{3.33}$$

and

$$k^*|_c = \frac{\partial \mu_t}{\partial k}|_f \frac{\mu_t^*|_f}{\rho U_i n_i} \qquad \text{in} \qquad \Omega_c. \tag{3.34}$$

for which $\partial\mu_t/\partial k|_f$ embeds the sensitivity of the direct wall law. It is determined by differentiating equations 3.27 and 3.28 with respect to k at the first cell center.

Some numerical tests have shown that this alternative solution led to identical results on the initial sensitivity field than the non-homogeneous Neumann boundary condition. Hence, with this treatment, wall conditions for the adjoint system are now fully consistent

with the initial RANS model and should leads us to a consistent minimisation procedure.

3.4 Conclusion

This chapter was dedicated to build a data assimilation methodology that can be applied to any turbulence closure arbitrarily complex. Based on optimal control theory, a differentiation, consistent with the realizable $k-\epsilon$ transport equations and the near-wall law has been performed. Note that the construction of the adjoint flow equations shed light on the role of the adjoint boundary conditions. This has resulted in the definition of a continuous adjoint model, together with its consistent boundary conditions, of the tangent linear operator of the RANS model. The adjoint boundary conditions at the wall induced by the closure wall function has been derived. Moreover, specific treatments related to the finite volume discretisation have been given. Given the adjoint dynamics, the sensitivity of any parameter can be obtained from the optimality condition (7.5) without additional costs.

Beyond providing an efficient data-driven reconstruction technique, in the thesis framework, the proposed adjoint methodology will be also investigated as an in-depth analysis tool of the turbulence closure. In chapter 4, some methodological settings are explored to that end.

Chapter 4

DATA-ASSIMILATION AS A DIAGNOSIS TOOL FOR TURBULENCE CLOSURE STRUCTURE

4.1 Introduction

In this chapter, we explore a methodological setting, based of the variational data assimilation procedure derived in the previous chapter, for diagnosis of the turbulence closure. After a first inspection of the adjoint state maps in their ability in providing complete informations on the sensitivity fields, we will then use this methodology to investigate the sensitivity fields of the global closure coefficients of the realizable $k-\epsilon$ model (Shih et al., 1995) introduced in chapter 2. Their physical interpretation will then enable us to point out limits on the applicability of such closure models for data-model coupling purposes, and more particularly for wind flows around buildings. For a further investigation, we consider optimising global constants parameters of the turbulence model for reducing the observation error; and to relax/enforce constraints on these parameters to test physical hypotheses. This framework will discuss limitations and improvements in estimating wind loads and mean velocities surrounding the high-rise building after applying the proposed data-model coupling technique.

4.2 Adjoint state as a basis for sensitivity analysis

While in general, adjoint variables are usually considered as a purely mathematical object, they do have physical meaning which have been explored in several works (Hall and Cacuci, 1983; Giles and Pierce, 2000; Gunzburger, 2003). Although we know that RANS models with Boussinesq eddy viscosity hypothesis does not always allow an accurate representation of complex flows, they nevertheless provide some usefull global insights on the flow. With this in mind, the reconstructed adjoint state enables to highlight a misrepresentation of the turbulent flow by the RANS model, hence, pointing where it is possible to optimise the RANS model parameters to optimally reduce the difference between the CFD state and a given experimental dataset. Moreover, from an optimisation perspective, one may interpret them as a steepest descent direction of an objective cost function, for a particular control parameter. For instance, the adjoint velocity can be seen as the influence of an arbitrary forcing $\mathbf{f}_u$ acting on the mean momentum equation. This

can be shown when deriving an optimality condition by a perturbation of this force,

$$\begin{aligned} \mathbf{M_u}(\mathbf{X},\alpha) = \mathbf{f}_u \qquad &\rightarrow \qquad \frac{\partial \mathcal{J}}{\partial \mathbf{f}_u} = \mathbf{U}^*. \\ \text{Momentum equation} \qquad &\rightarrow \qquad \text{Optimality condition.} \end{aligned}$$

Then, as we perform a first update of this forcing by a gradient-descent minimisation algorithm, one obtain

$$\mathbf{f}_u^{it_1} = \underbrace{\mathbf{f}_u^{it_0}}_{=0} - \lambda U^*,$$

while λ is a positive non-dimensional marching step factor. Through dimensional analysis, one may scale $\mathbf{U}^*$, which has the dimension of an acceleration, as $U^* \sim \frac{U_{\text{ref}}^2}{H_{\text{ref}}}$. The adjoint velocity features are thus immediately representing a missing term, that can be interpreted as a correction of the Reynolds stress divergence. Examining the adjoint turbulence variables of a $k-\epsilon$ model, namely k^*, ϵ^* and μ_t^*, similar interpretations can be drawn as we consider arbitrary forcing such as

$$\begin{aligned} M_k(\mathbf{X},\alpha) = f_k \qquad &\rightarrow \qquad \frac{\partial \mathcal{J}}{\partial f_k} = k^*, \\ M_\epsilon(\mathbf{X},\alpha) = f_\epsilon \qquad &\rightarrow \qquad \frac{\partial \mathcal{J}}{\partial f_\epsilon} = \epsilon^*, \\ M_{\mu_t}(\mathbf{X},\alpha) = f_{\mu_t} \qquad &\rightarrow \qquad \frac{\partial \mathcal{J}}{\partial f_{\mu_t}} = \mu_t^*. \end{aligned}$$

The adjoint variables shed some light on the flow regions that are sensitive to an eventual correction of the turbulence model. As this will be shown in the case study of section 4.4, this interpretation is very helpfull to analyze the incorporation of additional variables to define efficient data-driven turbulence closure. These forcings can indeed be associated to any of the modeled terms meant to adress a particular turbulence modelling error (e.g. energy production, backscaterring, redistribution or dissipation). The sensitivity of the associated parametric shapes and hyper-parameter can be efficiently obtained and inspected through the adjoint operator.

4.3 Adjoint diagnosis on global closure coefficients

Given the adjoint dynamics, the sensitivity of any parameter can be obtained from the optimality condition (7.5). Free constants of the RANS model can be finely tuned knowing their sensitivities. We choose here these parameters to be constant over the domain of the flow over the building. In this problem, the number of degrees of freedom which we authorise ourselves to calibrate is quite small, and the solution will still be constrained to follow a realizable $k-\epsilon$ model. We qualify this constraint as "model rigidity". The risk

of this rigidity is to not be able to perform high reconstruction performances, however, the goal in this chapter is to use the adjoint method for evaluating *i)* to what extend a caibrated $k-\epsilon$ model is able to reconstruct the flow, *ii)* what are the sensitive model parameters, *iii)* which physical hypotheses linking these constants are relevant to adopt. In the next chapters, this rigidity will be relaxed.

4.3.1 A sensitivity field

Considering the vector $\alpha = (A_0, C_2, \sigma_k, \sigma_\epsilon)$ of closure parameters, the optimality condition (7.5) is obtained by differentiating the Lagrangian (3.3) in the directions $\delta\alpha = (\delta A_0, \delta C_2, \delta\sigma_k, \delta\sigma_\epsilon)$:

$$\begin{aligned}
\frac{\partial \mathcal{L}}{\partial A_0}\delta A_0 = \left\langle \frac{\partial M_{\mu_t}}{\partial A_0}\delta A_0, \mu_t^* \right\rangle_\Omega = \langle -\frac{\partial C_\mu}{\partial A_0}\rho\frac{k^2}{\epsilon}\delta A_0, \mu_t^* \rangle_\Omega = \langle -\mu_t C_\mu, \mu_t^*, \rangle_\Omega \, \delta A_0 \\
\frac{\partial \mathcal{L}}{\partial C_2}\delta C_2 = \left\langle \frac{\epsilon^2}{k+\sqrt{\mu\epsilon}}, \epsilon^* \right\rangle_\Omega \delta C_2 \\
\frac{\partial \mathcal{L}}{\partial \sigma_k}\delta\sigma_k = \left\langle -\frac{\partial}{\partial x_j}\left[\frac{\mu_t}{\sigma_k^2}\frac{\partial k}{\partial x_i}\right], k^* \right\rangle_\Omega \delta\sigma_k \\
\frac{\partial \mathcal{L}}{\partial \sigma_\epsilon}\delta\sigma_\epsilon = \left\langle -\frac{\partial}{\partial x_j}\left[\frac{\mu_t}{\sigma_\epsilon^2}\frac{\partial \epsilon}{\partial x_i}\right], \epsilon^* \right\rangle_\Omega \delta\sigma_\epsilon.
\end{aligned} \tag{4.1}$$

So far, this does not include any explicit dependency of the cost on the set of parameters, such as a penalisation term. It can be observed that the optimality conditions reduce drastically the high dimensional dependency of the model to the lower dimensional parameter space. This reduction, performed via the inner product $\langle ., . \rangle_\Omega$, does reflect the global compromising character of the closure coefficients. This results in a rather rigid situation when seeking data-model fitting. However, this rigidity can be understood as a strong confidence in the model structure. This strongly constrains the solutions but enables, on the other hand, to assimilate very sparse measurements. The examination of the spatially varying adjoint variables to diagnose the parameter sensitivity provides useful piece of information even though we deal with a rigid parametric model for the reconstruction. This type of analysis will be exploited in our case study.

4.3.2 Penalty range

To ensure realistic numerical solutions, relevant physical range for each of the closure coefficients is defined. These constraints are introduced via penalty terms on the control parameters through an error covariance matrix, in cost function (3.2). Values of the parameters outside of a range defined by the standard deviation are hence strongly penalised. These standard deviations are in practice fixed from experiments on prototypical configurations of boundary layer or decaying turbulence. This may become questionable in regions where the fluid and building interact and near flow separations associated with

strong shears. As a matter of fact, the assumptions underlying the concept of eddy viscosity starts to be less reasonable in these regions (Pope, 2000). Thus, as a compromise, the range limits are fixed from experiments as intervals $\Delta\alpha_i$ centered around the background a priori value. The covariance matrix is finally expressed as follows

$$B_{ii}^{-1} = \zeta_i \left(\frac{|\frac{\partial \mathcal{J}_0}{\partial \alpha}|}{\Delta \alpha_i} \right).$$

As mentioned earlier, this covariance has two roles: first, to impose the trusted (or recommended) ranges $\Delta\alpha_i$ and secondly, to ensure a dimensional homogeneity of the cost function through the norm of the sensitivity derivative given at the first minimisation iteration $|\frac{\partial \mathcal{J}_0}{\partial \alpha}|$. The importance of control variables with high values of sensitivity derivatives is strengthen in the objective function in comparison to less sensitive parameters. The parameters ζ_i are dimensionless free parameters allowing to give more or less global *a priori* confidence on each parameter. In practice these parameters can be fixed from a priori considerations.

4.4 Results

In this section, we validate the proposed data assimilation scheme for global turbulence model parameters. An adjoint state analysis is conducted to obtain the sensitivities to model control closure parameters. We assess the limits of global closure optimization performances and exhibit the ability of the proposed method to enable turbulence closure analysis.

4.4.1 Adjoint state analysis

The normalised adjoint fields (by their maximum in-plane values), shown in figures 4.1, 4.2 and 4.3, highlight the areas of interest in terms of turbulence modelling on two horizontal plans (at normalised height $z/H_{ref} = \{0.19, 1\}$) and on the symmetry plane (at $y/D = 0$). These areas correspond to regions, whose state is observable by the sensors, and where the turbulence closure model fails to reproduce the physical behaviour of the flow; this corresponds to the recirculation regions behind and at the top of the building (as seen in the centered streamwise vertical plans on figure 4.3), the area of the vortex shedding due to flow separation (seen in the horizontal plans on figure 4.1 and 4.2) and the flow impingement region of the building. Based on these adjoint fields, the cost functional's sensitivity to any control parameter (be distributed or not) can be obtained through its associated optimality condition.

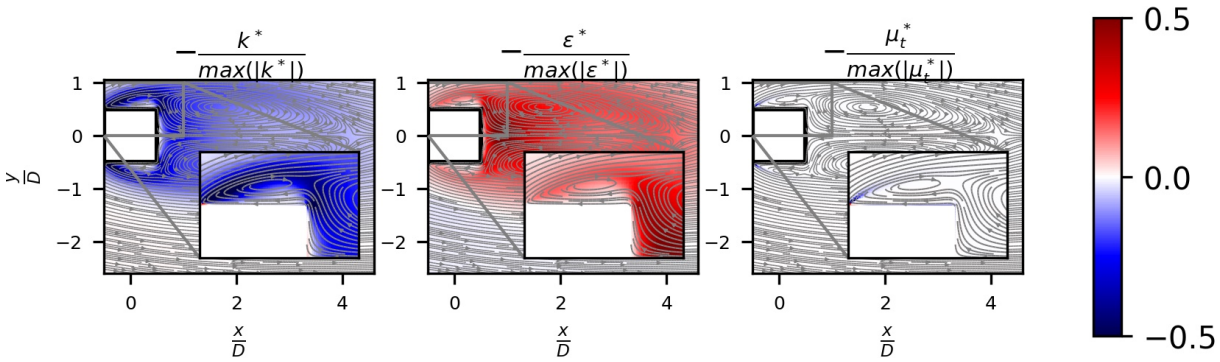

Figure 4.1 – Adjoint turbulence variables at horizontal plane with normalised height $z/H_{ref} = 0.19$:(a), ϵ^*; (b), k^*; (c), μ_t^*. Variables are normalised by their in-plane peak values.

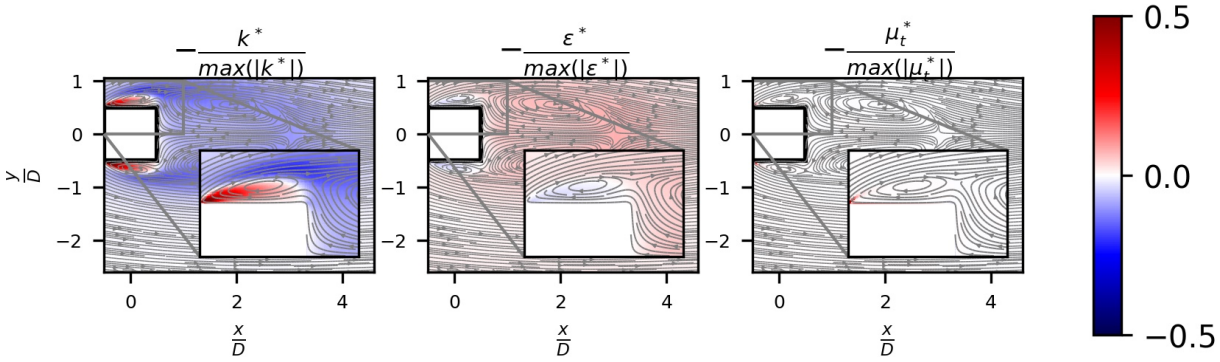

Figure 4.2 – Adjoint turbulence variables at horizontal plane with normalised height $z/H_{ref} = 1$:(a), ϵ^*; (b), k^*; (c), μ_t^*. Variables are normalised by their in-plane peak values.

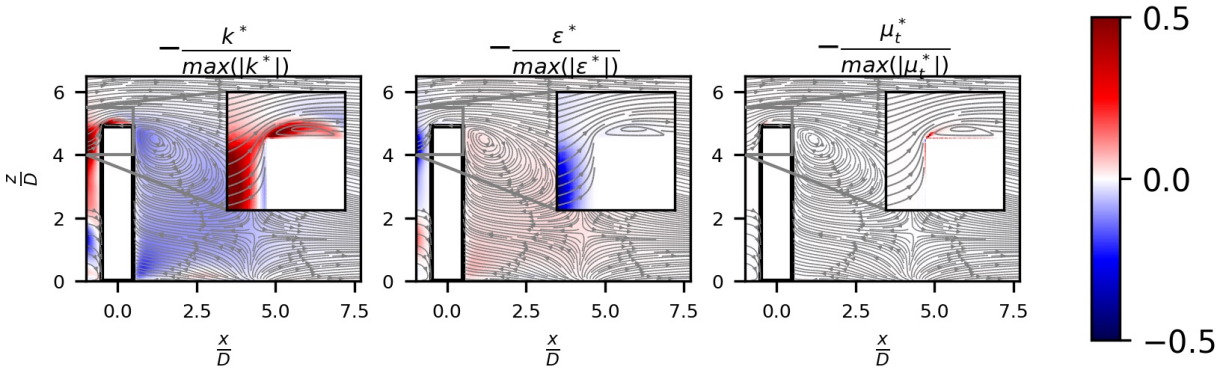

Figure 4.3 – Adjoint turbulence variables at symmetry plane :(a), ϵ^*; (b), k^*; (c), μ_t^*. Variables are normalised by their in-plane peak values.

	$\frac{\partial \mathcal{J}}{\partial A_0}(\times 10^7)$	$\frac{\partial \mathcal{J}}{\partial \sigma_k}(\times 10^7)$	$\frac{\partial \mathcal{J}}{\partial \sigma_\epsilon}(\times 10^7)$	$\frac{\partial \mathcal{J}}{\partial C_2}(\times 10^7)$
AD	1.371	-2.756	0.712	-8.583
FD ($\delta\alpha_i = 10^{-1}$)	2.39	-3.11	0.683	-6.699
FD ($\delta\alpha_i = 10^{-2}$)	2.07	-3.76	0.77	-11.4
FD ($\delta\alpha_i = 10^{-3}$)	2.05	-3.04	–	-11.9

Table 4.1 – Sensitivity derivative values computed from the proposed adjoint model (AD) and the finite difference (FD).

4.4.2 Results for the global coefficients

This section exhibits the adjoint approach's capability to provide a complete information on the cost sensitivity to the model's global coefficients. First, we analyse the sensitivity fields to highlight the spatial locations where a modification of these global coefficients could efficiently correct the model errors. Then, we discuss the results of a data assimilation procedure. The data assimilation is performed to investigate some closure hypotheses validity in the RANS modelling.

Sensitivity analysis

First, a validation test has to be performed to check the validity of the sensitivity fields. In order to highlight the relevant informations, a specific innerproduct is employed in the variational formulation by considering an integration over a volume of interest, where the sensitivities are the most important. This volume of interest, Ω_{in}, is centred around the building and has a size of $2.5H \times 4H \times 1.5H$. It is introduced in equation (3.3), and used to compute the optimality condition through the following weighted sum

$$\left.\frac{\partial \mathcal{J}}{\partial \alpha_i}\right|_{AD} = \left\langle \frac{\partial \mathcal{M}}{\partial \alpha_i}, \mathbf{X}^* \right\rangle_{\Omega_{in}} \equiv \sum_{j}^{\text{nCells}} \left(\frac{\partial \mathcal{M}}{\partial \alpha_i} . \mathbf{X}^* \right) \omega_j,$$

where ω_j denotes the volume of the j^{th} cell. The validation metric is chosen to be the error between this weighted sum and the finite difference gradient computed by the cost function variations resulting from a small variation of the global coefficients in the volume of interest,

$$\left.\frac{\partial \mathcal{J}}{\partial \alpha_i}\right|_{FD} = \frac{(\mathcal{J}(\alpha_i + \delta\alpha_i) - \mathcal{J}(\alpha_i))}{\delta\alpha_i}.$$

The sensitivity (gradient) of $\mathcal{J}$ with respect to the four closure coefficients computed using the proposed adjoint approach and the finite differences are given in table 4.1. The comparison shows that the adjoint-based sensitivities are very close to the finite difference values. A fair agreement is obtained for the sensitivity associated with the coefficients involved in the redistribution of k and ϵ. However, deviations appear to be notably more important for the eddy viscosity pre-factor A_0. These deviations are typical of the error

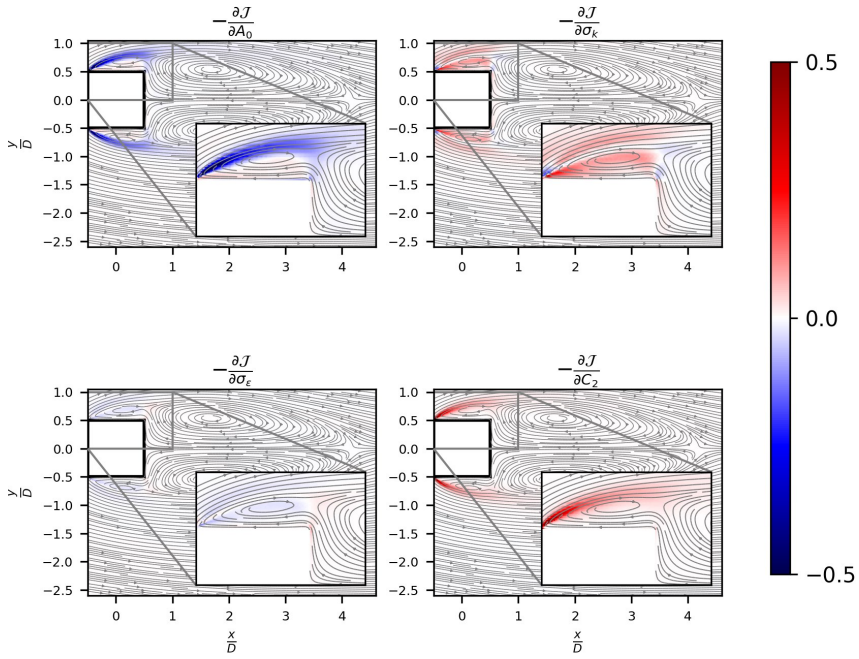

Figure 4.4 – Closure coefficient sensitivities at horizontal plane with normalised height $z/H_{ref} = 0.19$: (a), sensitivity to A_0, (b), σ_k, σ_ϵ (c), and, (d), C_2 (d). Sensitivities are normalised by their in-plane peak values.

levels associated to continuous adjoint methods. (Othmer, 2008; Zymaris et al., 2010). This validates hence the procedure.

In order to explore the effect of the turbulence model's global coefficients, their associated sensitivity maps (plotted in figure 4.4, 4.5, and 4.6, and defined by the spatially distributed operand inside the integral in the optimality condition (4.1)) are discussed.

We can see there is high interest in optimising these coefficients at the shear layers resulting from flow separations at the leading lateral edges and on top of the building. However, there is very little sensitivity in the bulk of the recirculation wake region. Moreover, with regards to the regularity of the sensitivity fields, $\frac{\partial \mathcal{J}}{\partial \sigma_k}$ and $\frac{\partial \mathcal{J}}{\partial \sigma_\epsilon}$ (Figures 4.4 and 4.5 (a) and (b)) have the largest local variations compared to the others. In fact, this is explained by the high (second) order derivative associated with the diffusion of k and ϵ, in the optimality conditions. Now, regarding the local signs and overall values of each sensitivity field, we observe systematic change of sign over the domain. The L^2 inner product in (4.1) leads to an averaged compromise solution over the whole domain for the global coefficient values. This compromise is likely to provide a far too weak amplitude for these coefficients in key regions of the flow.

As shown in table 4.1, C_2 is the most sensitive coefficient. Its large value suggests that the coefficient is less subject to sign cancellations in the sensitivity maps. This is especially observed in the horizontal map at lower elevations far enough from the high-end (plot at $z/H_{ref} = 0.19$ where $H_{ref} = 2/3H = 3.3D$). This suggests that adjusting its value is a

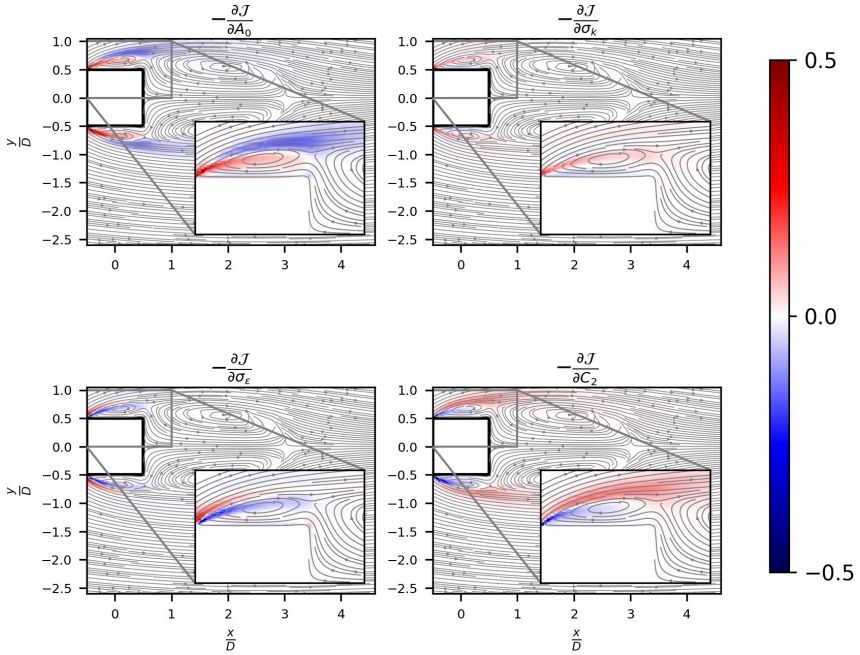

Figure 4.5 – Closure coefficient sensitivities at horizontal plane with normalised height $z/H_{ref} = 1$: (a), sensitivity to A_0, (b), σ_k, σ_ϵ (c), and, (d), C_2 (d). Sensitivities are normalised by their in-plane peak values.

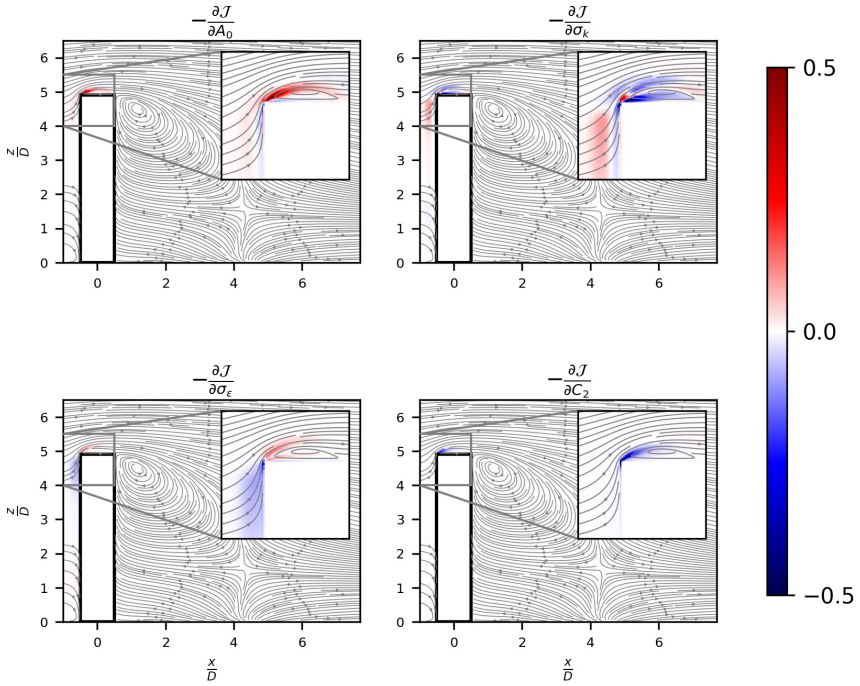

Figure 4.6 – Closure coefficient sensitivities on the symmetry plane with normalised: (a), sensitivity to A_0, (b), σ_k, σ_ϵ (c), and, (d), C_2 (d). Sensitivities are normalised by their in-plane peak values.

good compromise in between the wake flow features. Its global tendency, hence, seems to give the closest represenstaion to the the spatially distributed trends. With regards the other coefficients, their global sensitivity derivatives suggest, a decrease of both the eddy-viscosity pre-factor A_0, the turbulent energy diffusivity pre-factor $1/\sigma_k$ and an increase of the diffusivity pre-factor $1/\sigma_\epsilon$ of the energy dissipation. This implies, in the one hand, that the turbulence dissipation rate is under-predicted all over the domain and that a better redistribution of the flow field can be obtained by increasing C_2. Inversely, by decreasing the eddy viscosity pre-factor A_0 (which increases C_μ), this trend shows that the original turbulence model tends globally to under-estimates the momentum mixing and thus it globally advocates higher turbulent diffusion. By looking at local sensitivities to this coefficients, these global directions are strongly driven by the high interest giving to the lateral free-stream (surrounding lateral recirculating flow) entrained toward the wake region. Thus, upon calibration, we may expect some preferential improvement of the wake extension and, inversely, a retrogression in the extension of lateral separated flow.

Closure hypothesis analysis through data assimilation

In this section, the optimisation problem is solved iteratively by following Algorithm 1, and we discuss ability of the data assimilation procedure to estimate the flow state. Guided by the work of Shih et al. (1995), we intend here to devise some penalty ranges for the coefficients. Concerning the coefficients which are involved in the energy dissipation rate budget, referring to the work (Shih et al., 1995), the C_2 coefficient is actually expressed as $C_2 = \beta/\eta$, in which $\beta = \eta+1$ is the dissipation decay rate (such as $\epsilon/\epsilon_{t_0} = (t/t_0)^{-\beta}$ where t_0 is an initial time) and η is the energy decay exponent (such as $k/k_{t_0} = (t/t_0)^{-\eta}$) that varies from 1.08 to 1.3 in decaying homogeneous turbulence experiments (Shih et al., 1995). Thus, a range for this coefficient can be set as $C_2 \in [1.76, 1.93]$, where the background value is 1.9.
For σ_ϵ, the inertial turbulence assumption near the wall allows to establish

$$\sigma_\epsilon = \frac{\kappa^2}{C_2\sqrt{C_\mu} - C_1} \tag{4.2}$$

were the von Kármán constant $\kappa = 0,41$, the eddy viscosity coefficient $C_\mu = 0.09$ and $C_1 = 0.43$. Assuming a quasi-linear dependency between the two constants (see figure 4.8), knowing the range on C_2, we obtain $\sigma_\epsilon \in [1.14, 1.71]$. To possibly relax the underlying assumption of decaying turbulence for this range, two cases study will be considered for this constant. In the first scenario, it will be assumed that relation (4.2) holds beyond the inertial layer, as established by Shih et al. (1995). On the second scenario, this constraint is relaxed and coefficient σ_ϵ is assumed to be an independent control parameter. In that case, the closure is thus performed by the data. The second case is expected to bring more degree of freedom in the optimisation process, due to the independent adaptation of the two coefficients.

Scenario	σ_k	σ_ϵ	C_2	A_0	$\frac{\mathcal{J}-\mathcal{J}_0}{\mathcal{J}_0}$
Default value	1.0	1.2	1.9	4.0	
A	1.14	0.99	1.92	4.05	10.7%
B	1.0	0.74	1.96	4.08	15.7%
C	1.03	1.07	1.95	3.99	9.8%

Table 4.2 – Summary of the optimisation results, closure coefficients and the relative decrease of cost function.

In the transport equation of k, the coefficient σ_k, which adjusts the level of turbulent energy mixing with respect to the momentum eddy diffusivity, is commonly fixed to unity (as in any $k-\epsilon$ turbulent model). This generally assumes a quasi-equality between the scalar and the momentum mixing. Due to the lack of comparative studies in the literature between the *realizable* model results and experiments, estimating a physical range for this coefficient is not possible. Therefore, we considered two optimisation procedures where in the first one we maintain $\sigma_k = 1$ while in the other case we relax this constraint letting σ_k evolves in the reasonably chosen range: $\sigma_k \in [0.9, 1.1]$. Similarly, for the bounds on A_0, without any *a priori* informations on its physical range, we fixed a larger range of possible value: $A_0 \in [3.6, 4.4]$, where the background usual value is 4.0.

Based on the remarks of the previous section, the results of three data-assimilation scenarios are discussed and compared. A first straightforward approach corresponds to the optimisation of the four coefficients independently. This is referred to as scenario **A**. Then, two scenarios are considered to investigate the two closure assumptions mentioned in the previous section. First, we consider the equality between the mixing of turbulent kinetic energy and momentum, referred as scenario **B**. Secondly, keeping σ_k a free parameter, the scenario **C** consists in enforcing the inertial constraint and defining σ_ϵ using (4.2). Three criteria are considered to evaluate the agreement between the CFD results and the measurements. The first is the relative reduction of cost function $\frac{\mathcal{J}-\mathcal{J}_0}{\mathcal{J}_0}$, $\mathcal{J}_0$ being the initial cost. This depicts the improvement of the global effect of wind on the building. Next, C_p, the dimensionless pressure, is compared locally on the facades of the building. Third, to quantify the accuracy of the recovered mean flow field, the streamwise length of the recirculation region behind the building is compared to the one observed from the PIV plans.
Regarding the update of the coefficients, a steepest descent algorithm is used with an adaptive step. A maximum step size is set to 10^{-2} while a minimum step size inferior to 10^{-4} is considered as an optimisation convergence criteria. The confidence coefficients are all set to $\zeta_i = 5 \times 10^{-2}$. This low uniform values represent a relative degree of confidence on the background closure values. The variations of the closure coefficients along the optimisation iterations are shown in figure 4.7. The maximum reduction of the cost and the optimal coefficients values for the three considered scenarios are summarised in table 4.2. In terms of mismatch between CFD and experimental mean pressure, it is shown that

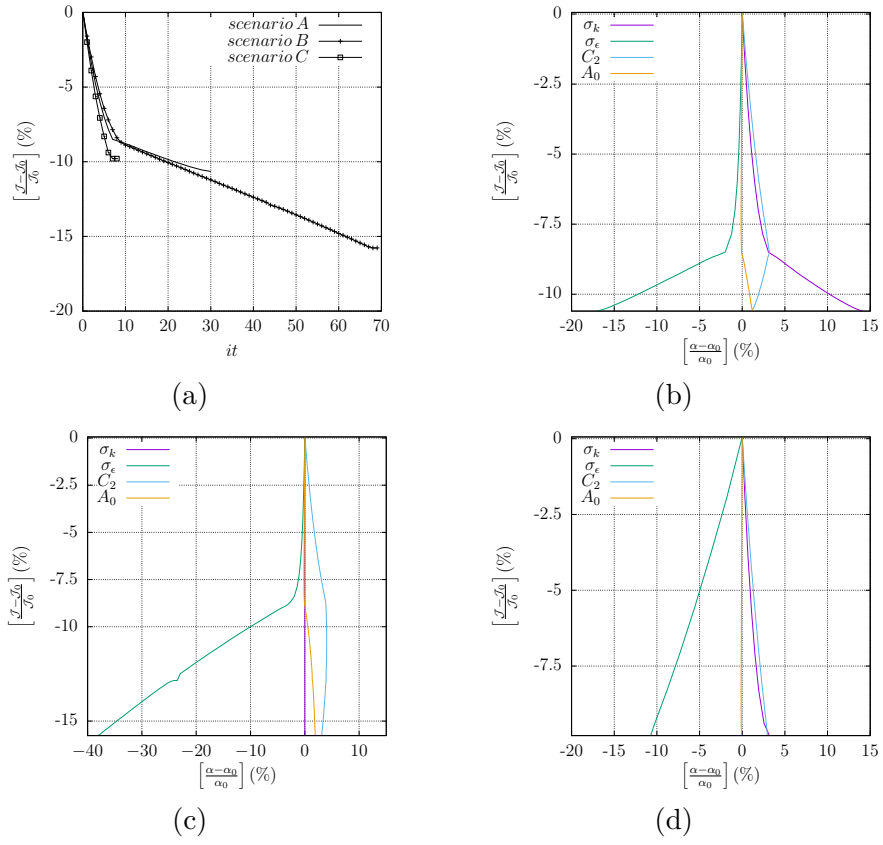

Figure 4.7 – Cost function reduction, (a), and closure coefficient variations: (b), scenario **A**; (c), scenario **B**; (d), scenario **C**.

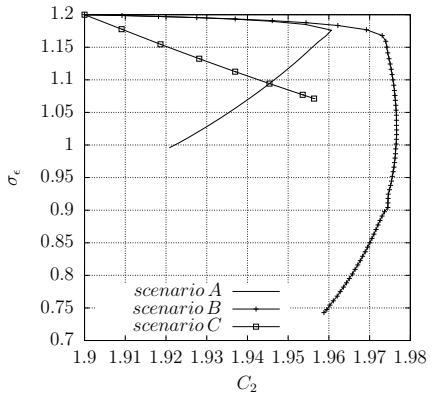

Figure 4.8 – σ_ϵ variations with respect to C_2 for all scenarios.

the highest reduction can be achieved through the optimisation scenario **B**. Conversely, scenario **C** leads to the least improvement in the cost function. However, we note a faster convergence rate for **C**, for which the optimal solution is reached 10 times faster than for **B**. Furthermore, a shift between the two regimes can be noticed in scenarios **A** and **B**. Indeed, this shifting occurs when the penalisation on the variation of C_2 becomes of the same order of magnitude than the required advancement for the cost minimisation. Whereas in **B**, σ_k is not optimised and the trend on C_2 until convergence is mainly dominated by its penalisation. In all scenarios, the optimal value of C_2 increases while it stays within 5% of the background value. Considering A_0, a minor variation is observed during optimisation in all scenarios. On the contrary, a higher variation of σ_ϵ below the recommended range is necessary to reduce the cost function. In figure 4.8, we show the variation of σ_ϵ with respect to C_2. In scenario **C**, a quasi-linear dependency is established through relation (4.2). However, we retrieve the two regimes in **B** and **A** where this dependency is broken.

In general, it can be concluded that a better agreement between the turbulence model (e.g *realizable* $k-\epsilon$) and wind tunnel experiments, in terms of wind load on the facades of high-rise buildings, can be achieved through optimisation of the closure coefficients. Even if it offers less degrees of freedom in the optimisation, better results are obtained when enforcing the constraint that equals turbulence mixing in the equation of transport of k to momentum mixing by the eddy viscosity (scenario **B**). This suggests that it is a physically valid hypothesis in our case study. It helps structuring the data assimilation process and leads to a robust procedure. It states that the turbulent mixing of the momentum and kinetic energy are of same nature. At the opposite, by relaxing the constraint and establishing relation (4.2) as valid out of the inertial layer (scenario **C**) may lead to lower agreement with measurements. Indeed, this assumption may hold reasonably in flows where turbulence behaviour is isotropic. However, in the presence of bluff body, e.g flows with separation and recirculation dynamics, this assumption is undoubtedly unrealistic. Scenario **B** might be considered as the best optimisation choice to get better wind load representation on high-rise building given the considered turbulence closure (*i.e.* realizable

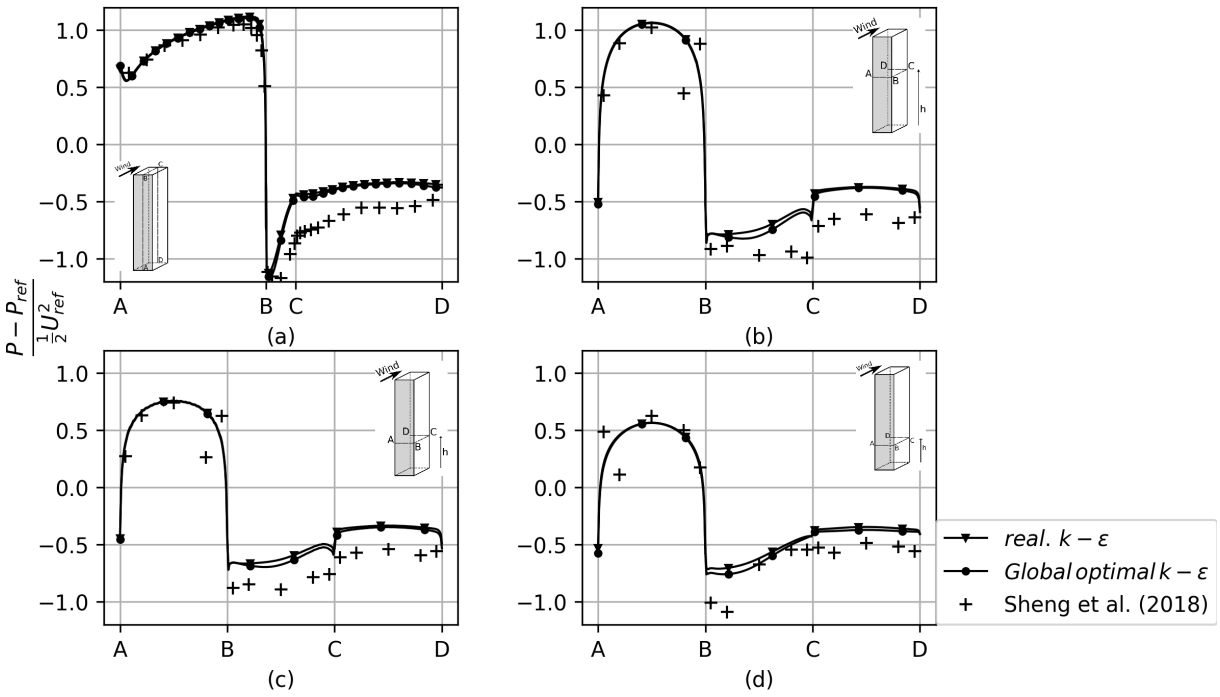

Figure 4.9 – Comparison of pressure coefficient profiles between CFD (scenario **B**) and experimental results along building facades. Contours are token at building symmetry plan, (a) and three horizontal plans at $z/H_{ref} = 1$, (b), $z/H_{ref} = 0.27$, (c) and $z/H_{ref} = 0.19$, (d), respectively.

$k-\epsilon$). Following the best optimisation scenario, 15% gain on the overall predicted loads are obtained. Furthermore, a comparison of the predicted pressure coefficient at the building facades (see figure 4.9) this gain is associated to the slight improvement observed especially along the side facades.

Nearly no change at the windward facade and along the upfront corners is observed. As a matter of fact, this observations confirms what was earlier mentioned in the sensitivity analysis where the rigidity of the considered turbulence model is shown to play a major role on the degree of improvement that can be achieved to fit with measurements.

With regard to the mean flow reconstruction, adopting the best optimisation scenario (scenario **B**), the contours of the mean velocity field are compared with the available PIV plans reported from the work of Sheng et al. (2018). It is a strong validation since these mesurements are not used in the data assimilation. Figures 4.10, 4.11 and 4.12 show the normalised streamwise velocity at the streamwise central plane (top) and at two horizontal plans, *i.e.* $z/H_{ref} = 0.19$ and $z/H_{\text{ref}} = 1$. The CFD with background values and optimised values following **B** are compared with the PIV measurements.

In order to show the effect of data assimilation, velocity contours are superimposed (right column) and thicker lines are plotted to track the size of the recirculation region. The reattachment length on the ground, is reported in table 4.3. After optimisation,

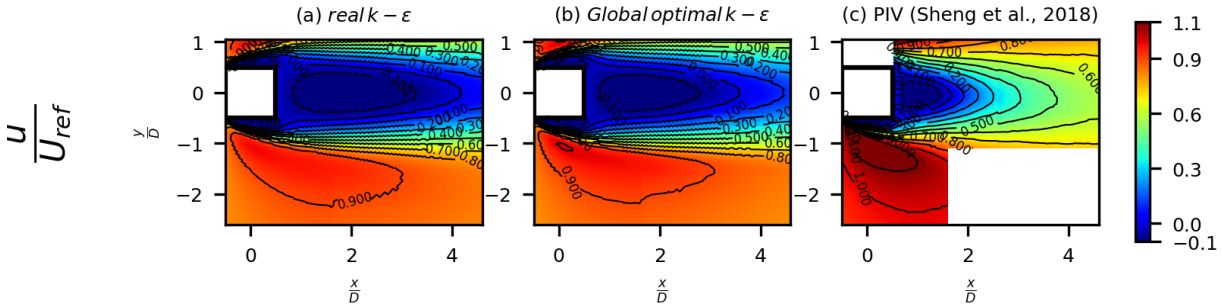

Figure 4.10 – Comparison of mean stream-wise contour between CFD (scenario **B**) and Re. Sheng (PIV) experiments at horizontal plane with normalised height $\frac{z}{H_{ref}} = 0.19$.

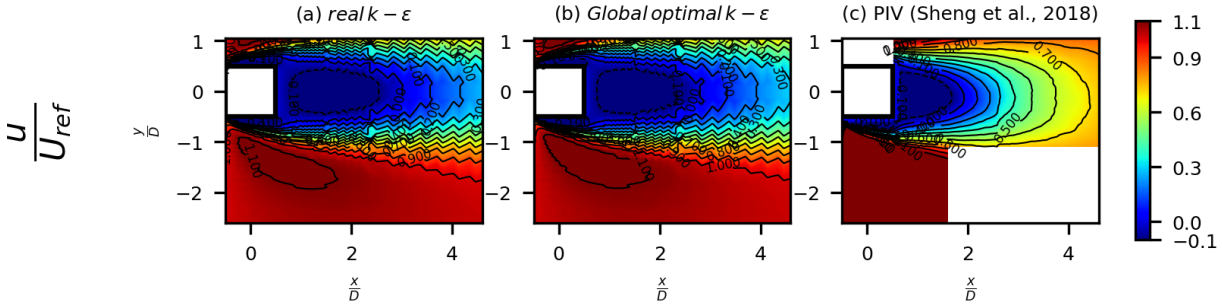

Figure 4.11 – Comparison of mean stream-wise contour between CFD (scenario **B**) and Re. Sheng (PIV) experiments at horizontal plane with normalised height $\frac{z}{H_{ref}} = 1$.

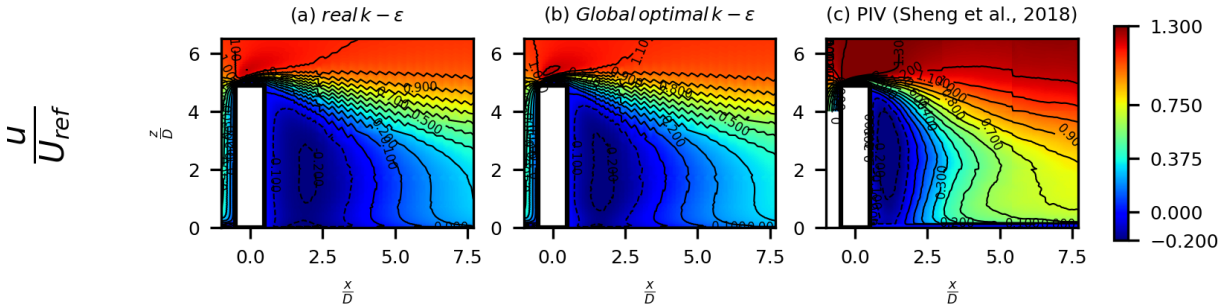

Figure 4.12 – Comparison of mean stream-wise contour between CFD (scenario **B**) and Re. Sheng (PIV) experiments at symmetry plane with normalised height $\frac{z}{H_{ref}} = 1$.

	Exp	*realizable* $k-\epsilon$	*optimised*
$Y^f(m)$	~ 50	139.8	117.1
$Y^r(m)$	-	13.6	11.7

Table 4.3 – Comparison of the (dimensional) reattachment lengths on the roof and floor, CFD optimised with global constant calibration (scenario **B**).

velocity contours show a better estimation of the recirculation region length which is shorter compared to the non-optimised model. This improvement is more affirmed near the ground, where the relative error of reattachment length Y with respect to PIV, $\varepsilon_Y = \frac{\nabla Y_0}{\nabla Y_{\text{end}}}$, with the default ($Y_0$) and the optimised ($Y_{\text{end}}$), is reduced by 25%. Despite this enhancement, it should be pointed out that CFD model still under-predicts the flow in the wake region. This is the best improvement of this specific turbulence model we obtained by assimilating the pressure measurements. The two limiting ingredients are the model rigidity and the partial sparse observations (pressure at the boundary) of the complex flow. We will show in the next chapters that the former is the most limiting.

4.5 Conclusions

Given the dual description of the dynamics composed of the RANS direct model (see chapter 2) and the adjoint of its tangent linear representation (see chapter 3) , we have explored a methodological setting that provides an efficient sensitivity analysis and an in-depth diagnosis of the turbulence closure adopted on such flows. At first we inspected the adjoint state variables in relation with their physical meaning. Then, a further study was dedicated to provide a better understanding of the model output variabilities in terms of the global constants associated with the model closure. These settings have been applied to the high-rise building case study.

Sensitivity maps of the $k-\epsilon$ global coefficients had revealed high interest in optimising them mainly at the shear layers resulting from flow separations at the leading lateral edges and on top of the building. Moreover, little sensitivity in the bulk of the recirculation wake region has been observed. Despite all the spatial variability of the sensitivity fields, it was shown that the optimality condition drastically reduces the high dimensional dependency of the model to each coefficient.

Regarding the model hypotheses which guided the choice for the non-calibrated values, a better data coupling is obtained by enforcing the constraint that equates turbulence energy mixing to momentum mixing, event though its initial sensitivity suggest globally a thinner turbulent mixing layer and offers fewer degrees of freedom in the optimisation. This suggests that it is a physically valid hypothesis that structures the model and then helps for convergence. Conversely, by relaxing this constraint and establishing the relation (4.2), which dictates a strong bound limiting the production of energy dissipation rate to its redistribution (supposedly valid in the inertial layer near the wall), this leads to lower agreement with experiments. As both assumptions constitute a common practice for closure to most eddy viscosity models, it is expected that these results extend to several other models of similar forms. The limited performance of the DA procedure, achieved when controlling global turbulence parameters, points out the rigidity of the considered turbulence model when used with realistic wall pressure measurements. We remind that, with the proposed DA coupling methodology, one can investigate any model sensitive parameters of an arbitrary size with no additional computational costs. Finally, since the methodology was applied on an isolated buildings, it can be applied nearly with no

changes (but larger computational resources) for urban dense areas.

Chapter 5

DATA-ASSIMILATION FOR SPATIALLY DISTRIBUTED CORRECTIONS OF DEFORMATION

5.1 Introduction

As it was observed in chapter 4 and reported by many authors (Kato and Obayashi, 2013; Edeling et al., 2014), data-assimilation techniques (for instance variational) are able to provide insights on the model variability through calibration of model closure coefficients. However, due to the rigidity of the model, variabilities of the solution are strongly constrained and does not allow the flow to reach enough states for accurate estimations. To overcome such restrictions, one may approach the problem considering a *weak constraint* as it is called in the data assimilation community, *by* defining an additive forcing term as an additional control parameter in order to allow the solution to deviate from the default model constraints.

This chapter is organized as follows. First (section 5.2), we present the modified set of RANS equations. Then, on section 5.3, we introduce the changes to be made to the adjoint models and, hence, on the optimality conditions. With the strongly partial observations and the consideration of spatially distributed control parameters, the control parameter can be any function in $L^2(\Omega)$, which includes highly irregular functions, needs to be smoothed to penalize the emergence of local minima and irregular solutions. To that purpose, we propose the examination of two regularization approaches. In section 5.4, after an initial sensitivity analysis, we present the data-assimilation results by comparing reconstructed flows obtained with both regularization techniques. Since, forcing here is not affixed with the specified turbulence model, we hence investigates the effects of assumption of constant eddy viscosity (CEV), which enables a major simplification to the adjoint model and its boundary conditions. To asses the importance for the coupled terms in the adjoint model derivation, reconstructed flow using CEV is then confronted to those from an exact continuous adjoint derivation. Finally, we consider a simple structuration of the forcing so as to provide some physical constraints to the reconstructed flow features.

5.2 Equations of motions

By examining the structure of the RANS modeling, we can address the choice of the control parameters as a correction of the deformation field. Indeed, an exact modeling of the deformation should properly include the mechanisms of energy transfer between the mean field towards the turbulence and vice versa. However, under the unidirectional energy transfer hypothesis (by Boussinesq analogy), these interactions are often modeled by a classical diffusion process. From this point of view, an optimization parameter to be proposed would then be a volume force bringing the direct adjustment to the wind field. In theory, such a force corresponds to a relaxation of the Boussinesq hypothesis and should embed the missing transport mechanisms of the mean field by turbulence. This corrected model of deformation with the new forcing f_{u_i} term reads:

$$\frac{\partial(\rho U_j U_i)}{\partial x_j} = -\frac{\partial P}{\partial x_i} + \mu \frac{\partial}{\partial x_j}\left[\frac{\partial U_i}{\partial x_j}\right] - \frac{\partial}{\partial x_j}\left(\rho \overline{u_i' u_j'}\right) - f_{u_i}. \tag{5.1}$$

In the line of the work done by (Foures et al., 2014; Symon et al., 2017; Franceschini and Sipp, 2020), we consider the calibration of a vector force which, we refer to as a "raw form".

Let us note that, in attempt to provide an alternative force which mimics the one induced by a shear stress, another form $f_u = \nabla \cdot (\mathbf{f} + \mathbf{f}^T)$, in which $\mathbf{f}$ is a tensor field, has been also experimented. Through this form, we seek eventually to account for the missing components of the modelled shear stress. However, this choice leads in practice to strong difficulties. First, it is noteworthy to mention that the tensor form is a field of larger dimension (six degree of freedom) than the raw form (three degrees of freedom). Boundary conditions need to be specified to deal with all the stress components in the DA procedure. Besides, upon deriving an optimality condition, the sensitivity field is defined as $\nabla(U^*) + \nabla^T(U^*)$. Such a sensitivity field appears to be irregular with very localized peaks next to the building walls, thus, making the numerical procedure unstable.

5.3 Optimality conditions

Being independent of the flow state variables, this additive force does not involve any modification on the derivation of the adjoint model and nor on its boundary conditions. Moreover, by definition, the sensitivity of the Lagrangian compared to a disturbance of an arbitrary force δf_{u_i} is defined by

$$\langle \frac{\partial \mathcal{L}}{\partial f_{u_i}}, \delta f_{u_i} \rangle_\Omega = \langle \frac{\partial \mathcal{J}}{\partial f_{u_i}}, \delta f_{u_i} \rangle_\Omega + \langle \frac{\partial M_{u_i}}{\partial f_{u_i}} \delta f_{u_i}, U_i^* \rangle_\Omega. \tag{5.2}$$

with the compact notation M_{u_i} standing for the component i of equation (5.1). In its generic form, an optimality condition is presented as

$$\frac{\partial \mathcal{L}}{\partial f_{u_i}} = \langle \frac{\partial \mathcal{J}}{\partial f_{u_i}}, \delta f_{u_i} \rangle + U_i^*. \tag{5.3}$$

With the strongly partial observations and the consideration of spatially distributed control parameters, the risks of obtaining local minima or unphysical irregular flow reconstructions is strong. The control parameter can be any function (possibly irregular) of $L^2(\Omega)$. Regularisation is a way to mitigate the risk in smoothing the solution. In order to achieve this, two different solutions can be proposed: a regularisation by penalty (section 5.3.1) and by use of Sobolev gradient (section 5.3.2).

5.3.1 Regularisation through penality

For that purpose, penalty of spatial gradients of the control parameter is often considered (Franceschini and Sipp, 2020). This type of additional term enables to efficiently smooth the irregularities of the solution. As it is classically done, we consider here L^2-norm penalisation of the gradient of the parameter field. In its integral form, the penalized cost function reads now as follow

$$\mathcal{J}_1(P, f_u) = \frac{1}{2}||\rho U_{\text{ref}}^2 \Delta C_p^w||_{R^{-1}}^2 + \int_\Omega |\nabla f_u|_{B^{-1}}^2 dv$$

Where B is a confidence matrix to be estimated. Its role is to ensure both homogeneity (in addition to scaling) and to adjust the degree of regularity to be prescribed. The scaling parameter should not be taken too small, such that it becomes inefficient, and not too large, so that it enforces too smooth solution in which all the spatial variabilities are rubbed out.. This trade-off is often performed by L-curve method (Hansen, 1992). In this specification, the first term of the right hand side of (5.2) is differentiated and yields to

$$\langle \frac{\partial \mathcal{J}}{\partial f_u}, \delta f_u \rangle_\Omega = \langle -\nabla \cdot (B^{-1} \nabla f_u), \delta f_u \rangle_\Omega. \tag{5.4}$$

We note that boundary integral resulting from the integration by part cancels as we let f_u vanish at all boundary parts. Thus, an optimality condition (5.3) which writes as

$$\frac{\partial \mathcal{L}}{\partial f_{u_i}} = -\nabla \cdot (B^{-1} \nabla f_u) + U_i^*. \tag{5.5}$$

does involve an evaluation of a Laplacian operator applied on the current parameter field. Indeed, assuming a spatial homogeneity for this constraint, the confidence matrix B can be considered as diagonal and uniform and its inverse is straightforwardly expressed as

$$B_{ii}^{-1} = \zeta_i \left(\max |U^{*,0}| \right).$$

in which ζ_i is a positive free parameter and subscript i stands for the vector's (and matrix's) component, $.^0$ mark the initial adjoint field (before the first update of the parameter). It should be noted that, by considering B as constant and diagonal, embeds only uniform diffusive effects. Note that one may consider covariances (or correlations) between forces in neighbour cells and hence construct a multi-band matrix. This choice might be investigated in future works and might be usefull to express space dependent preferential directions of diffusion. Let us recall that for $\langle a, a \rangle_{B^{-1}}$ to be a norm, this matrix must be symmetric and positive definite.

So far, sensitivity as computed by (5.5) can effectively ensure regularity of the parameter field. However, the magnitude for ζ_i have to be determined,this constitutes a difficult question in itself. Most of the times, those parameters are empirically selected by successive trials to get an *a priori* trade-off between performance and regularity.

5.3.2 Regularisation through Sobolev gradient

In the following, we consider an alternative Sobolev gradient regularisation (Protas et al., 2004; Tissot et al., 2020). It consists in searching the control parameter in the Sobolev space $H^1(\Omega)$. This space includes more regular functions than $L^2(\Omega)$, by considering an innerproduct with a regularity constraint on the function first derivatives.. With this approach, the functional is defined in its basic form as

$$\mathcal{J}(P) = \frac{1}{2}||\rho U_{\text{ref}}^2 \Delta C_p^w||_{R^{-1}}^2.$$

Hence, the optimality condition (5.3) bolls down to

$$\frac{\partial \mathcal{L}}{\partial f_{u_i}} = U_i^*.$$

Furthermore, with this condition and for an arbitrary functions ψ and ϕ in $H^1(\Omega)$, the Sobolev gradient is defined such that

$$\langle \frac{\partial \mathcal{L}}{\partial f_{u_i}}, \psi \rangle = \langle \frac{\partial \mathcal{L}}{\partial f_{u_i}}^{H^1}, \psi \rangle_{H^1}, \tag{5.6}$$

with the scalar product definition

$$\langle \phi, \psi \rangle_{H^1} = \int_\Omega \phi\psi + l_{sob}^2 (\nabla\phi . \nabla\psi) d\Omega, \tag{5.7}$$

in which l_{sob}^2 is a free parameter. We recall that $\langle \cdot, \cdot \rangle$ stands for the standard L^2 inner product. Through integration by part of the second term in 5.7 (involving the function gradients), the equality (5.6) yields to the new optimality condition expressed as

$$\frac{\partial \mathcal{L}}{\partial f_{u_i}}^{H^1} = \left(\frac{1}{1 + l_{sob}^2} (\mathbb{I} - l_{sob}^2 \Delta) \right)^{-1} \frac{\partial \mathcal{L}}{\partial f_{u_i}}, \tag{5.8}$$

and in which Δ stands for the Laplacian differential operator. Equation (5.8) corresponds to the filtering of the sensitivity. Hence, under this approach, it turns out that a regularized sensitivity field arises as a solution of a simple Helmoltz equation. Now, since high dimensional matrix inversion is not an option in such large system, the Poisson equation (5.8) is solved through an iterative technique. Regarding its discretization, the same finite volume scheme can be adopted as for the direct RANS equations. Here, it is noteworthy to mention that this type of regularization offers two main advantages in comparison with the conventional penalisation approach. In the one hand, as opposed to the penalization approach which requires an estimate of a non-dimensional confidence factor (for instance ζ as with global coefficients) with no physical significance, the free parameter involved with the use of Sobolev gradient is indeed a physical quantity. Through dimensional analysis of (5.8), l_{sob} has the dimensions of a length. In fact, this parameter can be seen as a filtering length scale below which sensitivity field is smoothed. Thus, providing a characteristic length scale relevant to a given flow region (*e.g.* the building width), the parameter can be straightforwardly defined as a function of this length. In the other hand, the Sobolev gradient does ensure a descent direction. Indeed, applying a Taylor expansion of the cost function around an initial guess f_{u_i} in the direction $\delta f_{u_i} = -\frac{\partial \mathcal{L}}{\partial f_{u_i}}^{H^1}$ can be expressed as follows

$$\mathcal{J}(f_{u_i} + h\delta f_{u_i}) = \mathcal{J}(f_{u_i}) + h\langle \frac{\partial \mathcal{L}}{\partial f_{u_i}}, \delta f_{u_i} \rangle + \mathcal{O}(h^2)$$

Substituting the second term in the RHS by using the equality (5.6) yields to

$$\mathcal{J}(f_{u_i} + h\delta f_{u_i}) = \mathcal{J}(f_{u_i}) - h \left\| \frac{\partial \mathcal{L}}{\partial f_{u_i}}^{H^1} \right\|_{H^1}^2 + \mathcal{O}(h^2)$$

in which we define the norm $\|a\|_{H^1}^2 = \langle a, a \rangle_{H^1}$. Thus, for a small enough perturbation $h\delta f_{u_i}$, we have $\mathcal{J}(f_{u_i} + h\delta f_{u_i}) < \mathcal{J}(f_{u_i})$. Now, injecting this optimality condition into a steepest descent algorithm, an update of the forcing at iteration n is given as:

$$f_{u_i}^{n+1} = f_{u_i}^n - \lambda \left(\frac{\partial \mathcal{L}}{\partial f_{u_i}}^{H^1} \right)^n, \tag{5.9}$$

in which the step size is constrained by $\lambda = \beta / max(\partial \mathcal{L} / \partial f_{u_i}{}^{H^1})$ where β is a free parameter.

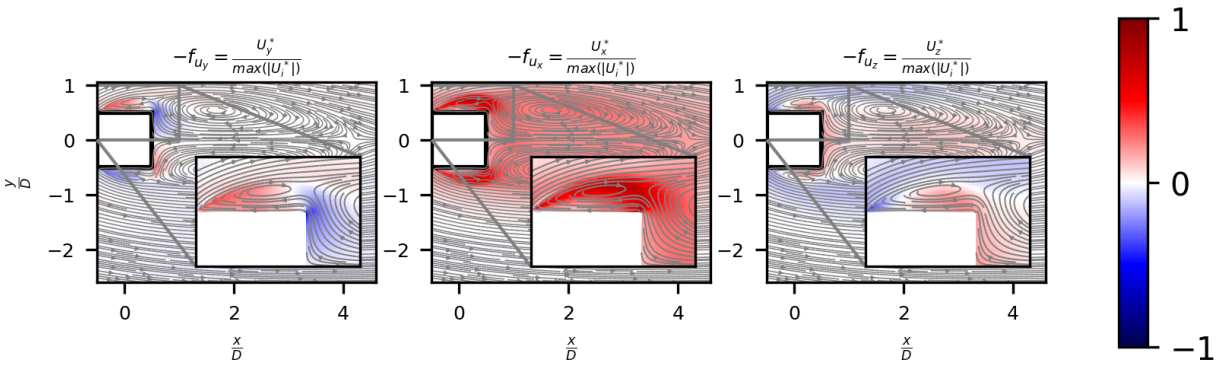

Figure 5.1 – Initial update of the force (e.g opposite sensitivity) field in horizontal plane at normalized height $z/D = 0.63$: f_{U_y}, f_{U_x} and f_{U_z} are, respectively, transverse, streamwise and spanwise component. Each component is normalized by in-plan overall (components) peak value.

5.4 Results

In this section, we will first analyse the initial sensitivity field corresponding to the first iteration of the assimilation procedure before regularization. Then, the results of the reconstructed flow after the whole data assimilation procedure with both regularisation approaches will be compared. In a third time, the CEV assumption will be investigated and compared with the optimal solution.

5.4.1 Sensitivity fields

Before conducting the full data assimilation procedure, we first analyse the sensitivity fields, associated with the tangent linear system taken for $f_u = 0$, *i.e.* before optimisation. Figures 5.1, 5.2 and 5.3 present the distributions of the sensitivity to the added force superposed with streamlines. Sensitivities are thus illustrated at three plans, constituted by two horizontal plans (at normalized height $z/H_{ref} = \{0.19, 1\}$) and the symmetry plane (at $y/D = 0$) which highlight the different areas of relevance. The sensitivity to the control vector reveals a variability among its three components in term of the amount of interest for an adjustment depending on the local flow features, i.e ranging from the upstream impingement and a dominant 2D wake at the bottom to a strongly 3D wake as we span upward toward the high end. High sensitivities of the streamwise velocity component are revealed on the upstream flow impingement (see figure 5.3) and the lateral shear layers, more specifically at the junction with the wake (see figures 5.1 and 5.2). As we go downstream into the wake, a similar order of magnitude is observed for all velocity components. With regards to the impingement region, it is observed that the streamwise sensitivity exhibits two peaks at different elevations (see zoomed figure 5.3 on f_{u_x}). Theses peaks are associated with streamlines which have high curvature, due to the radial pressure gradient, such as on the near upstream of the stagnation point

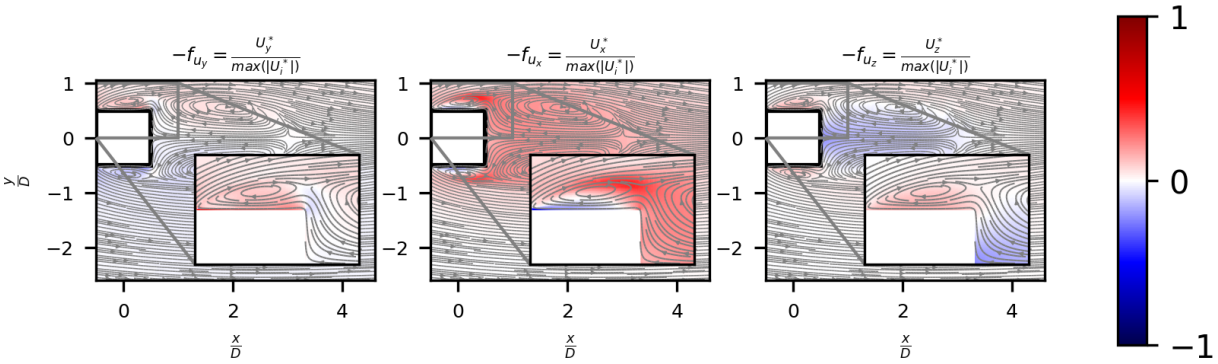

Figure 5.2 – Initial update of the force (e.g inverse sensitivity) field in horizontal plane at normalized height $z/D = 3.3$: f_{U_y}, f_{U_x} and f_{U_z} are, respectively, transverse, streamwise and spanmwise component. Each component is normalized by in-plan overall (components) peak value.

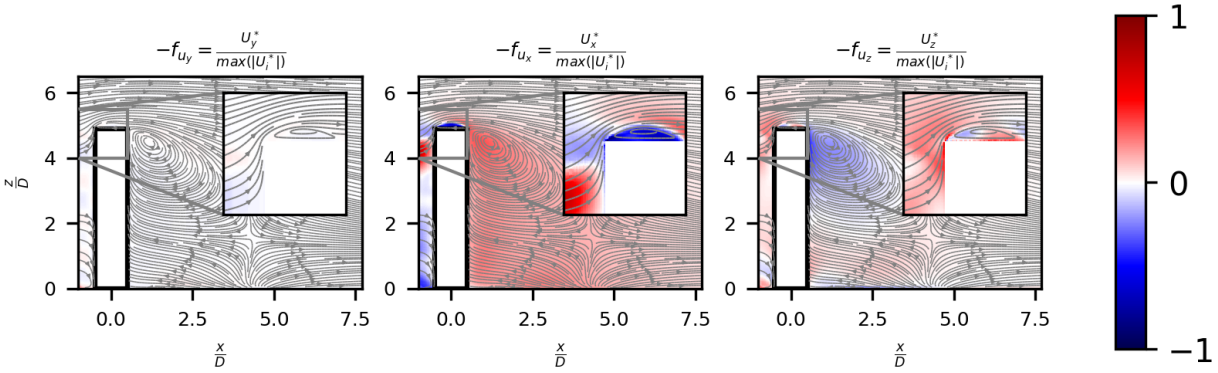

Figure 5.3 – Initial update of the force (e.g inverse sensitivity) field in symmetry plan: f_{U_y}, f_{U_x} and f_{U_z} are, respectively, transverse, streamwise and spanmwise component. Each component is normalized by in-plan overall (components) peak value.

($z/D \simeq 4$) and close to the ground at the formation of the horseshoe vortex. In fact, we note that this tendency remains whether or not pressure information is giving at the windward facade. This shows that these regions affect the wake recirculation region driving the back pressure. This means that upstream perturbations affect downstram regions trough advection, which translates in the adjoint model to a retrograde advection and an additional source term. We can recall that the adjoint inlet boundary condition is a Dirichlet Boundary condition, i.e $\mathbf{U}^* = 0$ at $\partial\Omega_{in}$ and the outlet $\partial\Omega_{out}$ authorises penetration. Moreover, inhomogeneous Dirichlet condition is apllied on the adjoint model at the sensor position.

Regarding the signs, contributions from the force are of the same sign as the adjoint velocity. Thus, fluid travelling downstream (or more generally for positive $\mathbf{U}_i$, $i = \{x, y, z\}$) experiments acceleration from positive contributions. Otherwise, an upstream flow (or more generally for negative $\mathbf{U}_i$) exhibits deceleration instead. Therefore, regarding the positive peak upstream the stagnation point at $z/D \simeq 4$ (figure 5.3 on U_x^*), sensitivity on the streamwise suggests an acceleration to the approaching flow, which later separates partly on the sides and mainly at the high-end. However, as we span downward, negative sensitivity, assumedly stemming from the backward transport of the (windward) wall-pressure errors, infers deceleration to the upcoming flow. This tendency tends to decrease the stagnation pressure along the front, by giving more (tangent) momentum to the upward flow and hopefully reduces the total pressure along the stagnation streamlines in the bottom part of the impinging flow. This feature may explain the stagnation anomaly noted by (Issa, 1995) where the total pressure (along upstream streamlines) is not conserved but rather increased by the (con-traverse) effects of the eddy viscosity.

At the high end at the top of the building (figure 5.3), an acceleration is prescribed in the streamwise direction inside the recirculation bubble (see f_{U_x}). The overall effect tends to reduce the recirculation bubble, reduce the top pressure and favor an earlier reattachment. Let us recall that errors here constrain the vertical component solely, $U_z^* = \Delta C_p^w \mathbf{z} > 0$, and that streamwise sensitivity is reconstructed from the adjoint model, from the incompressibility condition of the field.

In the downstream (i.e. wake), giving the under predicted pressure, positive streamwise adjoint component is enforced on the leeward facade. Regarding the down-wash flow, *i.e.* the descending velocities around $z/D > 2, x/D > 0.5$, sensitivities ($U_z^* < 0$ and $U_x^* > 0$) advocate downward acceleration at the wake edge (as $U_z < 0$ and $U_x > 0$) and upward deceleration close to the facade (as $U_z > 0$ and $U_x < 0$) (figure 5.3). At height $z/D = 0.63$ where the flow is progressively shifting to span-wise vortex structure (figure 5.2), an acceleration is prescribed in the streamwise direction inside the recirculation bubble (see f_{U_x}), and with a change of sign for f_{U_z} in such a way to intensify the vorticity in the transverse extension to the recirculation region. Examining the up-wash ($z/D < 2, x/D > 0.5$), in which flow is dominated by lateral spanwise structures, in a similar way, control suggests streamwise acceleration at the wake transverse edges and decelerating at the symmetry plane (figure 5.1). Therefore, this would, conceivably, tend to reduce the wake region as streamwise velocity is surged (toward positive ranges).

	$\frac{\partial \mathcal{J}}{\partial f_{u_x}}(\times 10^8)$	$\frac{\partial \mathcal{J}}{\partial f_{u_y}}(\times 10^8)$	$\frac{\partial \mathcal{J}}{\partial f_{u_z}}(\times 10^8)$
AD	2.476	0.055	0.635
FD ($\delta\alpha_i = 10^{-2}$)	2.352	0.0647	0.773
FD ($\delta\alpha_i = 10^{-3}$)	2.275	0.072	0.769
FD ($\delta\alpha_i = 10^{-4}$)	2.274	-	0.775

Table 5.1 – Sensitivity derivative w.r.t. f_{u_i}, $i = \{x, y, z\}$ computed from the proposed adjoint model (AD) and the finite difference (FD) with different perturbation sizes.

Yet, it is noteworthy to mention that this initial force field is the result of the strong coupling between mean velocity and turbulence related quantities in turbulence model (e.g, production of k by mean shear). Due to non-linearity, this tangent-linear analysis is only relevant around the default (*i.e.* not corrected) solution. This trend of the correction by the control parameter is expected to change through the minimization. Nevertheless, this constitutes only a qualitative validation test of the adjoint model. Sensitivities need to be validated through quantitative comparison with a more simple, but expensive, differentiation method. Here, again, finite difference (FD) will be considered as a reference method. However, to ensure accuracy of the finite difference method, step size dependency is checked, and different perturbation sizes were considered for validation test, where $\delta f_{u_i} = \varepsilon \in \Omega_{in}$ and zero otherwise. The region of interest Ω_{in} is chosen as in chapter 4. Table 5.1 shows values of the summed sensitivities. Thus, overall, adjoint based sensitivity is very close to the finite difference values, with a relative error ranging between $5 - 9\%$ for the dominant streamwise component.

5.4.2 Reconstructed flow

Regarding the minimization procedure, a steepest descent algorithm is used with an adaptive step. A maximum step size $\lambda = 0.1\text{max}(\partial\mathcal{L}/\partial f_u)^{-1}$ is fixed based on the sensitivity validation test, while a minimum pre-factor for the step size of 10^{-4} is considered as an optimization convergence criteria. As for regularisation, the confidence coefficient is set to $\zeta_i = 10^{-1}$ for the penalisation approach. Concerning the filtering choice, we note that with $l_{sob} = 0$, *i.e.* no smoothing, this yielded to an unstable procedure, thus, recalling the importance of regularisation of the sensitivity fields. A higher values have led to an over smoothing since the sensitivity varies with length scales which are quite small in comparison to this filtering length scale (as $l_{sob} \approx$ lateral recirculation width). Therefore, following previous work (Tissot et al., 2020), a filtering length scale equivalent to 10% of the building width seems to give a fair compromise to filter unphysical small-scales. Comparison of the cost reduction results using both regularisation approaches are shown in the figure 5.4. We can see that Sobolev gradient leads to the lowest level of discrepancy ($\frac{\mathcal{J}}{\mathcal{J}_0} \simeq 0.2$) compared to gradient penalisation ($\frac{\mathcal{J}}{\mathcal{J}_0} \simeq 0.3$). With regards to the convergence speed, minimisation with Sobolev gradient reaches the minimum in less than 70 iterations

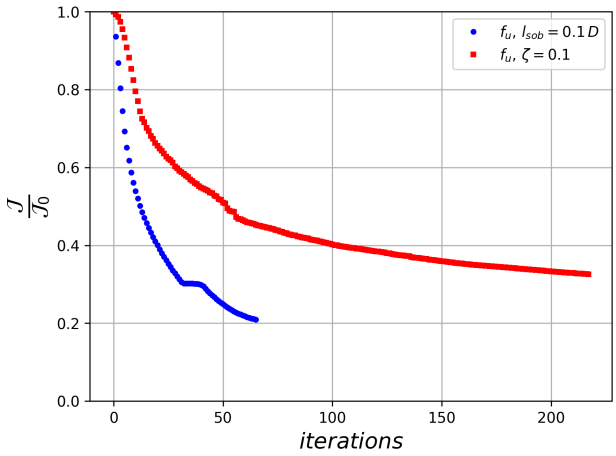

Figure 5.4 – Cost function reduction with local deformation correction. Comparison between regularisation approaches: penalisation ($\zeta = 0.1$) compared with parametrization in H^1 ($l_{sob} = 0.1D$).

while it is achieved in over 200 steps by penalisation. The convergence process with the Sobolev gradient is therefore much faster and more accurate than with the penalisation. This might come due to the fact that adding the gradient to the cost does change the original descent direction that is prescribed by the discrepancy to data.

Wind load profiles Results for the reconstructed pressure loads at and around measurement locations are compared with the experimental data (Sheng et al., 2018) and the default model in figure 5.5. In figure 5.5(a), pressure distribution is shown along "ABCD" path in the symmetry plane; in which, "AB", "BC" and "CD" are three lines token each at front, roof-top and leeward facades, respectively. At points subject to recirculation $C_p < 0$ ("BC" and "CD"), reconstructed pressure using force with Sobolev regularisation (solid line with circle marker) shows perfect fitting to data (with "+" marker) as compared with the penalisation (solid line with square marker). Along windward facade ("AB"), perfect match is also observed at the highest stagnation pressure ($z/D \simeq 4$) and at the bottom section; however, we note an overly reduced pressure on the section $1.5 < z/D < 3.5$. As noted in the sensitivity analysis section 5.4.1, this is seen to be related with the retrograde convection effects of data-informations from recirculation regions. In other words, this means that the amount of adjustment of the pressure at the front is partly guided by the amount of reduction of the discrepancy at regions subject to separation. Figure 5.6 illustrates this by presenting the converged f_u distribution at the symmetry plane. As the positive peak around the stagnation point ($-f_{u_x} > 0$, $z/D \simeq 4$) is shifted upstream further from the wall, optimal force decelerates the approaching flow near the wall, with negative values of $-f_{u_x}$ being transported leeward from the high-end. Accompanied by an upward acceleration ($-f_{u_z} > 0$), this provides a suction effect which tends to over-reduce the pressure at stagnation points. Let us note that approaching the ground, as it was observed in the initial sensitivity field (figure 5.3), adjoint force is seen to be partly affected

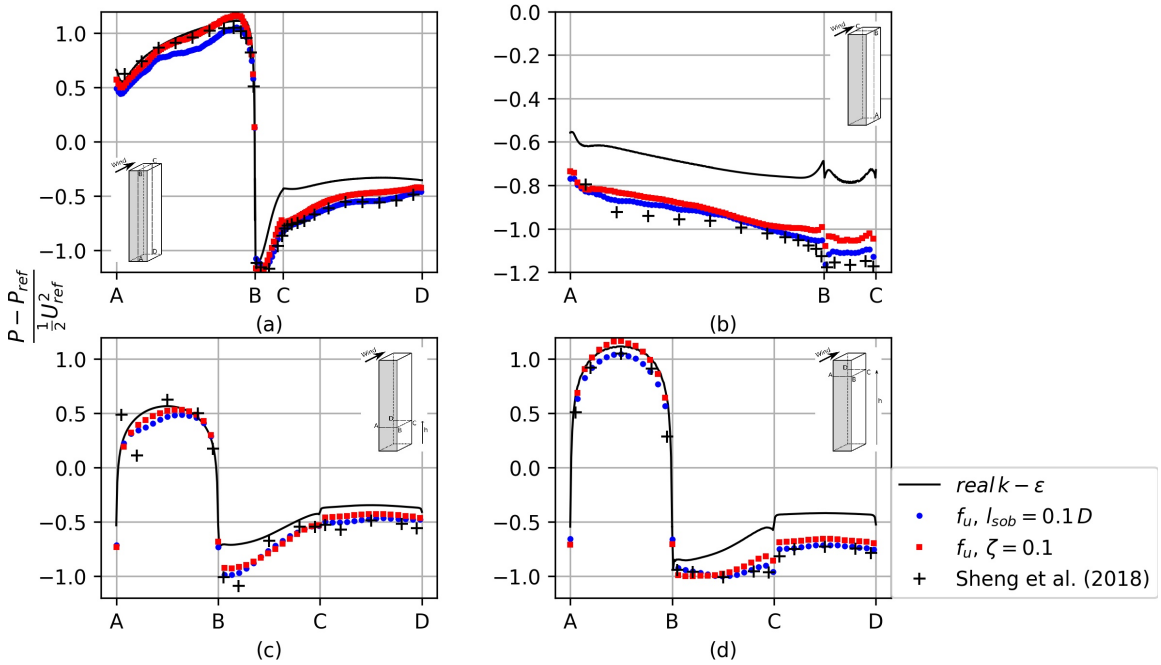

Figure 5.5 – Pressure coefficient profiles along building facades with local deformation correction. Comparison between regularisation approaches: penalisation ($\zeta = 0.1$) compared with parametrization in H^1 ($l_{sob} = 0.1D$).

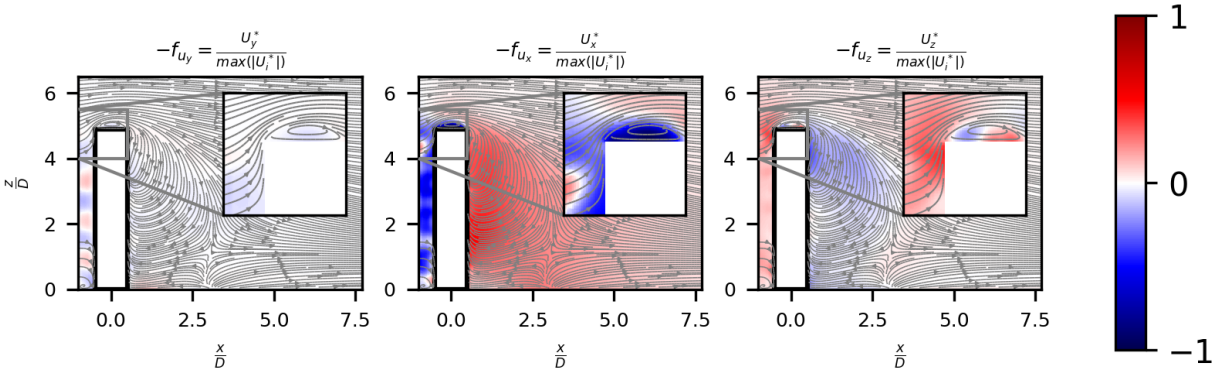

Figure 5.6 – Converged corrective force, with Sobolev gradient, on the symmetry plane. f_{U_y}, f_{U_x} and f_{U_z} are, respectively, transverse, streamwise and spanmwise component. Each component is normalized by in-plan overall (components) peak value.

by the pressure errors at the windward facade which explains the better fitting there.

Moreover, pressure profiles are also compared along "ABC" path at spanwise transverse plane on the centre of the structure (the plane $x/D = 0$), as shown in figure 5.5(b). "ABC" is sweeping the lateral facade along the span ("AB") and goes on the transverse direction at the roof top ("BC"). Along this path, both forcing leads to a very good agreement with experiments; yet, with Sobolev gradient, pressure predictions matches even better the data.

Further, at transverse horizontal plane (with plane normal to $\mathbf{z}$), as presented in figures 5.5(c) and (d), we look at paths at two different heights; on (c), the height corresponds to the lowest measurement level ($z/D \simeq 0.3$), while, on (d), profiles are compared at the maximum stagnation point level ($z/D \simeq 4$). In (c), across the windward section "AB", both optimized profiles tend to break symmetry as it reaches an intermediate level between the default model and the non-symmetric data distribution which arises assumedly from inverted pressure taps. However, in (d), reconstructed profiles fits perfectly to data as the later is symmetric. Furthermore, along the side and across the back ("BC" and "CD"), both forces yields to a great match with experiments, with better fitting using the Sobolev gradient. Thus at this stage, although the small deviations related to such a reverse method (retrograde advection), we can say that reconstruction with such a force does provide a good interpolation between the measurement points. This, in particular, is achieved using a Sobolev-based descent direction.

Wake centreline profiles Results of the streamwise velocity on the wake centreline are further confronted to data from PIV experiments (Sheng et al., 2018) and uncorrected model in figure 5.7. In order to span both up-wash and down-wash motions, profiles are compared at two height levels ($z/D = 0.63$ and $z/H_{ref}1$). In terms of recirculation length, both models show a considerable reduction at both elevations. Regarding the peak value in the wake, both optimisation strategies yields a better prediction of the position even if they tend to under-estimate the pressure as we span upward.

Wake transverse profiles Transverse distributions of streamwise velocity at three streamwise locations; that is, $x - x_b = D$, $x - x_b = 2D$ and $x - x_b = 3D$ downstream of the building ($x_b = 0.5D$) are given in figures 5.8 and 5.9. Spanning the ascending and descending velocities (refferred as up-wash and down-wash motions), both optimized models yields to a reduction of the wake extent, yet, no significant difference is observed. Still, due to the overly-predicted recirculation length, both model results are incorrect regarding the magnitude and the sign. This inconsistent behaviour is worsen progressively going further downstream. Note that, for all streamwise locations, symmetry is well preserved by all models. Results on the streamwise velocity shows that penalisation choice does not matter as we go further into the bulk. Besides, both approaches yields to poor velocity reconstruction.

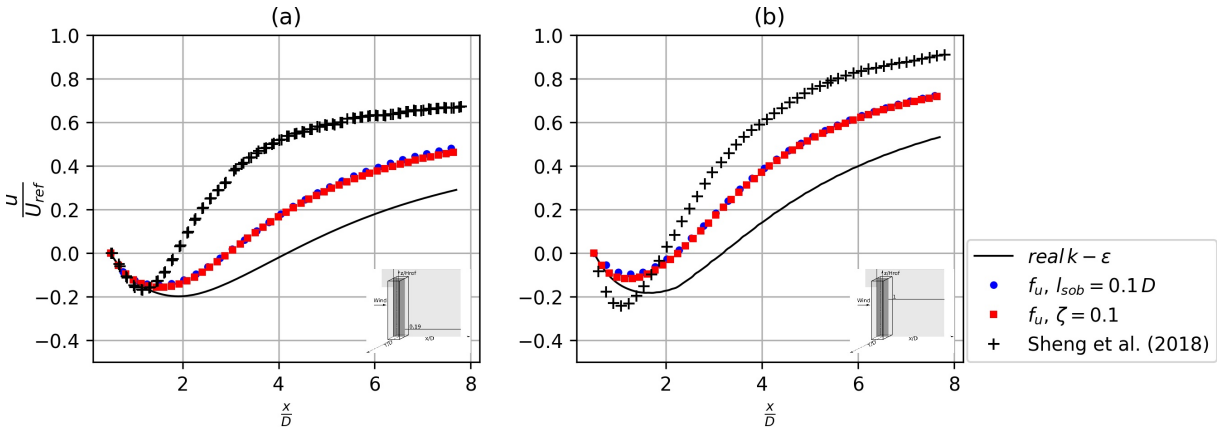

Figure 5.7 – Streamwise velocity along centreline at $z/D = 0.63$ and $z/D = 3.3$ elevations with local deformation correction. Comparison between regularisation approaches: penalisation ($\zeta = 0.1$) compared with parametrization in H^1 ($l_{sob} = 0.1D$).

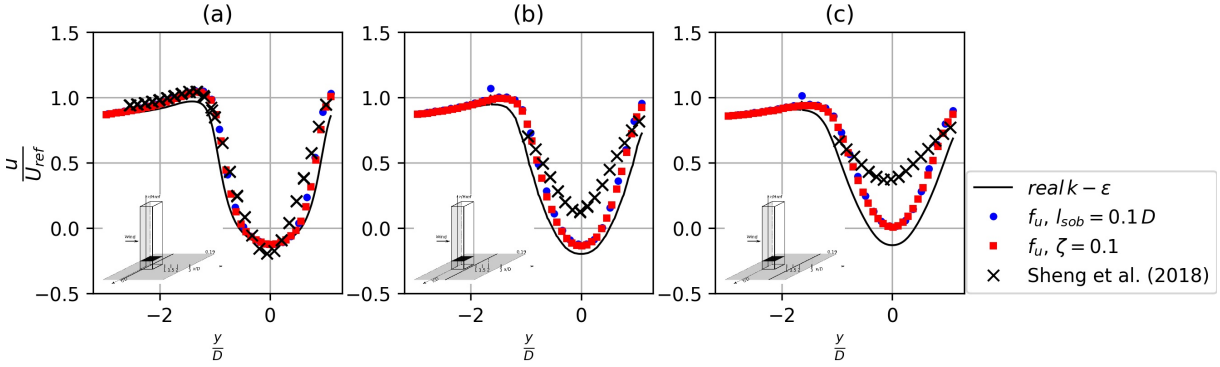

Figure 5.8 – Streamwise velocity in the wake transverse at $z/D = 0.63$ with local deformation correction. Comparison between regularisation approaches: penalisation ($\zeta = 0.1$) compared with parametrization in H^1 ($l_{sob} = 0.1D$) across streamwise positions $\frac{x}{D} = 1$,2 and 3.

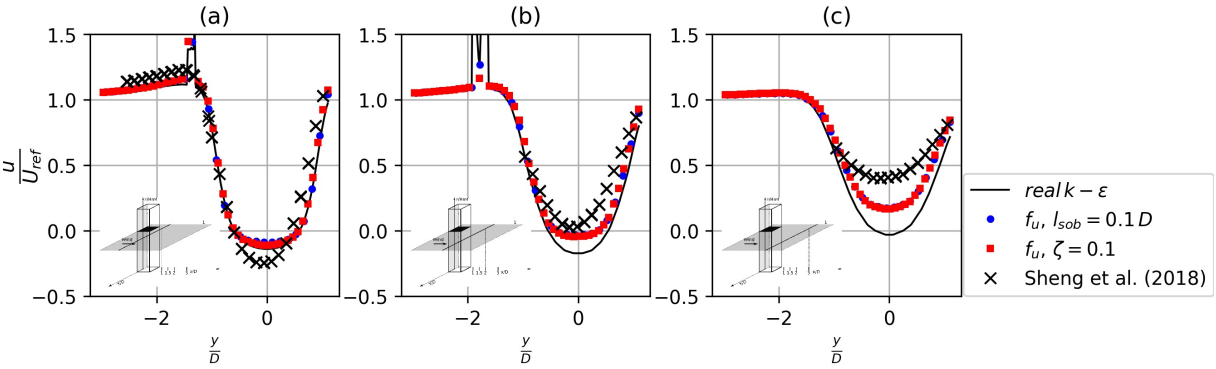

Figure 5.9 – Streamwise velocity in the wake transverse at $z/D = 3.3$ with local deformation correction. Comparison between regularisation approaches: penalisation ($\zeta = 0.1$) compared with parametrization in H^1 ($l_{sob} = 0.1D$) across streamwise positions $\frac{x}{D} = 1$,2 and 3.

Flow topology For a better insight on the reconstructed flow fields, this section is focused on the flow structure in the wake. Figure 5.10 shows time averaged sectional streamlines at symmetry plane. Here it is noteworthy that this sectional streamlines are computed by in-plane velocity components. In each figure, streamlines predicted with default model (sub-figure (a)) is being compared with parametrization in $H^1(\Omega)$ (b), with penalisation (c) and experiments (d). To discuss the flow topology, we propose to observe two specific points. The fist is the saddle point in 5.10 for the uncorrected RANS model around ($x/D \simeq 4$,$z/D \simeq 2$). This point, at the frontier of the recirculation region, results from the interaction between the descending velocities (down-wash) and ascending velocities (up-wash). The second is the focal point around ($x/D \simeq 1.5$,$z/D \simeq 4.5$) reminiscent of a large transversewise vortex structure , connecting the two symmetric recirculation vortices visible in the horizontal plans figure 5.11. This focal point is a sign of a local depression. In the PIV plan, the saddle point is located more upstream and slightly higher in z, while the focal point is located closer to the roof-top trailing edge. Both optimised models lead to a similar behaviour. The saddle point is pulled upstream, but not enough, and lower in z instead of being raised. The focal point is crushed to the wall, while it should be clearly detached regarding the PIV.

Globally, the recirculation region is reduced, but not in a fully satisfactory way. Apparently, the pressure reduction in the leeward facade is performed in the optimisation by approaching the focal point very close to the wall, instead of more drastically reduce the overall recirculation region. This is consistent with the results shown in the wake transverse profiles.

This can be seen by sectional streamlines which are plotted at height $z/D = 3.3$ (see figure 5.12) as the flow is entrained downward out of the plane. Nevertheless, let us note that as we span downward, far enough from the high-end, such that descending motions are negligible (say at $z/D = 0.63$), both forces tend to preserve the physical features (see figure 5.11).

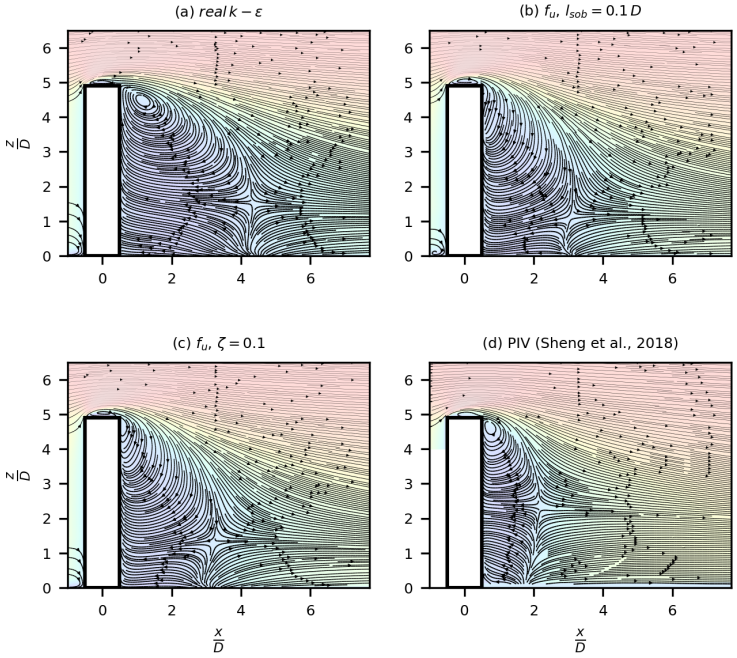

Figure 5.10 – Flow topology (2D) on symmetry plane with local deformation correction. Comparison between regularisation approaches: penalisation ($\zeta = 0.1$) compared with parametrization in H^1 ($l_{sob} = 0.1D$).

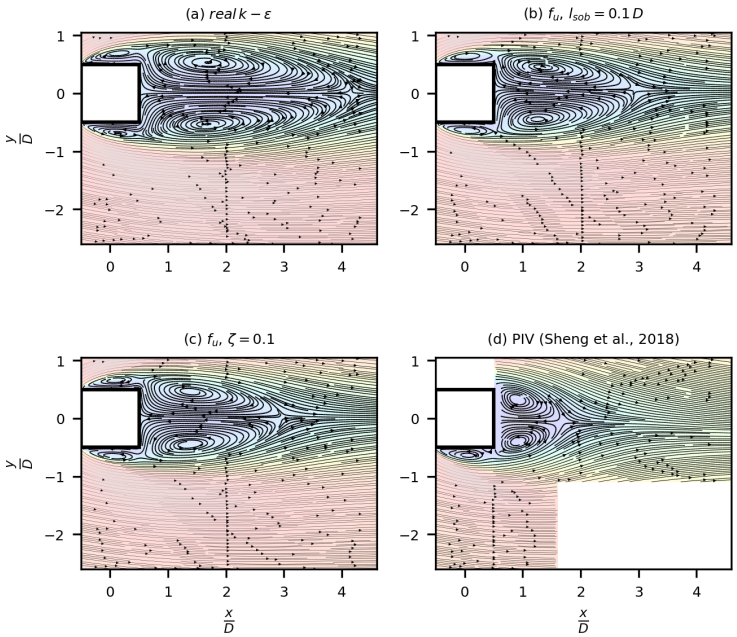

Figure 5.11 – Flow topology (2D) on horizontal plane at normalized height $z/D = 0.63$ with local deformation correction. Comparison between regularisation approaches: penalisation ($\zeta = 0.1$) compared with parametrization in H^1 ($l_{sob} = 0.1D$).

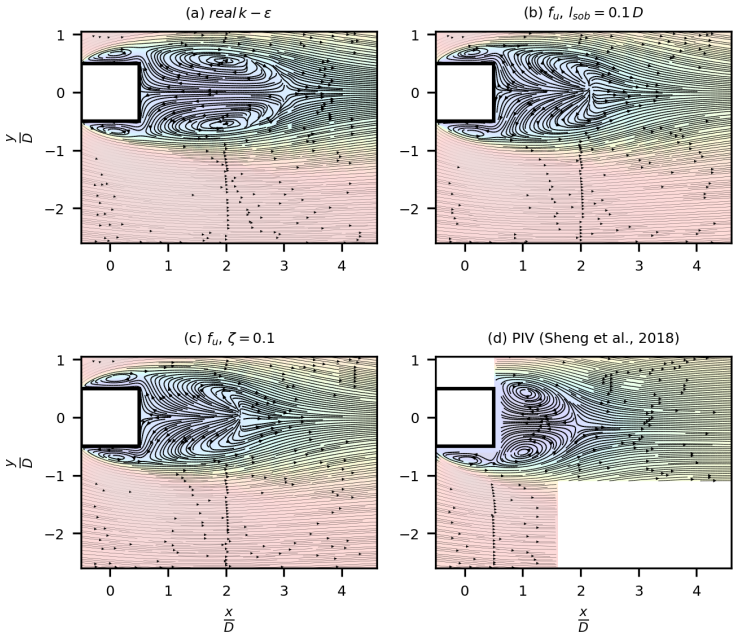

Figure 5.12 – Flow topology (2D) on horizontal plane at normalized height $z/D = 3.3$ with local deformation correction. Comparison between regularisation approaches: penalisation ($\zeta = 0.1$) compared with parametrization in H^1 ($l_{sob} = 0.1D$).

Frozen turbulence effects One of the most demanding part of the derivation of the adjoint RANS model concerns the turbulence model, partly due to the wide variety of blending functions, limiters, but mainly because of the many coupling terms to the mean-flow equations. Beside these technical details, it is very difficult to treat turbulence models in a continuous adjoint framework, as was seen through the complicated boundary conditions associated to the adjoint model. One of the common simplifying assumption (Othmer, 2008) is the frozen (or constant) eddy viscosity (CEV) in which we consider that μ_t is constant in between optimisation steps. With this assumption, the adjoint system reads as

$$-\frac{\partial U_j U_i^*}{\partial x_j} - U_j \frac{\partial U_j^*}{\partial x_i} - \frac{\partial}{\partial x_j}\left[\nu_{eff}\frac{\partial U_i^*}{\partial x_j}\right] - \frac{\partial}{\partial x_j}\left[\nu_{eff}\left(\frac{\partial U_j^*}{\partial x_i} - \frac{2}{3}\frac{\partial U_k^*}{\partial x_k}\right)\right] + \frac{\partial P^*}{\partial x_i} = 0 \quad (5.10)$$

$$\frac{\partial U_j^*}{\partial x_j} = 0 \quad (5.11)$$

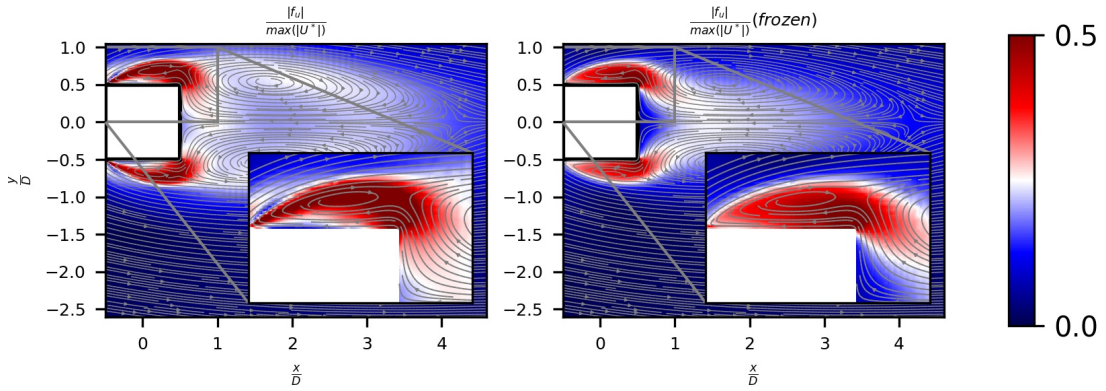

Figure 5.13 – Initial normalized magnitude of the force field in horizontal plane at normalized height $z/D = 0.63$. Comparison between full adjoint modeling and CEV assumption.

subject to the following boundary conditions:

$$P^* n_i = (U_i^* n_i)(U_i n_i) + U_j^* U_j n_i + \mu_{eff} \frac{\partial (U_j^* n_j)}{\partial x_i} n_i \quad \text{at outlet} \tag{5.12}$$

$$\mu_{eff} \frac{\partial (U_i^* t_i)}{\partial x_i} n_i + U_i^* t_i U_i n_i = 0 \quad \text{at outlet} \tag{5.13}$$

$$U_i^* n_i = \frac{\partial \mathcal{J}}{\partial P} \quad \text{at } \partial\Omega_{\text{tower}}, \tag{5.14}$$

$$U_i^* n_i = 0 \quad \text{at } \partial\Omega_{\text{gr}} \text{ and inlet}, \tag{5.15}$$

$$U_i^* t_i = 0 \quad \text{at } \partial\Omega_{\text{tower}} \cup \partial\Omega_{\text{gr}} \text{ and inlet}. \tag{5.16}$$

Albeit linear by definition, the structure of this adjoint system is very similar to the direct RANS equations. Thus, the main difference with the full adjoint model manifests on a simplified transport mechanisms. It states that adjoint informations are rather transported through only retrogade convection and isotopic diffusion.

In figures 5.13 and 5.14, sensitivity magnitude prior to the first update step, calculated using the CEV approximation is presented alongside the one issued from full derivation. It can be seen, that on the transverse plans (see figure 5.13), unlike the full adjoint model, the sensitivity under CEV assumption is more diffused inside the lateral separated flows (figure 5.13). With CEV hypothesis, the force seems to extend further downstream within the wake. Thus, it is apparent that coupling terms (between mean flow to turbulence model) does play a major role by restricting sensitivity fields to the shear layers.

Moreover, at the symmetry plane (figure 5.14) and depending on the projected flow feature, different changes have been observed. Starting with the upstream flow subject to adverse pressure gradient, we notice that the force spikes near the stagnation point ($z/D \simeq 4$), while it is absent with the CEV assumption. Thus, this highlights again the role of the coupled terms stemming from the turbulence model as it adds up to wall informations. On the other hand, we notice relatively higher sensitivity values close to the

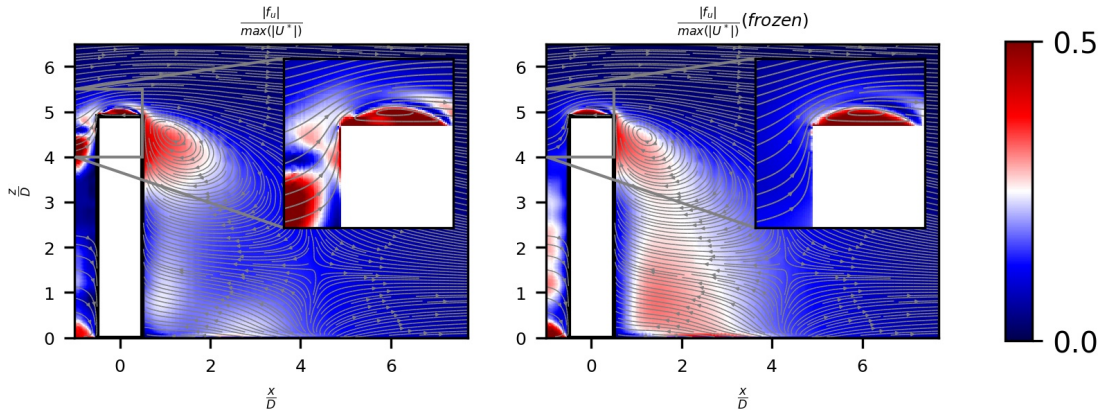

Figure 5.14 – Initial normalized magnitude of the force field in symmetry plane. Comparison between full adjoint modeling and CEV assumption.

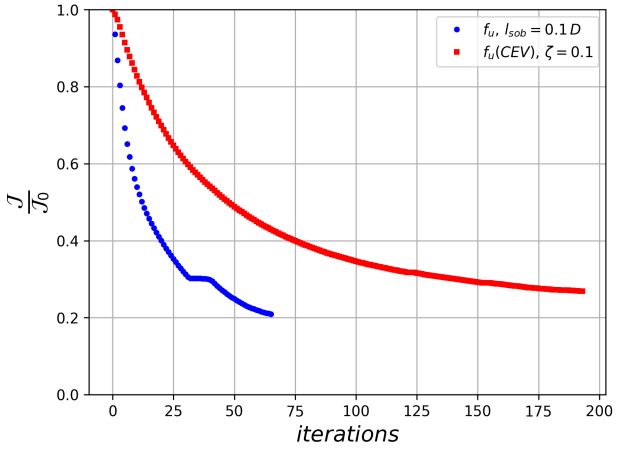

Figure 5.15 – Cost function reduction with local deformation correction (using Sobolev gradient). Comparison between full adjoint modeling and CEV assumption.

junction between the building and the ground stemming from horseshoe vortex formation.

Concerning the optimisation, it can be noticed in figure 5.15, that taking into account all coupling terms leads to a faster convergence and to a better performance. This shows the importance of relaxing the CEV assumption to obtain consistency of the gradients. Moreover, these performances are associated with very close levels of agreement with the pressure coefficients measured in the wind tunnel. Although, it should be noted that the performances are variable from one zone to another. While the pressure predicted by exact modelling fit better in recirculating areas, especially at the leeward wall, pressure predicted by approximation is slightly better along the windward facade (see figure 5.16).

With regard to the topology in the transverse plans, the same lack of physical features is found at the elevation $z/D = 1.3$ as the maximum depression is also shifted to the high-

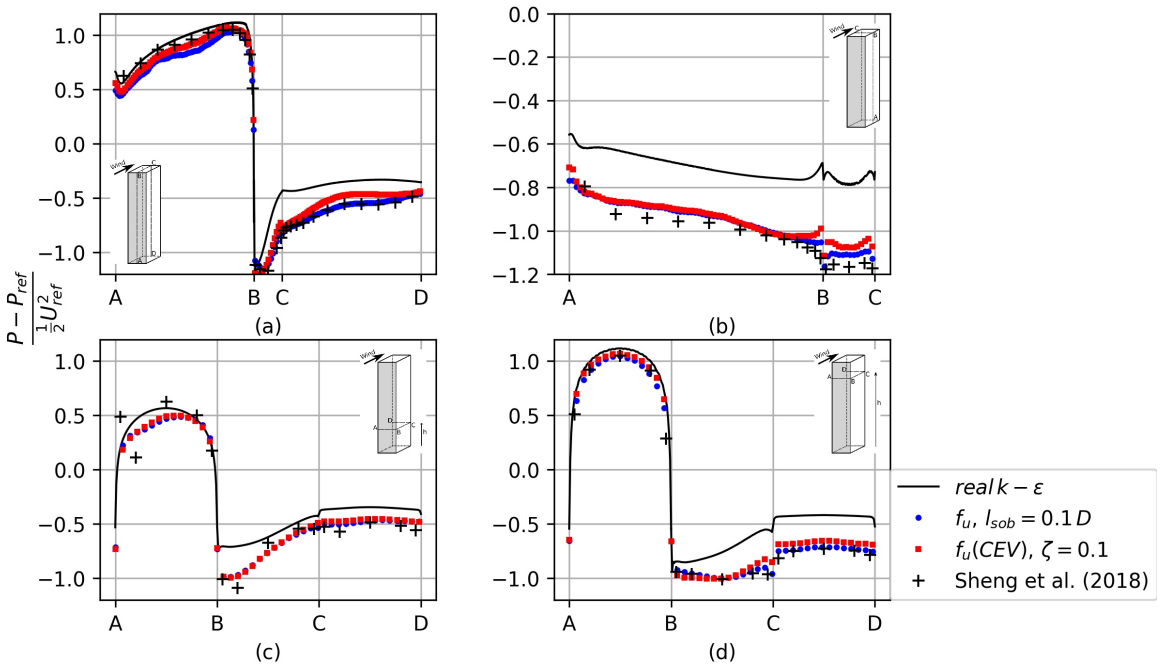

Figure 5.16 – Pressure coefficient profiles along building facades with local deformation correction (using Sobolev gradient). Comparison between full adjoint modeling and CEV assumtion.

end leeward wall. Nevertheless, we note a better agreement with PIV in term of wake flow separation as the saddle point is lifted up (figure 5.17). Thus we note again the poor flow reconstruction using non-structured force form by which sparse wall-informations are at most interpolated.

5.5 Minimal-structuring model

5.5.1 Modified equations of motion

In order to remedy the lack of structuration of a direct forcing on the momentum equation, we attempt here to refine the shape of the control parameter. Indeed, with the following approach, we aim to ensure some consistency between the deformation correction prescribed by this force and the fact that it is induced by Reynolds stress. We can restrict the corrections to the regions where the turbulence appears to be the most active and where we estimate that the turbulence model is likely to be prone to strong errors. Dealing with separated flows, a major challenge for turbulence models arises from the quantification of energy transfer toward turbulent scales in in-homogeneous and anisotropic shear layers. With anisotropy being quite poorly represented by eddy viscosity models (and the $k-\epsilon$ closure), we consider here addressing only corrections due to the flow inhomogeneity, that is, regions with a strong gradient of turbulent energy. Thus, a simple model of

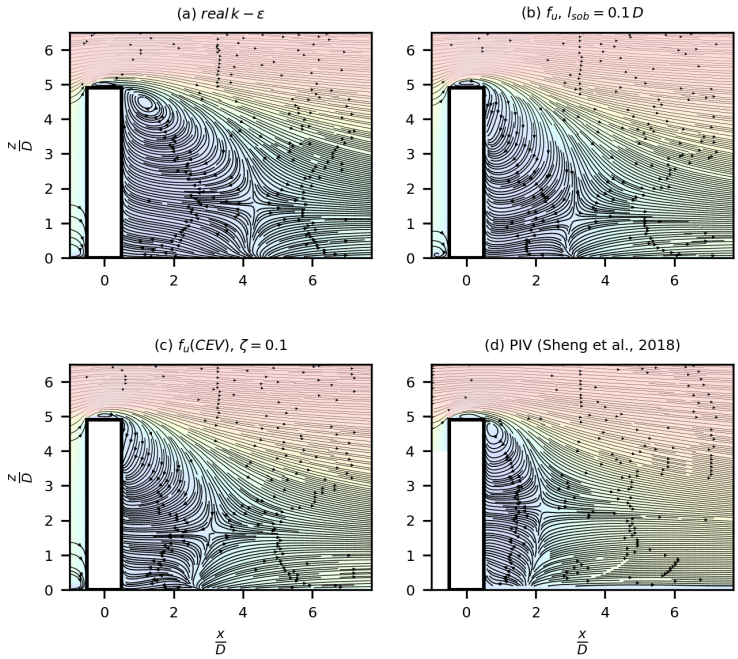

Figure 5.17 – Flow topology (2D) on symmetry plane with local deformation correction. Comparison between full adjoint modeling and CEV assumption.

structured force for direct deformation correction model reads as

$$\frac{\partial(\rho U_j U_i)}{\partial x_j} = -\frac{\partial}{\partial x_i}\left(P + \frac{2}{3}\rho k\right) + \frac{\partial}{\partial x_j}\left[\mu_{eff}\left(\frac{\partial U_i}{\partial x_j} + \frac{\partial U_j}{\partial x_i}\right)\right] - f_{u_i}|\nabla k|. \tag{5.17}$$

This choice of constraint enables to bring physical structure to the control space in a simple way.

5.5.2 Optimality condition

We note that this new force depends on the state, it requires thus a modification of the adjoint model. Considering the Lagrangian, for an arbitrary perturbation δk, an integration by part for the added term in the RHS of (5.17) results in

$$\int_\Omega f_{u_i}\frac{\partial}{\partial k}(|\nabla k|)\delta k k^* dv = -\int_\Omega \delta k \nabla\cdot\left(f_{u_i}\frac{\nabla k}{|\nabla k|}k^*\right)dv + \int_{\partial\Omega}\delta k k^* f_{u_i}\frac{\nabla k\cdot n}{|\nabla k|}ds.$$

It can be noted for physical interpretations that $\frac{\nabla k}{|\nabla k|}$ is the unitary vector aligned with turbulence inhomogeneity, and that $\nabla\cdot\left(\frac{\nabla k}{|\nabla k|}\right)$ is the curvature of isocontours of k. By using the fact that, on the one hand, the inlet profile of k is imposed and, on the other hand, its flux is zero at the other edges, the boundary integral is identically zero everywhere.

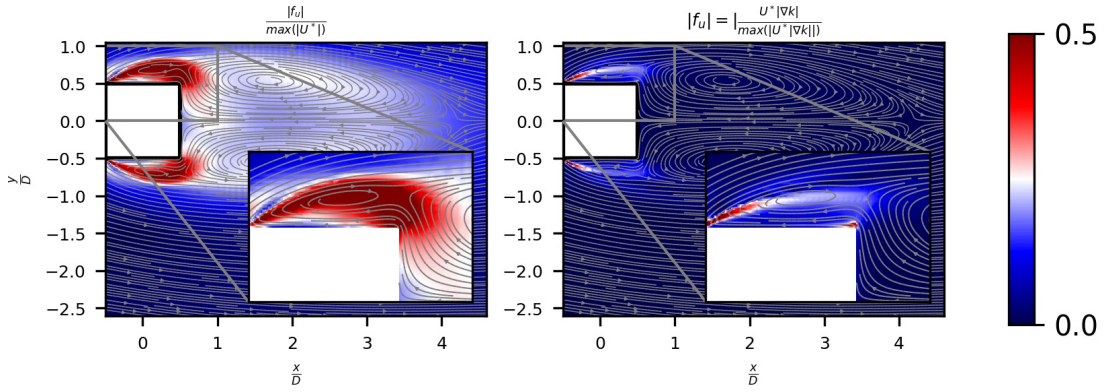

Figure 5.18 – Initial normalized magnitude of the force field in horizontal plane at normalized height $z/D = 0.63$. Comparison between raw forcing and minimal-structured forcing.

Thus, with only a volume contribution, the source term on k^* becomes

$$D_{k^*} = \rho \frac{\partial P_\epsilon}{\partial k} \epsilon^* - \rho \frac{\partial s_\epsilon}{\partial k} \epsilon^* + \nabla \cdot \left(f_{u_i} \frac{\nabla k}{|\nabla k|} k^* \right) \qquad \text{in } \Omega. \tag{5.18}$$

Moreover, by following the treatment proposed for the solid walls, on an adjacent elementary volume Ω_c centred in c, this source term can be rewritten as

$$D_{k^*} = \rho \frac{\partial P_\epsilon}{\partial k} \epsilon^* - \rho \frac{\partial s_\epsilon}{\partial k} \epsilon^* + \rho \left(\frac{\partial P_k}{\partial k}|_c - \frac{\partial \epsilon}{\partial k}|_c \right) k^*|_c + \nabla \cdot \left(f_{u_i} \frac{\nabla k}{|\nabla k|} k|_c^* \right) \qquad \text{in } \Omega_c. \tag{5.19}$$

The Gateaux derivation w.r.t. δf_{u_i}, leads to the following Lagrangian sensitivity

$$\frac{\partial \mathcal{L}}{\partial f_{u_i}} = |\nabla k| U_i^*. \tag{5.20}$$

The explicit dependency of the cost function to the parameter is omitted here and, thus, a regularization by Sobolev gradient as a regularization and descent direction.

5.5.3 Sensitivity fields

Figures 5.18 and 5.19 present the distributions of the structured control field. As expected, through additional constraint, its contribution to the momentum balance is even more restricted in space. Comparatively with the full control strategy, high sensitivity fields highlight more on regions where the local variations of turbulent kinetic energy are the most important.

In terms of peak values, as expected sensitivity is concentrated at the extension of the lateral shear on the near leading edges while low values are observed further down in the wake. Otherwise, considering the very low inhomogeneity levels of the approaching flow,

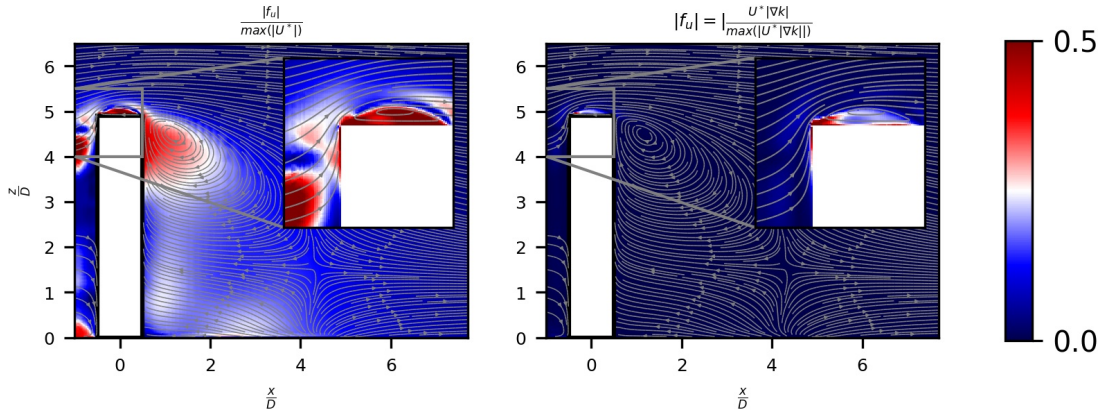

Figure 5.19 – Initial normalized magnitude of the force field in symmetry plane. Comparison between raw forcing and minimal-structured forcing.

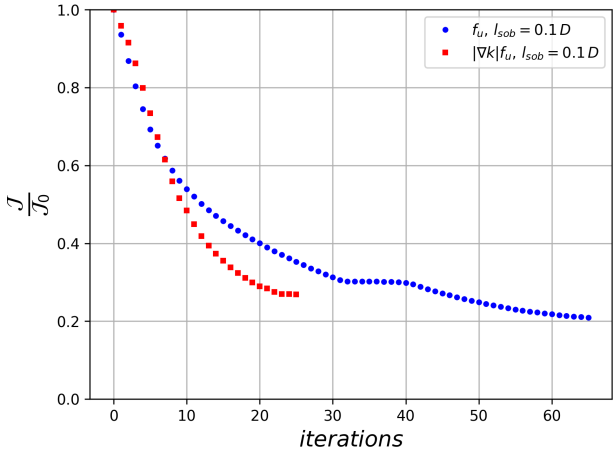

Figure 5.20 – Cost function reduction with local deformation correction. Comparison between direct forcing and minimal-structured forcing.

upstream the stagnation point, sensitivity is strongly damped.

5.5.4 Reconstructed flow

Reconstruction results using constrained force are compared with a direct forcing. We here consider only regularization using Sobolev gradient. In terms of objective, as shown in figure 5.20, globally, discrepancy with experiments has reduced significantly using structured force reaching levels closer to the structure-free force ($\mathcal{J}/\mathcal{J}_i < 0.3$). With regard to the convergence speed, the approach based on force structuration reaches its minimum in less than 30 iterations. This faster convergence suggests that adding a physical-based structure to the correction force seems to lead to a more efficient descent direction.

Results for the reconstructed pressure loads at measurement locations, using both

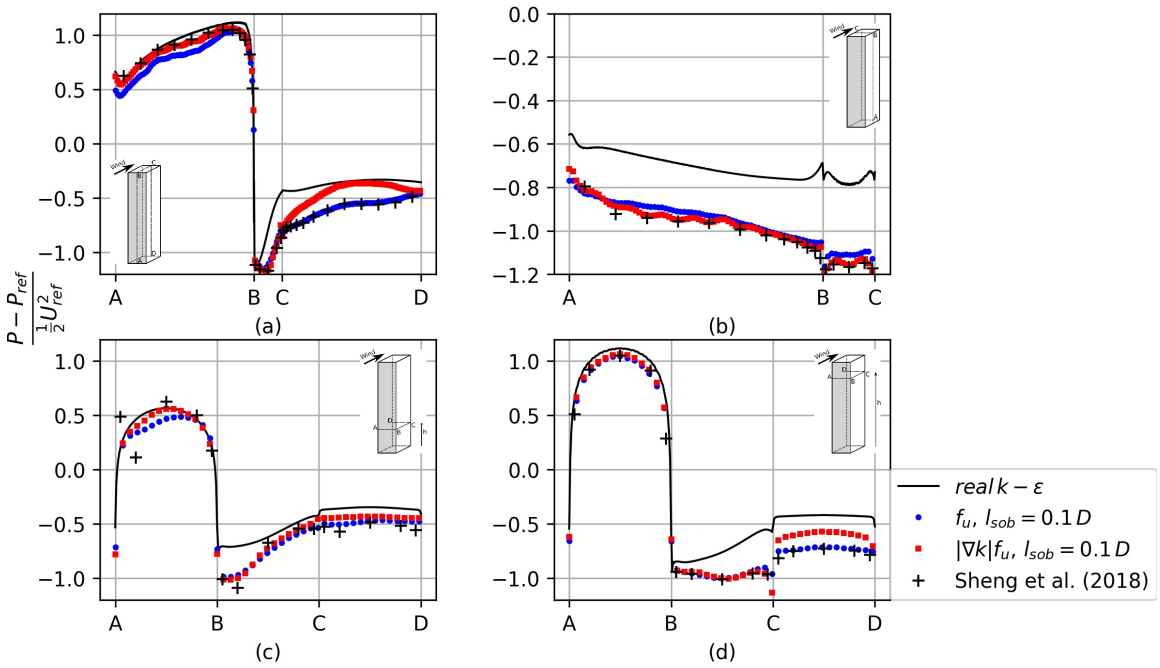

Figure 5.21 – Pressure coefficient profiles along building facades with local deformation correction (using Sobolev gradient). Comparison between direct forcing and minimal-structured forcing.

strategies, are compared with the experimental data (Sheng et al., 2018) and the default model in figure 5.21. At measurement points subject to recirculating motions, results are quite close, except the noticeable difference in the back ((d) $z/D = 1$).

Results of the streamwise velocity on the wake centreline using both strategies, are compared with data from PIV experiments (Sheng et al., 2018) and default model in figure 5.22. In term of recirculation length, both models show a considerable reduction, especially near the ground (see figure 5.22(a)). Yet, along $z/D = 3.3$, in figure 5.22(b), wake length reduction is worst compared to a direct forcing.

Results for the spanwise velocity component on the wake centreline are presented in figure 5.23. Within the up-wash, at $z/D = 0.63$ (see sub-figure 5.23(a)), structured forcing leads to noticeable improvement in the downstream region. Inversely, the direct forcing reduces significantly upward motions causing incorrect sign value inside the wake flow. In figure 5.23 (b), reconstructed velocity components is compared with data at $z/D = 3.3$ (within the down-wash motions). Predicted values using structured force stays well within the range of measured values in the downward motions. However, without structuration, the model over-corrects the downward flow yielding a rather large and more localized peak value (located at $x/D \simeq 2.25$).

Let us focus now on the study of the flow structure in the wake. Figure 5.24 shows time averaged sectional streamlines at the symmetry plane. In each figure, streamlines predicted with the uncorrected model (sub-figure (a)) is compared with structure-free

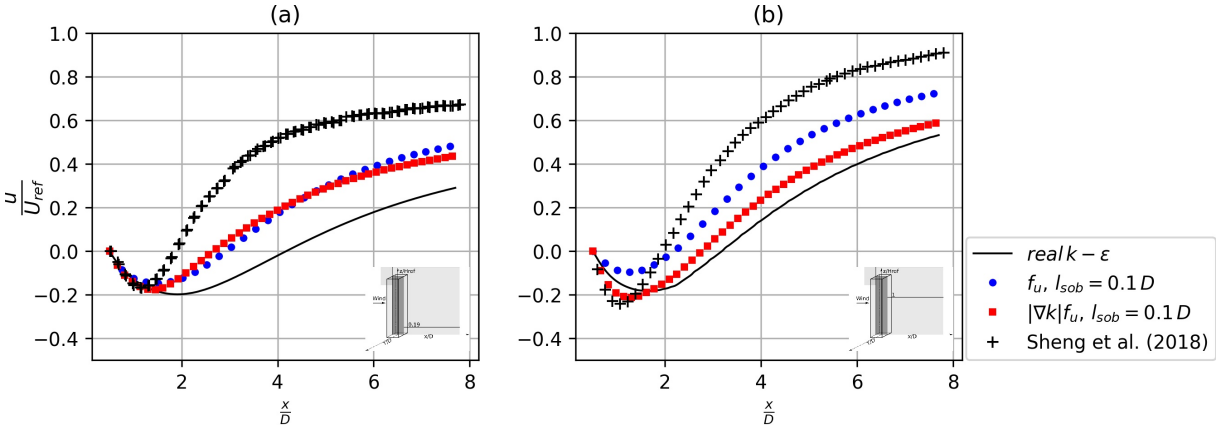

Figure 5.22 – Streamwise velocity profiles along centreline at $z/D = 0.63$ and $z/D = 3.3$ elevations with local deformation correction (using Sobolev gradient). Comparison between direct forcing and minimal-structured forcing.

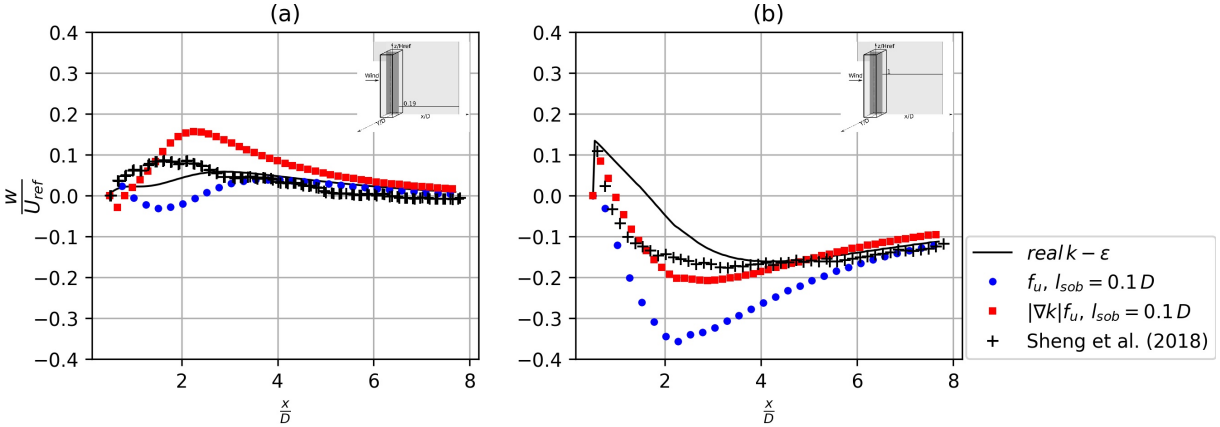

Figure 5.23 – Spanmwise velocity along centreline at $z/D = 0.63$ and $z/D = 3.3$ elevations with local deformation correction (using Sobolev gradient). Comparison between direct forcing and minimal-structured forcing.

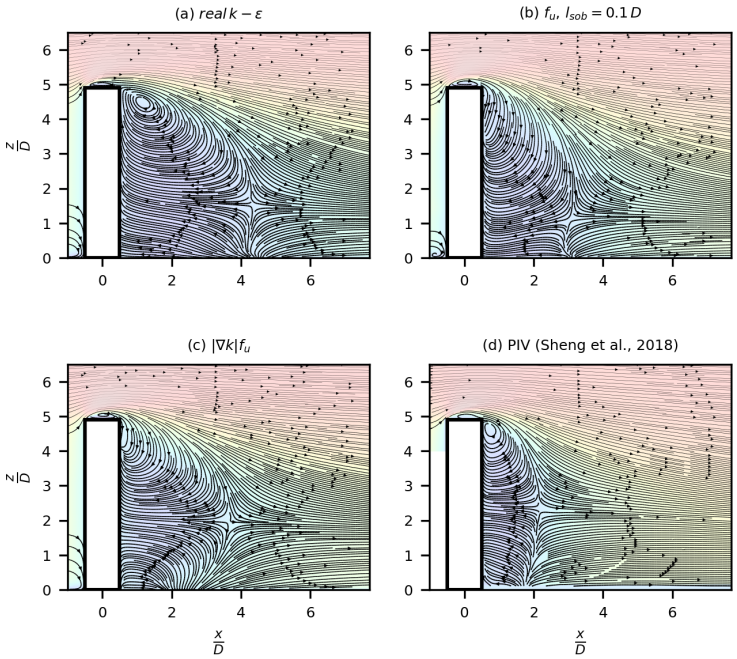

Figure 5.24 – Flow topology (2D) on symmetry plane with local deformation correction. Comparison between raw forcing and minimal-structured forcing.

optimised model (b), structured forcing (c) and experiments (d). Inspecting in particular the saddle point location, the structured forcing strategy shows a fair limitation of the down-wash flow; indeed with the saddle point being vertically centered in the wake. In the contrary, direct forcing yields to a configuration in which down-wash motions are dominant, thus, pushing the saddle point downward. Moreover, with respect to the wake's spanwise variations, results show s that the structured force approach preserves better the expected upstream inclination of the vortex rolls near the ground wall. Although, structure-free forcing gives globally a smaller recirculation bubble. Otherwise, averaged focal point (the focal of the average transverse vortex structure) resulting from the down-wash motion has been removed by the direct forcing; while, it is moved upstream in the vicinity of the leeward facade in the case of structured force optimisation. Regarding the roof top roll, both optimisation strategies show a more extended recirculation region. Yet, the flow subject to a structured force reattaches at the free-end, while, it is not the case with raw forcing.

Figures 5.25 and 5.26 shows sectional streamlines at height $z/D = 0.63$ and $z/D = 3.3$, respectively. At $z/D = 0.63$ level, both optimisation strategies fairly preserved a symmetric reverse flow. Observing the lateral reverse flow, we see that both models are in good agreement with experiments. In the wake, due to diminished recirculation length, both reconstructed reverse flow occurs closer to the cylinder in comparison to the default model. Indeed, wake focal points have moved slightly upstream and closer to the symmetry plane. These changes are more pronounced with the structured forcing through an

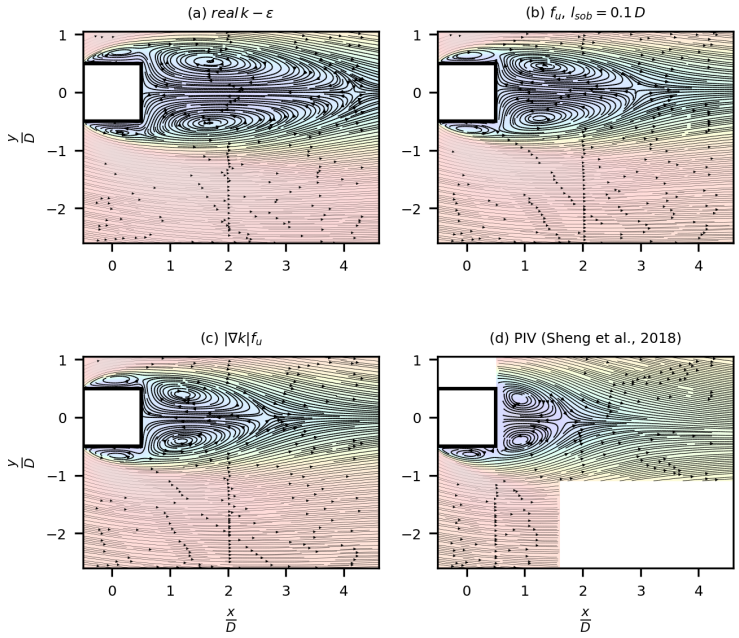

Figure 5.25 – Flow topology (2D) on horizontal plane at normalized height $z/D = 0.63$ with local deformation correction. Comparison between raw forcing and minimal-structured forcing.

upstream inclination of the vortex. However, at $z/D = 3.3$, the transverse topology of the reconstructed flows for both forms show disagreement with the experiments. Even if the lateral reverse structures are fairly preserved, wake vortices are not properly reconstructed. This flow distortion is more pronounced with the (unstructured) raw forcing strategy. In fact, with the structured force, we observe that reverse wake flow is fairly entrained around a spanwise vortex moved downstream. However, with no focal point, fluid is rather entrained with a spanwise motion out of the symmetry plane.

The structured-forcing strategy allows to strongly restrict the potential sources of mismatch of the modelled Reynolds stresses to a thin region within the shear layers. The fact that it accelerates the optimisation with comparable performances (even leading to an imperfect reconstruction) suggests that these regions corresponds to key regions for the turbulence model. It encourage a refining strategy of the control parameters structure.

In the next chapter 6 we will go one step further to shape this correction in relying more efficiently on the turbulence model structure. In contrast to the calibration of the model closure coefficients (in the previous chapter), we will address the modelling errors at different closure levels, i.e. starting from the eddy constitutive relation and going into each of the modeled terms of the chosen turbulence model. Then, after discussing the different offered possibilities to embed a control parameter, enforcing the robustness of the DA procedure, we will propose some forms for the parameter which ensure both robustness together with a better recovery of the flow features.

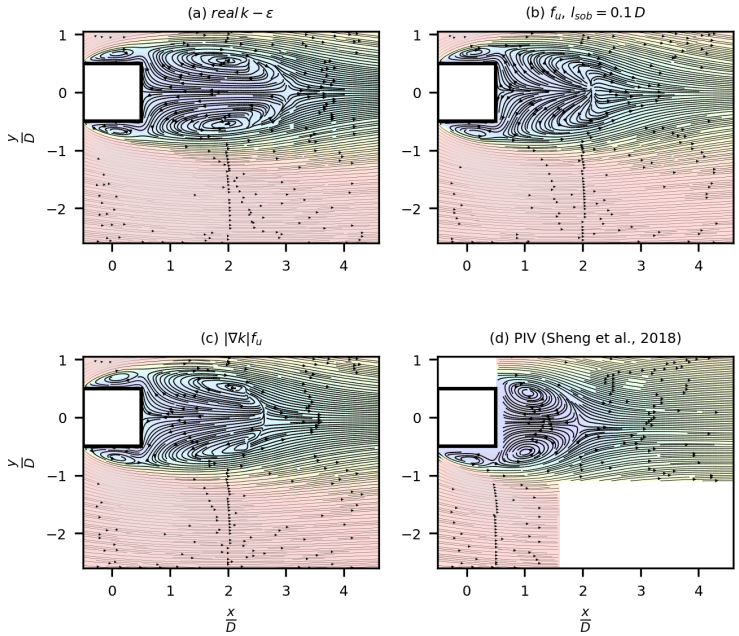

Figure 5.26 – Flow topology (2D) on horizontal plane at normalized height $z/D = 3.3$ with local deformation correction. Comparison between raw forcing and minimal-structured forcing.

5.6 Conclusions

The data assimilation framework developed in the chapter 3 was explored here for the purpose of flow reconstruction. To recover the mean flow from the pressure measurements, an unknown spatially distributed forcing is added to the momentum equation in order to infer correction to the Reynolds induced force. Without a priori knowledge of its nature, an initial raw form was considered similar to works by (Foures et al., 2014; Franceschini and Sipp, 2020). A sensitivity map analysis, before a first parameter update, reveals high interest of optimising the force at several regions encompassing several characteristic flow features; the upstream flow impingement (including upstream separation and horseshoe formation), the lateral and top shear layers, and the wake.

To reduce the risks of local minima and unphysical solutions, given the strongly partial observations and the consideration of spatially distributed control parameters, we proposed the examination of two regularization approaches. In the one hand, we considered augmenting the cost function by a penalty of spatial gradients of the control parameter. In the other hand, by the definition of an alternative inner product $H^1(\Omega)$, we considered searching for the control parameter in the Sobolev space (Protas et al., 2004; Tissot et al., 2020).

Regarding the regularisation, a comparison of the cost reduction results with the penalisation approach showed that using Sobolev gradient yields a much faster convergence and lower discrepancy levels. Regarding the reconstruction ability, compared with coeffi-

cient calibration, the corrective deformation model produced an excellent agreement with the wall-pressure experiments in most of the building's wall regions. We note that using the common assumption of constant eddy viscosity (CEV), on the derivation of the adjoint model, shows that taking into account all coupling terms led to a faster convergence and to a better performance. This confirmed the importance of relaxing the CEV assumption to obtain consistency of the gradients.

With regards to the recirculation length, model results show a considerable reduction of its downstream extension, yet, not in a fully satisfactory way. Apparently, the pressure reduction in the back facade is performed in the optimisation by approaching the focal point very close to the wall, instead of drastically reducing the overall recirculation region. This have resulted in a poor reconstruction quality of the near wake flow by producing non-physical-features. This recalled the lack of structuration to the raw forcing.

In order to remedy this situation, we have attempted refining the shape of the control parameter with the aim to ensure some consistency between the deformation correction prescribed by this force and a Reynolds stresses induced force. With anisotropy being quite poorly represented by eddy viscosity models (and the $k - \epsilon$ closure), we consider here addressing only corrections to the flow inhomogeneity, that is, regions with a strong gradient of turbulent energy. Indeed, parameter sensitivity selects drastically the potential sources of mismatch in the modelled Reynolds stresses to a thin region within the shear layers., i.e. the extension of the lateral shear of the separated flow from the leading edges. Meanwhile, it shows fewer interest further downstream in the wake.

In terms of objective, globally, discrepancy with wall-pressure experiments has reduced significantly reaching levels closer to the raw force. With regard to the convergence speed, structuring the force leads to a faster convergence. Moreover, with respect to the flow reconstruction, results with a structured force preserves better the expected wake's features, e.g. upstream inclination of the vortex rolls near the ground wall. Although, raw forcing gives globally a smaller recirculation bubble. The fact that it accelerates the optimisation with comparable performances (even leading to an imperfect reconstruction) suggests that these located regions are mainly responsible of the RANS failure. It encourages the strategy of refining the structure of the control parameters.

Chapter 6

DATA-ASSIMILATION FOR STRUCTURED CORRECTIONS THROUGH TURBULENCE MODELLING

6.1 Introduction

In this chapter, flow reconstruction is operated under a parametrization that satisfies physical constraints given by the turbulence model. In contrast to a direct forcing on the mean deformation field (examined in the chapter 5), corrections of the mean flow are instead given under the Boussinesq hypothesis, thus assuming that the Reynolds stresses are proportional to the deformation tensor. In other words, discrepancy-corrective parameters are embedded into the turbulence model equations rather than at the level of the momentum equations, and their effects on the mean flow are constrained to be a diffusive term by the specified relationship between stress and strain. Hence, since the reconstructed solutions are sought in the space of admissible solutions by a RANS model, we believe that it has the advantage of producing physically acceptable solutions. Indeed, this space is induced by the physical principles sustaining the definition of the turbulence model. This intuition is supported by the work of Singh and Duraisamy (2016); Franceschini and Sipp (2020). In their DA studies in canonical flows under the Boussinesq assumption, they reported that applying corrections in the transport equations of the eddy-viscosity in Spalart-Allmaras model Spalart and Allmaras (1992), or in the production of turbulent energy in Wilcox $k-\omega$ model Wilcox (1993), may be advantaged whenever sparse informations are considered, such as partial velocity field or wall-pressure and wall-friction. In addition, in the work of Singh and Duraisamy (2016), authors reported that, given few data inputs (such as wall-pressure and skin-friction), a complete set of realizations of the closure model was obtained. With this result in mind, we hope that given the sparse wall-pressure measurements in the building configuration, the reconstructed flow by correcting the turbulence model would keep most of the physical features and complexity of the real flow.

This chapter is organized as follows. First (section 6.2), we will start by addressing the possible errors of the model structure resulting from the choice of the eddy-viscosity and the realizable $k-\epsilon$ models. Comments will be given on the various possible corrections at each level of the closure vis-a-vis the robustness of the DA procedure. Conclusions will be valid only for the presented flow configuration, but we believe that practices can be

generalised to some extent to other aerodynamic studies. Then, in the light of these examinations (section 6.3), we will introduce corrective models with new spatially distributed forms of closure. Thus, in contrast with the rigid approach by calibration of global closure coefficients (examined in chapter 4), we attempt to address more efficiently the closure problem. Later on section 6.4, we introduce the changes to be made to the adjoint models and on the optimality conditions. In section 6.5, after an initial sensitivity analysis, we will present the data-assimilation results by comparing reconstructed flows obtained with the proposed corrective models. Finally, in an attempt for a more efficient reconstruction, a modified model that embeds a deformation corrective parameter in conjunction with turbulence closure adjustment is investigated in section 6.5.

6.2 The choice of the parameter

Assumptions are introduced in several stages whilst constructing a Reynolds-averaged model. These multi-layer simplifications start from applying the time (or ensemble) averaging operator to the non-linear advection term. This makes appear the Reynolds stress tensor, and the first assumption consists in relating this tensor to the mean flow through an eddy viscosity. This eddy viscosity is determined by an algebraic equation involving turbulence variables that are statistical quantities governed by transport equations. The choice of these variables defines the class of considered turbulence model. Let us recall that, considering a transport by the mean velocity, a diffusion mechanism, and through scaling analysis (often related to the role of the mean strain in vortex stretching), source/sink terms are often included with a set of coefficients that must be calibrated to represent some known flow features, as in the data-driven process presented in chapter 4. This constitutes a second layer of approximation. In the present section, we first address the closure uncertainties at the first layer, i.e. the linear eddy viscosity model. Then, we will consider the second layer in which a specific model structure is invoked: the realizable $k-\epsilon$ model.

6.2.1 Parametrising the Reynolds stress modelling

In the first layer, it is a question of defining a constitutive relation, which relates the Reynolds stress to the strain, function of the mean velocity gradients. This relation, by analogy with Newtonian behaviour of molecular viscosity, is usually considered as

$$\rho\overline{\mathbf{u}\otimes\mathbf{u}} = -2\mu_t\left(\mathbf{S}\right) + \frac{2}{3}\mathbf{I}\rho k,$$

where $\mathbf{S}$ is the strain tensor (symmetric part of the mean velocity gradient). The commonly denoted turbulent viscosity μ_t is a scaling factor. This factor, assumed to depend on the local turbulent agitations, is then expressed as a function of quantities considered to characterize the turbulence (e.g., turbulence length scales, turbulent energy, and energy dissipation rate).

The validity of this modelling of the Reynolds stresses for turbulent flows were questioned by many authors Shih and Lumley (1993); Pope (1975); Schmitt (2007), and a brief historical remark can be found inSchmitt (2007). Nevertheless, as being acceded by Shih and Lumley (1993), a more general constitutive relation for turbulent stress $\overline{\mathbf{u} \otimes \mathbf{u}}$ can be possibly derived at condition that turbulence length and time scales are smaller than those of the mean flow. However, as in our situation, the turbulence scales(stemming from atmospheric boundary layer) are of the same order of magnitude as those of the mean aerodynamic flow. The validity of such approximations is not *a priori* guaranteed. As proposed by Lumley Lumley and McMichael (1995), a formal procedure of deriving more general constitutive relations may includes two steps. Through dimensional analysis (π theorem), the first step is to assume the relationship between the unresolved turbulent correlation and some reduced number of resolved statistics. In the second step, using the invariant theory, various forms of the relationship can be derived. In brief, using generalized Cayley-Hamilton formulas, that relates matrices of higher extension [1] to matrices of lower extension Spencer and Rivlin (1959), the most important procedure is to determine the number of tensor's independent invariants, such as the trace or the determinant.

Therefore, when applied to the modelling of the Reynolds stress matrix, using the assumption that it is only dependent on the mean velocity gradients (and not only its strain $\mathbf{S}$) and the characteristic turbulence statistics (say k and ϵ), this is shown to provide full information of the mean flow while respecting the symmetric nature of the stress tensor, i.e. combinations of matrix product between the mean rotation $\mathbf{\Omega}$ and the mean strain part $\mathbf{\Omega}$ weighted by matrix invariants and calibrated coefficients Shih et al. (1995).

If embedded in a data-driven process, this generalised constitutive relation would offer more degrees of freedom of the control parameter. Under this framework, we interpret the polynomial expansion physically as a progressive loosening of the Boussinesq's hypothesis, as one may truncate at any order. The second order Reynolds stress algebraic relationship, proposed by Shih et al. (1995), can be considered along with the realizable $k-\epsilon$ turbulence model:

$$\rho\overline{\mathbf{u} \otimes \mathbf{u}} = -2\mu_t\left(\mathbf{S}\right) + \frac{2}{3}\mathbf{I}\rho k + 2C_2\frac{k^3}{\epsilon^2}(-\mathbf{S\Omega} + \mathbf{\Omega S}). \tag{6.1}$$

In the present work, the algebraic relationship was implemented. However, sever numerical instabilities were encountered. In fact, after few iterations, the RANS budgets were hardly satisfied, especially while imposing the incompressibility condition. This caused the RANS solution to diverge rapidly. Although some attempts for more relaxations along the iterative SIMPLE step and the asymptotic pre-treatments that avoid evaluating function outside the domain of their arguments, this behavior is persistent, and no solution could be found at the first iteration of the data assimilation procedure. In fact, we think that this is mostly due to the relatively high turbulence level and momentum of the atmospheric boundary layer and relatively high shear, since $\frac{Sk}{\epsilon} \gg \mathcal{O}(1)$ at the separations at the building sharp angles. This presents challenges for the realizability constraints, i.e.

1. For a given matrices A and B, the matrix product A^nB^m with $n, m \in \mathbb{N}$ leads to the $p = n+m \in \mathbb{N}$ polynomial extension

$\overline{u_i^2} > 0$ and $\frac{\overline{u_i u_j}^2}{\overline{u_i^2 u_j^2}} \leq 1$, to be verified. Nevertheless, we believe that with intermediate levels of shear, such a model may be token as a key entrance for flow reconstructions under a loose relaxation of the Boussinesq hypothesis. In fact, we do expect that the structure of the force induced by the Reynolds stresses would correspond to an intermediate between an added direct forcing on the deformation and the default predicted one relying on the Boussinesq assumption. However, in the present work, no further investigation has proceeded along this strategy. Therefore in what follows, we choose to maintain the Boussinesq approximation and, hence, structural errors [2] will be all addressed to the last layer of closure. Thereafter, we will refer to uncertainties underlying the closure terms in the transport equations of the turbulence variables k and ϵ.

6.2.2 Parametrising the turbulence variables transport equations

Similar to Singh and Duraisamy (2016); Franceschini and Sipp (2020), functional errors arising from the modelled transport of the turbulence quantities are targeted. Before proceeding with the turbulence model chosen in this thesis, we recall the generic structure of the turbulence equation, and we present the possible ways of correction. In a general manner, turbulence variables (*e.g.* k, ϵ) would have to respect a balance equation of the form

$$0 = T_{mean} + T_{turb} + T_{vis} + P - D$$

in which T_{mean}, T_{turb} and T_{vis} are their spatial redistribution by the mean flow, by fluctuations, and through viscous diffusion, respectively. P stands for production and D for sink. Hence, possible corrections on their balance could be interpreted either as "punctual" sources (or sinks) adjustments, as well as "fluxes" balancing effects (*e.g* convective or diffusion fluxes). However, in practice, depending on the specific mechanisms we are addressing, some corrections might not be admissible. As a matter of fact, this is related to the degree of regularity in space that might have the modelled term once discretized. While irregularities are fairly treated in common turbulence models, due to well-balanced mechanisms that ensure, for instance, enough diffusion, treatment may, however, not hold when the turbulence budgets are "strongly" guided by data. That is per saying, given a noticeable deviation from data, what we may call "term-by-term" adjustment might involve undesirable behaviors causing the budget to be strongly biased by the corrections and may affects the conditioning of the matrices. In the next section, functional errors will be investigated to the realizable $k - \epsilon$ model under our flow configurations. Hence, model corrective parameters will be proposed.

2. By structural errors, we refer to the uncertainties in the structure of the model, at any layer of approximation.

6.3 Corrective models for turbulent statistics budget

In the present work, various attempts for a term-by-term correction have been tested. Only spatially distributed additive parameters are considered in this work, allowing to maintain good conditioning of the adjoint system during the optimisation procedure. Before introducing these new variables, some comments can be made on the issues encountered in identification of the term-by-term error and correction. Let the exact transport equation of the turbulent kinetic energy for a homogeneous turbulence Pope (2000) be,

$$\underset{\mathbf{I}}{\nabla \cdot (\mathbf{U}\, k)} = \underset{\mathbf{II}}{-\nabla \cdot \overline{\mathbf{u}' \left(\frac{p'}{\rho} + k \right)}} \underset{\mathbf{III}}{- \overline{\mathbf{u}' \otimes \mathbf{u}'} \cdot \nabla \mathbf{U}} \underset{\mathbf{IV}}{+ \nu \Delta k} \underset{\mathbf{V}}{- \nu \overline{\nabla \mathbf{u}' \cdot \nabla \mathbf{u}'}}.$$

It turns out that most of the terms in the turbulence model (except **I** and **IV**) are modeled. Hence, one may straightforwardly address corrections to these uncertain terms.

Regarding the redistributions mechanisms (**II** and **IV**), exact terms are modeled by a simpler diffusive transport, i.e $\nabla \cdot \left((\nu + \frac{\nu_t}{\sigma_k}) \nabla k \right)$. An explicit correction case consists of multiplying by a pre-factor the effective diffusivity into the divergence, as $(1 + f_k)(\nu + \frac{\nu_t}{\sigma_k})$. Thus, guided by the data, one may expect some adjustment to how the energy is redistributed. Proceeding for correction have led to a highly non-robust procedure, in particular for the resolution of k^*. An explanation of this lack of robustness is that f_k is free to change sign, as a consequence a negative value can reduce strongly the diagonal dominance of the matrices solved for k^* and then the conditioning. This issue concerns the adjoint model more than the direct RANS model; this might points out the poor conditioning of the adjoint matrices. This observation is consistent with the results of chapter 4, with the optimisation of σ_k coefficient, in which the robustness was conditioned by the scaling of the turbulent energy mixing. Indeed, $\sigma_k = 1$ improved robustness compared to higher values.

Further attempt on the correction of the modeled production (**III**) term has led to similar undesirable behavior. Aside from numerical issue encountered with the adjoint system, this choice raised some concerns with the treatment at the wall region denoted Ω_w. Such a correction choice seems to violate the modelled physics in the logarithmic sub-layer. By only correcting the turbulence production, the inertial equilibrium, i.e $P_k - \epsilon = f_k P_k \neq 0$ in Ω_w, is no more represented and does not provide a physical constraint to the turbulence model in the bulk. With regards to the adjoint field k^*, positive deviations from the equilibrium (i.e $f_k P_k > 0$) would translate to a very localized source term in the adjoint equation. In that situation, diffusion is not strong enough by itself compared to the adjoint production to redistribute k^*. We believe however that additional spatially distributed information on turbulence, *e.g* velocity fluctuations, would help to balance these local peaks. Nevertheless, the measure of this kind of quantity would require sophisticated experimental apparatus (such us PIV measurements) making flow reconstruction

impractical from a wind engineering perspective. Summing up, such a correction choice might indeed be discarded in urban full-scale studies in which flow cannot be solved until the viscous sublayer.

This would leave one last term in which the errors can be addressed, that is, the modeled dissipation rate term (**V**). In this case, a similar issue is indeed encountered regarding the inertial equilibrium constraint near the wall. Hence, to overcome this issue, we might come up with two possible corrective solutions. On the one hand, we propose an additional corrective term that balances the budget of the turbulent kinetic energy. The whole balance between all terms is corrected with this choice, and we safely impose the equilibrium within the inertial sublayer. Moreover, with the data, we hopefully reconstruct a smooth and continuous parameter field in Ω . We can assume either that f_k is an additive term without any particular structure, or that it is an explicit function of k. As proposed in chapter 5, a parameter constrained by the state variable would damp unphysical behaviours compared to a direct additive term. Without loss of generality, expressing it as a linear function of k ensures both consistency of the correction field vis-a-vis turbulence model structure and, hence, the robustness of the DA procedure. This dependency actually adds some (minimalistic) physical structuration to the added parameter as we expressed as a function of the state variable. Thus, a model of correction to the turbulent kinetic energy transport may read

$$\frac{\partial \rho U_j k}{\partial x_j} - \frac{\partial}{\partial x_j}\left[\left(\mu + \frac{\mu_t}{\sigma_k}\right)\frac{\partial k}{\partial x_i}\right] - \mu_t\left(\frac{\partial U_i}{\partial x_j} + \frac{\partial U_j}{\partial x_i}\right)\frac{\partial U_i}{\partial x_j} + \rho\epsilon = -f_k k. \tag{6.2}$$

The basic idea is to state that corrections of the transport of k are due to the turbulence and thus, we reject unphysical corrections in regions with no turbulent kinetic energy.

On the other hand, concerning the dissipation rate **V**, it is modelled by ϵ the solution of a dedicated transport equation. In order to correct it, one can consider an additive corrective term on this equation. A corrective model on the dissipation rate budget may read as

$$\frac{\partial \rho U_j \epsilon}{\partial x_j} - \frac{\partial}{\partial x_j}\left[\left(\mu + \frac{\mu_t}{\sigma_\epsilon}\right)\frac{\partial \epsilon}{\partial x_i}\right] - C_1(S,k,\epsilon)S\epsilon + C_2\frac{\epsilon^2}{k+\sqrt{\mu\epsilon}} = -f_\epsilon \epsilon, \tag{6.3}$$

Like the energy transport equation, we choose an additive term offering both robustness and some physical structuration through premultiplication by the variable ϵ. In fact, it can be understood that this alternative model might allow a more structured representation to the uncertainty underling the term (**V**) in the k budget. Corrections brought to the energy dissipation rate budget in (6.3) are, first, redistributed before to being taken into account in the kinetic energy budget model.

Given these two possibilities, it can be seen that a direct correction of the kinetic energy budget would target both modeled energy input (from mean-shear by **III**) and energy output (or dissipation by **V**). The effect would be similar to the correction through the transport of eddy-viscosity in a model such as Spalart and Allmaras (1992), constituted

by one closure equation, in the work by Franceschini and Sipp (2020). However, having in hand what we call a two-equation model, structural errors is indeed targeted only at the level of the kinetic energy output.

6.4 Sensitivities estimation

6.4.1 Adjoint models

The fact that, in both proposed models, additive terms are dependent on the state variables, some modifications of the adjoint model are required. Yet, due to the linear dependency of the source term on the state variable, the additional adjoint term is similar to the term in the direct equations. Thus, in the case of a direct turbulent energy budget correction, the adjoint equation on k^* reads, in compact form, as

$$M_{k^*} = -f_k k^*, \tag{6.4}$$

where M_{k^*} is the adjoint turbulent kinetic equation derived from the original model (see derivation in chapter 3). The minus sign on the right hand side is chosen only for convenience, since it enables straightforward interpretation of the additive term as an energy sink. Similarly, with the alternative correction model, the adjoint equation on ϵ^* is introduced as

$$M_{\epsilon^*} = -f_\epsilon \epsilon^*, \tag{6.5}$$

for which M_{ϵ^*} is the default adjoint equation for ϵ. With regards to the adjoint boundary conditions, since no flux are involved through the boundaries, no changes have to be performed here. Hence, the same boundary conditions, derived from the original model, is applied.

6.4.2 Optimality conditions and descent direction

Model correction for k budget Augmenting the cost by (6.4) and assuming no explicit dependency of the cost to the parameter f_k, directional derivative of the Lagrangian w.r.t. infinitesimal variations δf_k leads to

$$\left\langle \frac{\partial \mathcal{L}}{\partial f_k}, \delta f_k \right\rangle_\Omega = \langle k \delta f_k, k^* \rangle_\Omega \,,$$

leading straightforwardly to express Lagrangian sensitivity to f_k as

$$\frac{\partial \mathcal{L}}{\partial f_k} = k k^*. \tag{6.6}$$

Model correction for ϵ budget Similarly, the Lagrangian sensitivity to the parameter f_ϵ reads

$$\frac{\partial \mathcal{L}}{\partial f_\epsilon} = \epsilon\epsilon^*. \tag{6.7}$$

Regularization Here the explicit dependency of the cost function to both parameter cases is omitted. For its remarkable improvement to the steepest descent algorithm (addressed in chapter 5), sensitivity fields are first projected onto the Sobolev space, i.e. providing an alternative inner product than L^2, in order to provide the descent directions and a regularization. Hence, the optimality condition with Sobolev gradient can be determined by solving the following Helmholtz equation

$$\frac{\partial \mathcal{L}}{\partial \beta}^{H_1} = \left(\frac{1}{1+l_{sob}^2}(\mathbf{I} - l_{sob}^2\Delta)\right)^{-1} \frac{\partial \mathcal{L}}{\partial \beta} \qquad \text{for} \qquad \beta = f_k \, or \, f_\epsilon,$$

in which the characteristic length scale l_{sob}, i.e. the filtering size, is chosen to smooth non-physical small scales.

6.5 Results

This section is dedicated to the results related to the investigation of the adjunction on the realizable $k-\epsilon$ model of a distributed control parameter. First, we analyse parameter sensitivity fields given by each of the two models, which corresponds to the first iteration step of the data assimilation procedure, i.e. the gradient of the cost functional with respect to the distributed control parameters for $f_k = f_\epsilon = 0$. Qualitative comparisons with an additive forcing independent of the state variable are presented on the three planes (two horizontal planes at $z/D = 3.33, 0, 63$ and the symmetry plane). Then, the data-assimilation results are analysed.

6.5.1 Sensitivity fields

.

Structured control for k budget correction We analyse the sensitivity fields to highlight the spatial locations where the transport equation of k requires a structural correction. A quantitative validation is first performed to check the numerical consistency of these sensitivity fields. As in the previous chapters, the computed sensitivities are integrated into a volume of interest that surrounds the regions where sensitivities are the most important to account for, *e.g.* the building and the wake region. We choose the same volume of interest as before (centered around the building and of size $2.5H \times 4H \times 1.5H$) in which we perform the cell-volume weighted sum. This sum is then compared with

	$\frac{\partial \mathcal{J}}{\partial f_k}(\times 10^8)$
AD	7.06
FD ($\delta f_k = 10^{-2}$)	12.89
FD ($\delta f_k = 10^{-3}$)	9.87
FD ($\delta f_k = 10^{-4}$)	9.56
FD ($\delta f_k = 10^{-5}$)	9.56

Table 6.1 – Sensitivity derivative w.r.t. f_k computed from the proposed adjoint model (AD) and the finite difference (FD) with different perturbation sizes.

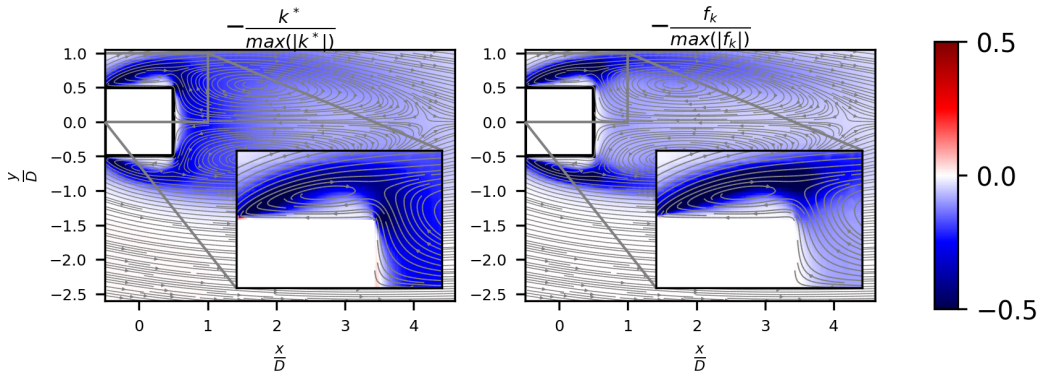

Figure 6.1 – Adjoint turbulence kinetic and the constrained control at horizontal plane with normalized height $z/D = 0.63$. Variables are normalized by their in-plan peak values.

the finite differences on the cost value for various uniform step sizes δf_k, as shown in table 6.1. The comparison shows that the adjoint based sensitivities become close to the finite differences values as the step size decreases and converges to error levels of the continuous adjoint method (Othmer, 2008; Zymaris et al., 2010).

Figures 6.1, 6.2 and 6.3 compare the sensitivity maps for the added control parameter against a direct forcing, which corresponds to the adjoint variable on k^*. Let us recall that the effect of pre-multiplication is to reject regions of high sensitivity but with less relevance for turbulence modeling. For instance, in contrast with very diffused sensitivity maps for the direct forcing, we note a tendency to bring significant adjustments starting from the leading edges and progressing within the lateral shear layers, and more downstream in the edges of the wake region. More specifically, constrained sensitivity maps show peaks of interest in both shear layers from leading edges to the saddle point near the opposite edge of the building around $z/D = 0.63$.

Moreover, let us note that the multiplication of the corrective source by the variable k has damped sensitivities at regions where actually both production and dissipation terms should contribute very slightly in the energy budget. This can be seen in figure 6.4 at the high peaks of sensitivity observed around the wake centerline for the direct forcing visible in figure 6.1.

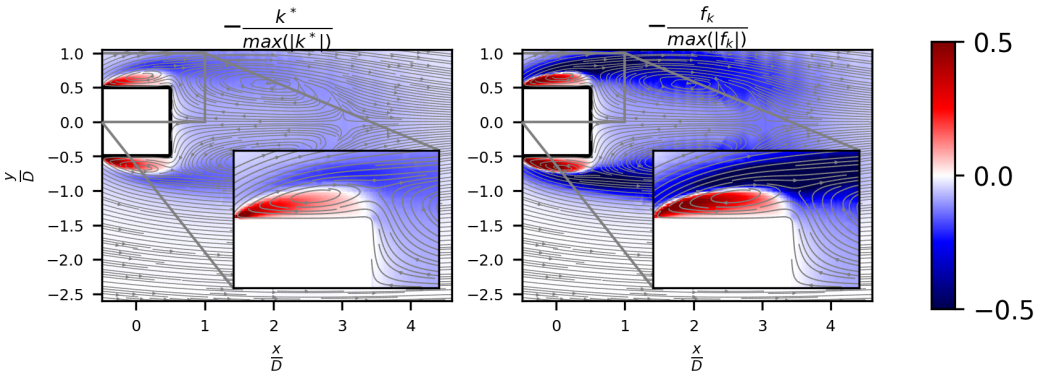

Figure 6.2 – Adjoint turbulence kinetic and the constrained control at horizontal plane with normalized height $z/D = 3.33$. Variables are normalized by their in-plan peak values.

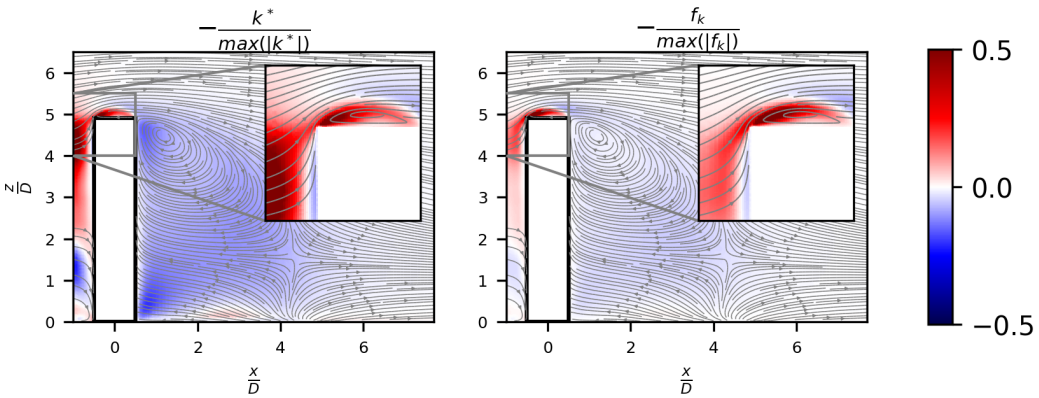

Figure 6.3 – Adjoint turbulence kinetic and the constrained control at symmetry plane. Variables are normalized by their in-plan peak values.

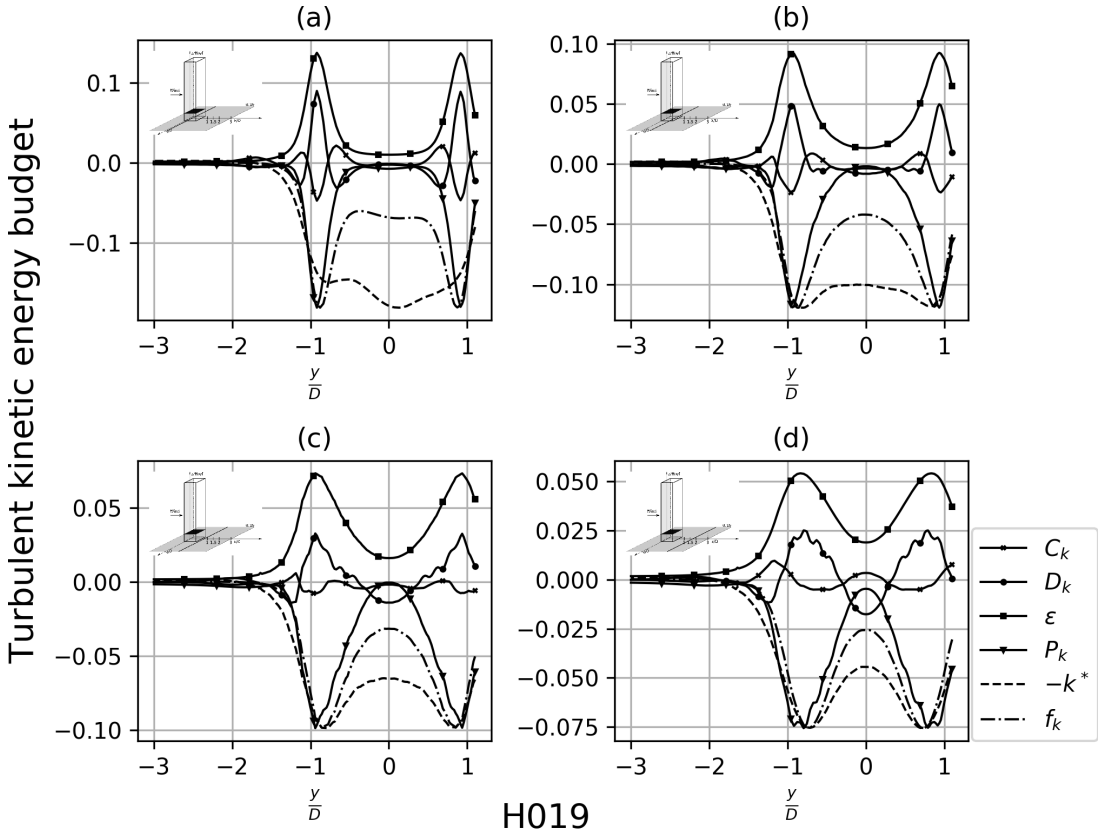

Figure 6.4 – Adjoint turbulence kinetic and the constrained control at horizontal plane with normalized height $z/D = 0.63$. Variables are normalized by their in-plan peak values.

	$\frac{\partial \mathcal{J}}{\partial f_\epsilon}(\times 10^8)$
AD	-3.55
FD ($\delta f_\epsilon = 10^{-1}$)	-14.03
FD ($\delta f_\epsilon = 10^{-2}$)	-4.03
FD ($\delta f_\epsilon = 10^{-3}$)	-4.45
FD ($\delta f_\epsilon = 10^{-4}$)	-4.48

Table 6.2 – Sensitivity derivative w.r.t. f_ϵ computed from the proposed adjoint model (AD) and the finite difference (FD) with different perturbation sizes.

Further remarks regarding the upstream flow, due to a relatively low level of inhomogeneity of turbulent kinetic energy (being originally homogeneous at the far inlet), sensitivity is reduced with the modified forcing term as compared with a direct forcing (see figure 6.3).

Due to the sign convention in model (6.4), we have to keep in mind that contributions to the k budget correspond to a loss of kinetic energy. In other words, a negative f_k would be counted as an energy source and, inversely, it relates to a sink when it is positive. Along leading top and lateral shear layers ($x/D < 0.5$), the additive term suggests to reduce the energy production. Thus, parameters here deals with a commonly encountered issue of an over-production by most $k-\epsilon$ closure models Singh and Duraisamy (2016); Murakami (1990, 1997). Whereas in contrary, in the wake region, the parameter would act as a feeding source of turbulent energy around x/D 0.5. This can be explained by the fact, that in the standard $k-\epsilon$ model, the overly produced energy in the upstream region is not enough entrained downstream to the recirculation region. This tendency is indeed consistent with the need for a higher turbulent mixing (eddy viscosity) in the wake region behind the building Shirzadi et al. (2017).

Structured control for ϵ budget correction This paragraph analyses the sensitivity fields to highlight the spatial locations where the closure form of ϵ budget appears inadequate to reproduce the measurements. For quantitative validation, adjoint sensitivities are compared with finite differences in table 6.3 for different perturbations, $\delta f_\epsilon = \{10^{-5}, \ldots, 10^{-1}\}$ constant inside Ω_{in} and zero elsewhere. Thus, the lower deviation obtained for a step size of 10^{-2}, for which rounding errors are less effective, confirms the validity of the implementation.

Figures 6.5, 6.6, and 6.7 compare the sensitivity maps for the added control parameter against a direct forcing, which corresponds to the adjoint variable on ϵ^*. Globally, sensitivity to the proposed parameter f_ϵ shows a strong response in a restricted flow area. They correspond, though, to the same regions as those designated by the sensitivity maps of the global constants and the added control on k in the previous section: the shear layers and the wake frontier.

As shown at height $z/D = 3.33$ in figure 6.6, the maps actually reveal a change of

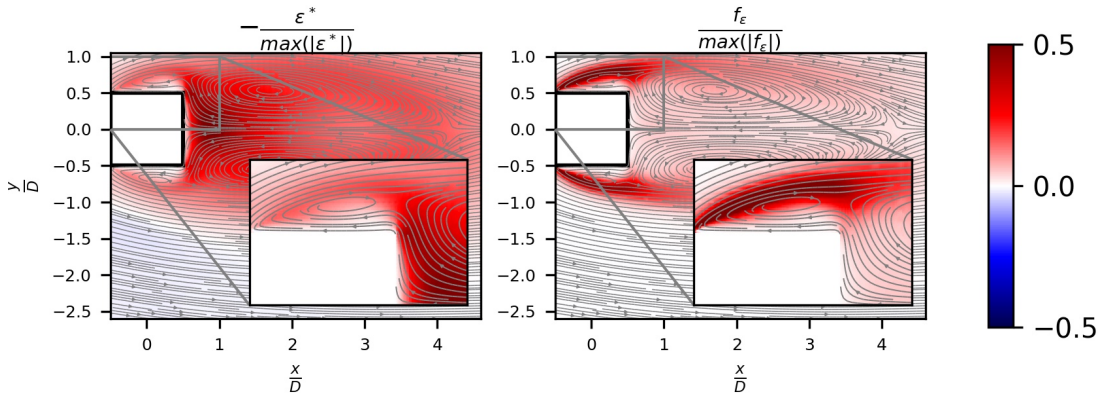

Figure 6.5 – Adjoint turbulence dissipation and the constrained control at horizontal plane with normalised height $z/D = 0.63$. Variables are normalised by their in-plan peak values.

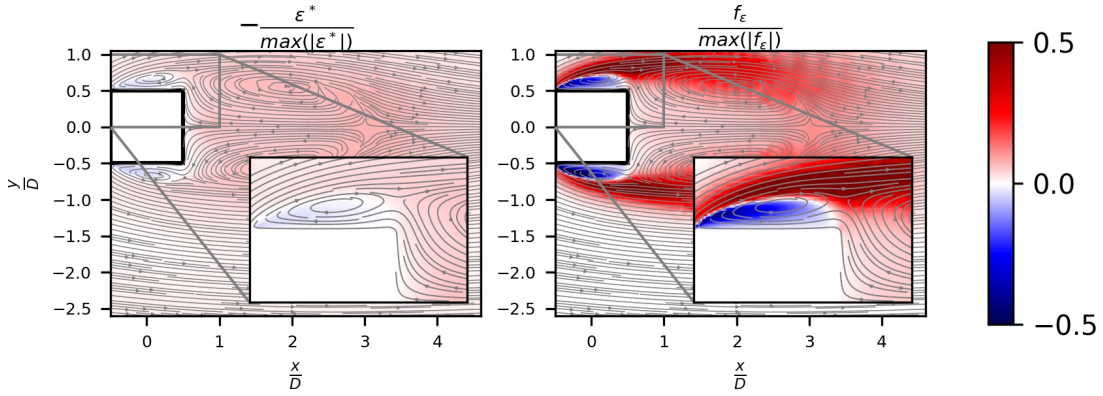

Figure 6.6 – Adjoint turbulence dissipation and the constrained control at horizontal plane with normalised height $z/D = 3.33$. Variables are normalised by their in-plan peak values.

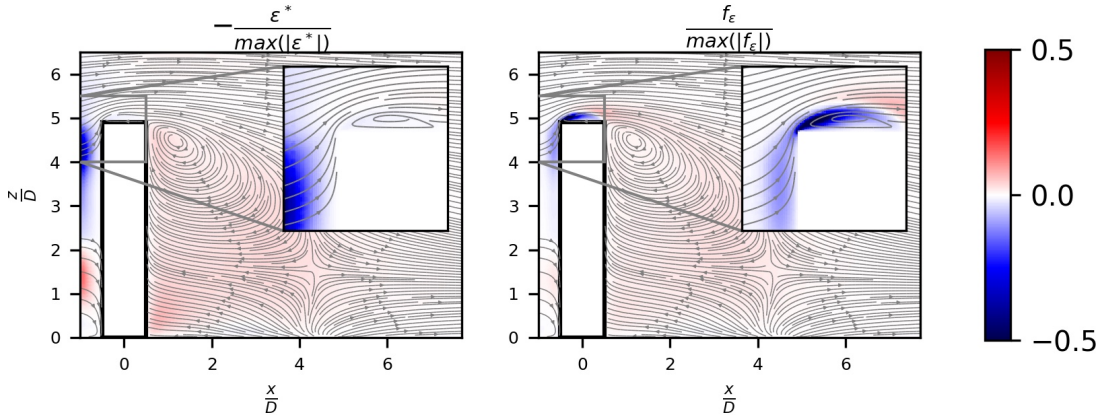

Figure 6.7 – Adjoint turbulence dissipation and the constrained control at symmetry plane. Variables are normalised by their in-plan peak values.

sign as we go from separated flow regions, *i.e.* bounded by the lateral and top shear layers, toward the wake region. This change of sign is not observed at $z/D = 0.63$, where the interest in correction is focused at the leading-edge extended shear layers. Furthermore, concerning the sign, eventual contributions to the ϵ budget are interpreted as follows. A negative value of f_ϵ would increase the dissipation rate, while a positive value would instead decrease it. Hence, on both lateral and top separated flows, the parameter suggests an increase of the dissipation rate. The sensitivity analysis points here an over-production of turbulent kinetic energy, a common default of the $k-\epsilon$ closure models in such flow configurations. This has been reported for instance in (Murakami, 1990, 1997; Rodi, 1997). Moreover, along the outer edges of the lateral shears toward the wake edges, the sensitivity maps suggest reducing the dissipation rate. This tendency is consistent with an under-predicted turbulent mixing, resulting in the overly extended wake region behind the building (Tominaga and Stathopoulos, 2010, 2017).

6.5.2 Reconstructed flows

We consider now the solutions of the data-model coupling using each of the modified closure equations (6.5) and (6.4) . A steepest descent algorithm is used with the Sobolev gradient descent direction. Regarding the choice of filtering, two values $l_{sob} = 0.1D$ and $0.2D$ are tested. Let us note that with $l_{sob} = 0$, *i.e* no smoothing of the L^2 gradient, the procedure is notably unstable, showing the need for regularisation. As for a higher value of $l_{sob} = 0.2D = 6\,\mathrm{m}$, this choice leads to an over smoothing. As the sensitivity varies by length scales that are quite small in comparison to this length, this advocates a value of $l_{sob} \sim$ lateral recirculation width. Therefore, a filtering length scale equivalent to 10% of the building's width seems to give a good compromise to filter the small-scales, also suggested also in Tissot et al. (2020). A maximum step size $\lambda = 0.05\frac{1}{max(\frac{\partial \mathcal{L}}{\partial \alpha})}$ is fixed for both models based on the sensitivity validation test, providing an upper bound to the line-search. This upper bounding has provided a well scaled search direction and, therefore a step length that is accepted in most iterations. Moreover, it is worth-noting that shifting toward a first order upwind scheme, in both direct and adjoint computations, was necessary to ensure the robustness of the procedure. Such a choice was mandatory since second order schemes caused poor conditioning of the adjoint matrices and more diffusion where it is needed.

In terms of objective, as shown in figure 6.8, the discrepancy with experiments has reduced significantly using both models. In direct energy correction, the reduction of the cost functional is of the order $\frac{\mathcal{J}}{\mathcal{J}_0} \simeq 0.3$. This is more accurate than with ϵ budget correction where $\frac{\mathcal{J}}{\mathcal{J}_0} \simeq 0.42$. Indeed, this difference is consistent with the fact that the effect of the additive parameter f_k is less constrained by the turbulence model than f_ϵ. Moreover, as compared to calibration in chapter 4, the cost functional reduction has more than doubled compared to the calibration results obtained using the best scenario **B** ($\frac{\mathcal{J}}{\mathcal{J}_0} \simeq 0.85$). Indeed, this difference is consistent because the additive parameter f_ϵ is less constrained by the parametric rigidity associated with the global coefficients.

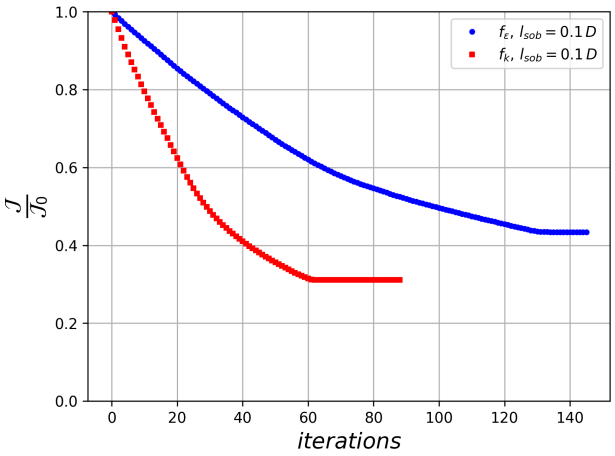

Figure 6.8 – Cost function reduction with local turbulence budget correction. Comparison is made between a direct k budget correction and ϵ budget correction.

Wind load profiles The reconstructed pressure loads are compared with the experimental data (Sheng et al., 2018) and the non-assimilated model in figure 6.9. We can see that, in comparison with the coefficient calibration, the modified closure models produce far better results in most of the building's wall regions. Yet, globally, direct correction on the k budget yields relatively better results. In figure 6.9(a), both models give a very good agreement with data along the windward facade in the symmetry plane. At the leading edges, both modified closure models manage to capture well suction at both top edge in the symmetry plane (point B in sub-figure(a)) and lateral edges (see figure 6.9(b), (c), and (d)). However, while a good agreement with the data is obtained along the lateral facades, minor to important deviations are apparent as we get closer to the trailing edges, and especially when we approach the high-end. This gradually leads to poorer pressure interpolation as the discrepancy reaches a maximum value at the upper leeward facade around H_{ref} (sub-figure(a) and (b)). However across the windward facade, although the presumable erroneousness within data (near B in sub-figure(b) and (c)), both reconstructed profiles preserve the symmetry. Therefore, both closure models improve the data-model capability, at this level of comparison compared with the calibration process, with slightly better results being achieved by direct correction in the k budget. The remaining regions where no improvement is seen might reflect the limited controllability of such turbulence model with wall pressure measurement, in comparison with the deformation corrections (in the previous chapter). Nevertheless, it is noteworthy to mention that reconstructed wall-pressure is robust vis-a-vis any eventual localized errors within the data. This shows the advantage of giving confidence in the model structure by choosing a more "indirect" parameter.

Wake centreline profiles Further results of the streamwise velocity in the wake centreline, at two height levels ($z/D = 0.63$ and $z/D = 3.33$), are confronted to data from the non-assimilated PIV results Sheng et al. (2018) in figure 6.10. In term of recirculation

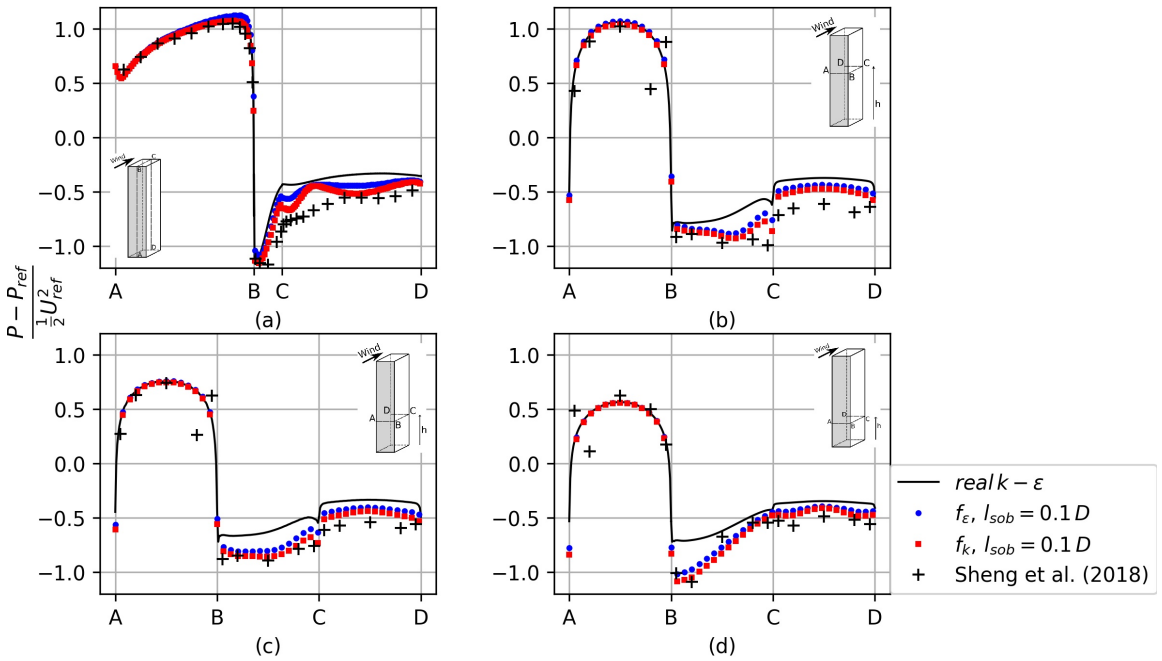

Figure 6.9 – Pressure coefficient profiles along building facades with local turbulence budget correction. Comparison is made between a direct k budget correction and ϵ budget correction.

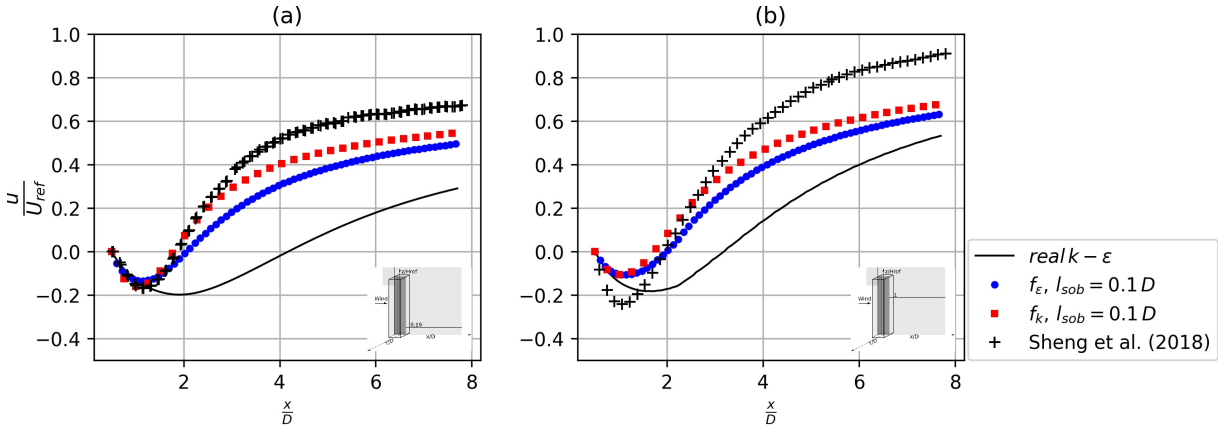

Figure 6.10 – Streamwise velocity along centreline at $z/D = 0.63$ and $z/D = 3.33$ elevations with local turbulence budget correction. Comparison is made between a direct k budget correction and ϵ budget correction.

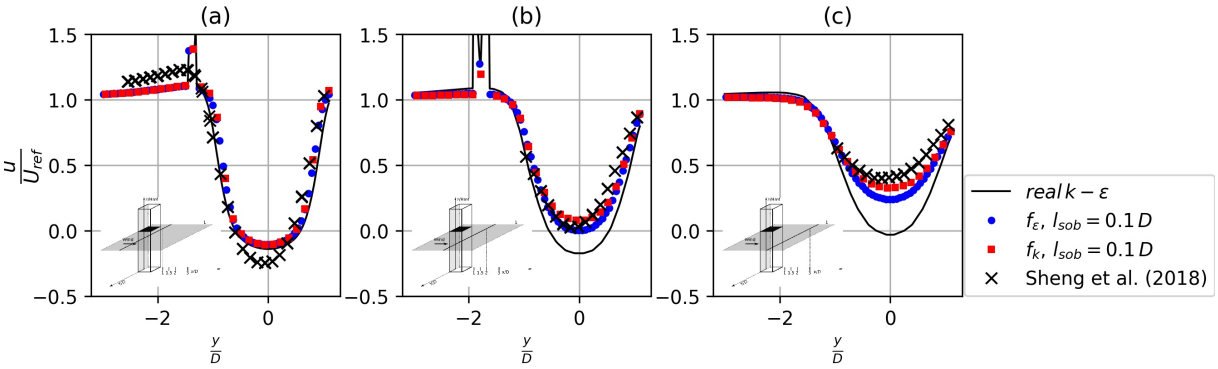

Figure 6.11 – Streamwise velocity in the wake transverse at $z/D = 3.33$ with local constraint correction. Comparison is made between a direct k budget correction and ϵ budget correction across streamwise positions $\frac{x}{D} = 1$,2 and 3.

length, both models show a considerable reduction leading to a great agreement with the experimental length at both elevations. Near the ground ($z/D = 0.63$), reconstructed velocity profiles fits well with the experiments in the near wake. On the other hand, along the upper recirculation motions at $z/D = 3.33$, a significant difference with data was obtained with both models, in which the peak of streamwise velocity is under-predicted. Let us note that the default model does already under-estimate this peak, which is related to the under prediction of wall-pressure observed at the upper half of the leeward wall. In fact, this tendency has to be expected as turbulence model output will always extract momentum from high to low momentum flow regions through eddy diffusion effects. As previously seen in the sensitivity analysis for both models, control parameters advocate higher turbulent energy (and equivalently lower dissipation for ϵ) at the wake edges. With this informations being entrained toward the symmetry plan, this seems to increase the extraction of mean streamwise momentum, as k, ϵ and hence μ_t have seen their value increased at the symmetry plane. This effect continues to play a role as we go downstream with the far wake ($x/D > 2$) that deviates progressively from the data.

Wake transverse profiles With regards to the transverse-wise distributions (in the y direction), streamwise velocity distribution is also shown at three streamwise locations $\frac{x-x_b}{D} = 1, 2, 3$ downstream of the building leeward wall ($x_b = 0.5D$) in figure 6.11. Despite the significant mismatch around the wake centerline at ($z/D = 3.33$), both reconstructed profiles agree well with experiments on the recirculation edges (see 6.11(a)). Note that globally, symmetry with the plane $y/D = 0$ is well preserved by both corrective models.

Further results on the transverse velocity component are compared in figures 6.12 and 6.13. Across the wake, both reconstruction strategies leads to a significant profile's adjustment at $y/D \simeq \pm 0.9$, as the free-stream flow (with high streamwise momentum) is being entrained toward the symmetry plane. As we go downstream, both reconstructed profiles gradually deviate toward the non-assimilated model's predictions.

In addition, the fact we correct the quantity of the turbulence description, which

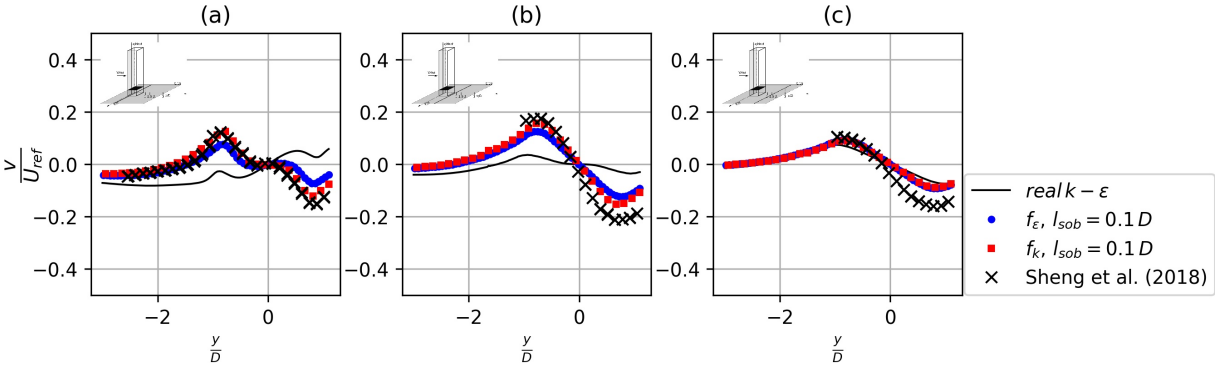

Figure 6.12 – Transverse-wise velocity in the wake transverse at normalized height $z/D = 0.63$ with local constraint correction. Comparison is made between a direct k budget correction and ϵ budget correction across streamwise positions $\frac{x}{D} = 1$,2 and 3.

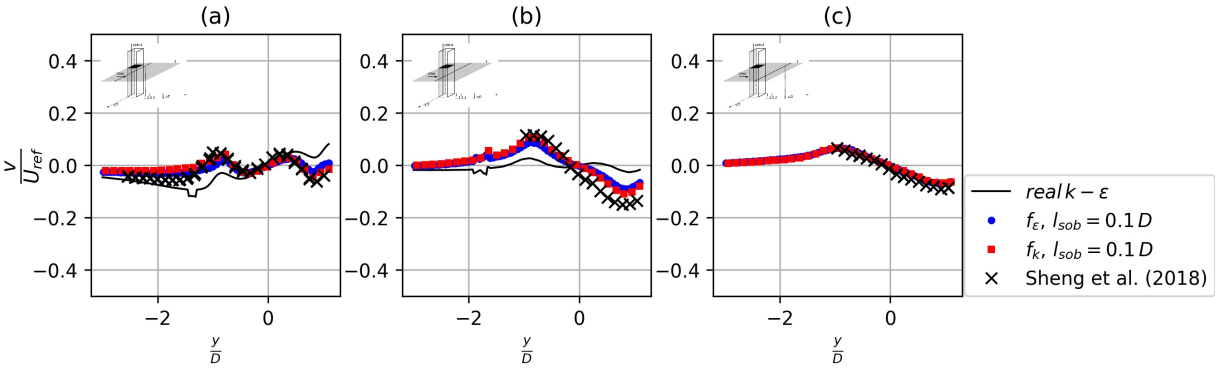

Figure 6.13 – Transverse-wise velocity in the wake transverse at normalized height $z/D = 0.63$ with local constraint correction. Comparison is made between a direct k budget correction and ϵ budget correction across streamwise positions $\frac{x}{D} = 1$,2 and 3.

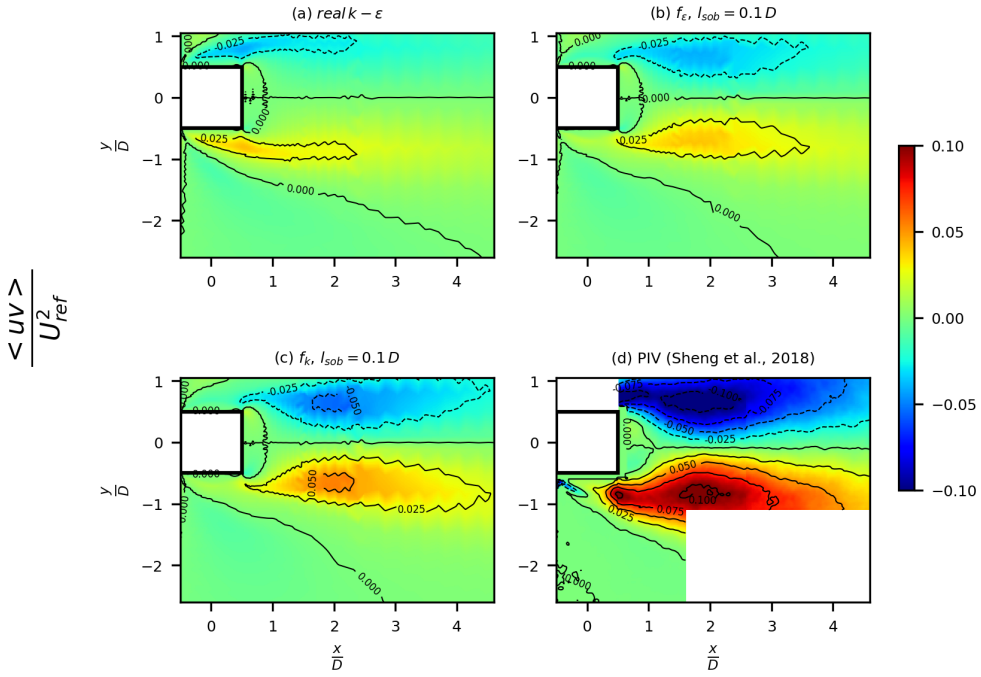

Figure 6.14 – 2D contours of Reynolds stress component $< uv >$ on horizontal plane at normalized height $z/D = 3.33$ with local constraint correction. Comparison is made between a direct k budget correction and ϵ budget correction

is directly involved in the eddy viscosity relationship, comments on the reconstructed Reynolds tensor by each of the models can then be addressed. Two dimensional contours of the off-diagonal component $\overline{\mathbf{u} \otimes \mathbf{v}}$ (transverse-wise) are presented in comparison with the processed PIV data (see figures 6.15 and 6.14). Within the upper recirculation region (figure 6.14), compared with the non-assimilated model (figure 6.14(a)), both reconstructed maps show increased turbulent stress component particularly on the edges of the wake region. This increase is remarkably achieved with a direct correction in the k budget (figure 6.14(c)). Although the better agreement on the location of the peak anisotropy ($(x/D, y/D) \simeq (2, \mp 0.9)$), both models still under-predicts this peak value, as anisotropy still arises from the mean flow strain and not from turbulent scales. Nevertheless, the tendency is indeed consistent with the data while the default model fails.

Flow topology In order to assess if the solution can be considered as physical, the reconstructed flow structure is further analysed here. Figure 6.16 shows time averaged sectional streamlines at the $y = 0$ symmetry plane. Thus, regarding the wake's extension, the modified closure models leads to a drastic reduction of the recirculation region (figures 6.16(b) and (c)). Two types of typical average streamlines are produced: an upper recirculation starting at the roof-top and a lower recirculation region raised from the ground wall. Both are separated by a saddle point. This can be quantified by the position

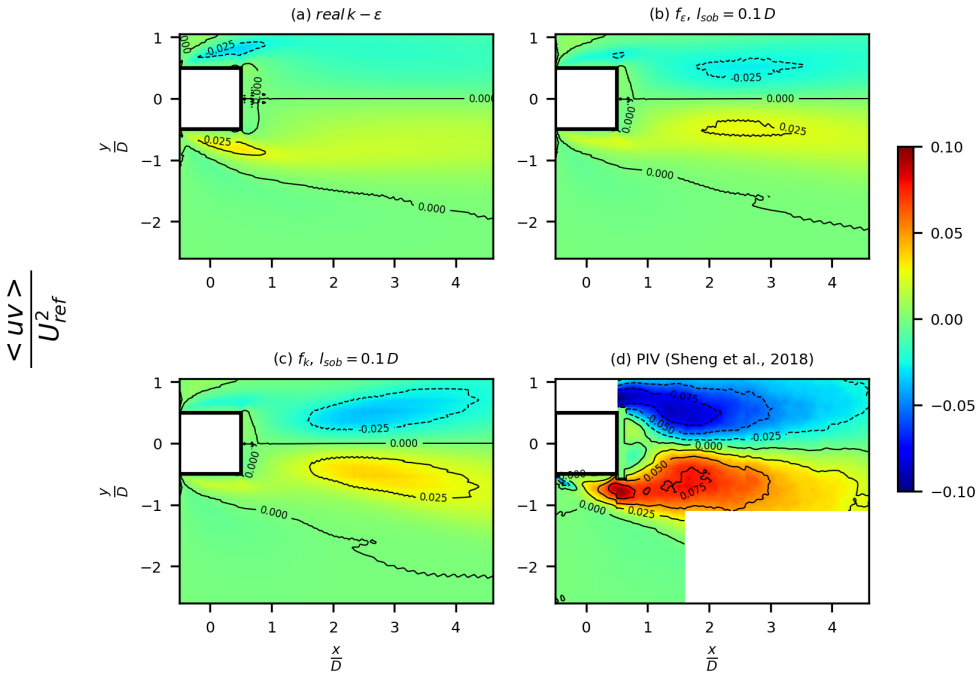

Figure 6.15 – 2D contours of Reynolds stress component $< uv >$ on horizontal plane at normalized height $z/D = 0.63$ with local constraint correction. Comparison is made between a direct k budget correction and ϵ budget correction.

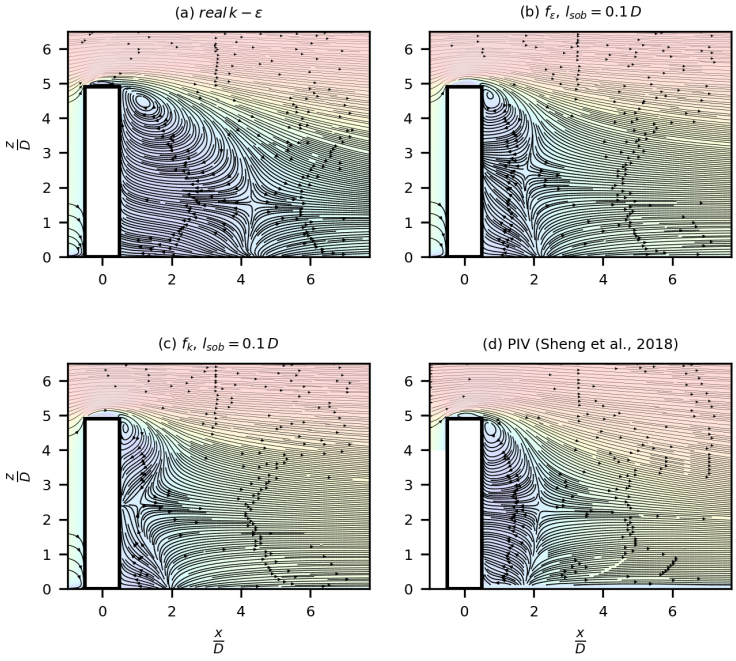

Figure 6.16 – Flow topology (2D) on symmetry plane with local constraint correction. Comparison is made between a direct k budget correction and ϵ budget correction.

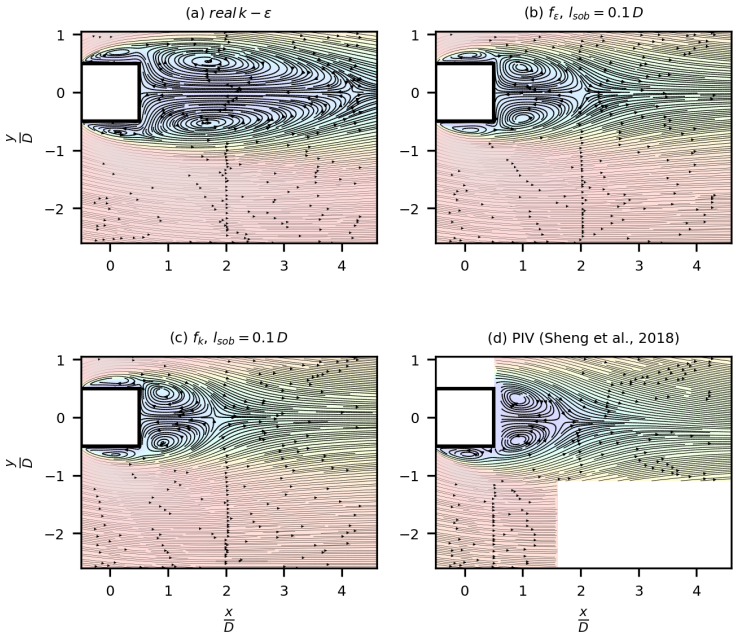

Figure 6.17 – Flow topology (2D) on horizontal plane at normalized height $z/D = 0.63$ with local constraint correction. Comparison is made between a direct k budget correction and ϵ budget correction.

of the saddle point ($x/D = 4$,$z/D = 2$) in the RANS model which has been moved around ($x/D = 2$,$z/D = 2$) with f_ϵ as a parameter and ($x/D = 1$,$z/D = 2$) with f_k instead. This striking result is mitigated by the fact that this saddle point has been pulled slightly too far upstream, especially with the correction on the k budget. It should be recalled that only pressure measurements in the facade have been available and that PIV measurements are used here only for validation. This good agreement with external data proves that we are neither in overfitting nor in an over-constrained situation. So far, parameter structuration through ϵ closure equation seems to yields a more realistic upper/lower recirculation flow topology.

With regards to the spanwise flow structure, figures 6.17 and 6.18 show sectional streamlines at both $z/D = 0.63$ and $z/D = 3.33$ heights, respectively.

Both reconstruction models preserved symmetry of the two distinct pairs of averaged vortex structures at both elevations. Moreover, note a fair agreement in its transverse extension and the position of their respective focal points. At both elevations, no major difference is observed in between the two reconstructions. However, due to the overly retracted recirculation in the case of k budget correction, connections between the base and top vortices was broken around the saddle point level, as shown in 3D reconstructed streamlines (see figure 6.19(a)). Nevertheless, with f_ϵ as a control parameter, the two-dimensional vortices at both elevations ($z/D = 0.63$, 3.33) are a transverse projection of the three-dimensional rolls, one on each side of the wake symmetry plan, reminiscent of the vortex shedding. The saddle point thus marks the early change of orientation of the mean

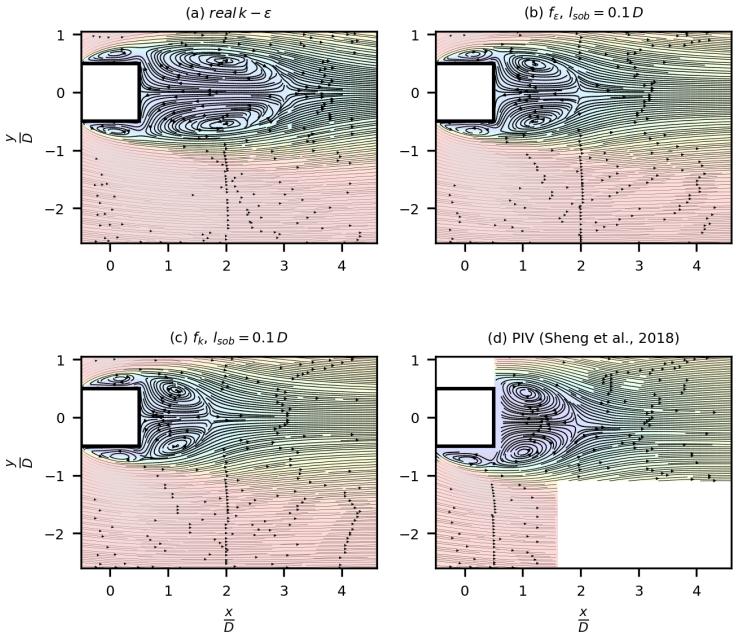

Figure 6.18 – Flow topology (2D) on horizontal plane at normalized height $z/D = 3.33$ with local constraint correction. Comparison is made between a direct k budget correction and ϵ budget correction.

wake vortices; from spanwise rolls (although the PIV suggests an arch-like structure with upstream inclination) in the bottom, toward a transverse down-wash vortex resulting from the high end. Such structure is consistent with some model descriptions brought on wakes of finite length square cylinders, with similar height/width ratio, subject to boundary layer flows of various thicknesses (Kawamura et al., 1984; Wang and Zhou, 2009).

Note that the exaggerated retraction of the saddle point, for f_k as a parameter, coincides with the height $z/D \simeq 3$ where wall-pressure errors reach their minimum at the leeward wall (6.9(a) section '"CD"'). Indeed, to achieve lower pressure discrepancy under recirculating fluid, model have significantly increased turbulent diffusivity, leading to an over-estimation of the diagonal components of the Reynolds stress tensor (dominated by $\overline{u_z}^2$). The latter peak value was reached in the vicinity of the leeward wall region (centred on the symmetry plan) at the saddle point. This observation holds with the f_ϵ parameter, yet, with lower peak values and with slight shift upward and downstream (but still missing the PIV measured position). This explains the slightly better wake extension. This recalls an intrinsic limiting factor of the turbulence model, i.e. isotropic assumption of the eddy viscosity, which prevents the DA reconstruction from a proper redistribution of turbulent shears. However, we suspect that this would have concerned other turbulence models built based on this assumption.

Besides, as the corrections to the flow should come only from diffusive effects (Boussinesq assumption), this clearly adds another limiting barrier as we still miss other energy exchange mechanisms. For instance, some authors denoted a possibly negative eddy vis-

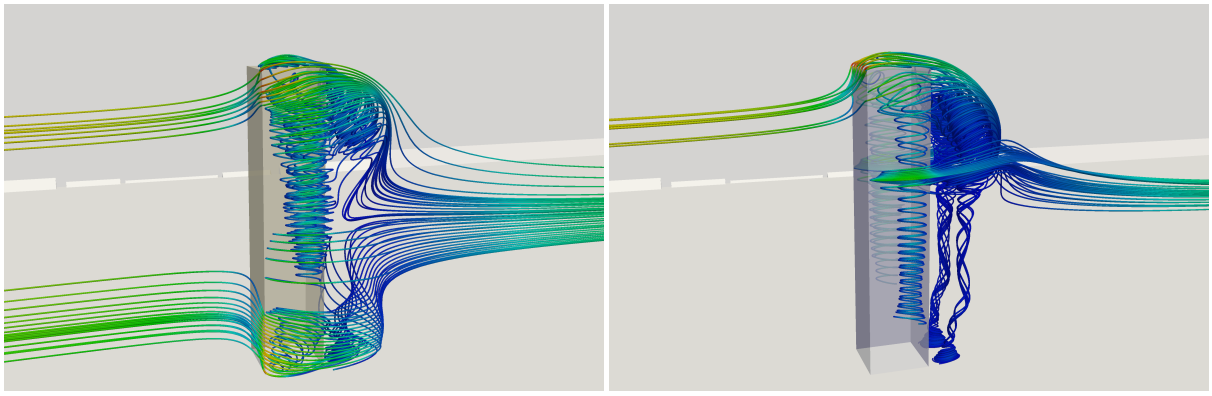

(a) (b)

Figure 6.19 – Flow topology (3D) with local constraint correction. Comparison is made between a direct k budget correction, (a) and ϵ budget correction, (b).

cosity, i.e. acting as an anti diffusion. It provides instead energy into the mean flow, e.g in the shear of separated flow (Cimarelli et al., 2019). Note that computing the stress tensor from the available PIV data by assuming the Boussinesq relation between the measured Mean-strain and the shear-stress components, suggest that this is a plausible idea for the flow configuration we are considering at the symmetry plane. To propose an alternative solution, while maintaining the positive assumption on ν_t, we propose to investigate the coupling of the two kind of corrections; the ones considered in the direct correction of deformation (from chapter 5) and the one which acts on the turbulence closure equation. The choice of the forms of control parameter plays a huge role here, as we intend an efficient hybridization such that their contributions complement themselves. We note that this is far from being an easy task as it requires a proper scaling between the two corrections.

6.6 Guidelines for efficient flow reconstruction

6.6.1 Control parameter

In order to refine flow reconstructions, we consider in this section to consider two kind of control parameters; one forcing vector field acting on the momentum equations and a scalar forcing field acting on the transport equation of ϵ. A structured form of the forcing on the momentum equation is chosen. The present choice is motivated based on the numerical tests performed in the previous chapters, in view of acting on two different physical mechanisms.

This choice is motivated based on the following observations. It has been shown in chapter 5, that forcing directly on the momentum equation leads to overfitting. Indeed, the wall-pressure is well represented, but the flow field is unphysical. A way to structure this forcing on the momentum equation is to premultiply it by $|\nabla k|$. This leads to a good

reduction of the wall-pressure discrepancy, with perfromances comparable to the direct forcing. However with regards to the flow field, from its sensitivity maps, the corrections are mainly performed in the lateral and top shear layers, but not in the wake region. Consequently, it was observed that this forcing did not lead to reduction of the wake extension. This can be interpreted as a missing component necessary for better momentum mixing representation.

On the other hand, forcing on the transport of ϵ leads to impressive reduction of the recirculation length. We interpret this by the fact that it acts on the turbulent mixing, relevant to predict the shape of the wake. The counterpart uses a very structured model, whose constraints forbid to reach some states that could be physical.

With the objective of performing the best flow reconstruction possible, we believe that it is important to combine the advantages of both strategies, since they apparently act on two separate mechanisms. The model proposed here reads as

$$\frac{\partial(\rho U_j U_i)}{\partial x_j} + \frac{\partial}{\partial x_i}\left(P + \frac{2}{3}\rho k\right) - \frac{\partial}{\partial x_j}\left[\mu_{eff}\left(\frac{\partial U_i}{\partial x_j} + \frac{\partial U_j}{\partial x_i}\right)\right] = -f_{u_i}|\nabla k| \tag{6.8}$$

$$\frac{\partial U_i}{\partial x_i} = 0 \tag{6.9}$$

$$M_k = 0, \tag{6.10}$$

$$M_\epsilon = -f_\epsilon \epsilon \tag{6.11}$$

where M_k and M_ϵ embeds the terms from of the base model (see chapter 2).

6.6.2 Descent direction

The adjoint model is simply the combination of the adjoints to the individual models (along with their boundary conditions). Thus, given the adjoint state, the optimality conditions are collected as follow:

$$\frac{\partial \mathcal{L}}{\partial f_{u_i}} = |\nabla k| U_i^*, \tag{6.12}$$

$$\frac{\partial \mathcal{L}}{\partial f_\epsilon} = \epsilon \epsilon^*. \tag{6.13}$$

The explicit dependency of the cost function to the parameter is omitted here and, thus, a regularization of the descent direction using Sobolev gradient (in H^1)was chosen. Moreover, we have investigated the combinations of the two regularization techniques; i.e. the penalization of the gradient and the use of Sobolev gradient. Given the very sparse observations, we believe that combining both ensures at the same time an improved descent for the minimization algorithm and a robust data-model coupling.

6.6.3 Quality assessment for flow reconstructions

Results of the reconstruction by the model are discussed herein compared to the previously investigated models. The quality of the reconstruction by each coupling strategy is particularly evaluated upon the definition of some validation metrics. These metrics are proposed to compare the interpolation quality, i.e. the ability to reconstruct the wall pressure on the building based on sparse measurements, and the extrapolation/generalisation quality, i.e. the velocity field reconstruction. For the former purpose, we consider the pressure coefficient error, rescaled by the initial error of the uncorrected RANS model (with subscript ^{0}). The considered pressure is taken at particular positions, where the experimental measurements reach a maximum or a minimum. Four positions have been chosen: along the symmetry plane $y/D = 0$, the stagnation point, and the maximum suction position at the roof top. Moreover, maximum suction at one of the lateral facades at $z/D = 0.3$ and $z/D = 3.33$ have been selected. These strategic points are important to be accurately predicted in terms of structural dimensioning of the building, since they can be linked to an estimate of the instantaneous peak pressure values if they are informed by the turbulent intensity (as recommended in (EN, 2005)). At a position j, the pressure criteria is as follows:

$$\mathcal{M}_1^j = \left|\Delta C_p^j / \Delta C_p^{j,0}\right|.$$

Since a criteria based on a punctual value can lack of robustness, an average metric for the predicted peaks of mean wind loads is defined as

$$A^1(\mathcal{M}_1) = \frac{1}{n_p} \sum_j^{n_p} \mathcal{M}_1^j. \tag{6.14}$$

where n_p denote the number of selected points. We note that, from a structural view point only, the metric $\mathcal{M}_1$ (along with the objective function) is a sufficient validation quantity as it permits to assess the estimate of peak temporal pressure that results from wind gusts.

Regarding the prediction of the wind surrounding the building, since the physical features of the flow may not be retrieved even with accurate wall-pressure predictions, additional flow metrics are needed. To asses extrapolation performances, we consider two criteria, namely $\mathcal{M}_2^j$ which quantifies the degree of reduction of the recirculation length $L_x^{\star,j}$ (* indicate non dimensionality) measured at a height z_j and $\mathcal{M}_3^j$ that measures the error made in the prediction of the largest upstream velocity $U_{x_{\min}}^{\star,j}$ along the line on the symmetry plane at the height z^j. Flow metrics are also normalised by the values of the uncorrected model

$$\mathcal{M}_2^j = \left|\Delta L_x^{\star,j} / \Delta L_x^{\star,j,0}\right|,$$

$$\mathcal{M}_3^j = \left|\Delta U_{x_{\min}}^{\star,j} / \Delta U_{x_{\min}}^{\star,j,0}\right|.$$

Given these two quantities, two measures of the flow reconstruction quality can be given by defining their corresponding averages $A^1(\mathcal{M}_2)$ and $A^1(\mathcal{M}_3)$, similarly than equa-

tion (6.14). Moreover, a third metric representing the overall wake extend prediction is defined as a weighted sum of the ratio between the improvement made in $L^\star$ over the loss in precision on $U^\star_{x_{\min}}$,

$$A^2(\mathcal{M}_2, \mathcal{M}_3) = \frac{(1 - \frac{1}{n_z}\sum_j^{n_z} \mathcal{M}_2^j)}{\frac{1}{n_z}\sum_j^{n_z} \mathcal{M}_3^j}$$

where n_z denote the number of considered heights. Note that this averaged metric is considered to be the most relevant among the three flow averaged metrics (the other two are $A^1(\mathcal{M}_2), A^1(\mathcal{M}_3)$) as it enables evaluating the compromise between the two measures and provides an insight to the quality of reconstruction. The choice of metric is not unique, and the present choice has the advantage to be more sensitive than a standard $L^2(\Omega)$ norm, by being oriented toward a worst-case scenario in identifying maximum values. The average over several peak values confers robustness in the metric.

The first wall-pressure metric ($\mathcal{M}_1$) was computed for four measurement points at the locations $(x/D, y/D, z/D)$ where mean pressure reaches its local extrema (table 6.3); at the stagnation point $(-0.5, 0, 4.13)$ and at the maximum suction points $(0, 0, 4.9 = H/D)$, $(0.45, 0.5, 3.3)$ and $(-0.33, 0.5, 0.33)$. The other two metrics are given in table 6.4, measured at three heights, namely $z/D = 0.33, 2, 5, 3.33$ in the symmetry plane.

Averaged metrics are collected in table 6.5. Tables summarize results of the current (hybrid) parametrization with different regularization levels, the individual, direct forcing form, the structured force alone, and the corrected closure on ϵ budget alone.

These quantitative comparisons are accompanied with plot of the cost function reduction, illustrated in figure 6.20, and wall-pressure distributions, in figure 6.21.

Objective reduction assessment Here, we explore the effect of adding a penalty regularisation in addition to the Sobolev descent direction. Three penalization scaling factors of the momentum forcing were considered: $\zeta_{f_{u_i}} = 0.1, 0.25, 0.5$, with a given penalization to ϵ fixed at $\zeta_{f_\epsilon} = 15$. At the opposite, let us note that fixing instead $\zeta_{f_{u_i}}$ and sweeping ζ_{f_ϵ}, leads to a symmetric trend. As expected, high values of $\zeta_{f_{u_i}}$ leads to large constraints to the optimisation, while lower values does not efficiently suppress non-physical oscillations. For the penalty on ϵ, low values of $0 \ll \zeta_{f_\epsilon} < 15$ tested with $\zeta_{f_{u_i}} = 0.1$ does not lead to a further improvement in the objective. The fact that penalization of f_ϵ has only a slight effect on the minimum objective, confirms the dominance of the direct forcing in correcting the wall-pressure. Nonetheless, a high impact on the flow field should be expected; as f_ϵ affects the bulk momentum diffusion.

Optimizing with Sobolev filtering solely shows that the added force with modified closure allows further reduction of the objective compared with the same forcing and no closure correction. Yet, with the addition of penalty terms, the coupled scaling $(\zeta_{f_{u_i}}, \zeta_{f_\epsilon}) = (0.1, 15)$ enables the objective to reach its lowest level so far. However, the average wall-metric ($A^1(\mathcal{M}_1)$) favours the structured force with both standard and modified closure, with an average reduction by $85-89\%$ from the uncorrected model. This was particularly observed without penalty. Thus, the conjunction of L^2penalization/Sobolev gradient bury

	$C_{p_{\max}}, C_{p_{\min}}(y/D=0)$	$C_{p_{\min}}(z/D=3.33,\ 0.33)$	$\mathcal{M}_1$ (%)
Sheng et al. (2018)	1.05, -1.166	-0.99, -1.087	-
$realizable\, k-\epsilon$	1.117, -0.799	-0.569, -0.706	100
f_u, $l_{sob}=0.1\,D$	1.046, -1.115	-0.873, -0.972	5.97, 13.89, 27.79, 30.18
$\lvert\nabla k\rvert f_u$, $l_{sob}=0.1\,D$	1.065, -1.160	-0.996, -1.006	22.38, 1.63, 1.42, 21.26
$\lvert\nabla k\rvert f_u\, f_\epsilon$, $l_{sob}=0.1\,D$	1.069, -1.168	-0.960, -1.001	28.35, 0.54, 7.12, 22.57
$\lvert\nabla k\rvert f_u$, f_ϵ, $l_{sob}=0.1\,D$, $(\zeta_{f_u},\zeta_{f_\epsilon})=(0.1,15)$	1.0298, -1.152	-0.924, -0.974	30.15, 3.81, 15.67, 29.66
$\lvert\nabla k\rvert f_u$, f_ϵ, $l_{sob}=0.1\,D$, $(\zeta_{f_u},\zeta_{f_\epsilon})=(0.25,15)$	1.040, -1.144	-0.883, -0.949	14.92, 5.99, 25.41, 36.22
$\lvert\nabla k\rvert f_u$, f_ϵ, $l_{sob}=0.1\,D$, $(\zeta_{f_u},\zeta_{f_\epsilon})=(0.5,15)$	1.060, -1.127	-0.842, -0.931	14.92, 10.62, 35.15, 40.94
f_ϵ, $l_{sob}=0.1\,D$	1.124, -0.918	-0.699, -0.983	110.4, 67.57, 69.12, 27.29

Table 6.3 – Maximum stagnation (located by the dotted line in figure 6.21 (a)) and maximum suction (located by the dashed lines in figure 6.21(a),(b),(d)) with different parametrization.

	$L_x^\star$	$U_{x_{\min}}^\star$	$\mathcal{M}_2(\%)$	$\mathcal{M}_3(\%)$
Sheng et al. (2018)	1.855, 2.132, 1.934	-0.1697, -0.4696, -0.421	-	-
$realizable\, k-\epsilon$	4.154, 4.01, 3.177	-0.197, -0.203, -0.181	100, 100, 100	100, 100, 100
f_u, $l_{sob}=0.1\,D$	2.924, 2.89, 2.16	-0.146, -0.138, -0.095,	46.49, 40.3, 18.18	86.81, 124.4, 135.83
$\lvert\nabla k\rvert f_u$, $l_{sob}=0.1\,D$	2.635, 3.56, 2.75	-0.177, -0.264, -0.211	33.9, 76, 65.64	26.74, 77.1, 87.5
$\lvert\nabla k\rvert f_u\, f_\epsilon$, $l_{sob}=0.1\,D$	2.433, 2.404, 2.332	-0.158, -0.12, -0.158	25.14, 14.5, 32.02	43.22, 131.1, 109.6
$\lvert\nabla k\rvert f_u$, f_ϵ, $l_{sob}=0.1\,D$, $(\zeta_{f_u},\zeta_{f_\epsilon})=(0.1,15)$	2.289, 2.42, 2.361	-0.1148, -0.105, -0.1435	18.87,15.3, 34.35	201, 136.7, 115.6
$\lvert\nabla k\rvert f_u$, f_ϵ, $l_{sob}=0.1\,D$, $(\zeta_{f_u},\zeta_{f_\epsilon})=(0.25,15)$	2.188, 2.32, 2.303	-0.0989, -0.091, -0.1345	14.48, 10, 29.68	259.3, 142, 119.3
$\lvert\nabla k\rvert f_u$, f_ϵ, $l_{sob}=0.1\,D$, $(\zeta_{f_u},\zeta_{f_\epsilon})=(0.5,15)$	2.217, 2.174, 2.245	-0.104, -0.08, -0.1197	15.74, 2.2, 25.02	240.65, 147, 125.54
f_ϵ, $l_{sob}=0.1\,D$	2.055, 1.766, 1.983	-0.1345, -0.055, -0.1063	8.69,18.9, 3.94	128.9, 155.5, 131.1

Table 6.4 – Normalized Recirculation length $L_x^\star$ and peak streamwise velocity $U_x^\star$ inside the recirculating flow at two height $z/D=(0.63, 2.5, 3.33)$ on the symmetry plane $(y/D=0)$ with different parametrization. Variables are normalized by D and U_{ref}, respectively.

	$\varepsilon_{\mathcal{J}} = \mathcal{J}^{end}/\mathcal{J}^0(\%)$	$A^1(\mathcal{M}_1)(\%)$	$A^1(\mathcal{M}_2)$ (%)	$A^1(\mathcal{M}_3)$ (%)	$A^2(\mathcal{M}_2, \mathcal{M}_3)$
heng et al. (2018)	-	-	-	-	-
$ealizable\, k-\epsilon$	100	100	100	100	-
$_u,\, l_{sob} = 0.1\, D$	20.9	19.45	34.99	115.68	0.56
$\nabla k \vert f_u,\, l_{sob} = 0.1\, D$	26.9	<u>11.67</u>	58.51	<u>63.78</u>	0.65
$\nabla k \vert f_u\, f_\epsilon,\, l_{sob} = 0.1\, D$	23.69	14.645	23.89	94.64	<u>0.8</u>
$\nabla k \vert f_u,\, f_\epsilon,\, l_{sob} = 0.1\, D,\, (\zeta_{f_u}, \zeta_{f_\epsilon}) = (0.1, 15)$	<u>20.25</u>	19.82	22.84	151.1	0.51
$\nabla k \vert f_u,\, f_\epsilon,\, l_{sob} = 0.1\, D,\, (\zeta_{f_u}, \zeta_{f_\epsilon}) = (0.25, 15)$	25.2	20.63	18.05	173.5	0.47
$\nabla k \vert f_u,\, f_\epsilon,\, l_{sob} = 0.1\, D,\, (\zeta_{f_u}, \zeta_{f_\epsilon}) = (0.5, 15)$	28.97	25.40	14.32	171.06	0.50
$_\epsilon,\, l_{sob} = 0.1\, D$	43.4	68.59	<u>10.51</u>	138.5	0.64

Table 6.5 – Summarizing scores for reconstruction quality assessment.

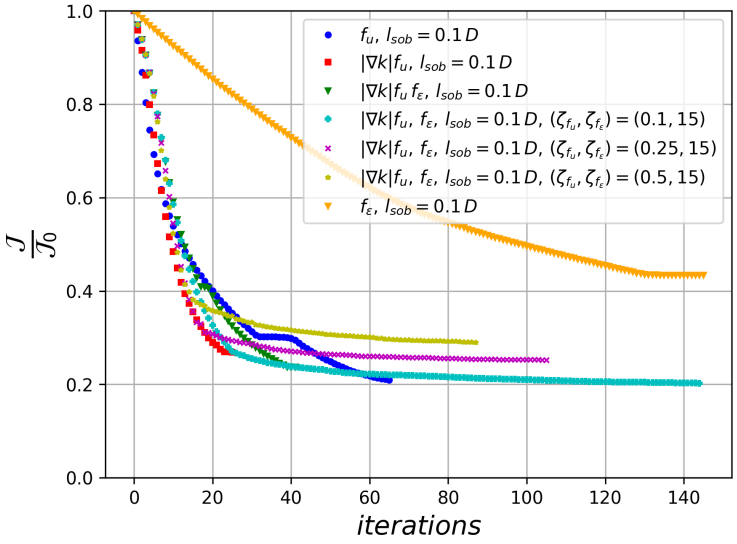

Figure 6.20 – Cost function reduction under a correction of a structured force with a modified closure applied on ϵ budget for different penalization $(\zeta_{f_u}, \zeta_{f_\epsilon}) = ([0.1\, 0.25\, 0.5], 15)$. Comparison is made with the separate optimisation of:(black cercle), raw-force, (blue square), structured force, with default closure, and (yellow triangle), modified closure made at the ϵ budget. The steepest descent direction is improved for all algorithms by the use of Sobolev gradient with filtering length scale $l_{sob} = 0.1\, D$.

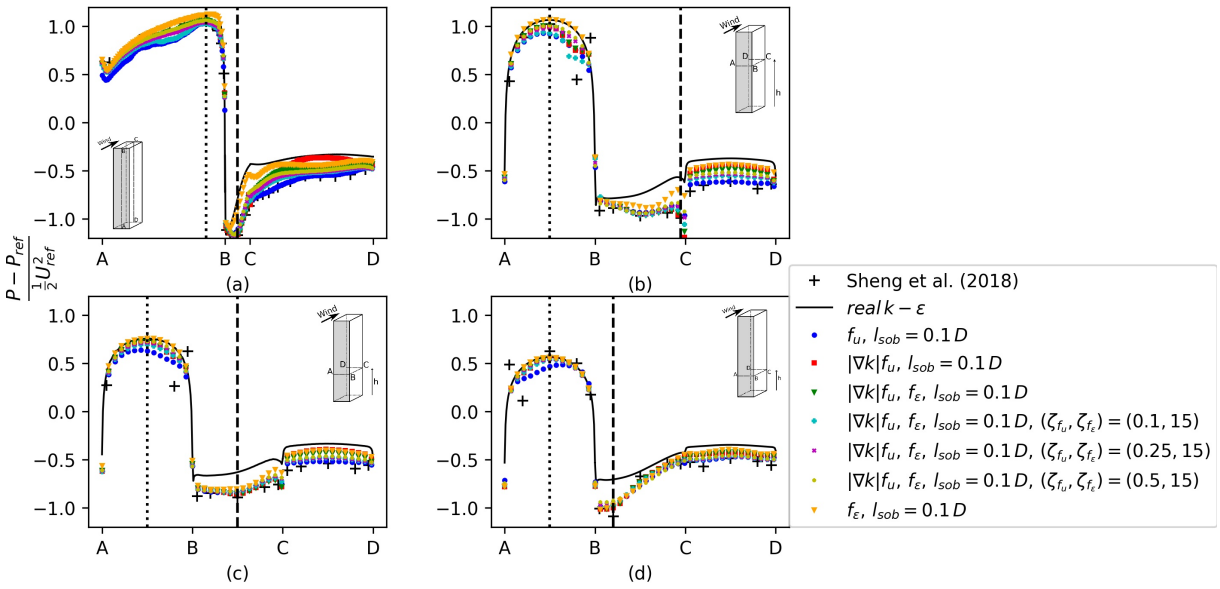

Figure 6.21 – Pressure coefficient profiles along building facades under a correction of a structured force with a modified closure applied on ϵ budget for different penalization $(\zeta_{f_u}, \zeta_{f_\epsilon}) = ([0.1\,0.25\,0.5], 15)$. Comparison is made with the separate optimisation of:(black cercle), raw-force, (blue square), structured force, with default closure, and (yellow triangle), modified closure made at the ϵ budget. The steepest descent direction is improved for all algorithms by the use of Sobolev gradient with filtering length scale $l_{sob} = 0.1\,D$.

a limited capability to capture theses extrema. Let us note that dealing with experimental data, that are susceptible to imperfections, leads to errors deemed important whatever parametrization is used. For instance, this can be seen in the suction point located at the lateral face (at $z/D = 0.33$) in which improvement stays within $60 - 79\%$ for all models (in table 6.3). Moreover, although the qualitatively good agreement with data obtained in the leeward faces with the direct forcing (see figure 6.21), averaged wall-metric does not favour it over a more structured forcing. Recall that the great agreement in the leeward was associated with a consequent loss of flow features in the near wake, especially the spanwise vortex created downstream of the roof-top trailing edge. So far, with this wall-metric, it can be concluded that a structured forcing is actually better suited to estimate peak wall pressure than a highly flexible form. Moreover, a good prediction of the momentum diffusion adjustment can be achieved by the closure parameter f_ϵ. Evermore, by combining structured forcing on the momentum equation and correction on the closure parameter f_ϵ with a slight penalty still leads to good performances for wall-pressure reconstruction.

Wake predictions Examining the averaged flow metrics $A^1(\mathcal{M}_2), A^1(\mathcal{M}_3)$ reveals a reversed trend between them. As a matter of fact, the more reduction of the recirculation length, the worst the prediction of the peak streamwise velocity. With no penalization took into consideration, the only adjustment of the closure (by f_ϵ) enables the lowest bubble extension but leads to the least accurate predictions, falling outside the base model error. On the other hand, the only correction of the structured force leads to the least wake contraction and the best error decrease.

With the penalty, this dis-proportionality is more accentuated, as the parameter is further smoothed. In order to properly account for this dis- proportionality and derive a concise performance evaluation, the compromise quantity $A^2(\mathcal{M}_2, \mathcal{M}_3)$ becomes relevant (table 6.5). We recall that this quantity relates the degree of improvement in recirculation length (and not the error itself) with the peak error upstream velocity. Since both quantities have opposite trend, it measures the compromise between them. From table 6.5, it can be observed that the synchronous adjustment of the closure with the force provides the better compromise ($A^2 = 0.8$), and this is better achieved with no penalization, A^2 with penalty ranging around 0.5. It can be also seen that the direct forcing gives even a lower compromise ($A^2 = 0.56$) as compared with the most constrained parametrization by only correcting f_ϵ ($A^2 = 0.64$). This suggests that this metric can be partially representative of the quality of reproduction of flow features. As the former fails in reproducing physical patterns in the recirculation region, such as the spanwise vortex in at the high end, while the latter fairly reproduces it. So far, it is noteworthy to mention that the trend of the performance given by A^2 for each parametrization seems to agree with the trend of the wall-pressure accuracy. Both point out that the structured form with and without closure adjustment offers overall better quality in reconstruction. Let us note that this agreement suggests a consistency between wall pressure and wake, since dynamics of the wake drives the back pressure of the building. In such a complex three-dimensional flow, this consistency between metrics is not staightforward and is dependant on the metric definition.

The conditions for consistency may be investigated in future work.

As we go further and examine the actual flow topology, illustrated in figures 6.23 and 6.22, it can be seen that correcting at the same time $(|\nabla k| f_u, f_\epsilon)$ leads to a solution, intermediate between both individual corrections $(|\nabla k| f_u, 0)$ and $(0, f_\epsilon)$.

In the symmetry plan, we clearly see a recirculation bubble greatly reduced and a saddle point location in a good agreement with PIV data. It is however still noted that the model pulls the focal point near the high end to the leeward facade, effect performed to (over)fit the wall-pressure at the high end of the leeward facade. Nonetheless, this remaining overfitting artefact is very limited in space as the transverse structures are greatly retrieved. The reconstructed flow still recovers the lateral vortex rolls, which extend from the ground and meet at the high-end vortex on the symmetry plan, with the focal points in the horizontal planes being well captured until height $z/D = 3.33$ with downstream location of $x/D \simeq 1.5$. This location is right intermediate between the base RANS and the PIV $(x/D \simeq 1)$ (see figure 6.23). Note that, except with the correction of f_ϵ solely, both structured/raw form of forcing with default closure does not capture them at all.

Therefore, by considering both the qualitative observations of the flow features and the proposed wall/flow metrics, it can be summarized that combination of a direct forcing on the momentum equation with simple structuring form along with a forcing on the transport equation of ϵ is a quite promising strategy, as it ensures overall a good quality to the reconstruction. However, it is worth-noting that although the quantitative flow metric A^2 did not favours the penalization, examining the qualitative flow topology suggests possible restitution of some physical features. This was observed by the re-capturing of the high-end focal point with the couple of scaling $(\zeta_{f_{u_i}}, \zeta_{f_\epsilon}) = (0.5, 15)$, which is otherwise absent (see figure 6.24). Therefore, providing a penalization plays an important role in refining the flow features; yet, an adequate couple of scaling is required to provide a good compromise between a well interpolated wall-pressure and a best retrieval of realistic flow patterns.

Despite the quality benefits on the final flow field, it can be noticed that with a penalty, a robust DA procedure can be ensured. In this study, the L^2 norm of the gradient was minimized. Regularisation in minimisation problems is a wide research area in itself, and other strategies exist, such as L-curve method, physical-based background covariance matrix definitions, or sparsity promoting with L^1 norm regularisation (Farchi and Bocquet, 2019). Moreover, by further expanding its dimension, a supervised tuning of the scaling factor can be performed on a specific region.

6.7 Conclusions

In this chapter, we performed a further investigation of the variational approach for the reconstruction of mean flow around the high-rise building. We recall that only pressure measurements in the facades have been assimilated. After addressing possible sources of modelling errors, underlying the different layer of assumptions used to build the closure, it was seen that inferring a control parameter embedded in a term-by-term basis, yields

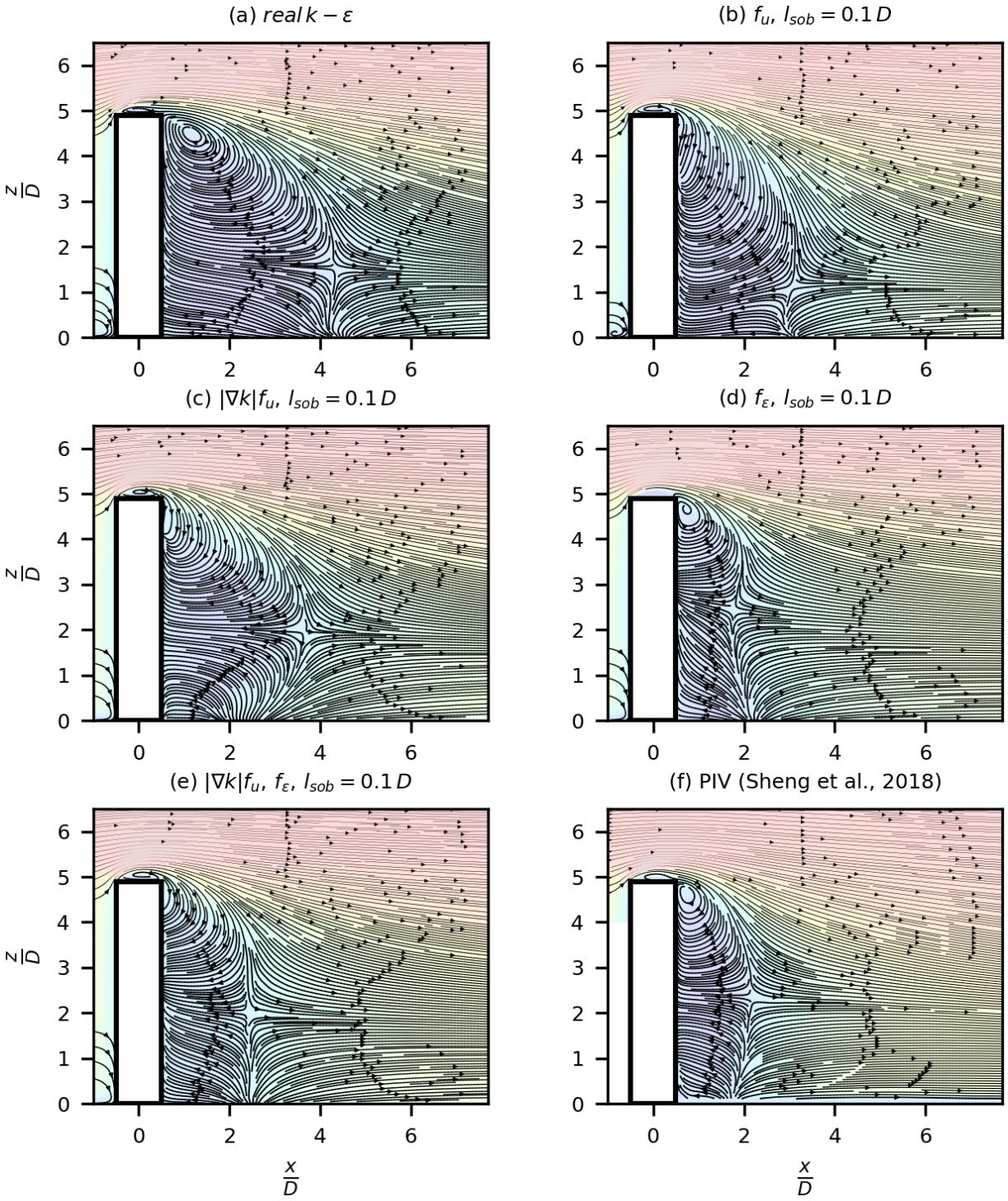

Figure 6.22 – Flow topology (2D) on symmetry plane. Comparison with flow reconstruction,(e) , under a correction of a structured force with a modified closure applied on ϵ budget with no penalization, (b), raw-force, (c), structured force, with default closure, and (d), modified closure made at the ϵ budget. The steepest descent direction is improved for all algorithms by the use of Sobolev gradient with filtering length scale $l_{sob} = 0.1\,D$.

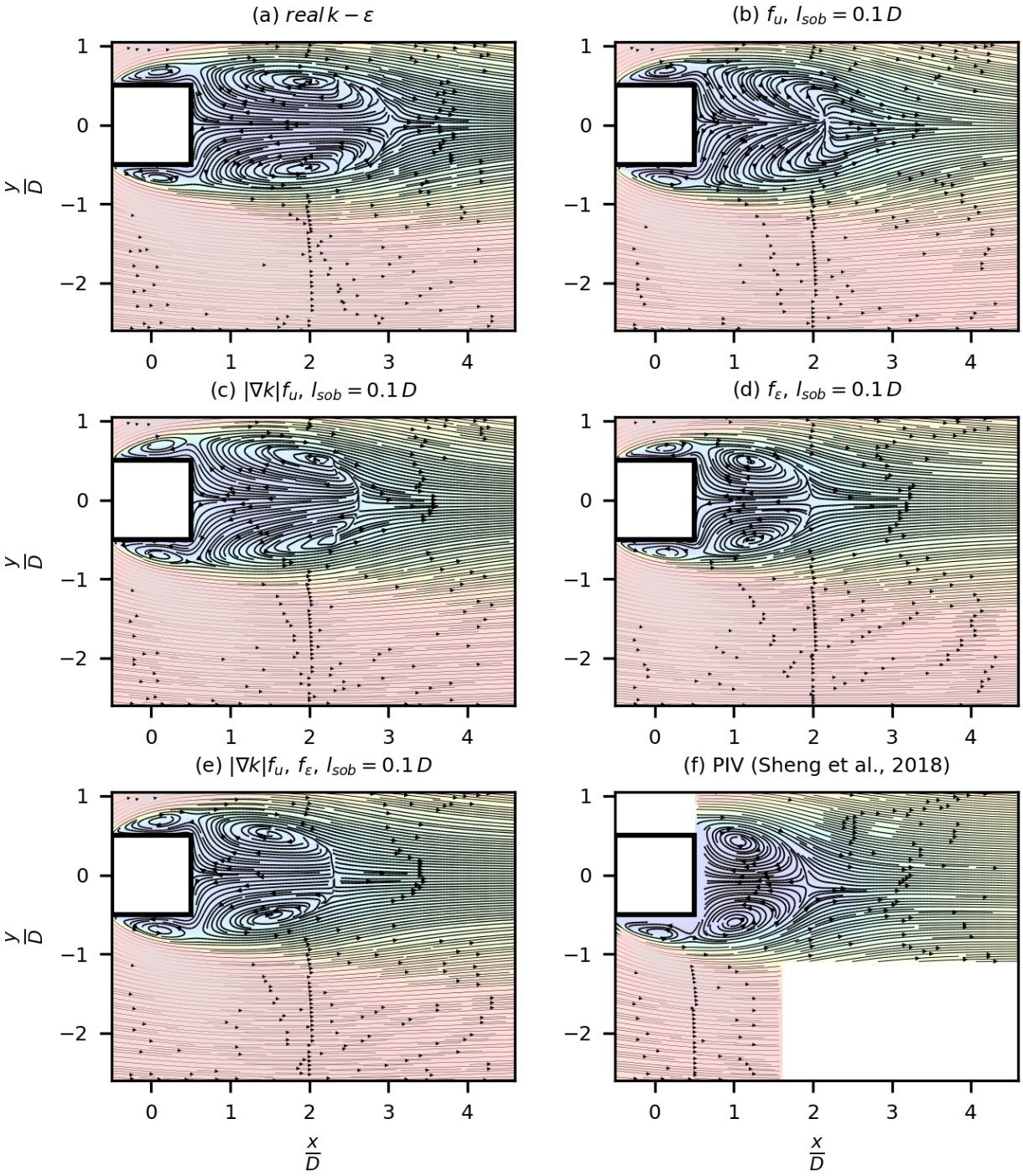

Figure 6.23 – Flow topology (2D) on horizontal plane at normalized height $z/D = 3.33$. Comparison with flow reconstruction,(e) , under a correction of a structured force with a modified closure applied on ϵ budget with no penalization, (b), raw-force, (c), structured force, with default closure, and (d), modified closure made at the ϵ budget. The steepest descent direction is improved for all algorithms by the use of Sobolev gradient with filtering length scale $l_{sob} = 0.1\,D$.

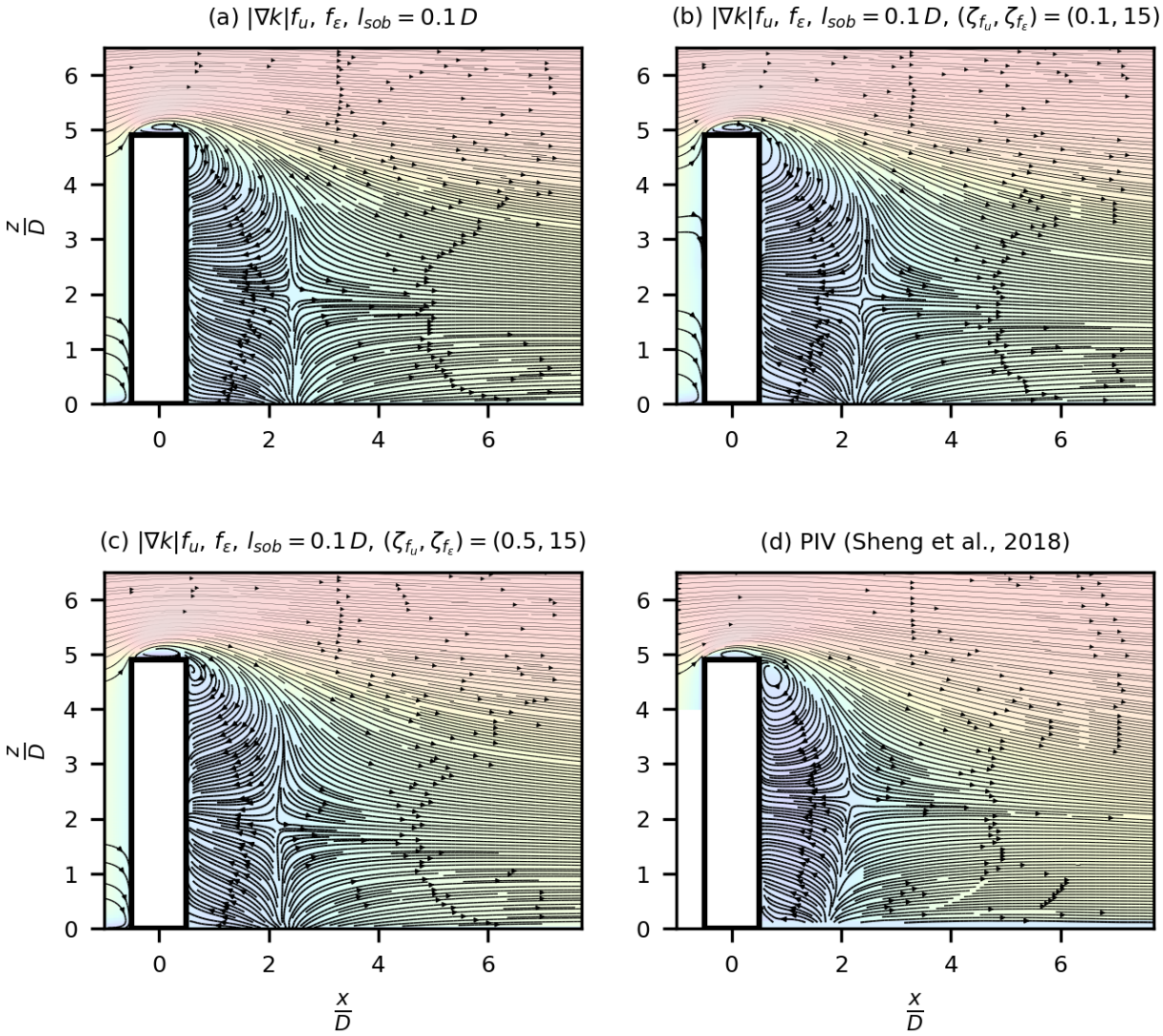

Figure 6.24 – Flow topology (2D) on symmetry plane. Comparison with flow reconstruction,(a) , under a correction of a structured force with a modified closure applied on ϵ budget with no penalization, (b), with penalization $(\zeta_{f_{u_i}}, \zeta_{f_\epsilon}) = (0.1, 15)$, (c), $(\zeta_{f_{u_i}}, \zeta_{f_\epsilon}) = (0.5, 15)$. The steepest descent direction is improved for all algorithms by the use of Sobolev gradient with filtering length scale $l_{sob} = 0.1\,D$.

ill-conditioned matrices of the adjoint model which leads to numerical instabilities. For example, a correction of the production term for k just by itself, causes inconsistency of the model with the near-wall treatment. To overcome these limiting factors, we have considered the adjunction of distributed parameters, enabling the reconsideration of the closure at a structural level. With the considered turbulence model, we have introduced two corrective strategies for its closure; one on the transport equation for the energy k, and the second one on its dissipation rate ϵ. The shape of the parameters were chosen to complement the turbulence model in terms of local source/sink mechanism. As a sensitivity field is generally not very regular for distributed parameters, searching for the control parameter in Sobolev's space $H^1(\Omega)$ was proposed here for both a regularisation purpose and to define an improved descent direction for the minimising technique. Let us note that, along with the use of Sobolev gradient, the robustness of the DA procedure was enabled as a first order numerical scheme to solve the dual dynamics.

Both parameters sensitivity maps highlighted regions where global constants (from chapter 4) are not too sensitive (i.e. the wake) and exhibit relatively less variability in term of sign changes. Their maps have actually revealed binary tendencies, separating the lateral and top shear regions and the wake flow. Regarding the reconstruction ability, compared with coefficient calibration, the modified closure models produced better results in most of the building's wall regions in terms of wind load profiles. An excellent agreement with PIV experiments was obtained in wake transverse extension. This good agreement with measurements of different nature and that have not been used in the assimilation proved that we are neither overfitting the data nor in an over-constrained situation

Yet, as the flow adjustment comes only from diffusive effects (Boussinesq assumption), results suggest some remaining restrictions as reconstructed profiles tend toward the original model in some regions and limiting barrier as we still miss other energy exchange mechanisms. To propose an alternative solution, while maintaining the Boussinesq assumption, we proposed investigating the coupling of a direct correction of deformation and the adjustement the turbulence closure equation. Toward an efficient hybridization, control parameter forms has played a huge role here. The structured force were chosen over the raw form for its consistency and for its close relation (in its effect) with Reynolds isotropic part. The reconstruction results were then discussed, and the quality of the reconstruction was evaluated visually and by the definition of some wall/flow validations metrics. Comparison is made with the direct correction with standard closure. Both the qualitative observations of the flow features and the proposed wall/flow metrics show that the combination of a direct forcing with simple structuring form and local closure adjustment is a quite promising strategy as it ensures overall a good quality to the reconstruction. Moreover, the conjunction of Sobolev gradient $/L^2$ gradient penalization may help refine the quality of the flow feature; yet, an adequate couple of scaling is still needed to provide a satisfactory compromising between wall-pressure interpolation and retrieval of realistic flow patterns. Besides the quality benefits on the final flow field, it was noticed that a rather robust DA procedure could be ensured with the addition of penalty. It is thus suggested that an L^1 norm might help to improve toward that end.

Chapter 7

Conclusion

7.1 Work summary

The present investigation aimed to devise and investigate variational data assimilation (VDA) methodologies for the prediction of turbulent wind flows around big-structures. The Reynolds Averaged Navier-Stokes equations (RANS) constitute the base mathematical model to describes the mean flow state. For its improved capability to account for the energy transfer with strong strain rates, the realizable revision developed by Shih et al. (1995) is chosen also as a reference turbulence closure. The inflow wind profile models the lower part of the atmospheric boundary layer, under the assumption of horizontal homogeneity. The case on which we focus on in this study is dedicated to the analysis of a high-rise building with a square section and an aspect ratio of $H/D \sim 5$. The data we have considered for the assimilation is the averaged wall-pressure measured on a scaled model of the building in a wind tunnel experiment by Sheng et al. (2018) at CSTB (Nantes, France). This constitutes a first step towards the application of VDA procedure to practical situations in structural wind engineering in which field measurements on significant part of the whole flow volume are generally not affordable and/or too time consuming. Note that, in this thesis, the assessment of the quality of the data-assimilated flow field was conducted with some PIV data plans from the same experiment.

A brief historical review on structural wind engineering studies and a survey of literature studies on VDA techniques and their application in CFD are provided in chapter 1.

In chapter 2, It has been demonstrated that the numerical grid is sufficiently refined to obtain approximately a grid-independent reference solution, such that the only remaining data-model discrepancy arises (almost) only from conceptual consistencies.

Local sensitivity analysis of model closure coefficients conducted in chapter 4 points out one of the common reasons for the deficiencies of RANS predictions in the regions of recirculating flow. Indeed, high sensitivites have been located at the formation of shear layers, which originate from the sharp edges of the body, suggesting strong discrepancies of turbulence modelling in these regions. Despite all the spatial variability of theses sensitivity maps, it was shown that the optimality condition drastically reduces the high dimensional dependency of the model to each coefficient, reflecting thus a "rigid" character of such closure. Moreover, it was observed that data-assimilation techniques are able to provide insight on the model variability through coefficient calibration. Regarding the model hypotheses underlying such closure, a better data coupling can be obtained by enforcing the constraint that equates turbulence energy to momentum mixing, even though

its initial sensitivity suggests globally a thinner turbulent mixing layer. This suggests that it is a physically valid hypothesis that structures the model and then helps for convergence. On the other hand, a constraint on the local increase of energy dissipation rate linked to its redistribution (supposedly valid in the inertial layer near the wall), has led to stiff situation. As both assumptions constitute a common practice for closure definition in most eddy viscosity models, it is expected that these results extend to several other models of similar forms when used with realistic wall pressure measurements. Due to the rigidity of the model, variabilities of the solution were strongly constrained and does not allow the flow to reach a sufficiently large state space domain for accurate estimations.

To overcome such restrictions, in chapters 5, a reconstruction viewpoint to the problem was first considered by adopting a *weak constraint*, *i.e.* defining an additive forcing term as control parameter in order to allow the solution to deviate from the default model constraints. Without a priori knowledge of its nature, an initial raw form was considered similarly to works by (Foures et al., 2014; Franceschini and Sipp, 2020). Sensitivity maps analysis has revealed high interest to force at regions encompassing all flow features; the upstream flow impingement (e.g. upstream separation, horseshoe formation), the lateral and top shear layers, the wake. To suppress unphysical oscillations of the force, given the strongly partial observations, we have investigated two regularization approaches; a first one is performed by penalizing the L^2 norm of its gradient, while the second was instead conducted by the definition of an alternative inner product $H^1(\Omega)$ of the optimality condition. We have particularly considered the search for a control parameter in Sobolev's space (Protas et al., 2004; Tissot et al., 2020). Regarding the effects of regularisation, cost reduction results with the use of Sobolev gradient yields a much faster convergence and lower discrepancy levels. With regards to the wall-pressure interpolations, in comparison to the coefficients calibration, the model allowed an excellent agreement with the wall-pressure experiments in most of the building's wall regions. With regards to flow reconstruction ability, the models results show a considerable reduction of its downstream extension, yet, not in a fully satisfactory way by producing non-physical-features in the near wake flow. This have raised the point about the lack of structuration to the forcing. In order to remedy this situation, we proceeded by refining the shape of the force with the aim to ensure some consistency between the deformation correction prescribed by the direct enforcing and a Reynolds stresses induced force. With anisotropy being quite poorly represented by eddy viscosity models (and the $k-\epsilon$ closure), we considered addressing only corrections to the flow inhomogeneity, i.e. regions with a strong gradient of turbulent energy. From the sensitivity map, it was indeed clear that its new shape has enabled us to delineate the potential sources of mismatch in the modelled Reynolds stress to a thin region within the shear layers, i.e the region resulting from the first flow separation at the leading edges. Meanwhile, it shows fewer interest further downstream in the wake. In terms of objective, globally, discrepancy with wall-pressure experiments has been reduced significantly, and in faster way, reaching a state very close to the one achieved with raw forcing. Moreover, a better retrieval of the wake's features, e.g. upstream inclination of the vortex rolls near the ground wall, was noticed. Although, being less sensitive in the

downstream wake, it only leads to a small contraction recirculation bubble. Even leading to an imperfect reconstruction, the fact that it accelerates the optimisation with comparable performances suggests that these located regions are mainly responsible of the RANS failure, and encourages the strategy of refining the structure of the control parameters.

Finally, in chapter (6), we performed a further investigation of the variational approach for the reconstruction under a parametrization that satisfies the physical constraints given by the turbulence model, yet, in a more efficient way. After addressing possible sources of modelling errors, underlying the different layer of assumptions used to build the closure, it was seen that inferring a control parameter embedded in a term-by-term basis, yields ill-conditioned matrices of the adjoint model leading hence to numerical instabilities. Thus, we have considered instead the adjunction of distributed parameters which enables the reconsideration of the closure at a structural level. With the considered turbulence model, we have introduced two corrective strategies for its closure; one on the transport equation for the energy k, and the second one on its dissipation rate ϵ. Following the similar reasoning as with the structured force, the shape of the parameters were chosen so as to complement the turbulence model in terms of local source/sink mechanisms. A search onto the Sobolev space $H^1(\Omega)$ was then performed for both a regularisation purpose and to define the descent direction. Sensitivity maps to theses new closures highlighted regions where global constants are not too sensitive, i.e. the wake. Besides, a step tendency was revealed separating the lateral and top shear regions and the wake flow. As for the VDA procedure, the modified closure models produced improved results in most of the building's wall regions in terms of wind load profiles, compared with coefficient calibration, and an excellent agreement with PIV experiments was obtained in wake transverse extension. The good agreement with the non-assimilated measurements (of different nature) proved that we are neither overfitting the data nor in an over-constrained situation. Yet, as the flow adjustment comes only from diffusive effects (with other energy exchange mechanisms that are still missing), results suggest some remaining restrictions as reconstructed profiles tend toward the original model in some regions. To propose an alternative solution, while maintaining the Boussinesq assumption, we proposed investigating the coupling of a direct correction of deformation and the local adjustment of turbulence closure. Toward an efficient hybridization, the structured shape of force were chosen over the raw form for its close relation (in its effect) with Reynolds isotropic part. Both the qualitative observations of the flow features and a defined wall-pressure/flow validation metrics has showed that the combination of a direct forcing with a simple structuring form along with local closure adjustment is a promising strategy as it ensures overall a good quality to the reconstruction. Moreover it was observed that the conjunction of Sobolev gradient/L^2 gradient penalization may help refining the recovery of the flow features. Beside the improvement of the qualitative flow features, it was noticed that with the addition of penalty a more robust VDA procedure can be ensured especially when approaching minimal cost where the descent direction, giving by the continuous adjoint, is scrambled with numerical inconsistency.

7.2 Suggestions for future work

Under the same framework, i.e continuous adjoint model of the realizable $k-\epsilon$, several tools for robust minimization can be further explored. The first important component is the regularization. Indeed, in the current study we have considered solely the Euclidien norm L^2 of the spatial gradient of the parameter in question. However, this is not the only way to proceed, and various strategies can be considered instead. Note for instance that by considering a different measure of the magnitude of the gradient, one may promote more efficiently the sparsity of the parameter field and hopefully yields better interpretation to the corrections, e.g. L^1 norm. Another way to deal with parameter irregularity may be by penalizing the magnitude itself, provided an initial smooth guess. Of course, the desired degree of regularity depends on the chosen norm. Moreover, an alternative and less direct manner of sensitivity regularization can be transmitted through state regularization. This is formally achieved by augmenting the objective by a distance (L^1 or L^2 norm) that measures the deviation of the optimised state from a background one. This state deviation is then transfered as a constraint to the adjoint system preconditioning thus the adjoint state for the optimality condition. So far, regardless the penalty term, the trust given in the local state/parameter deviations were assumed uniformly distributed in space and non-correlated with neighbouring spatial locations. This uniform and local character might be a too strong assumption when dealing with flow statistics that cannot be only determined in local basis (e.g. the Reynolds stress). Relaxing this assumption can be done by devising a more elaborated covariance matrices that better account for non local effects and considering the likely correlation between neighbour measures. Furthermore, instead of a scalar factor, this can lead to a more supervised tuning of the penalty, e.g by adjustment on specific regions.

Once we ensure some degree of regularity to the sensitivity field, a second major component is the descent direction itself. In analogy with the locality issue of the trust given to the penalty, a more precise estimate of the gradient can be attempted by considering the curvature of the cost of the parameter. This can be formally achieved using second order estimate quasi-Newton method, by which the curvature can be estimated by the Hessian w.r.t to the parameter. As in our study, i.e. dealing with large scale optimization, the limited memory quasi-Newton methods L-BFGS (Byrd et al., 1995) can be seen as an adequate tool to accelerate convergence. We note that this latter approach can be seen as another alternative for gradient projection methods, such as in the Sobolev space, and an extension to the conjugate gradient.

Another technical solution for the estimation of the gradient, which requires major changes of the framework we have established in this thesis, consists in the implementations of the so-called numerically "exact" gradient. A discrete derivation of the adjoint model can indeed be considered. This will also require integrating the so-called "Automatic" Differentiation tools well suited to the specific structure of the OpenFOAM library. The "operator overloading" approach seems to be the most appropriate to adopt here such as ADOL-C (Griewank and Walther, 2008). In practice, this approach consists in evaluat-

ing (and storing) for each elementary calculation instruction the value of a scalar variable and its derivative with respect to a variable considered independent. Because at the elementary level of instruction only simple operators (addition, subtraction, multiplication) or usual functions (cosine, sine, log) of which we know how to calculate their derivatives analytically are involved, we would approach orders of "zero machine" error. On the other hand, in the presence of thresholds (e.g. flux limiter schemes, upwind, max and min), its performance depends on the way by which we treat these sources of discontinuity.

Otherwise, from a modelling viewpoint, to enrich the understanding of the structures and limits of turbulence modeling with a viewpoint of data-assimilation, this study can be applied in conjunction with different turbulence models. Besides, as the Boussinesq assumption clearly enforces a limiting barrier by not representing all the energy exchange mechanisms (e.g. through the organized big turbulent scales and the possibly negative eddy viscosity which may acts as an anti diffusion), high fidelity closure to the Reynolds stress (e.g. RSM) might present an interesting alternative constraint.

Moreover, from a methodological point of view, given only partial pressure measurements, an extension of modal decomposition approaches (decomposition into balanced truncation modes, resolvent analysis) would present an alternative to provide some structuration to to the optimal parameter. In the context of data-assimilation for flow reconstruction, resolvent analysis was recently investigated by various authors (Beneddine et al., 2017; Symon et al., 2020; Franceschini, 2019). Indeed, these methods have proved their efficiency in configurations (2D flow) with matrices of reasonable sizes. Thus, it may well fit into a future work to be investigated, as in such complex configurations (3D) and higher, i.e with matrix size $\sim 1.8\,10^7$ in the present study, such methodology has not yet been explored.

Finally, without going through turbulence models, stochastic modeling where turbulence is assimilated to a random process guided by data can also be investigated as an alternative (Mémin, 2014; Harouna and Mémin, 2017; Bauer et al., 2020b,a).

APPENDIX : CONTINUOUS ADJOINT DERIVATION OF RANS MODEL WITH REALIZABLE $k - \epsilon$ CLOSURE

Under differentiability condition, it can be shown (Le Dimet and Talagrand, 1986; Gunzburger, 2003) that the problem of determining the optimal set of flow state variables,

$$\mathbf{X} = (\mathbf{U}, P, k, \epsilon, \mu_t)$$

and the set of parameters α, of the cost function $\mathcal{J}(\mathbf{X}, \alpha)$ under the constraint

$$\mathbf{M}(\mathbf{X}, \alpha) = 0$$

is equivalent to the problem of determining the optimal set of theses variables in addition to an adjoint state

$$\mathbf{X}^* = (\mathbf{U}^*, P^*, k^*, \epsilon^*, \mu_t^*)$$

of the associated Lagrangian functional $\mathcal{L}(\mathbf{X}, \mathbf{X}^*, \alpha)$. With the inner product defined as $\langle \psi, \phi \rangle_\Omega = \int_\Omega \psi^T \phi \, \mathrm{d}\Omega$ where ψ and ϕ are any two regular vectorial functions defined on the domain Ω, the Lagrangian, is

$$\mathcal{L}(\mathbf{X}, \mathbf{X}^*, \alpha) = \mathcal{J}(P, \alpha) + \int_\Omega (\mathbf{X}^*)^T \mathbf{M}(\mathbf{X}, \alpha) \, \mathrm{d}\Omega. \tag{7.1}$$

This extended variable formulations allows to transform a constrained optimisation problem to an unconstrained optimisation problem. Differenciating the Lagrangian leads to the resolution of the optimisation problem. The minimum is found by vanishing its directional derivatives with respect to each of the variables.

Duality principle and optimality system

The first order variation $\delta\mathcal{L}$ resulting from perturbation $(\delta\mathbf{X}, \delta\mathbf{X}^*, \delta\alpha)$ of $(\mathbf{X}, \mathbf{X}^*, \alpha)$, in compact form, is equal to

$$\begin{aligned}\delta\mathcal{L} = \frac{\partial\mathcal{J}}{\partial P}\delta P + \frac{\partial\mathcal{J}}{\partial\alpha}\delta\alpha + \int_\Omega \underbrace{(\mathbf{X}^*)^T\left(\frac{\partial\mathbf{M}}{\partial\mathbf{U}}\delta\mathbf{U}\right)}_{I}\,\mathrm{d}\Omega + \int_\Omega \underbrace{(\mathbf{X}^*)^T\left(\frac{\partial\mathbf{M}}{\partial P}\delta P\right)}_{II}\,\mathrm{d}\Omega \\ + \int_\Omega \underbrace{(\mathbf{X}^*)^T\left(\frac{\partial\mathbf{M}}{\partial k}\delta k\right)}_{III}\,\mathrm{d}\Omega + \int_\Omega \underbrace{(\mathbf{X}^*)^T\left(\frac{\partial\mathbf{M}}{\partial\epsilon}\delta\epsilon\right)}_{IV}\,\mathrm{d}\Omega + \int_\Omega \underbrace{(\mathbf{X}^*)^T\left(\frac{\partial\mathbf{M}}{\partial\mu_t}\delta\mu_t\right)}_{V}\,\mathrm{d}\Omega \\ + \int_\Omega (\mathbf{X}^*)^T\left(\frac{\partial\mathbf{M}}{\partial\alpha}\delta\alpha\right)\,\mathrm{d}\Omega + \int_\Omega (\delta\mathbf{X}^*)^T\mathbf{M}(\mathbf{X},\alpha)\,\mathrm{d}\Omega. \end{aligned} \tag{7.2}$$

We note that terms $(I - V)$ will be expanded later in the next section. For conciseness, we keep it herein compact. Using the duality identity defined as

$$\int_\Omega \underbrace{(\mathbf{L}\phi)\,\psi}_{i}\,\mathrm{d}\Omega = \int_{\partial\Omega} (\mathbf{L_B}\phi)\;\;(\mathbf{L_C}\psi)\,\mathrm{d}\partial\Omega + \int_\Omega \underbrace{\phi\,(\mathbf{L}^*\psi)}_{i^*}\,\mathrm{d}\Omega$$

where $\mathbf{L}$ is a linear differential operator and ($\mathbf{L_B}$,$\mathbf{L_C}$) are lower order differential operators, resulting from the integration by part, that embed the natural boundary condition. The variation $\delta\mathcal{L}$ becomes

$$\begin{aligned}\delta\mathcal{L} = \frac{\partial\mathcal{J}}{\partial P}\delta P + \frac{\partial\mathcal{J}}{\partial\alpha}\delta\alpha - \int_\Omega \underbrace{\left(\frac{\partial\mathbf{M}}{\partial\mathbf{U}}^*\mathbf{X}^*\right)^T\delta\mathbf{U}}_{I^*}\,\mathrm{d}\Omega + \int_\Omega \underbrace{\left(\frac{\partial\mathbf{M}}{\partial P}^*\mathbf{X}^*\right)^T\delta P}_{II^*}\,\mathrm{d}\Omega \\ + \int_\Omega \underbrace{\left(\frac{\partial\mathbf{M}}{\partial k}^*\mathbf{X}^*\right)^T\delta k}_{III^*}\,\mathrm{d}\Omega + \int_\Omega \underbrace{\left(\frac{\partial\mathbf{M}}{\partial\epsilon}^*\mathbf{X}^*\right)^T\delta\epsilon}_{IV^*}\,\mathrm{d}\Omega + \int_\Omega \underbrace{\left(\frac{\partial\mathbf{M}}{\partial\mu_t}^*\mathbf{X}^*\right)^T\delta\mu_t}_{V^*}\,\mathrm{d}\Omega \\ + \int_\Omega \left(\frac{\partial\mathbf{M}}{\partial\alpha}^*\mathbf{X}^*\right)^T\delta\alpha\,\mathrm{d}\Omega + \int_\Omega (\delta\mathbf{X}^*)^T\mathbf{M}(\mathbf{X},\alpha)\,\mathrm{d}\Omega + \int_{\partial\Omega}(\delta\mathbf{X})^T(\mathbf{C}\mathbf{X}^*)\,\mathrm{d}\partial\Omega \\ + \int_{\partial\Omega}(\delta\alpha)^T(\mathbf{D}\mathbf{X}^*)\,\mathrm{d}\partial\Omega + \int_{\partial\Omega}(\mathbf{B}\delta\mathbf{X})^T\mathbf{X}^*\,\mathrm{d}\partial\Omega + \int_{\partial\Omega}(\mathbf{E}\delta\alpha)^T\mathbf{X}^*\,\mathrm{d}\partial\Omega, \end{aligned} \tag{7.3}$$

where ($\mathbf{B}$,$\mathbf{C}$,$\mathbf{D}$, $\mathbf{E}$) are boundary differential operators. Terms $(I^* - V^*)$ are the adjoint to their counterpart terms in (7.2), which will be expanded later.

So far, it is worth-noting to mention that prior to the integration by part, eventual discontinuities underlying the direct terms has to be treated properly, e.g. replacing step functions by hyperbolic tangents. These discontinuities are most often a result of thresholds, flux limiters of numerical schemes and some times it is purely numerical as it avoid evaluating function outside the domain of their arguments. If not pretreated, adjoint model would not be consistent with the tangent linear of the model.

Since the perturbations are arbitrary, setting the first variation of $\mathcal{L}$ with respect to

the Lagrangian arguments equal to zero leads to an optimality system. With respect to an arbitrary variation of the adjoint state, we recover the constraint equations; while for an arbitrary variation of the state $\mathbf{X}$ all the terms that include the product of adjoint state to the tangent linear of the constraint has to vanish. Further, with respect to the set of parameters, vanishing the total variation leads to an optimality condition that constitute the optimality system. Collecting these results yields to

$$\begin{aligned} \textit{state equations} \quad &\Rightarrow \quad \mathbf{M}(\mathbf{X}, \alpha) = 0 \\ \textit{adjoint equations} \quad &\Rightarrow \quad \left(\frac{\partial \mathbf{M}}{\partial \mathbf{X}}\right)^* \mathbf{X}^* = 0 \\ \textit{optimality condition} \quad &\Rightarrow \quad \frac{\partial \mathcal{J}}{\partial \alpha} + \left(\frac{\partial \mathbf{M}}{\partial \alpha}\right)^* \mathbf{X}^* = 0, \end{aligned}$$

where $\left(\frac{\partial \mathbf{M}}{\partial \alpha}\right)^*$ is the adjoint of the model derivative with respect to the parameters. If it is possible to solve this coupled optimality system through one-shot methods, then optimal states and parameters can be obtained without an optimisation iteration. However, due to non linearity and the very large size of this system ($\sim 3 \times size(\mathbf{X})$) one still have to iterate in order to solve the optionality system. Thus, having solved the state equations for $\mathbf{X}$ and then $\mathbf{X}^*$ solution of the adjoint system, model parameters can be iterated by a gradient based optimisation algorithm until optimality condition is satisfied. In a steepest descent algorithm, the parameter is updated at an iteration n according to:

$$\alpha^{n+1} = \alpha^n - \lambda_n \, d_n \tag{7.4}$$

where d_n is the descent direction which is defined recursively by:

$$d_n = \frac{\partial \mathcal{L}}{\partial \alpha} = \left(\frac{\partial \mathbf{M}}{\partial \alpha}\right)^* \mathbf{X}^* + \frac{\partial \mathcal{J}}{\partial \alpha}. \tag{7.5}$$

Concerning adjoint based optimisation methods, we refer the reader to (Gunzburger, 2003; Gronskis et al., 2013).

Duality with the realizable $k - \epsilon$

In this section, more details regarding the derivation of the adjoint model are brought. We illustrate the manner in which model specificities are treated in the adjoint procedure. More precisely, we consider the modification of the $k - \epsilon$ model to ensure realizability condition, .

Thus, expanding the integrands, the expression (7.1) is rewritten as follow,

$$\begin{aligned}\mathcal{L}(\mathbf{X},\mathbf{X}^*,\alpha) = \mathcal{J}(P,\alpha) &+ \int_\Omega \sum_{i=1}^{3} U_i^* \underbrace{\left(\frac{\partial(\rho U_j U_i)}{\partial x_j} + \frac{\partial}{\partial x_i}P - \frac{\partial}{\partial x_j}\left[\mu_{eff}\left(\frac{\partial U_i}{\partial x_j} + \frac{\partial U_j}{\partial x_i}\right)\right]\right)}_{M_{U_i}} \mathrm{d}\Omega \\ &+ \int_\Omega P^* \underbrace{\left(\frac{\partial U_j}{\partial x_j}\right)}_{M_P} \mathrm{d}\Omega + \int_\Omega k^* \underbrace{\left(\frac{\partial \rho U_j k}{\partial x_j} - \frac{\partial}{\partial x_j}\left[\left(\mu + \frac{\mu_t}{\sigma_k}\right)\frac{\partial k}{\partial x_i}\right] - \mu_t\left(\frac{\partial U_i}{\partial x_j} + \frac{\partial U_j}{\partial x_i}\right)\frac{\partial U_i}{\partial x_j} + \rho\epsilon\right)}_{M_k} \mathrm{d}\Omega \\ &+ \int_\Omega \epsilon^* \underbrace{\left(\frac{\partial \rho U_j \epsilon}{\partial x_j} - \frac{\partial}{\partial x_j}\left[\left(\mu + \frac{\mu_t}{\sigma_\epsilon}\right)\frac{\partial \epsilon}{\partial x_i}\right] - \underbrace{C_1(S,k,\epsilon)S\epsilon}_{P_\epsilon} + \underbrace{C_2\frac{\epsilon^2}{k+\sqrt{\mu\epsilon}}}_{S_\epsilon}\right)}_{M_\epsilon} \mathrm{d}\Omega \\ &+ \int_\Omega \mu_t^* \underbrace{\left(\mu_t - C_\mu(U_i,k,\epsilon)\rho\frac{k^2}{\epsilon}\right)}_{M_{\mu_t}} \mathrm{d}\Omega \end{aligned} \tag{7.6}$$

In fact, upon a first variation of the Lagrangian w.r.t each state component, each one of the terms $(I - V)$ in (7.2) is indeed the weighted sum of partial derivative of the designated terms $(M_{U_i} - M_{\mu_t})$ in (7.6).

We detail here the directional differentiation w.r.t the state vector. The derivations w.r.t the parameter α are straightforward for both global coefficients cases, given in chapter (4), and the adjunction of terms in last chapters (5 and 6). In what follows, directional derivatives of (7.6) are expressed separately.

The Gateau derivation

Term (I) expansion : The partial derivative of (7.6) in direction δU_i leads to the following:

$$\begin{aligned}\left\langle \frac{\partial \mathcal{L}}{\partial U_i}, \delta U_i \right\rangle_\Omega = \int_\Omega \Bigg[&\sum_{i=1}^{3} U_i^* \underbrace{\left(\frac{\partial(\rho\delta U_j U_i + U_j \delta U_i)}{\partial x_j} - \frac{\partial}{\partial x_j}\left[\mu_{eff}\left(\frac{\partial \delta U_i}{\partial x_j} + \frac{\partial \delta U_j}{\partial x_i}\right)\right]\right)}_{\frac{\partial M_{U_i}}{\partial U_i}} \\ &+ P^* \underbrace{\left(\frac{\partial \delta U_j}{\partial x_j}\right)}_{\frac{\partial M_P}{\partial U_i}} + k^* \underbrace{\left(\frac{\partial \rho \delta U_j k}{\partial x_j} - \mu_t\left(\frac{\partial \delta U_i}{\partial x_j} + \frac{\partial \delta U_j}{\partial x_i}\right)\frac{\partial U_i}{\partial x_j} - \mu_t\left(\frac{\partial U_i}{\partial x_j} + \frac{\partial U_j}{\partial x_i}\right)\frac{\partial \delta U_i}{\partial x_j}\right)}_{\frac{\partial M_k}{\partial U_i}} \\ &+ \epsilon^* \underbrace{\left(\frac{\partial \rho \delta U_j \epsilon}{\partial x_j} - \frac{\partial P_\epsilon}{\partial U_i}\delta U_i\right)}_{\frac{\partial M_\epsilon}{\partial U_i}} - \mu_t^* \underbrace{\left(\frac{\partial C_\mu}{\partial U_i}\delta U_i \rho \frac{k^2}{\epsilon}\right)}_{\frac{\partial M_{\mu_t}}{\partial U_i}} \Bigg] \mathrm{d}\Omega \end{aligned} \tag{7.7}$$

where

$$\begin{aligned}\frac{\partial P_\epsilon}{\partial U_i}\delta U_i &= \frac{\partial C_1}{\partial U_i}\delta U_i S\epsilon + C_1\frac{\partial S}{\partial U_i}\delta U_i\epsilon \\ &= \left(\frac{5k}{\epsilon(5+\eta)^2}+1\right)\frac{\partial S}{\partial U_i}\delta U_i \\ &= \frac{1}{2S}\left(\frac{5k}{\epsilon(5+\eta)^2}+1\right)S_{ij}\left(\frac{\partial \delta U_i}{\partial x_j}+\frac{\partial \delta U_j}{\partial x_i}\right),\end{aligned}$$

while

$$\frac{\partial C_\mu}{\partial U_i}\delta U_i = -C_\mu^2\frac{k}{\epsilon}\left(\frac{\partial A_s}{\partial U_i}\delta U_i U_s + A_s\frac{\partial U_s}{\partial U_i}\delta U_i\right),$$

which, after applying the chain rule, can be rewritten as

$$\frac{\partial C_\mu}{\partial U_i}\delta U_i = -C_\mu^2\frac{k}{\epsilon}\left(\underbrace{\frac{\partial A_s}{\partial \phi}\frac{\partial \phi}{\partial W}\frac{\partial W}{\partial S_{ij}}}_{\frac{\partial A_s}{\partial S_{ij}}}\underbrace{\frac{\partial S_{ij}}{\partial U_i}\delta U_i}_{\delta S_{ij}} + A_s\left[\frac{\partial U_s}{\partial S_{ij}}\delta S_{ij} + \frac{\partial U_s}{\partial \widetilde{\Omega}_{ij}}\underbrace{\frac{\partial \widetilde{\Omega}_{ij}}{\partial U_i}\delta U_i}_{\delta\widetilde{\Omega}_{ij}}\right]\right),$$

for which

$$\begin{aligned}\frac{\partial A_s}{\partial S_{ij}} = \left(-\sqrt{6}\sin(\phi)\right)&\left(-\frac{\sqrt{6}}{6}\frac{\left[\tanh(s(\sqrt{6}W+1))-\tanh(s(\sqrt{6}W-1))\right]}{\sqrt{1-\min(\max(\sqrt{6}W,-1),1)}}\right) \\ &\left(2\sqrt{2}\left[\frac{3S_{ij}S_{jk}S^3 - S_{ij}S_{jk}S_{kl}(2S+4)S_{ij}}{S^6}\right]\right),\end{aligned}$$

and

$$\begin{aligned}\frac{\partial U_s}{\partial S_{ij}} &= \frac{S_{ij}}{U_s}, \\ \frac{\partial U_s}{\partial \widetilde{\Omega}_{ij}} &= \frac{\widetilde{\Omega}_{ij}+\widetilde{\Omega}_{ji}}{2U_s}.\end{aligned}$$

Note that $s >> 1$ is a free parameter to the hyperbolic step function, thus dealing with local discontinuity resulting from min/max operators.

As S_{ij} and $\widetilde{\Omega}_{ij}$ being linear operators of U_i, their total variations are straightforward,

$$\begin{aligned}\delta\widetilde{\Omega}_{ij} &= \frac{\partial \widetilde{\Omega}_{ij}}{\partial U_i}\delta U_i = \frac{1}{2}\left(\frac{\partial \delta U_i}{\partial x_j}-\frac{\partial \delta U_j}{\partial x_i}\right), \\ \delta S_{ij} &= \frac{\partial \widetilde{\Omega}_{ij}}{\partial U_i}\delta U_i = \frac{1}{2}\left(\frac{\partial \delta U_i}{\partial x_j}+\frac{\partial \delta U_j}{\partial x_i}\right).\end{aligned}$$

It is worth mentioning that $\partial M_{\mu_t}/\partial U_i$ in (7.7) arises from the so called "realizable form" of the eddy viscosity relation in (Shih et al., 1995), which for other revision of $k-\epsilon$ model vanishes naturally.

Term (II) expansion : With no dynamics being solved for the mean pressure, due to incompressibility, the expanded form of the term (II) is straightforward. The directional derivative of the Lagrangian with respect to δP leads to

$$\left\langle \frac{\partial \mathcal{L}}{\partial P}, \delta P \right\rangle_{\Omega} = \int_{\Omega} \frac{\partial \mathcal{J}}{\partial P} \delta P \, \mathrm{d}\Omega + \int_{\Omega} U_i^* \frac{\partial \delta P}{\partial x_i} \, \mathrm{d}\Omega. \tag{7.8}$$

Term (III) expansion : Differentiation w.r.t the turbulent kinetic reads as follow:

$$\begin{aligned}\left\langle \frac{\partial \mathcal{L}}{\partial k}, \delta k \right\rangle_{\Omega} = \int_{\Omega} \Bigg[k^* \underbrace{\left(\frac{\partial \rho U_j \delta k}{\partial x_j} - \frac{\partial}{\partial x_j} \left[\left(\mu + \frac{\mu_t}{\sigma_k} \right) \frac{\partial \delta k}{\partial x_i} \right] \right)}_{\frac{\partial M_k}{\partial k}} + \epsilon^* \underbrace{\left(-\frac{\partial C_1}{\partial k} \delta k S \epsilon + \frac{\partial S_\epsilon}{\partial k} \delta k \right)}_{\frac{\partial M_\epsilon}{\partial k}} \\ - \mu_t^* \underbrace{\left(\frac{\partial C_\mu}{\partial k} \delta k \rho \frac{k^2}{\epsilon} + 2 \rho C_\mu \frac{k}{\epsilon} \delta k \right)}_{\frac{\partial M_{\mu_t}}{\partial k}} \Bigg] \mathrm{d}\Omega.\end{aligned} \tag{7.9}$$

with

$$\frac{\partial C_1}{\partial k} \delta k = \frac{5}{\epsilon (5+\eta)^2} S \delta k, \quad \frac{\partial S_\epsilon}{\partial k} \delta k = -\left(\frac{\epsilon}{k + \sqrt{\mu \epsilon}} \right)^2 \delta k, \quad \frac{\partial C_\mu}{\partial k} \delta k = -\frac{C_\mu^2 A_s U_s}{\epsilon} \delta k.$$

Term (IV) expansion : Differentiation w.r.t the energy dissipation rate reads as follow:

$$\begin{aligned}\left\langle \frac{\partial \mathcal{L}}{\partial \epsilon}, \delta \epsilon \right\rangle_{\Omega} = \int_{\Omega} [\, k^* \underbrace{(\rho \delta \epsilon)}_{\frac{\partial M_k}{\partial \epsilon}} + \epsilon^* \underbrace{\left(\frac{\partial \rho U_j \delta \epsilon}{\partial x_j} - \frac{\partial}{\partial x_j} \left[\left(\mu + \frac{\mu_t}{\sigma_\epsilon} \right) \frac{\partial \delta \epsilon}{\partial x_i} \right] - \frac{\partial C_1}{\partial \epsilon} \delta \epsilon S \epsilon - C_1 S \delta \epsilon + \frac{\partial S_\epsilon}{\partial \epsilon} \delta \epsilon \right)}_{\frac{\partial M_\epsilon}{\partial \epsilon}} \\ - \mu_t^* \underbrace{\left(\frac{\partial C_\mu}{\partial \epsilon} \delta \epsilon \rho \frac{k^2}{\epsilon} - 2 \rho C_\mu \frac{k}{\epsilon^2} \delta \epsilon \right)}_{\frac{\partial M_{\mu_t}}{\partial \epsilon}}] \, \mathrm{d}\Omega.\end{aligned} \tag{7.10}$$

with

$$\frac{\partial C_1}{\partial \epsilon} \delta \epsilon = -\frac{5 \eta}{\epsilon (5+\eta)^2} S \delta \epsilon, \quad \frac{\partial S_\epsilon}{\partial \epsilon} \delta \epsilon = -\left(\frac{\epsilon}{k + \sqrt{\mu \epsilon}} \right)^2 \delta \epsilon, \quad \frac{\partial C_\mu}{\partial \epsilon} \delta \epsilon = -\frac{C_\mu^2 A_s U_s}{\epsilon} \delta \epsilon.$$

Term (V) expansion : Differentiation w.r.t the eddy viscosity leads to

$$\left\langle \frac{\partial \mathcal{L}}{\partial \mu_t}, \delta\mu_t \right\rangle_\Omega = \int_\Omega \sum_{i=1}^{3} U_i^* \underbrace{\left(-\frac{\partial}{\partial x_j}\left[\delta\mu_t \left(\frac{\partial U_i}{\partial x_j} + \frac{\partial U_j}{\partial x_i} \right) \right] \right)}_{\frac{\partial M_{U_i}}{\partial \mu_t}} + k^* \underbrace{\left(-\frac{\partial}{\partial x_j}\left[\frac{\delta\mu_t}{\sigma_k}\frac{\partial k}{\partial x_i} \right] - \delta\mu_t \left(\frac{\partial U_i}{\partial x_j} + \frac{\partial U_j}{\partial x_i} \right)\frac{\partial U_i}{\partial x_j} \right)}_{\frac{\partial M_k}{\partial \mu_t}} + \epsilon^* \underbrace{\left(-\frac{\partial}{\partial x_j}\left[\frac{\delta\mu_t}{\sigma_\epsilon}\frac{\partial \epsilon}{\partial x_i} \right] \right)}_{\frac{\partial M_\epsilon}{\partial \mu_t}} + \mu_t^* \underbrace{(\delta\mu_t)}_{\frac{\partial M_{\mu_t}}{\partial \mu_t}} \mathrm{d}\Omega. \tag{7.11}$$

The duality application

In this section, integral terms ($I^* - V^*$) are expanded except the boundary integrals ($B.I$) which are discussed in chapter (3). In what follows, each collected volume integrals are constitutive of each of the adjoint differential equations.

Term (I^*) expansion :

$$\begin{aligned}\left\langle \frac{\partial \mathcal{L}}{\partial U_i}, \delta U_i \right\rangle_\Omega = & \int_\Omega \sum_{i=1}^{3} \delta U_i \left(-\rho \frac{\partial U_j U_i^*}{\partial x_j} - \rho U_j \frac{\partial U_j^*}{\partial x_i} - \frac{\partial}{\partial x_j}\left[\mu_{eff}\left(\frac{\partial U_i^*}{\partial x_j} + \frac{\partial U_j^*}{\partial x_i} \right) \right] \right) \mathrm{d}\Omega \\ & + \int_\Omega \delta U_i \frac{\partial P^*}{\partial x_i} \mathrm{d}\Omega \\ & - \int_\Omega \delta U_i \left(k\frac{\partial k^*}{\partial x_i} - \frac{2}{3}\frac{\partial k k^*}{\partial x_i} + \frac{\partial}{\partial x_i}\left[\mu_t 4 S_{ij} k^* \right] \right) \mathrm{d}\Omega \\ & - \int_\Omega \delta U_i \left(\epsilon \frac{\partial \epsilon^*}{\partial x_i} \right) \mathrm{d}\Omega \\ & + \int_\Omega \delta U_i \frac{\partial}{\partial x_i}\left[\frac{2C_1 \epsilon \epsilon^* S_{ij}}{S} + \frac{5}{(5+\eta)^2}\left(0.5\tanh(\frac{s\eta}{5+\eta}) - 0.43 \right) + 0.5 \right) k\epsilon^* 2 S_{ij} \Big] \mathrm{d}\Omega \\ & + \int_\Omega \delta U_i \frac{\partial}{\partial x_i}\left(\frac{\partial \mu_t}{\partial U_i}\mu_t^* \right) \mathrm{d}\Omega \\ & + B.I \end{aligned} \tag{7.12}$$

Term (II^*) expansion :

$$\left\langle \frac{\partial \mathcal{L}}{\partial P}, \delta P \right\rangle_\Omega = \int_\Omega \frac{\partial \mathcal{J}}{\partial P} \delta P \mathrm{d}\Omega + \int_\Omega \delta P \frac{\partial U_j^*}{\partial x_j} \mathrm{d}\Omega + B.I. \tag{7.13}$$

Term (III^*) expansion :

$$\begin{aligned}\left\langle \frac{\partial \mathcal{L}}{\partial k}, \delta k \right\rangle_\Omega &= \int_\Omega \delta k \left(-\frac{\partial \rho U_j k^*}{\partial x_j} - \frac{\partial}{\partial x_i}\left[\left(\mu + \frac{\mu_t}{\sigma_k}\right) \frac{\partial k^*}{\partial x_j} \right] - \rho \frac{2}{3} \frac{\partial U_i}{\partial x_i} k^* \right) \mathrm{d}\Omega \\ &- \int_\Omega \delta k \left(\rho 5 S^2 \frac{\epsilon^*}{(5+\eta)^2} \left(0.5 \tanh(\frac{s\eta}{5+\eta}) - 0.43) + 0.5 \right) + \rho\rho C_2 \epsilon \frac{\epsilon^*}{(k+\sqrt{\mu\epsilon})} \right) \mathrm{d}\Omega \\ &+ \int_\Omega \delta k \left((2\frac{\mu_t}{k} - A_s U_s \frac{{\mu_t}^2}{k}) \mu_t^* \right) \mathrm{d}\Omega + B.I. \end{aligned} \tag{7.14}$$

Term (IV^*) expansion :

$$\begin{aligned}\left\langle \frac{\partial \mathcal{L}}{\partial \epsilon}, \delta \epsilon \right\rangle_\Omega &= \int_\Omega \delta\epsilon \left(\rho k^*\right) \mathrm{d}\Omega \\ &+ \int_\Omega \delta\epsilon \left(-\frac{\partial \rho U_j \epsilon^*}{\partial x_j} - \frac{\partial}{\partial x_i}\left[\left(\mu + \frac{\mu_t}{\sigma_\epsilon}\right) \frac{\partial \epsilon^*}{\partial x_j} \right] \right) \mathrm{d}\Omega \\ &- \int_\Omega \delta\epsilon \left(\rho C_1 S \epsilon^* + 5 \left(0.5 \tanh(\frac{s\eta}{5+\eta}) - 0.43) + 0.5 \right) k S^2 \frac{\epsilon^*}{([5+\eta]\epsilon)^2} \right) \mathrm{d}\Omega \\ &- \int_\Omega \delta\epsilon \left(2\rho C_2 \frac{\epsilon\epsilon^*}{(k+\sqrt{\mu\epsilon})} - 0.5\rho C_2 \sqrt{\mu} \frac{\epsilon^* \epsilon^{\frac{3}{2}}}{(k+\sqrt{\mu\epsilon})^2} \right) \mathrm{d}\Omega \\ &+ \int_\Omega \delta\epsilon \left((A_s U_s \frac{\mu_t^2}{k\epsilon} - \frac{\mu_t}{\epsilon}) \mu_t^* \right) \mathrm{d}\Omega + B.I. \end{aligned} \tag{7.15}$$

Term (V^*) expansion :

$$\begin{aligned}\left\langle \frac{\partial \mathcal{L}}{\partial \mu_t}, \delta \mu_t \right\rangle_\Omega &= \int_\Omega \delta\mu_t \left(-\left(\frac{\partial U_i}{\partial x_j} + \frac{\partial U_j}{\partial x_i} \right) \frac{\partial U_j^*}{\partial x_i} \right) \mathrm{d}\Omega \\ &+ \int_\Omega \delta\mu_t \left(\frac{\partial P_k}{\partial \mu_t} k^* - \frac{1}{\sigma_k} \frac{\partial k}{\partial x_i} \frac{\partial k^*}{\partial x_i} \right) \mathrm{d}\Omega \\ &+ \int_\Omega \delta\mu_t \left(-\frac{1}{\sigma_\epsilon} \frac{\partial \epsilon}{\partial x_i} \frac{\partial \epsilon^*}{\partial x_i} \right) \mathrm{d}\Omega \\ &- \int_\Omega \delta\mu_t (\mu_t^*) \mathrm{d}\Omega + B.I. \end{aligned} \tag{7.16}$$

Bibliography

Adrian, R.J., 1991. Particle-imaging techniques for experimental fluid mechanics. Annual review of fluid mechanics 23, 261–304.

Bagheri, S., Åkervik, E., Brandt, L., Henningson, D.S., 2009. Matrix-Free Methods for the Stability and Control of Boundary Layers. AIAA Journal 47, 1057–1068.

Bailey, A., 1933. Wind pressures on buildings. Selected Engineering Papers 1.

Baker, C., 1980. The turbulent horseshoe vortex. Journal of Wind Engineering and Industrial Aerodynamics 6, 9–23.

Bauer, W., Chandramouli, P., Chapron, B., Li, L., Mémin, E., 2020a. Deciphering the role of small-scale inhomogeneity on geophysical flow structuration: A stochastic approach. Journal of Physical Oceanography 50, 983–1003.

Bauer, W., Chandramouli, P., Li, L., Mémin, E., 2020b. Stochastic representation of mesoscale eddy effects in coarse-resolution barotropic models. Ocean Modelling 151, 101646.

Beneddine, S., Mettot, C., Sipp, D., 2015. Global stability analysis of underexpanded screeching jets. European Journal of Mechanics - B/Fluids 49, 392–399.

Beneddine, S., Sipp, D., Arnault, A., Dandois, J., Lesshafft, L., 2016. Conditions for validity of mean flow stability analysis. Journal of Fluid Mechanics 798, 485–504.

Beneddine, S., Yegavian, R., Sipp, D., Leclaire, B., 2017. Unsteady flow dynamics reconstruction from mean flow and point sensors: an experimental study. Journal of Fluid Mechanics 824, 174–201.

Bergthörsson, P., Döös, B.R., 1955. Numerical weather map analysis. Tellus 7, 329–340.

Beyou, S., Cuzol, A., Subrahmanyam Gorthi, S.A.I., Mémin, E., 2013. Weighted ensemble transform kalman filter for image assimilation. Tellus A: Dynamic Meteorology and Oceanography 65, 18803.

Blocken, B., Stathopoulos, T., Carmeliet, J., 2007. CFD simulation of the atmospheric boundary layer: wall function problems. Atmospheric Environment 41, 238–252.

Bocquet, M., Brajard, J., Carrassi, A., Bertino, L., 2019. Data assimilation as a learning tool to infer ordinary differential equation representations of dynamical models. Nonlin. Processes Geophys. 26, 143–162.

Brunton, S., Noack, B., Koumoutsakos, P., 2020. Machine Learning for Fluid Mechanics. Annu. Rev. Fluid Mechanics 52, 477–508.

Bryson, A.E., 1975. Applied optimal control: optimization, estimation and control.

Byrd, R., Lu, P., Nocedal, J., Zhu, C., 1995. A limited memory algorithm for bound constrained optimization. SIAM Journal on scientific computing 16, 1190–1208.

Cermak, J., 1956. Wind tunnel for the study of turbulence in the atmospheric surface layer. CER; 58-42 .

Cermak, J.E., Albertson, M.L., 1958. Use of wind tunnels in the study of atmospheric phenomenon. CER; 58-18 .

Cermak, J.E., Koloseus, H.J., 1954. Development of a miniature air velocity indicator: experimental study to determine sensitivity of new designs. CER; 54-23 .

Cermak, J.E., Peterka, J.A., 1966. Simulation of wind fields over point arguello, california, by wind-tunnel flow over a topographic model. CER; 65-64 .

Chandramouli, P., Memin, E., Heitz, D., 2020. 4D large scale variational data assimilation of a turbulent flow with a dynamics error model. Journal of Computational Physics , 109446.

Cheung, S.H., Oliver, T.A., Prudencio, E.E., Prudhomme, S., M., R.D., 2011. Bayesian uncertainty analysis with applications to turbulence modeling. Reliability Engineering & System Safety 96, 1137–1149.

Cimarelli, A., Leonforte, A., De Angelis, E., Crivellini, A., Angeli, D., 2019. On negative turbulence production phenomena in the shear layer of separating and reattaching flows. Physics Letters A 383, 1019–1026.

Cochran, L., Derickson, R., 2011. A physical modeler's view of computational wind engineering. Journal of Wind Engineering and Industrial Aerodynamics 99, 139–153.

Colburn, C., Cessna, J., Bewley, T., 2011. State estimation in wall-bounded flow systems. part 3. the ensemble kalman filter. Journal of Fluid Mechanics 682, 289–303.

Courtier, P., Talagrand, O., 1987. Variational assimilation of meteorological observations with the adjoint vorticity equation. ii: Numerical results. Quarterly Journal of the Royal Meteorological Society 113, 1329–1347.

Courtier, P., Thépaut, J., Hollingsworth, A., 1994. A strategy for operational implementation of 4d-var, using an incremental approach. Quarterly Journal of the Royal Meteorological Society 120, 1367–1387.

Dagnew, A.K.., Bitsuamlak, G.T., 2010. LES evaluation of wind pressures on a standard tall building with and without a neighboring building , 8.

Davenport, A., 1965. The relationship of wind structure to wind loading, in: Proc. Conf. on Wind Effects on Buildings & Structures, HMSO.

Dow, E., Wang, Q., 2011. Quantification of structural uncertainties in the $k-\omega$ turbulence model, in: 52nd AIAA/ASME/ASCE/AHS/ASC Structures, Structural Dynamics and Materials Conference 19th AIAA/ASME/AHS Adaptive Structures Conference 13t, p. 1762.

Duraisamy, K., Iaccarino, G., Xiao, H., 2019. Turbulence modeling in the age of data. Annual Review of Fluid Mechanics 51, 357–377.

Duraisamy, K., Zhang, Z.J., Singh, A.P., 2015. New approaches in turbulence and transition modeling using data-driven techniques, in: 53rd AIAA Aerospace Sciences Meeting, Kissimmee, Florida.

Durbin, P., 1993. A reynolds stress model for near-wall turbulence. Journal of Fluid Mechanics 249, 465–498.

Duynkerke, P.G., 1988. Application of the $E-\epsilon$ turbulence closure model to the neutral and stable atmospheric boundary layer. Journal of the Atmospheric Sciences 45, 865–880.

Edeling, W.N., Cinnella, P., Dwight, R.P., Bijl, H., 2014. Bayesian estimates of parameter variability in the $k-\epsilon$ turbulence model. Journal of Computational Physics 258, 73–94.

Elsinga, G., Scarano, F., Wieneke, B., van Oudheusden, B.W., 2006. Tomographic particle image velocimetry. Experiments in fluids 41, 933–947.

Emory, M., Larsson, J., Iaccarino, G., 2013. Modeling of structural uncertainties in Reynolds-averaged Navier-Stokes closures. Physics of Fluids 25, 110822.

EN, N., 2005. 1-4: Eurocode 1: Actions sur les structures–partie 1-4: Actions générales–actions du vent.

Errico, R.M., 1997. What is an adjoint model? Bulletin of the American Meteorological Society 78, 2577–2592.

Etling, D., Detering, H.W., Theunert, F., 1985. On the simulation of wind-driven currents in shallow water. Archives for meteorology, geophysics, and bioclimatology, Series A 33, 355–363.

Evensen, G., 2003. The ensemble kalman filter: Theoretical formulation and practical implementation. Ocean dynamics 53, 343–367.

Fadai-Ghotbi, A., Friess, C.and Manceau, R., Borée, J., 2010. A seamless hybrid rans-les model based on transport equations for the subgrid stresses and elliptic blending. Physics of Fluids 22, 055104.

Farchi, A., Bocquet, M., 2019. On the efficiency of covariance localisation of the ensemble kalman filter using augmented ensembles. Frontiers in Applied Mathematics and Statistics 5, 3.

Ferrero, A., Iollo, A., Larocca, F., 2019. RANS closure approximation by artificialneural networks , 15.

Ferziger, J.H., 1990. Approaches to turbulent flow computation: Applications to flow over obstacles , 19.

Ferziger, J.H., 1993. A computational fluid dynamicist's view of CWE, in: Computational Wind Engineering 1, pp. 879–880.

Ferziger, J.H., Perić, M., Street, R.L., 2020. Computational Methods for Fluid Dynamics. Cham.

Foures, D.P.G., Dovetta, N., Sipp, D., Schmid, P.J., 2014. A data-assimilation method for Reynolds-Averaged Navier-Stokes-driven mean flow reconstruction. Journal of Fluid Mechanics 759, 404–431.

Franceschini, L., 2019. Modeling Strategies for Aerodynamic Flow Reconstruction from partial measurements. Ph.D. thesis. Université Paris Saclay.

Franceschini, L., Sipp, D.and Marquet, O., 2020. Mean-flow data assimilation based on minimal correction of turbulence models: Application to turbulent high reynolds number backward-facing step. Phys. Rev. Fluids 5, 094603.

Franke, J., Hirsch, C., Jensen, A., Krüs, H., Schatzmann, M., Westbury, P., Miles, S., Wisse, J., Wright, N., 2004. Recommendations on the use of CFD in predicting pedestrian wind environment, in: Cost action C.

Gatski, T.B., Hussaini, M.Y., Lumley, J.L. (Eds.), 1996. Simulation and modeling of turbulent flows. ICASE/LaRC series in computational science and engineering, New York.

Giles, M.B., Pierce, N.A., 2000. An introduction to the adjoint approach to design. Flow, Turbulence and Combustion 65, 393–415.

Godunov, S.K., 1954. Different methods for shock waves. Moscow State University .

Gosman, A., 1999. Developments in CFD for industrial and environmental applications in wind engineering. Journal of Wind Engineering and Industrial Aerodynamics 81, 21–39.

Griewank, A., Walther, A., 2008. Evaluating derivatives: principles and techniques of algorithmic differentiation.

Grinstein, F.F., Fureby, C., 2005. On monotonically integrated large eddy simulation of turbulent flows based on fct algorithms, in: Flux-Corrected Transport, pp. 79–104.

Gronskis, A., Heitz, D., Mémin, E., 2013. Inflow and initial conditions for direct numerical simulation based on adjoint data assimilation. Journal of Computational Physics 242, 480–497.

Gunzburger, M.D., 2003. Perspectives in flow control and optimization. volume 5.

Hall, M.C.G., Cacuci, D.G., 1983. Physical interpretation of the adjoint functions for sensitivity analysis of atmospheric models. Journal of the Atmospheric Sciences 40, 2537–2546.

Hamill, T.M., Snyder, C., 2000. A hybrid ensemble kalman filter–3d variational analysis scheme. Monthly Weather Review 128, 2905–2919.

Hanjalić, K., Launder, B.E., 1972. A Reynolds stress model of turbulence and its application to thin shear flows. Journal of Fluid Mechanics 52, 609–638.

Hansen, P.C., 1992. Analysis of Discrete Ill-Posed Problems by Means of the L-Curve. SIAM Rev. 34, 561–580.

Hargreaves, D., Wright, N., 2007. On the use of the k– model in commercial CFD software to model the neutral atmospheric boundary layer. Journal of Wind Engineering and Industrial Aerodynamics 95, 355–369.

Harouna, S.K., Mémin, E., 2017. Stochastic representation of the reynolds transport theorem: revisiting large-scale modeling. Computers & Fluids 156, 456–469.

Hirsch, C., Bouffioux, V., Wilquem, F., 2002. Cfd simulation of the impact of new buildings on wind comfort in an urban area, in: Workshop proceedings, cost action C, pp. 3–4.

Hirt, C., Cook, J., 1972. Calculating three-dimensional flows around structures and over rough terrain. Journal of Computational Physics 10, 324–340.

Holmes, J.D., 1975. Aeroelastic tests on the CAARC standard building model.

Hunt, J., 1971. Further aspects of the theory of wakes behind buildings and comparison of theory with experiment. Central Electricity Research Laboratory Rep. RD/L/R/1665 .

Hunt, J., Smith, G., 1969. Theory of Wakes Behind Buildings and Some Provisional Experimental Results.

Iglesias, M.A., Law, K.J.H., Stuart, A.M., 2013. Ensemble Kalman methods for inverse problems. Inverse Problems 29, 045001.

Irwin, P.A., 2008. Bluff body aerodynamics in wind engineering. Journal of Wind Engineering and Industrial Aerodynamics 96, 701–712.

Irwin, P.A., Kochanski, W.W., 1995. Measurement of structural wind loads using the high frequency pressure integration method, in: Restructuring: America and Beyond, ASCE. pp. 1631–1634.

Issa, R.I., 1995. Rise of total pressure in frictional flow. AIAA journal 33, 772–774.

Jasak, H., 1996. Error analysis and estimation in the finite volume method with applications to fluid flows. Ph.D. thesis. Imperial College, University of London. 1028.

Jasak, H., Weller, H., Gosman, A., 1999. High resolution NVD differencing scheme for arbitrarily unstructured meshes. International Journal for Numerical Methods in Fluids 31, 431–449.

Jensen, M., 1958. The model-law for phenomena in natural wind. Ingenioren 2, 121–128.

Kalitzin, G., Medic, G., Iaccarino, G., Durbin, P., 2005. Near-wall behavior of RANS turbulence models and implications for wall functions. Journal of Computational Physics 204, 265–291.

Kalman, R.E., 1960. A new approach to linear filtering and prediction problems .

Kato, H., Obayashi, S., 2013. Approach for uncertainty of turbulence modeling based on data assimilation technique. Computers & Fluids 85, 2–7.

Kato, H., Obayashi, S., 2014. Data Assimilation for Turbulent Flows, in: 16th AIAA Non-Deterministic Approaches Conference, National Harbor, Maryland.

Kawamura, T., Hiwada, M., Hibino, T., Mabuchi, I., Kumada, M., 1984. Flow around a finite circular cylinder on a flat plate: Cylinder height greater than turbulent boundary layer thickness. Bulletin of JSME 27, 2142–2151.

Launder, B.E., Reece, G.J., Rodi, W., 1975. Progress in the development of a Reynolds-stress turbulence closure. Journal of Fluid Mechanics 68, 537–566.

Launder, B.E., Sharma, B.I., 1974. Application of the energy-dissipation model of turbulence to the calculation of flow near a spinning disc. Letters in Heat and Mass Transfer 1, 131–137.

Le Dimet, F.X., Talagrand, O., 1986. Variational algorithms for analysis and assimilation of meteorological observations: theoretical aspects. Tellus A: Dynamic Meteorology and Oceanography 38, 97–110.

Leonard, B.P., 1988. Simple high-accuracy resolution program for convective modelling of discontinuities. International journal for numerical methods in fluids 8, 1291–1318.

Li, Y., Zhang, J., Dong, G., Abdullah, N.S., 2020. Small-scale reconstruction in three-dimensional Kolmogorov flows using four-dimensional variational data assimilation. Journal of Fluid Mechanics 885.

Li, Z., Zhang, H., Bailey, S.C., Hoagg, J.B., Martin, A., 2017. A data-driven adaptive Reynolds-Averaged Navier–Stokes $k-\omega$ model for turbulent flow. Journal of Computational Physics 345, 111–131.

Ling, J., Templeton, J., 2015. Evaluation of machine learning algorithms for prediction of regions of high Reynolds averaged Navier Stokes uncertainty. Physics of Fluids 27, 085103.

Lions, J.L., 1971. Optimal control of systems governed by partial differential equations problèmes aux limites .

Loiseau, J.C., Bucci, M.A., Cherubini, S., Robinet, J.C., 2018. Time-stepping and Krylov methods for large-scale instability problems. arXiv:1804.03859 [physics] .

Lorenc, A.C., 2003. The potential of the ensemble kalman filter for nwp?a comparison with 4d-var. Quarterly Journal of the Royal Meteorological Society: A journal of the atmospheric sciences, applied meteorology and physical oceanography 129, 3183–3203.

Lumley, J.L., McMichael, J.M., 1995. Turbulence Modeling. Technical Report. SIBLEY SCHOOL OF MECHANICAL AND AEROSPACE ENGINEERING ITHACA NY.

Manceau, R., Hanjalić, K., 2002. Elliptic blending model: A new near-wall reynolds-stress turbulence closure. Physics of Fluids 14, 744–754.

Manceau, R., Wang, M., Laurence, D., 2001. Inhomogeneity and anisotropy effects on the redistribution term in Reynolds-averaged Navier–Stokes modelling. Journal of Fluid Mechanics 438, 307–338.

Margheri, L., Meldi, M., Salvetti, M.V., Sagaut, P., 2014. Epistemic uncertainties in rans model free coefficients. Computers & Fluids 102, 315–335.

McKeon, B., Sharma, A., 2010. A critical layer model for turbulent pipe flow. arXiv preprint arXiv:1001.3100 .

Melbourne, W., 1980. Comparison of measurements on the CAARC standard tall building model in simulated model wind flows. Journal of Wind Engineering and Industrial Aerodynamics 6, 73–88.

Meldi, M., Poux, A., 2017. A reduced order model based on Kalman filtering for sequential data assimilation of turbulent flows. Journal of Computational Physics 347, 207–234.

Mémin, E., 2014. Fluid flow dynamics under location uncertainty. Geophys. & Astro. Fluid Dyn. 108, 119–146.

Meng, F., He, B., Zhu, J., Zhao, D., Darko, A., Zhao, Z.Q., 2018. Sensitivity analysis of wind pressure coefficients on CAARC standard tall buildings in CFD simulations. Journal of Building Engineering 16, 146–158.

Menter, F.R., 1994. Two-equation eddy-viscosity turbulence models for engineering applications. AIAA journal 32, 1598–1605.

Meroney, R.N., Derickson, R., 2014. Virtual reality in wind engineering: the windy world within the computer. Journal of Wind Engineering and Industrial Aerodynamics 11, 11–26.

Moarref, R., Sharma, A.S., Tropp, J.A., McKeon, B.J., 2013. Model-based scaling of the streamwise energy density in high-Reynolds number turbulent channels. Journal of Fluid Mechanics 734, 275–316.

Mohammadi, B., Puigt, G., 2006. Wall functions in computational fluid mechanics. Computers & Fluids 35, 1108–1115.

Mons, V., Chassaing, J., Gomez, T., Sagaut, P., 2014. Is isotropic turbulence decay governed by asymptotic behavior of large scales? an eddy-damped quasi-normal markovian-based data assimilation study. Physics of Fluids 26, 115105.

Mons, V., Chassaing, J.C., Gomez, T., Sagaut, P., 2016. Reconstruction of unsteady viscous flows using data assimilation schemes. Journal of Computational Physics 316, 255–280.

Mons, V., Margheri, L., Chassaing, J.C., Sagaut, P., 2017. Data assimilation-based reconstruction of urban pollutant release characteristics. Journal of Wind Engineering and Industrial Aerodynamics 169, 232–250.

Moukalled, F., Mangani, L., Darwish, M., 2016. The finite volume method in computational fluid dynamics. volume 113.

Murakami, S., 1990. Computational wind engineering. Journal of Wind Engineering and Industrial Aerodynamics 36, 517–538.

Murakami, S., 1993. Comparison of various turbulence models applied to a bluff body, in: Computational Wind Engineering 1, pp. 21–36.

Murakami, S., 1997. Current status and future trends in computational wind engineering. Journal of Wind Engineering and Industrial Aerodynamics 67, 3–34.

Murakami, S., Mochida, A., 1989. Three-dimensional numerical simulation of turbulent flow around buildings using the k- ε turbulence model. Building and Environment 24, 51–64.

Murakami, S., Mochida, A., Hayashi, Y., Sakamoto, S., 1992. Numerical study on velocity-pressure field and wind forces for bluff bodies by $k-\epsilon$, asm and les. Journal of Wind Engineering and Industrial Aerodynamics 44, 2841–2852.

Murakami, S., Mochida, A., Hibi, K., 1987. Three-dimensional numerical simulation of air flow around a cubic model by means of large eddy simulation. Journal of Wind Engineering and Industrial Aerodynamics 25, 291–305.

Nozawa, K., Tamura, T., 2002. Large eddy simulation of the flow around a low-rise building immersed in a rough-wall turbulent boundary layer. Journal of Wind Engineering and Industrial Aerodynamics 90, 1151–1162.

Othmer, C., 2008. A continuous adjoint formulation for the computation of topological and surface sensitivities of ducted flows. International Journal for Numerical Methods in Fluids 58, 861–877.

Ozmen, Y., Baydar, E., van Beeck, J., 2016. Wind flow over the low-rise building models with gabled roofs having different pitch angles. Building and Environment 95, 63–74.

Papadakis, N., Mémin, É., Cuzol, A., Gengembre, N., 2010. Data assimilation with the weighted ensemble kalman filter. Tellus A: Dynamic Meteorology and Oceanography 62, 673–697.

Parente, A., Gorlé, C., van Beeck, J., Benocci, C., 2011. A comprehensive modeling approach for the neutral atmospheric boundary layer: consistent inflow conditions, wall function and turbulence model. Boundary-Layer meteorology 140, 411.

Parish, E.J., Duraisamy, K., 2016. A paradigm for data-driven predictive modeling using field inversion and machine learning. Journal of Computational Physics 305, 758–774.

Patankar, S.V., 1980. Numerical heat transfer and fluid flow(book). Washington, DC, Hemisphere Publishing Corp., 1980. 210 p .

Paterson, D., Apelt, C., 1989. Simulation of wind flow around three-dimensional buildings. Building and Environment 24, 39–50.

Peric, M., 1997. Numerical methods for computing turbulent flows , 61.

Peterka, J., Meroney, R., Kothari, K., 1985. Wind flow patterns about buildings. Journal of Wind Engineering and Industrial Aerodynamics 21, 21–38.

Peterka, J.A., Cermak, J.E., 1977. Turbulence in building wakes, 4th int. conf. on wind effects on buildings and structures, london, 1975.

Plessix, R.E., 2006. A review of the adjoint-state method for computing the gradient of a functional with geophysical applications. Geophysical Journal International 167, 495–503.

Pope, S.B., 1975. A more general effective-viscosity hypothesis. Journal of Fluid Mechanics 72, 331.

Pope, S.B., 2000. Turbulent flows. Cambridge ; New York.

Protas, B., Bewley, T.R., Hagen, G., 2004. A computational framework for the regularization of adjoint analysis in multiscale pde systems. Journal of Computational Physics 195, 49–89.

Rhie, C.M., Chow, W.L., 1983. Numerical study of the turbulent flow past an airfoil with trailing edge separation. AIAA journal 21, 1525–1532.

Richards, P., Norris, S., 2011. Appropriate boundary conditions for computational wind engineering models revisited. Journal of Wind Engineering and Industrial Aerodynamics 99, 257–266.

Richards, P.J., Hoxey, R.P., 1993. Appropriate boundary conditions for computational wind engineering models using the $k - \epsilon$ turbulence model, in: Computational Wind Engineering, pp. 145–153.

Roache, P.J., 1994. Perspective: A method for uniform reporting of grid refinement studies. Journal of Fluids Engineering 116, 405–413.

Roache, P.J., 1997. Quantification of uncertainty in computational fluid dynamics. Annual Review of Fluid Mechanics 29, 123–160.

Robertson, E., Choudhury, V., Bhushan, S., Walters, D., 2015. Validation of OpenFOAM numerical methods and turbulence models for incompressible bluff body flows. Computers & Fluids 123, 122–145.

Robinson, C., 2015. Image data assimilation with fluid dynamics models : application to 3D flow reconstruction , 194.

Rodi, W., 1997. Comparison of LES and RANS calculations of the flow around bluff bodies. Journal of Wind Engineering and Industrial Aerodynamics 69-71, 55–75.

Roe, P.L., 1986. Characteristic-based schemes for the euler equations. Annual review of fluid mechanics 18, 337–365.

Schlichting, H., 1968. Boundary layer theory. volume 960.

Schmitt, F., 2007. About Boussinesq's turbulent viscosity hypothesis: historical remarks and a direct evaluation of its validity. Comptes Rendus Mécanique 335, 617–627.

Schubauer, G.B., Dryden, H.L., 1935. The effect of turbulence on the drag of flat plates.

Sheng, R., Perret, L., Calmet, I., Demouge, F., Guilhot, J., 2018. Wind tunnel study of wind effects on a high-rise building at a scale of 1: 300. Journal of Wind Engineering and Industrial Aerodynamics 174, 391–403.

Shih, T.H., Liou, W.W., Shabbir, A., Yang, Z., Zhu, J., 1995. A new $k-\epsilon$ eddy viscosity model for high Reynolds number turbulent flows-model development and validation. Document ID: 19950005029 (Acquired Dec 28, 1995) Accession .

Shih, T.H., Lumley, J.L., 1993. Remarks on turbulent constitutive relations. Mathematical and Computer Modelling 18, 9–16.

Shirzadi, M., Mirzaei, P.A., Naghashzadegan, M., 2017. Improvement of k-epsilon turbulence model for CFD simulation of atmospheric boundary layer around a high-rise building using stochastic optimization and Monte-Carlo sampling technique. Journal of Wind Engineering and Industrial Aerodynamics 171, 366–379.

Singh, A.P., Duraisamy, K., 2016. Using field inversion to quantify functional errors in turbulence closures. Physics of Fluids 28, 045110.

Smagorinsky, J., 1963. General circulation experiments with the primitive equations: I. the basic experiment. Monthly weather review 91, 99–164.

Sohankar, A., Davidson, L., Norberg, C., 2000. Large Eddy Simulation of Flow Past a Square Cylinder: Comparison of Different Subgrid Scale Models. Journal of Fluids Engineering 122, 39–47.

Spalart, P., Allmaras, S., 1992. A one-equation turbulence model for aerodynamic flows, in: 30th Aerospace Sciences Meeting and Exhibit, Reno,NV,U.S.A.

Spencer, A.J.M., Rivlin, R.S., 1959. Further results in the theory of matrix polynomials. Matrix Polynomials , 17.

Steffen, R.C., Reddy, D., Zaman, K., 1995. Analysis of flowfield from a rectangular nozzle with delta tabs, in: Fluid Dynamics Conference, San Diego,CA,U.S.A.

Summers, D.M., Hanson, T., Wilson, C.B., 1986. Validation of a computer simulation of wind flow over a building model. Building and Environment 21, 97–111.

Surry, D., 1999. Wind loads on low-rise buildings: Past, present and future. Wind Engineering into the 21^{st} Century .

Suzuki, T., 2012. Reduced-order kalman-filtered hybrid simulation combining particle tracking velocimetry and direct numerical simulation. Journal of Fluid Mechanics 709, 249.

Sweby, P.K., 1984. High Resolution Schemes Using Flux Limiters for Hyperbolic Conservation Laws. SIAM Journal on Numerical Analysis 21, 995–1011.

Symon, S., Dovetta, N., McKeon, B.J., Sipp, D., Schmid, P.J., 2017. Data assimilation of mean velocity from 2D PIV measurements of flow over an idealized airfoil. Experiments in Fluids 58, 61.

Symon, S., Sipp, D., Schmid, P.J., McKeon, B.J., 2020. Mean and Unsteady Flow Reconstruction Using Data-Assimilation and Resolvent Analysis. AIAA Journal 58, 575–588.

Tabor, G., Baba-Ahmadi, M., 2010. Inlet conditions for large eddy simulation: A review. Computers & Fluids 39, 553–567.

Tamamidis, P., Assanis, D.N., 1993. Evaluation of various high-order-accuracy schemes with and without flux limiters. International Journal for Numerical Methods in Fluids 16, 931–948.

Tamura, T., Nozawa, K., Kondo, K., 2008. AIJ guide for numerical prediction of wind loads on buildings. Journal of Wind Engineering and Industrial Aerodynamics 96, 1974–1984.

Tavoularis, S., Karnik, U., 1989. Further experiments on the evolution of turbulent stresses and scales in uniformly sheared turbulence. Journal of Fluid Mechanics 204, 457–478.

Thomas, T.G., Williams, J.J.R., 1999. Simulation of skewed turbulent #ow past a surface mounted cube. J. Wind Eng. Ind. Aerodyn. , 14.

Thordal, M.S., Bennetsen, J.C., Koss, H.H.H., 2019. Review for practical application of CFD for the determination of wind load on high-rise buildings. Journal of Wind Engineering and Industrial Aerodynamics 186, 155–168.

Tissot, G., Billard, R., Gabard, G., 2020. Optimal cavity shape design for acoustic liners using helmholtz equation with visco-thermal losses. Journal of Computational Physics 402, 109048.

Tominaga, Y., Mochida, A., Yoshie, R., Kataoka, H., Nozu, T., Yoshikawa, M., Shirasawa, T., 2008. AIJ guidelines for practical applications of cfd to pedestrian wind environment around buildings. Journal of Wind Engineering and Industrial Aerodynamics 96, 1749–1761.

Tominaga, Y., Stathopoulos, T., 2010. Numerical simulation of dispersion around an isolated cubic building: model evaluation of RANS and LES. Building and Environment 45, 2231–2239.

Tominaga, Y., Stathopoulos, T., 2017. Steady and unsteady RANS simulations of pollutant dispersion around isolated cubical buildings: Effect of large-scale fluctuations on

the concentration field. Journal of Wind Engineering and Industrial Aerodynamics 165, 23–33.

Tschanz, T., Davenport, A.G., 1983. The base balance technique for the determination of dynamic wind loads. Journal of Wind Engineering and Industrial Aerodynamics 13, 429–439.

Tsuchiya, M., Murakami, S., Mochida, A., Kondo, K., Ishida, Y., 1997. Development of a new $k - \epsilon$ model for flow and pressure fields around bluff body. Journal of Wind Engineering and Industrial Aerodynamics 67, 169–182.

Versteeg, H.K., Malalasekera, W., 2007. An introduction to computational fluid dynamics: the finite volume method.

Walshe, D., J., E., 1974. Tests on the standard tall building proposed by the Commonwealth Advisory Aeronautical Research Council.

Walshe, J., 2003. CFD modelling of wind flow over complex and rough terrain. Ph.D. thesis. © John Walshe.

Wang, H.F., Zhou, Y., 2009. The finite-length square cylinder near wake. Journal of Fluid Mechanics 638, 453–490.

Warming, R.F., Beam, R.M., 1976. Upwind second-order difference schemes and applications in aerodynamic flows. AIAA Journal 14, 1241–1249.

Wilcox, D.C., 1993. Turbulence modeling for CFD. La Cãnada, CA.

Yakhot, V., Orszag, S.A., Thangam, S., Gatski, T.B., Speziale, C.G., 1992. Development of turbulence models for shear flows by a double expansion technique. Physics of Fluids A: Fluid Dynamics 4, 1510–1520.

Yamada, T., Meroney, R., 1971. Numerical and wind tunnel simulation of airflow over an obstacle, in: BULLETIN OF THE AMERICAN METEOROLOGICAL SOCIETY, p. 522.

Yang, Y., 2014. Study of variational ensemble methods for image assimilation. Ph.D. thesis. Rennes 1.

Yang, Y., Gu, M., Chen, S., Jin, X., 2009. New inflow boundary conditions for modelling the neutral equilibrium atmospheric boundary layer in computational wind engineering. Journal of Wind Engineering and Industrial Aerodynamics 97, 88–95.

Yang, Y., Mémin, E., 2019. Estimation of physical parameters under location uncertainty using an ensemble^2–expectation–maximization algorithm. Quarterly Journal of the Royal Meteorological Society 145, 418–433.

Yang, Y., Robinson, C., Heitz, D., Mémin, E., 2015. Enhanced ensemble-based 4DVar scheme for data assimilation. Computers & Fluids 115, 201–210.

Yoshie, R., Mochida, A., Tominaga, Y., Kataoka, H., Harimoto, K., Nozu, T., Shirasawa, T., 2007. Cooperative project for CFD prediction of pedestrian wind environment in the architectural institute of Japan. Journal of Wind Engineering and Industrial Aerodynamics 95, 1551–1578.

Zhang, D., Jiang, C., Liang, D., Cheng, L., 2015. A review on TVD schemes and a refined flux-limiter for steady-state calculations. Journal of Computational Physics 302, 114–154.

Zymaris, A.S., Papadimitriou, D.I., Giannakoglou, K.C., Othmer, C., 2010. Adjoint wall functions: A new concept for use in aerodynamic shape optimization. Journal of Computational Physics 229, 5228–5245.

UNIVERSITÉ DE RENNES 1

Titre : Étude du couplage modèle-données à l'aide de techniques adjointe pour l'ingénierie du vent

Mot clés : Assimilation de données variationnelle ; Modèle de turbulence ; Ingénierie du vent

Résumé : Dans cette thèse, nous étudions la modélisation de Navier-Stokes moyennée par Reynolds (RANS) avec modèle de fermeture dans le cadre d'assimilation de données variationnelle (VDA) prédictif des écoulements du vent autour de grandes structures. Les données considérées proviennent uniquement des mesures de pression pariétale menées dans des expériences en soufflerie. Ceci constitue une première étape vers l'application du VDA à des situations pratiques de l'ingénierie du vent où les mesures en volume de l'écoulement ne sont généralement pas abordables. La technique VDA est écrite comme un problème d'optimisation, que nous résolvons en utilisant la méthode adjointe. Une attention particulière est accordée à la dérivation du modèle de turbulence adjoint et de la loi de paroi adjointe. La méthodologie adjointe est utilisée dans cette thèse pour répondre à deux objectifs particuliers. D'une part, nous étudions un cadre méthodologique permettant un diagnostic approfondi de la fermeture de turbulence. Cela va de l'analyse des champs adjointe à l'analyse de sensibilité des coefficients et ensuite à leur calibration. D'autres part, visant un couplage efficace entre le modèle et les données, nous considérons la méthode comme un outil de reconstruction de l'écoulement. Dans cette optique, nous avons considéré une assimilation dite sous contrainte faible par intégration de nouveaux termes permettant de corriger les erreurs de modélisation. En diagnostic, l'analyse de sensibilité a révélé un grand intérêt pour l'optimisation des coefficients davantage au niveau des couches de cisaillement résultant de la séparation et moins dans la région de sillage. Dans la calibration, la validité de certaines hypothèses de modélisation a été explorée en observant l'effet de relâchement des relations entre les coefficients. L'application de la contrainte qui assimile le mélange d'énergie de turbulence au mélange d'impulsion a conduit à un meilleur accord avec les données. Par ailleur, il a été souligné qu'une telle fermeture de turbulence est trop rigide pour permettre à la solution s'écarter de son espace de base. En reconstruction, nous avons considéré des termes de forçage additif qui peuvent agir sur les équations de quantité de mouvement et/ou sur les équations de turbulence. Avec des observations parcimonieuses, le champ de sensibilité est généralement peu régulier pour des paramètres distribués, une recherche de paramètre de contrôle dans l'espace de Sobolev est proposée. Il a été démontré que cela conduit à une procédure d'assimilation des données très efficace car elle améliore la direction de descente et fournit un mécanisme de régularisation utile. En résultats, nous montrons que le forçage sur l'équation de la quantité de mouvement permet d'agir efficacement à proximité des capteurs pour corriger la pression, et se trouve en situation de sur-ajustement. Cela peut être amélioré en multipliant préalablement le forçage par le gradient de l'énergie cinétique. Au contraire, agir sur l'équation de transport du taux de dissipation de turbulences améliore la diffusion turbulente qui amène une réduction significative de la longueur de recirculation, mais avec une pénalité en termes de contrôlabilité. Enfin, nous montrons que des reconstructions d'écoulement plus précises peuvent être effectuées en combinant les deux stratégies.

Title: Investigating Data-Model coupling using adjoint techniques for wind engineering

Keywords: Variational data assimilation, Turbulence modeling, Wind engineering

Abstract: In this thesis, we study Reynolds-averaged Navier-Stokes modeling (RANS) with closure model in the framework of variational data assimilation (VDA) predictive of wind flows around large structures. The data considered come only from wall pressure measurements carried out in wind tunnel experiments. This is a first step towards the application of VDA to practical wind engineering situations where volume flow measurements are generally not affordable. The VDA technique is written as an optimization problem, which we solve using the adjoint method. Particular attention is given to the derivation of the adjoint turbulence model and the adjoint wall law. The adjoint methodology is used in this thesis to meet two particular objectives. On the one hand, we propose a methodological framework allowing an in-depth diagnosis of the turbulence closure. This goes from the analysis of fields added to the sensitivity analysis of the coefficients and then to their calibration. On the other hand, aiming at an efficient data-model coupling, we consider the method as a tool for reconstructing the flow. In this perspective, we have considered assimilation under weak constraint by the integration of new terms allowing us to correct closure modeling errors. In the diagnostic study, the sensitivity analysis revealed a great interest in optimizing the coefficients more at the level of the shear layers resulting from the separation and less in the wake region. Upon calibration, the validity of certain modeling assumptions was explored by observing the effect of relaxing the relationships between the coefficients. The application of the constraint which equates the mixture of turbulent kinetic energy to the impulse mixture led to a better agreement with the data. Moreover, it has been pointed out that such a turbulence closure is too rigid to allow the solution to deviate from its initial space. In the reconstruction study, additive forcing terms acting on the momentum equations and/or on the turbulence equations were considered. With sparse observations, the sensitivity field is generally not very regular for distributed parameters, the search for a control parameter in Sobolev's space is proposed. This has been shown to lead to a very efficient data assimilation procedure as it improves descent direction and provides a useful regularization mechanism. As a result, we have shown that forcing on the momentum equation makes it possible to act effectively near the sensors to correct the pressure, and the proposed data assimilation procedure is in a situation of over-fitting. This can be improved by first multiplying the forcing by the gradient of the kinetic energy. On the contrary, acting on the turbulence dissipation transport equation improve turbulent mixing which leads to a significant reduction in the recirculation length, but with a penalty in terms of controllability. Finally, we have shown that more precise flow reconstruction can be performed by combining the two strategies.